Model oriented irradiation experiments in Fe-Cr model alloys

Viacheslav Kuksenko

UNIVERSITÉ DE ROUEN
U.F.R. DE SCIENCES ET TECHNIQUES
Ecole doctorale "SPMII"

␣ ␣ ␣ ␣ ␣ ␣ ␣ ␣ ␣ ␣␣ N° attribué par la bibliothèque

THÈSE

Pour l'obtention du grade de

DOCTEUR DE L'UNIVERSITÉ DE ROUEN

Discipline : Physique – Sciences des Matériaux

Soutenue le 14 Novembre 2011

Viacheslav KUKSENKO

Directeur de Thèse : Philippe PAREIGE
Co-Encadrante : Cristelle PAREIGE

MODEL ORIENTED IRRADIATION EXPERIMENTS IN Fe-Cr MODEL ALLOYS

Membres du Jury :

Mme. Marie France BARTHE	Directrice de Recherches, CEMHTI	Présidente
M. Robin SCHÄUBLIN	Maître de Recherche, EPFL	Rapporteur
M. Philippe MAUGIS	Professeur des Universités, Marseille	Rapporteur
Mme. Mercedes HERNÁNDEZ-MAYORAL	Chargée de Recherches, CIEMAT	
Mme. Brigitte DECAMPS	Directrice de Recherches, CSNSM	
M. Pierre DESGARDIN	Chargé de Recherches, CEMHTI	
Mme. Cristelle PAREIGE	Maître de conférences, Université de Rouen	
M. Philippe PAREIGE	Professeur des Universités, Rouen	

Model oriented irradiation experiments in Fe-Cr model alloys

Abstract: In order to improve the fundamental understanding on the microstructural behavior of irradiated Fe-Cr alloys, model alloys of high-Cr ferritic-martensitic (F-M) steels candidates as structural materials for Gen IV nuclear power plants, a nanoscale description of the microstructure has been performed as a function of Cr concentration and irradiation temperature.

Two series of experiments have been undertaken:

● Fe-5%Cr, Fe-9%Cr and Fe-12%Cr model alloys have been neutron irradiated up to 0.6 dpa at 300°C (the minimum operating temperature of ferritic-martensitic steels in Generation IV reactors). 3D atom probe (3DAP) study has shown that the impurities are also involved in the microstructural evolution under irradiation. Two independent populations of clusters inside the grains have been revealed. The first family, NiSiPCr-enriched clusters have been observed in all the model alloys. The second one, Cr-enriched clusters which correspond to α' clusters, have been observed in the Fe-9%Cr and Fe-12%Cr model alloys. This work has shown that the NiSiPCr-enriched clusters are radiation induced segregations whereas the appearance of Cr-enriched clusters originates from radiation enhanced process. Enrichment in Si, P and Cr has been revealed on dislocation lines, low-angle and high-angle grain boundaries in all model alloys.

● Ion irradiation of the Fe-9%Cr and Fe-12%Cr model alloys has been performed at 500°C (temperature close to the maximum operating temperatures of ferritic-martensitic steels in Generation IV reactors). In-situ TEM study has shown that during 150 keV Fe^+ ion irradiation at 500°C up to 1.5 dpa, damage becomes apparent in the form of randomly distributed dislocation loops. In both model alloys after 1.5 dpa the loops are mainly of [100]-type. 3DAP study of the same alloys irradiated under the same conditions but in the form of sharp tips did not reveal any chemical species redistribution.

This work has been supported by the European Commission within the project GETMAT under grant agreement FP7-212175.

Key words: Fe-Cr Alloys, 3D atom probe, transmission electron microscopy, neutron irradiation, ion irradiation, phase transformation, precipitation, dislocation loops

Etude expérimentale d'alliages modèles Fe-Cr irradiés

Résumé: Afin d'améliorer la compréhension de l'évolution microstructurale des alliages Fe-Cr irradiés, alliages modèles des aciers ferrito-martensitiques (F-M) à haut Cr candidats comme matériaux de structure des réacteurs de génération IV, l'évolution de la microstructure a été étudiée à l'échelle nanométrique en fonction de la teneur en Cr et de la température d'irradiation.

Deux séries d'expériences ont été réalisées:

- Des alliages modèles Fe-5%Cr, Fe-9%Cr et Fe-12%Cr irradiés aux neutrons à 300°C (température minimale de service pour les aciers F-M) jusqu'à 0.6dpa ont été analysés par sonde atomique 3D (3DAP). Ces analyses ont montré que les impuretés sont également impliquées dans l'évolution microstructurale de ces alliages sous irradiation. Deux familles indépendantes de clusters ont été observées : des clusters de NiSiPCr observés dans tous les alliages et des clusters riches en Cr correspondant à la phase α' mais observés uniquement dans les alliages sursaturés en Cr (Fe-9%Cr et Fe-12%Cr). Ce travail a montré que l'apparition des clusters de NiSiPCr est induite par l'irradiation alors que celle des clusters riches en Cr est issue d'un processus accéléré par l'irradiation. Des enrichissements en Si, P et Cr ont été observés sur les lignes de dislocations ainsi que dans des joints de grain de faible et forte désorientation dans tous les alliages.
- Des alliages Fe-9%Cr et Fe-12%Cr ont été irradiés aux ions Fe^+ de 150 keV à 500°C (température maximale de service pour les aciers F-M). Des expériences de MET in situ entreprises jusqu'à une dose de 1.5 dpa, ont montré que le dommage apparaissait sous la forme de boucles de dislocations distribuées de façon homogène dans les grains. Dans les deux alliages modèles les boucles sont principalement du type <100>. L'analyse par 3DAP des mêmes alliages irradiés dans les mêmes conditions mais sous forme de pointes ne révèle aucune redistribution des espèces chimiques après irradiation.

Ce travail a été financé par la commission Européenne sous le projet GETMAT (FP7-212175).

Mots clés: Alliages Fe-Cr, sonde atomique, microscopie électronique en transmission, irradiation aux neutrons, irradiation aux ions, transformation de phase, précipitation, boucles de dislocation

Acknowledgements

My PhD period in the University of Rouen was extremely rich for me. Now, at the end of my thesis I have a lot of people to thank for having made my stay and work here so comfortable and lively.

First of all, I would like to express my deep and sincere gratitude to my supervisors, Pr. Philippe PAREIGE and Cristelle PAREIGE. Their wide experience, guidance, enthusiasm and patience enabled me to develop an understanding of the subject and added considerably to my scientific experience. I learned a lot during this time and I am convinced that this knowledge will help me in the future.

I want also acknowledge Pr. Didier BLAVETTE, director of the laboratory "Groupe de Physique des Materiaux" (GPM), for giving me the opportunity to conduct intensive research in the laboratory.

I would like to thank Mr. Robin SCHÄUBLIN Maître de recherche, École polytechnique fédérale de Lausanne and Pr. Philippe MAUGIS, Université de Marseille, who kindly accepted to review this PhD work, for their detailed and constructive comments which improve the quality of my manuscript.

My thanks also go to the president of the dissertation committee Mme. Marie-France BARTHE, Directrice de Recherches CEMHTI/CNRS, Orléans for her time and efforts in the evaluation of this work.

I am heartily thankful to Mme. Mercedes HERNÁNDEZ-MAYORAL, Chargée de Recherches CIEMAT, Madrid, Mme. Brigitte DECAMPS, Directrice de Recherches, CSNSM Orsay, and to Mr. Pierre DESGARDIN Chargé de Recherches – CEMHTI/CNRS, Orléans for the organization of my work within my research project. I would like to thank them for their kind help, trainings and advices on TEM and PAS experiments and for their consent to participate in the dissertation committee of my thesis.

During this work, I have collaborated with many colleagues for whom I have great regard, and I wish to extend my warmest thanks to all those who have helped me to do my work in GPM.

Big thanks to Bertrand RADIGUET, Gerald DA COSTA and Francois VURPILLOT for their help and for answering quickly all the questions I had about topics of their expertise.

I am thankful to the staff of GPM laboratory for providing me a wonderful working environment and all time support to perform experiments. Special thanks to Cecile GENEVOIS, Beatrice FOULON, Laurence CHEVALIER, Sylvain CHAMBRELAND and Charly VAUDOLON for the assistance they provided during my research project.

Appreciation also goes out to the laboratory office staff, in particular to Agnes DALLE, Christine MION, Caroline JORRY, Miryam MORAND, Romain VINCENT and

Germain MARTIGNY for their help in organization questions and in communication with state institutions, their goodwill and all the instances in which their assistance helped me along the way.

I also thank Dr. Frank BERGNER and collaborators for providing and shipping of the neutron irradiated samples for my investigations.

This work has been supported by the European Commission within the project GETMAT under grant agreement FP7-212175. The contributions to the financial support of my work have been also made by the EDF-CNRS join laboratory EM2VM (Study and Modeling of the Microstructure for Ageing of Materials). I express my gratitude to these organizations for the financial and organizational assistance.

I owe my deepest gratitude to Pr. V.I. BOLSHAKOV, Dr. D. LAUKHIN and Dr. V. BEKETOV. Their advices, exchanges of knowledge and support gave me important guidance during my first steps in materials science. Especially, I want to acknowledge Pr. G.D. SUKHOMLIN for his warmest friendship and encouragement at all times.

The years spent in Rouen would not have been as wonderful without my friends Elena, Viktor, Irina, Mathieu and Johan. I want also to acknowledge wonderful people with whom I shared my PhD years: Nicolas, Marilyne, Adeline, Manuel, Maria, Thomas, Julien, Hefei, Wanghua, Malin and all others my colleagues and friends.

I owe my sincere thanks to Alia GRECHNAIA for her care and belief in me at all times.

My sincere gratitude to my family, especially to my mother and father for the constant encouragement and care they provided me through my entire life.

KUKSENKO Slava

Table of content

Introduction

Decreasing of availability of resources and increasing of oil, gas and electricity prices together with global warming set the problem of development of innovative energetic systems to satisfy future energy demands while maintaining and improving the environment. In this context, nuclear power which provides a steady energy at low prices is one of the solutions allowing the limitation of the greenhouse effect. Nowadays nuclear power meets about 20% of the world's demand for electricity with more than 400 plants in operation [1] and this contribution is even more significant for the economically developed countries. In France, nuclear power is the primary source of electric power, where about 78% of electricity is derived from nuclear energy [2].

At the same time, nuclear energy remains permanently under investigation and development, especially concerning safety and efficiency. These researches become the objects of more and more international collaborations. Eventually, these efforts led to the launching of the development of the innovative Generation-IV nuclear energy systems [3,4] .

The combination of high temperature, high neutron dose and corrosive environment could be a major obstacle for the viability of some of Gen-IV innovative systems. In this context, the European Commission has launched in its 7th Euratom Framework Programme, a research project to qualify commercially available materials and for the longer term, to develop and qualify new materials and corrosion protection barriers for innovative systems. This project has been named ‘Generation IV and Transmutation Materials’ (GETMAT) [5].

Ferritic-martensitic (F-M) steels with an elevated chromium content (usually 7…14%) are considered for use in some Gen-IV reactors (for fuel assemblies, core support/internals, elements of primary system vessel [6–8]) because they have good corrosion/oxidation resistance, good void swelling resistance and relatively good creep resistance. That is why their characterisation under new working conditions is of a large scientific and industrial interest.

The current Ph.D. work, which is a part of the GETMAT project, intends to provide a wide range of experimental data on the microstructural evolution of Fe-Cr alloys (model alloys of F-M steels) during irradiation as a function of variables such as temperature and Cr concentration. The development of multi-scale modelling is one of the driving forces of GETMAT project. The obtained data are expected to allow the prediction of the behaviour of materials under working conditions. The experimental results obtained during the current Ph.D will contribute for model validation.

The Cr concentration in F-M steels is one of the key parameters to be optimized in order to guarantee the favourable properties of these materials under irradiation exposure. It is known that the influence of Cr content on some important technological properties is non-

monotonic. Indeed, the swelling of Fe-Cr base alloys under irradiation have a complex modulation versus Cr content (Figure 1). Indeed, some experiments showed that the measured swelling under irradiation decreases with the addition of small quantities of Cr, remains low for concentrations between 1% and 10% and then may increase for higher Cr contents (see [9,11,14,15]). At the same time, a more complex swelling evolution with a maximum at ~ 9%Cr have been reported in work [10,13]. Another remarkable non-monotonic effect of the Cr concentration with a minimum around 9%Cr [16] is observed in the shift of the ductile-to-brittle transition temperature in irradiated ferritic-martensitic steels. Thus, it becomes important to understand the main mechanisms responsible for such behaviours. Therefore, within the current Ph.D. the investigations of the microstructural response on the irradiation have been performed on three Fe-Cr model alloys with different Cr content, namely: Fe-5%Cr, Fe-9%Cr and Fe-12%Cr.

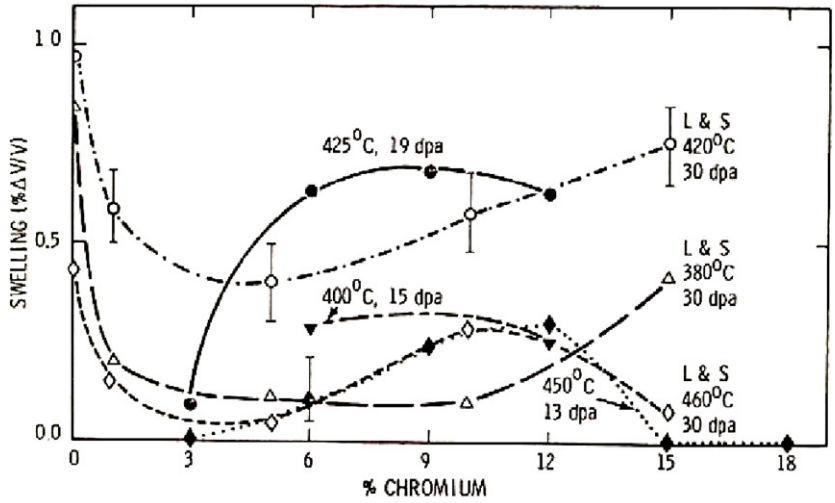

Figure 1. Comparison of swelling measurements as a function of alloy chromium content for the indicated irradiation conditions (data from [9–13]). The influence of Cr content on swelling is highly non-monotonic.

The lower operation temperature limit of high-Cr F-M steels in the reactors of new generation is set between 300 and 350°C. However, this family of steels is known to exhibit irradiation hardening and embrittlement at low temperatures [17,18] and this is one of the main issues which needs to be fully understood for safety reasons. Due to this, the irradiation effect on the structure at temperature equal to 300°C on the mentioned three model alloys has been studied by 3D Atom Probe at the atomic scale.

The operating temperatures of F-M steels in the commercial reactors operating today generally don't exceed 350 °C while the level of temperature required in GEN-IV systems is higher and for non-ODS F-M steels reaches 500 to 550°C. Due to this, the experimental data on the microstructural response of these steels and Fe-Cr model alloys at elevated temperatures are quite demanded. To contribute to the understanding of the formation and

evolution of the point defect clusters and chemical species segregation under high-temperature exposure, the Fe-9%Cr and Fe-12%Cr model alloys have been irradiated with 150keV Fe^+ ions at 500°C and investigated by TEM and 3DAP.

This thesis is divided into 5 chapters. The first chapter briefly describes the innovative nuclear systems focusing on their service conditions and the possible structural materials that can withstand this aggressive environment. Information is given on the high chromium ferritic-martensitic steels, their development and physical metallurgy. A large part of the first chapter is devoted to the effect of the irradiation on the microstructure of Fe-based alloys, such as the appearance of point defects clusters, segregation under irradiation, etc… The behavior of irradiated Fe-Cr based alloys is pointed out as well.

The second chapter deals with the description of the studied materials, their elaboration and irradiation conditions. The combination of three experimental techniques has been chosen: TEM for quantification of the evolution of the dislocation structure, 3D atom probe (3DAP), which provides 3D structure at near atomic scale and positron annihilation spectroscopy (PAS) which is sensitive to open volume defects. The basic concepts of these three experimental techniques as well as the microstructural data that can be achieved are also described in the second chapter. Attention is also paid on the explanation of 3DAP data treatment methods.

The third part describes the microstructure of the Fe-Cr model alloys (namely Fe-5%Cr, Fe-9%Cr and Fe-12%Cr) in the as-received state since the response of the microstructure on irradiation depends on the microstructure before exposure. Metallographic information on grain and dislocation structure, distribution of chemical elements and open-volume defects are covered by this chapter.

The forth chapter of the current thesis provides an atomic scale description of the industrial purity Fe-5%Cr, Fe-9%Cr and Fe-12%Cr model alloys, neutron irradiated at 300°C. The 3DAP studies are focused on the intra- and inter-granular microstructure. We have compared our findings with information on these model alloy collected by different techniques in other laboratories-participants of the GETMAT project (TEM [12,19], SANS [20–22]) in order to have a better understanding of the observed chemical species redistributions.

The fifth chapter deals with the microstructural data obtained on the Fe-9%Cr and Fe-12%Cr model alloys ion irradiated with 150keV Fe^+ ions at 500°C. The information on the microstructural response to the exposure is deduced from the combination of the data on dislocation structure evolution (in-situ TEM investigation) and the evolution of the chemical elements distribution (3DAP experiments). The results of 3DAP examinations of the Fe-9%Cr and Fe-12%Cr model alloys ion irradiated with 150keV Fe^+ ions at 300°C are presented in the chapter as well.

References

[1] M.M. Abu-Khader, Progress in Nuclear Energy 51 (2009) 225-235.
[2] IEA Energy Technology Essentials: Nuclear Power, http://www.iea.org/publications/free_new_Desc.asp?PUBS_ID=1916, 2007.
[3] A Technology Roadmap for Generation IV Nuclear Energy Systems. Issued by the U.S. DOE Nuclear Energy Research Advisory Committee and the Generation IV International Forum.(http://www.gen-4.org/Technology/roadmap.htm), 2002.
[4] T. Abram, S. Ion, Energy Policy 36 (2008) 4323-4330.
[5] Generation IV and Transmutation Materials (GETMAT) – Collaborative Project, Seventh European Commission Framework Programme, Fission – 2007 – 6.0.02 – Cross Cutting Topic: Materials for Transmutation Technologies and Advanced Reactors, FP7-212175, 2007.
[6] L.K. Mansur, A.F. Rowcliffe, R.K. Nanstad, S.J. Zinkle, W.R. Corwin, R.E. Stoller, Journal of Nuclear Materials 329-333 (2004) 166-172.
[7] C. Fazio, A. Alamo, A. Almazouzi, S. De Grandis, D. Gomez-Briceno, J. Henry, L. Malerba, M. Rieth, Journal of Nuclear Materials 392 (2009) 316-323.
[8] C. Fazio, D.G. Briceno, M. Rieth, A. Gessi, J. Henry, L. Malerba, Nuclear Engineering and Design In Press (2011).
[9] E.A. Little, D.A. Stow, Journal of Nuclear Materials 87 (1979) 25-39.
[10] D.S. Gelles, Journal of Nuclear Materials 225 (1995) 163-174.
[11] E.A. Little, Journal of Nuclear Materials 87 (1979) 11-24.
[12] Matijasevic M., Microstructure and Mechanical Properties of Fe-Cr Model Alloys and High Cr Steels Under Neutron Irradiation, PhD thesis., Gent University, 2007.
[13] F.A. Garner, M.B. Toloczko, B.H. Sencer, Journal of Nuclear Materials 276 (2000) 123-142.
[14] Y.V. Konobeev, A.M. Dvoriashin, S.I. Porollo, F.A. Garner, Journal of Nuclear Materials 355 (2006) 124-130.
[15] S.I. Porollo, A.M. Dvoriashin, A.N. Vorobyev, Y.V. Konobeev, Journal of Nuclear Materials 256 (1998) 247-253.
[16] A. Kohyama, A. Hishinuma, D.S. Gelles, R.L. Klueh, W. Dietz, K. Ehrlich, Journal of Nuclear Materials 233-237 (1996) 138 - 147.
[17] R.L. Klueh, D.R. Harries, High-Chromium Ferritic and Martensitic Steels for Nuclear Applications, ASTM, Bridgeport, 2001.
[18] Klueh R. L., International Materials Reviews 50 (2005) 287-310(24).
[19] M. Matijasevic, A. Almazouzi, Journal of Nuclear Materials 377 (2008) 147-154.
[20] F. Bergner, A. Ulbricht, C. Heintze, Scripta Materialia 61 (2009) 1060-1063.
[21] C. Heintze, A. Ulbricht, F. Bergner, H. Eckerlebe, J. Phys.: Conf. Ser. 247 (2010) 012035.
[22] C. Heintze, F. Bergner, A. Ulbricht, H. Eckerlebe, Journal of Nuclear Materials 409 (2011) 106-111.

CHAPTER 1.

BIBLIOGRAPHY

Most nuclear electricity is generated using the reactor systems which were developed in the 1950s and improved since. A brief overview of the history of nuclear power plants as well as an introduction to the most possible future installations for Generation IV reactor systems are given in the first section of the current chapter.

Despite the significant differences which exist among the various innovative reactor concepts, the operating conditions envisaged for whole of these systems are all highly demanding due to the specification of the innovative systems. Combination of high operating temperature, high neutron dose and corrosive environment represent a major challenge for the viability of the Generation IV systems. The nuclear power plant service conditions and the possible structural materials that can withstand this aggressive environment will be briefly described in the second part of this chapter.

High chromium ferritic-martensitic (F-M) steel is one of the leading candidates for structural material in innovative generation of nuclear power plants. This class of steel is designed to combine corrosion resistance, conferred by chromium, with a high resistance to irradiation damage as well as to retain the adequate toughness and elevated-temperature strength during service. Variation of chromium content in ferritic-martensitic steels as well as the addition of numerous alloying elements, such as Ni, Mo, W, Ti, V, Nb and others, enable a wide range of properties to be obtained. Thus, the third section of this chapter is devoted to a brief description of the development and the physical metallurgy of high-chromium F-M steels.

The fourth section focuses on the microstructural changes occurring in Fe and Fe-Cr base alloys under irradiation. The attention is paid to the effect of the conditions of irradiation and chemical composition of the material. The response of materials to the irradiation exposure is strongly dependent on these parameters. A detailed review of properties of F-M steels under irradiation exposure can be found in reviews of Klueh [1,2]. A concise description will be given in the forth section of the current chapter as well.

The chapter ends by a conclusion of the former sections.

TABLE OF CONTENT

I. Nuclear power plants

I.1. A brief history of nuclear energy systems

In 1932, James Chadwick discovered the neutron as a constituent of nucleus [3]. The series of experiments on the interaction between neutrons and nuclei undertaken by Frédéric and Irène Joliot-Curie led to the discovery of induced radioactivity in 1934. Further experiments of Enrico Fermi and his group in the 1930s led to the achievement of the first atomic fission by bombarding uranium with slow neutrons [4]. Shortly after, these results have been correctly interpreted as being nuclear fission by Hahn & Strassmann [5]. Meitner & Frisch [6] showed the first undeniable proof that uranium, when bombarded with neutrons, splits into few isotopes of lighter elements with release of energy (Figure 1.1).

By early 1939, it was verified that neutrons are emitted during fission reaction (as shown in Figure 1.1) and a self-sustaining nuclear reaction could occur. This was the start of an era with numerous technological achievements on this subject. This work was led by Enrico Fermi who culminated in the development and demonstration of the first operating nuclear reactor "Chicago Pile-1"on December 2nd 1942 at an improvised facility in Chicago (United States). It was a small reactor running with total power output of 200W. Further work proceeded over the course of the late 1940s and early 1950s in the United States, United Kingdom, Canada, and USSR and in December 20th 1951 electricity was for the first time generated by nuclear energy (initially about 100 kW) on the experimental reactor "EBR-I" near Arco (Idaho, United States). Finally, on June 27th 1954, first commercial nuclear power plant for electricity production was brought into service in Obninsk (USSR) with electric power output of about 5 MW.

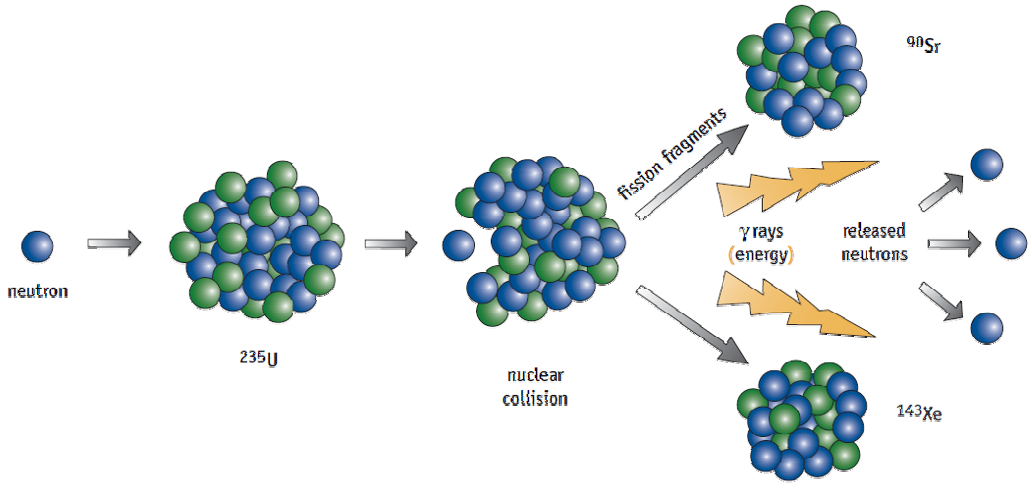

Figure 1.1. A typical fission reaction. When the nucleus of 235U absorbs an emitted neutron, it can fission or split into two fragments, releasing at the same time two or three neutrons and energy (from [7])

I.2. Generations of nuclear fission power plants

Basic principles of producing of nuclear electricity are the same for most types of reactor: the energy released from continuous fission of the atoms of the fuel is harnessed to heat a gas, water or other coolants, and finally to produce steam. The steam is used to drive the turbines which produce electricity (Figure 1.2).

Starting from the first rather small nuclear reactors made in the 1950s, nuclear power has grown till nowadays and became economically feasible and meets about 20% of the world's demand for electricity with more than 400 plants in operation [8]. In France, nuclear power is the primary source of electric power: about 78% of electricity is derived from nuclear energy [9].

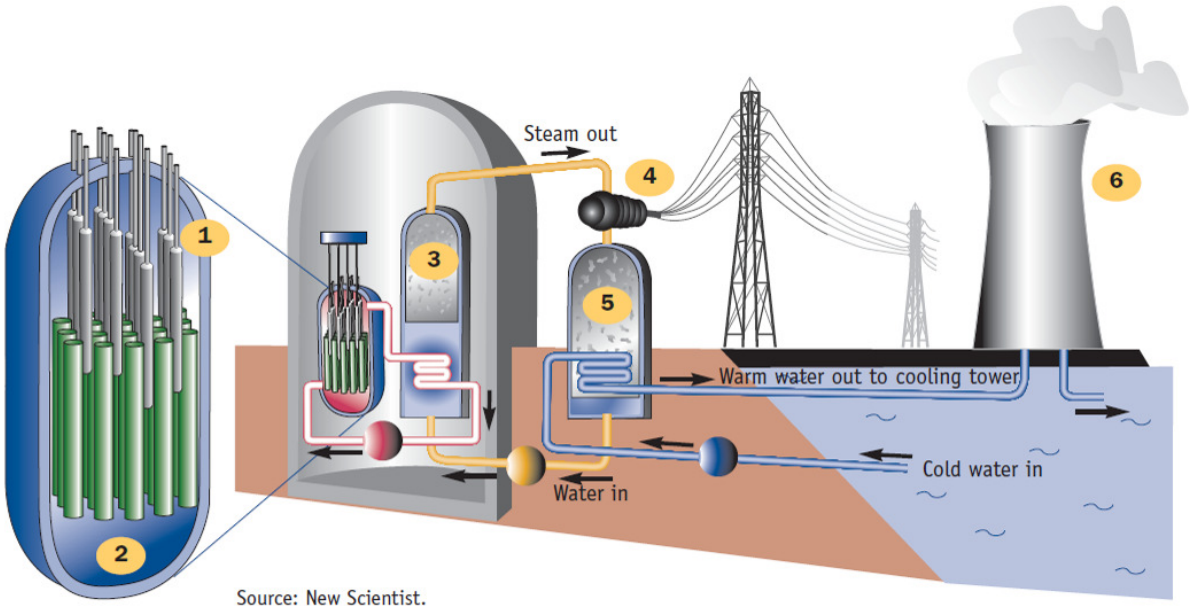

Figure 1.2. Basic components of a pressurized water reactor (from [12])
*1 – **Reactor**: fuel (green) heats pressurized water. Control rids (grey) absorb neutron to control or terminate fission.*
*2– **Coolant and moderator** – fuel and control rods are surrounded by water that serves as moderator (to slow the fast neutrons to increase their efficiency in causing further fission) and coolant.*
*3 – **Steam generator**: hot water from the reactor is pumped through a heat exchanger to generate high-pressure steam.*
*4 – **Turbine generator**: steam drives electricity generator to produce electricity.*
*5 – **Condenser**: removes heat to convert steam back to water;*
*6 – **Cooling tower**: removes heat to return cooling water to near-ambient temperature*

The progress of nuclear energy systems in time is expressed in terms of generations, as illustrated by Figure 1.3. [10]. The early small prototype Atoms-for-Peace-era plants made up the first generation of nuclear power plants developed in the 1950s and 60s in the USA, USSR, France and UK. They mostly used natural uranium fuel (to avoid the need to enrich), used graphite (or heavy water) as moderator and CO_2 as a coolant. Most of them are now stopped [11].

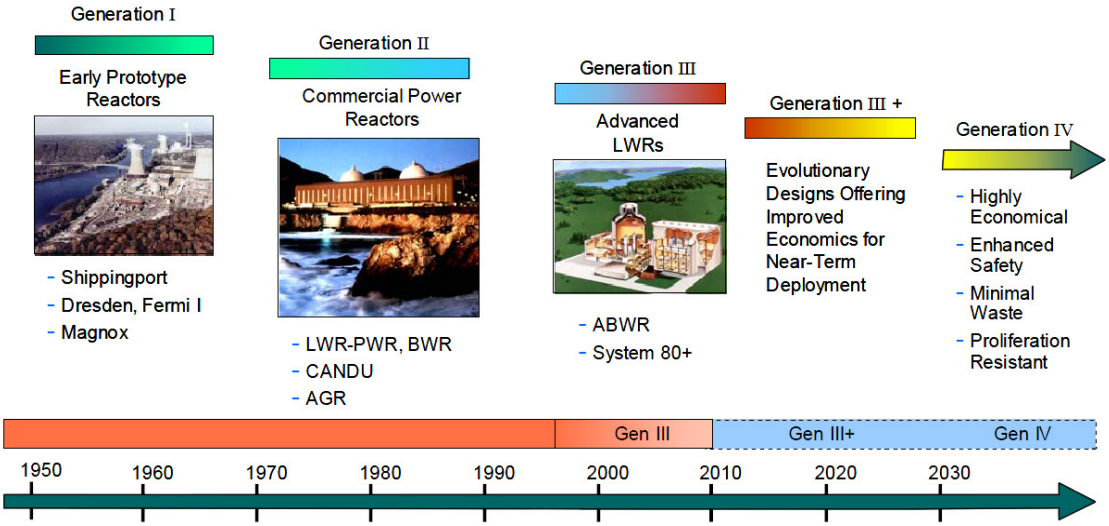

Figure 1.3. Overview of the generations of nuclear energy systems (from [10])

The second generation began in the 1970s in the large commercial power plants that are still operating today. They typically use enriched uranium fuel and are mostly cooled and moderated by pressurized water. In the US, France, Germany, Japan and some other countries, they are: the light-water reactors (LWR) (such as boiling water reactor (BWR) and the pressurized water reactor (PWR)). The fuel, ceramic uranium dioxide UO_2, is typically encased in long zirconium alloy tubes. The uranium-235 is enriched from its original 0.7% abundance to 3.5–5.0%. In the UK, the second generation of reactors is advanced gas-cooled reactors (AGRs). In Canada and Romania, they are the CANDU reactors (CANadian Deuterium Uranium heavy-water moderated and natural uranium fuelled). In the USSR, the so-called "Vodo-Vodjanoj Energeticheskij Reaktor"* (VVERs) and "Reaktor bolshoy moshchnosti kanalniy"** (RBMK) of the second generation operate. The description of the systems can be found in more details in reference [13], for example.

The third generation is represented by the Advanced Light Water Reactors (ALWRs) with a number of designs that offer significant advances. These include improved fuel technology, superior thermal efficiency, passive safety systems and

* *eng. Water-Water Energetic Reactor*
** *eng. High Power Channel-type Reactor*

standardized design for reduced maintenance and capital costs. Advances to Generation III are underway (so-called Generation III+), resulting in several near-term deployable plants that are actively under development and are being considered for deployment in several countries, for example the Franco–German "European Pressurized Reactor" (EPR) [14].

The International Generation-IV initiative was initiated in 2000 with the aim to promote the research to underpin the development of a new generation of nuclear energy systems. The Generation-IV systems, which comprise both the reactors and their associated fuel-cycle facilities, are intended to deliver significant advances compared with current ALWRs (Generation-III) systems with respect to economics, safety, environmental performance, and proliferation resistance [10,15]. The production of electricity is not the unique aim of Generation IV systems but also high temperature heat production for the industry, transmutation of the produced nuclear wastes, hydrogen production, water desalination etc. The chosen Generation-IV systems are announced to be deployed by 2040 [11].

Six Generation IV reactor types have been selected for further investigation. Figure 1.4 gives a schematic overview of these reactors along with other relevant information. Three systems are named thermal reactors and three – fast reactors. In the thermal reactors, almost all neutrons in the reactor core have a low energy (~0.025 eV), while in the fast reactors, the neutron energy is much higher (more than 1 MeV). Fast reactors offer therefore the possibility of burning actinides to further reduce the long-life waste and breeding fuel. The description of the mentioned Generation IV systems as well as the scientific and technological status of each of the systems can be found in references [10,15,16], for example.

Thermal reactors | Fast reactors

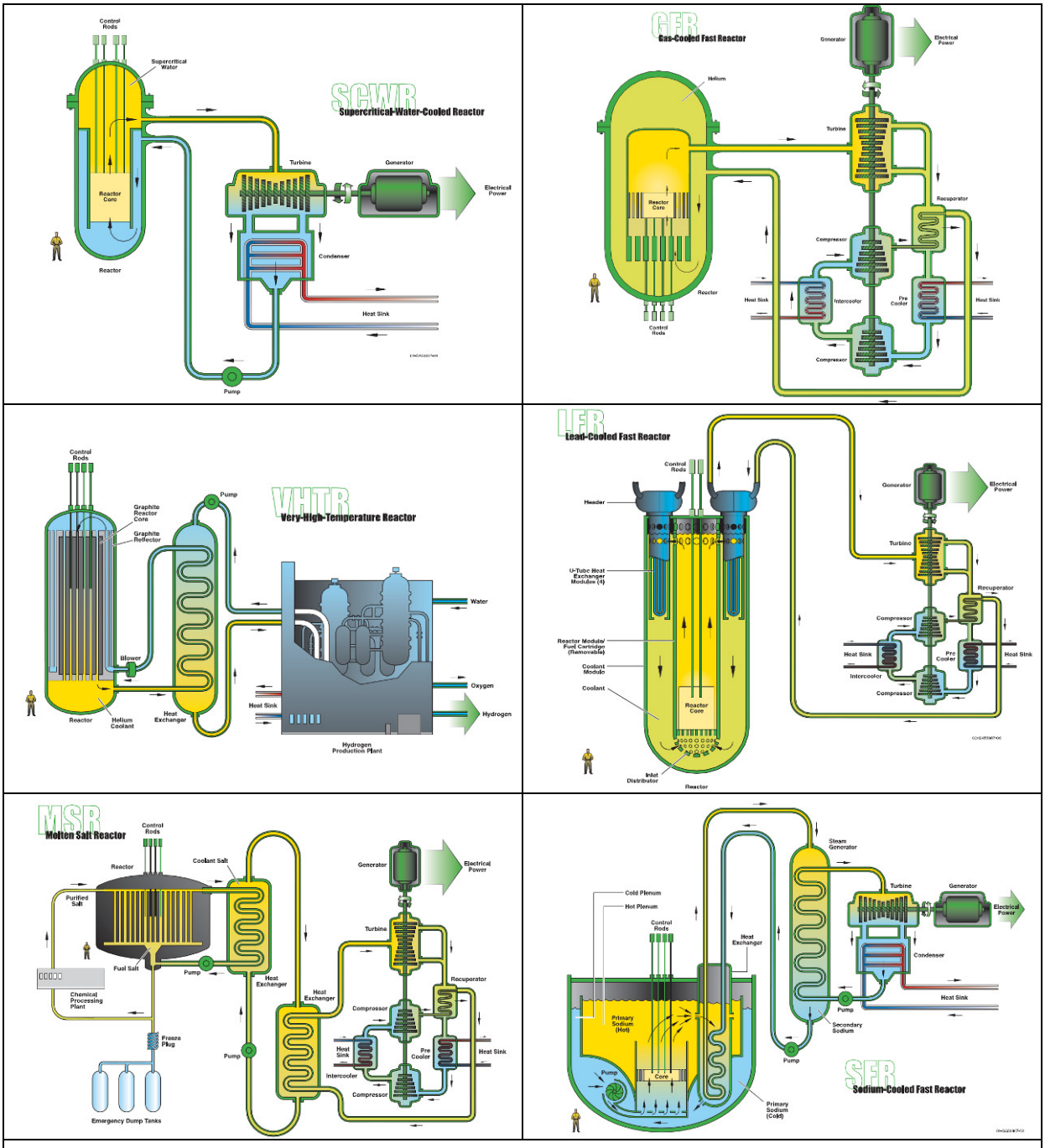

	Neutron spectrum	Coolant	Temperature (°C)	Fuel	Fuel cycle	Size(s) (MWe)
Sodium-cooled fast reactors (SFR)	Fast	Sodium	550	U-238 and MOX	Closed	50, 1700
Very high temperature gas reactors (VHTR)	Thermal	Helium	1000	UO_2 prism or pebbles	Open	275
Gas-cooled fast reactors (GFR)	Fast	Helium	850	U-238	Closed	300, 1500
Supercritical water-cooled reactors (SCWR)	Thermal or fast	Water	625	UO_2 or MOX	Open (thermal) or closed (fast)	1700
Lead-cooled fast reactors (LFR)	Fast	Pb or Pb–Bi	480–800	U-238	Closed	10–100, 600
Molten salt reactors (MSR)	Epithermal	Fluoride salts	700–800	UF in salt	Closed	1000

Figure 1.4. The schematic overview and relevant information on the different Generation IV reactors (after [10,11]).

II. Structural materials for GEN IV

II.1. Service conditions for structural materials

Despite the significant differences which exist among the proposed reactor concepts (see Figure 1.4.), the operating conditions envisaged for whole of these systems are demanding and they will impact the performance of the structural materials. In general, service conditions which will affect structural materials can be summarized as follows: (a) exposure to high temperatures (Figure 1.5), (b) high neutron doses (Figure 1.5), and (c) corrosive environment such as liquid metals, super critical water or gas. As shown in Figure 1.5, one can note that the coolant temperature of most of the commercial reactors operating today is not exceeding 350 °C while the level of temperature required in GEN-IV systems is much higher [16].

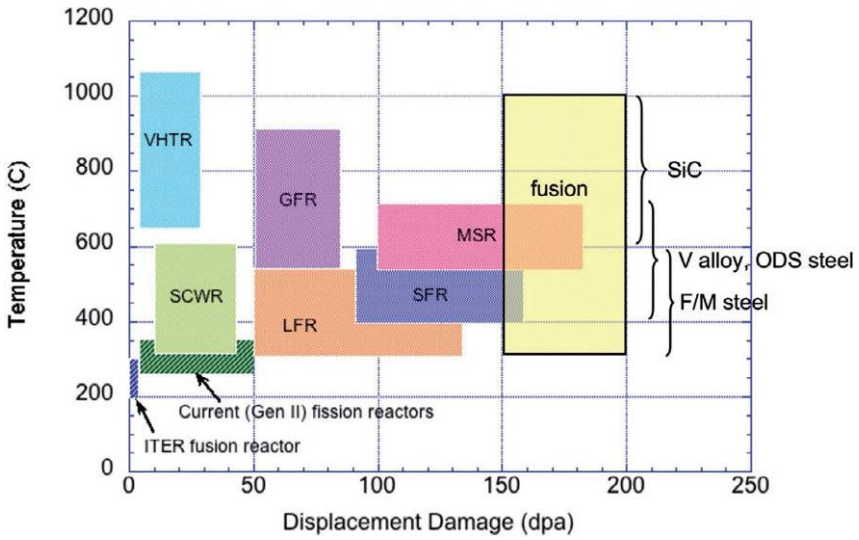

Figure 1.5. Overview of operating temperatures and displacement damage dose regimes for structural materials in current (Generation II) and proposed future (Generation IV) fission and fusion energy systems (from [16]).

The major characteristics for Gen-IV structural materials are the following [17,18]:

• The in-core materials need to exhibit dimensional stability under irradiation, whether under stress (irradiation creep or relaxation) or without stress (swelling, growth).

• The mechanical properties of all structural materials (tensile strength, ductility, creep resistance, fracture toughness, resilience) have to remain acceptable after ageing, and

• The materials have to retain their properties in corrosive environments (reactor coolant or process fluid).

Finally, workability, weldability etc. and economic concerns, are other important aspects that need to be looked and taken into account during the materials selection process.

II.2. Candidate structural materials

The combination of high temperature, high neutron dose and severe environment could prove to be a major obstacle for the viability of some of Gen-IV innovative systems. In this context, the European Commission has launched, in its 7th Euratom Framework Programme, a research project to qualify commercially available materials and for the long term – to develop and qualify new materials and their corrosion protection barriers for innovative systems. This project has been named 'Generation IV and Transmutation Materials' (GETMAT) [19].

Several candidate materials have been suggested for structural applications in Gen-IV reactors [17,18,20,21], as listed in Table 1.1 [18,19]. In this table, materials noted P (primary options) are materials for which a reasonable database is constituted, and only qualification needs to be carried out. The letter S (secondary options) refers to promising materials which need extensive research and development for database generation and subsequent qualification. The different aspects of candidate materials are briefly summarized below.

Ferritic-martensitic (F-M). Ferritic-Martensitic (F-M) steels with an elevated chromium content (usually between 7 and 14%) are considered for use in some Gen-IV reactors (for fuel assemblies, core support/internals, elements of primary system vessel [21–23]) because they tend to have elevated corrosion/oxidation resistance. Also they have good void swelling resistance and relatively good creep resistance. However, this class of materials has some shortcomings such as low long-term creep rupture strength at higher temperatures (T > 550 to 600°C) and irradiation embrittlement at low temperature (less than 400 °C) [1,2].

Table 1.1. Summary of materials considered for different systems [18,19]

Reactor system	F-M steel	Austenitic stainless steels	ODS steels	Ni-base alloys	Graphite	Refractory alloys	Ceramics
GFR	P*	P	P	P	–	P	P
Pb-LFR	P	P	S	–	–	S	S
MSR	–	–	–	P	P	S	S
SFR	P	P	P	–	–	–	–
SCWR	P	P	S	S	–	–	–
VHTR	S	–	–	P	P	S	P

***P** (primary options) – materials that has a reasonable database but the qualification needs to be carried out.*
***S** (secondary options) – refers to promising materials which need extensive research and development for database generation*

Oxide Dispersion Strengthened (ODS) alloys based on a Fe–Cr ferritic or ferritic-martensitic matrix (chromium content is about 9 to 18%), offer the potential of application to higher operating temperatures ($T > 550$°C), where conventional ferritic–martensitic steels cannot be used any longer because of their low creep resistance. ODS steels are made through mechanical alloying process, and are the only materials presenting jointly two important

properties: (a) a high dimensional stability under irradiation, i.e. high resistance to swelling and irradiation creep, due to their bcc structure, and (b) a potential high strength at high temperature resulting from the homogeneous dispersion of nanometric oxide (Y–Ti–O) particles [24–26]. This material class is expected to be used for claddings, targets and some other core and fuel structures of GEN-IV reactors [22].

Austenitic stainless steels have good creep resistance at high temperature coupled with a reasonable corrosion/oxidation resistance. However, they are prone to swelling at moderate neutron doses (Figure 1.6). This constitutes a major performance-limiting issue. It is noted that the extent of swelling is much higher in austenitic stainless steels than in ferritic or F–M ones [17,27–29]. Austenitic steels are also prone to intragranular corrosion in water or lead–alloy cooled systems because of radiation-assisted depletion of Cr at grain boundaries [27].

Ni-base alloys. Ni-base superalloys have good creep rupture properties and are traditionally used for high temperature applications [30]. The main disadvantages of Ni-base alloys are the radiation embrittlement and phase instability under neutron radiation [30]. These observations specify their applicability in balance-of-plant features where there is no radiation influence (turbines, steam-generators, etc.)

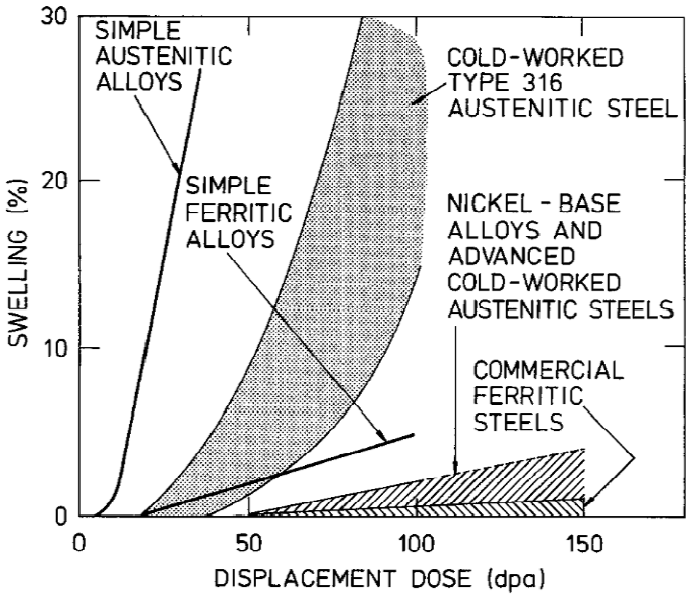

Figure 1.6. Schematic comparison of irradiation induced void swelling in austenitic, Ni-base and ferritic alloys as a function of displacement dose (from [27]).

Refractory alloys, graphite and ceramics. Refractory metals (such as Nb, Mo, Ta, V, W etc.) have melting temperatures higher than 2000 °C and they should have potential applications at very high temperatures. Refractory metals have good strength at elevated temperatures, good swelling and creep resistance, but they have poor oxidation resistance coupled with low temperature radiation embrittlement and manufacturing (joining) difficulties [18].

Graphite and ceramic matrix composites (C/C, C/SiC, SiC/SiC) are needed for very high temperature components (T ~ 1100°C up to 1600°C in accidental conditions) such as heat exchangers and thermal insulations in the primary system, as well as core components such as control rod sheath (V/HTR and GFR) and fuel constituents (GFR). It is worth noting that C/C composites are sensitive to oxidation at such temperatures and their behavior under irradiation is poorly known and this is particularly critical for operating control rods [17].

As it was shown in Table 1.1, two classes of materials have been identified for most of the new generation reactors: the high-Cr Ferritic/Martensitic (F/M) steels and Oxide Dispersion Strengthened (ODS) Fe–Cr alloys. Despite the existing sizeable experience on the high-Cr F-M steels (see [1,2]), further data are needed to qualify their use in the service conditions planned for the innovative nuclear systems. On the other hand, the use of ODS alloys for nuclear application is a nearly unexplored domain, where knowledge/improvement is considered as an essential task. In accordance to this, the focus of the GETMAT project is on the development and characterization of ODS and high-Cr F/M steels, their welding/joining and their qualification, in terms of mechanical and corrosion resistance in appropriate conditions [22].

The development of multi-scale modeling that will contribute to the understanding of the radiation effect on the material, is one of the driving forces of this project. It needs new experimental data base on model alloys. In this context, the main objective of the current Ph.D. work, which is a part of the GETMAT project, is to provide a wide range of data on microstructural behavior of irradiated Fe-Cr alloys, model alloys of F-M steels, as a function of three main variables, namely: irradiation dose, irradiation temperature and Cr concentration, in view of understanding of the role of these variables on the microstructure evolution and corresponding mechanical response of Fe-Cr alloys under irradiation. Therefore, concise description of physical metallurgy and irradiation properties of high-chromium ferritic-martensitic steels and their representatives – Fe-Cr model alloys are given in the next sections of this chapter.

III. Development and physical metallurgy of high-chromium ferritic-martensitic steels.

III.1. Development of high-chromium F-M steels

Detailed review of the history of the development of F-M steels can be found in different reviews [1,2,31]. The development of elevated-temperature ferritic/martensitic steels began in the 1920s with the introduction of Cr–Mo steels for conventional power-generation applications. The 9Cr–1Mo steel (composition given in Table 1.2) was introduced in the 1940s and is still widely used today [32]. Historically, one of the main properties to improve was the maximum temperature of application of F-M steels and in particular – their creep strength behavior. As for the nuclear power plants, development of this class of material can be expressed in terms of generations, as shown by Table 1.3 [32].

Table 1.2. Nominal composition of commercial and experimental steels (wt%) discussed (after [32])

Steel	C	Si	Mn	Cr	Ni	Mo	W	V	Nb	B	N	Other
9Cr–1Mo (T9)	0.12	0.6	0.45	9	0.2	1						
Mod 9Cr–1Mo (T91)	0.1	0.4	0.4	9	0.1	1		0.2	0.08		0.05	
NF616 (T92)	0.07	0.06	0.45	9	0.25	0.5	1.8	0.2	0.05	0.004	0.06	
F82H	0.1	0.2	0.5	8			2	0.2		0.003		0.04 Ta
EUROFER	0.11	0.05	0.5	8.5			1	0.25		0.005		0.08 Ta
12Cr–1MoWV (HT9)	0.2	0.4	0.6	12	0.5	1	0.5	0.25				
NF12	0.085	0.25	0.44	11.6	0.17	0.14	2.68	0.2	0.08	0.0026	0.045	2.48 Co

The comparison of the creep-rupture properties for commercial steels of different generation is shown in Figure 1.7. It illustrates that owing to improvements briefly listed in Table 1.3, a significant increase in creep strength was achieved from the first-generation of steels to the third generation (the forth generation is now under development). This strength advantage is evident when the values of “100 000 h rupture strengths” are compared for the five steels at 550°C, 600°C, and 650°C (Figure 1.7(b)) [32].

Table 1.3. Evolution of ferritic/martensitic steels for power-generation industry (after [32])

Gen.	Years	Steel modification	10^5 h Rupture strength, 600°C (MPa)	Examples of steels	Max use T (°C)
0	1940–1960		40	T22, T9	520–538
1	1960–1970	Addition of Mo, Nb, V to simple Cr–Mo steels	60	HT9	565
2	1970–1985	Optimization of C, Nb,V, N	100	T91	593
3	1985–1995	Partial substitution of W for Mo and add Cu, B	140	NF616 (T92)	620
4	Future	Increase W and add Co	180	NF12	650

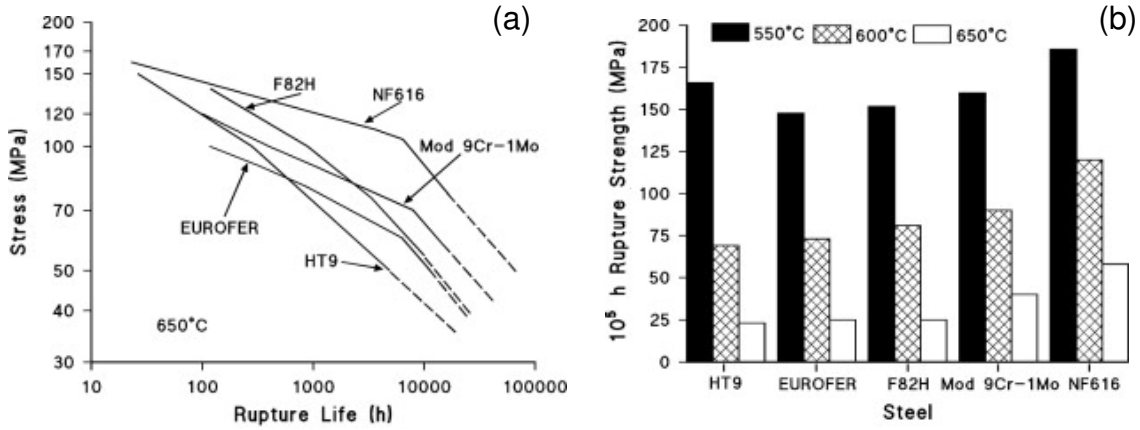

Figure 1.7. Comparison of the creep-rupture properties for commercial steels Sandvik HT9 (Gen - 1), modified 9Cr–1Mo(T91) (Gen - 2), NF616 (Gen - III), F82H (Gen – 1…2), and EUROFER (Gen – 1…2) (from [32])
(a) Comparison of the creep-rupture curves for tests at 650 °C
(b)A comparison of the 100 000 h rupture strengths for different temperatures.

III.2. Influence of alloying elements

a) Fe-Cr alloys

The Cr concentration in F-M steels is one of the key parameters to be optimized in order to guarantee the best corrosion resistance, together with favorable mechanical properties. The corrosion resistance increases with chromium content in Fe and the minimum concentration of chromium necessary to obtain an effective passive layer is about 10.5 to 11wt% [33,34]. Depending on operating temperature, the use of one of the steels with a Cr content from 7 to 14% may be required to provide adequate corrosion and oxidation

resistance of structural elements of nuclear power plants. However, economic and technical advantages exist for using lower-chromium (from 2.25 to 5 % Cr) steels [2].

Typical heat treatment of the high-chromium F-M steels consists of normalizing and tempering. Normalizing consists of annealing of the steel in the FCC γ-austenite state and air cooling to the BCC α-ferrite region. Cr affects the γ-α transformation during the final heat treatment. The morphology of the final structure changes from bainite (ferrite containing a high dislocation density and carbides), polygonal ferrite, or a combination of these two constituents for steels with less than about 5% Cr to martensite (body-centered-tetragonal structure) for steels with about 5 to 12%Cr [32]. Owing to the high number density of dislocations, martensite and bainite have a high strength. During tempering which consist on heating of the normalized steel up temperatures from 700 to 750°C, holding for few hours and air cooling to room temperature, the high number density of dislocations is reduced that increases toughness and ductility. In steels, the tempering process is also accompanied by precipitation of different carbides and nitrides as discussed below.

The binary Fe-Cr phase diagram is presented in Figure 1.8. For the temperatures of technological interest and for a wide range of alloy compositions, it indicates a phase separation reaction where ferrite decomposes into α phase (rich in iron) and α' phase (rich in chromium). As it was demonstrated by Grobner [35] this phase separation leads to hardening and embrittlement of the Fe-Cr alloys. This process is named "475°C embrittlement". However it may occur in the temperature range from 400°C to 550°C depending on the chemical composition of the steel and the time of exposure (see [1] and references cited).

The exact position of the of α–α' miscibility gap which is essential to be known, is still under debate since the experimental determination of the solubility limit is problematic due to the low mobility of chromium in iron at temperatures lower than 500°C. The phase diagram calculated with CALPHAD (CALculation of PHAse Diagrams) approach [36] predicts an extremely low solubility of Cr in Fe for low temperatures. This is in disagreement with experimental data and recent theoretical calculations (see reviews [37,38] and references cited). Thus, modified binary Fe-Cr phase diagrams (Figure 1.8(b)) are proposed by Bonny et al. [37] and by Xiong et al. [38]. The position of the α domain limit proposed by Bonny et al. [37], is based on the review of the experimental data found in the literature which deals with phase transformations in Fe-Cr alloys and Fe-Cr base steels under thermal ageing and irradiation exposure. Bonny et al. [37] made the hypotheses that the solubility limit is not modified under irradiation and that there is no influence of additional alloying elements on the α-α' miscibility gap position. These hypotheses are debatable (see section IV of the current chapter. p 26). Xiong et al. [38] does not show a line of the α domain limit but the area of the possible location of this line. This area is considered as a smooth connection between the solubility limit determined under equilibrium (thermal ageing data) and the solubility limit of Cr in (α'-Fe) at 0 K predicted by *ab initio* calculations.

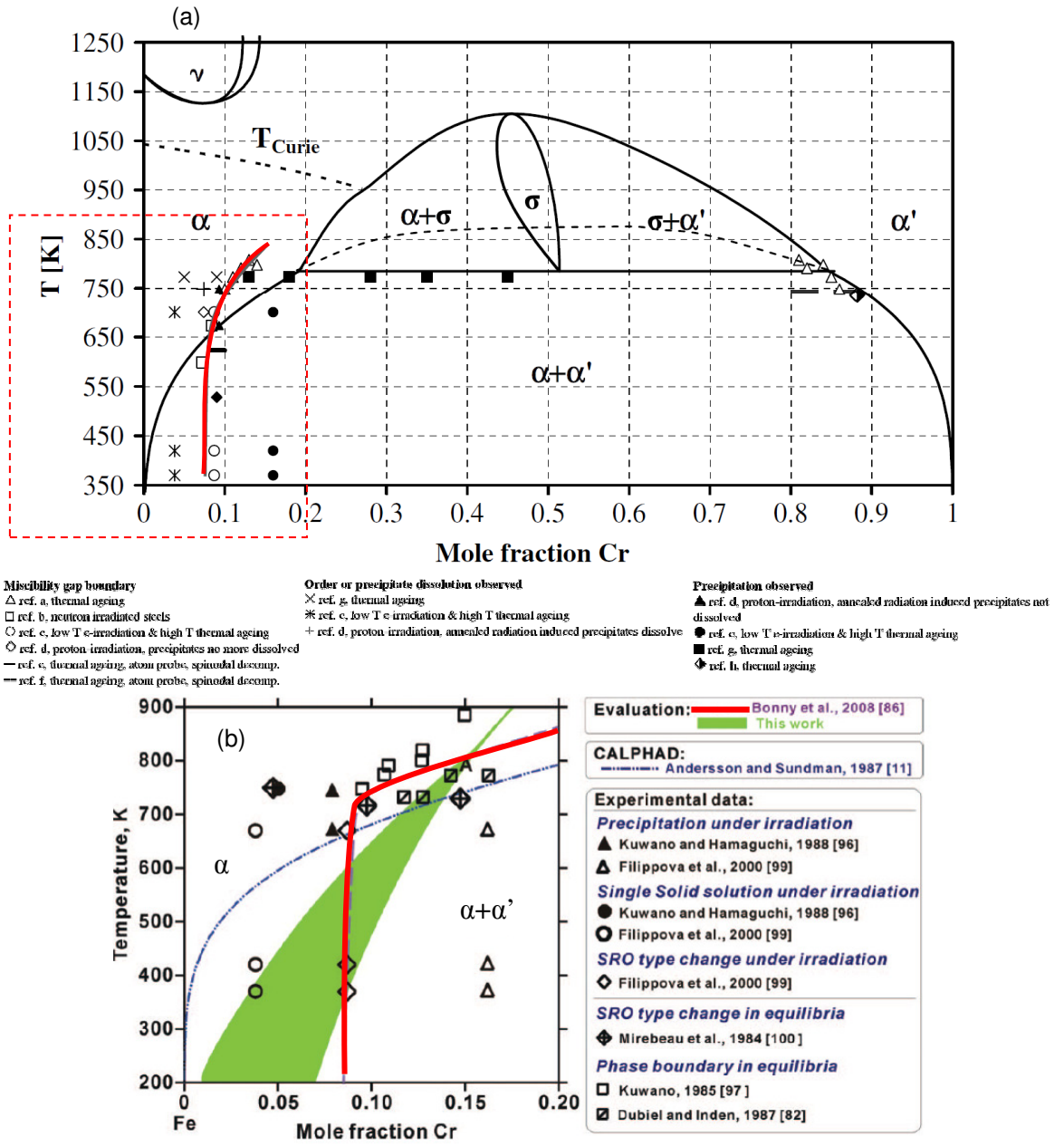

Figure 1.8. The binary Fe-Cr phase diagram.
(a) low temperature part according to CALPHAD calculations (from [39]). Some experimental data are presented as well as the new position of α domain limit (red line) proposed by Bonny et al. (see [37]); (b) low Cr part of the α-α` miscibility gap (after [38]); the position of the α domain limit, proposed by Bonny et al. is shown in red [37]; the possible location for Fe-rich solvus determined by Xiong et al. [38] is represented by the green area.

Another feature that could affect the mechanical properties of Fe-Cr alloys is the short range ordering (SRO) of the α matrix [40]. For the first time this transformation has been observed by Mirebeau et al. [41] by neutron scattering technique in an Fe-5at% Cr alloy aged at 427°C. It has been shown that, in this alloy at this temperature, Cr solute atoms tend to be surrounded by Fe atoms.

As it has been shown by theoretical calculations, these transformations (α–α' decomposition and SRO) originate from the change of the sign of the heat of mixing of Fe–Cr alloys from negative to positive [42]. This change has been recently rationalized in studies performed with various density functional theory (DFT) techniques in ferromagnetic Fe–Cr solid solutions [43–45] (Figure 1.9 and review [39]). The analysis of the DFT results provided a physical explanation for this effect in terms of electron band and magnetic properties of Fe and Cr [44,45]. A single Cr atom prefers to be surrounded by Fe atoms because of the lowering of the density of states at the Fermi level, i.e. of the total energy [44]. In addition, in their respective ground-states, pure Fe is ferromagnetic and pure Cr can be described as antiferromagnetic [45]. Thus, if a single Cr atom is inserted in the Fe matrix, its magnetic moment will be antiparallel to that of the surrounding Fe atoms. However, if a second Cr atom is introduced nearby, a situation of 'magnetic frustration' is produced, because either Cr atom tends to have its magnetic moment antiparallel to the surrounding Fe atoms or to the other Cr atoms. As it is impossible to have its magnetic moment antiparallel to both, when many Cr atoms are close to each other in Fe, different magnetic configurations can result from this frustration [45]. For low Cr concentrations, the energetically most favorable situation is obtained when the Cr atoms are distributed sufficiently far from each other to avoid magnetic frustration, i.e. by ordering the alloy. When, however, the concentration of Cr is high, Cr–Cr interactions cannot be avoided, leading to a positive formation enthalpy, i.e. to a tendency to segregate. Note that for the determination of the solubility limit at a fixed temperature, the entropic term (– TΔS) has to be added to the mixing enthalpy, where ΔS corresponds at least to the configurational entropy. In some cases, vibrational entropy is considered.

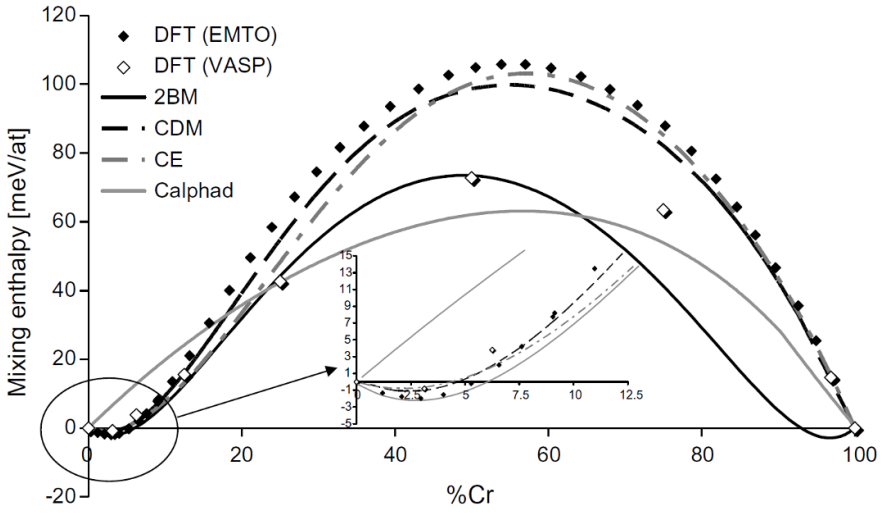

Figure 1.9. Mixing enthalpy at 0 K for the FeCr system calculated with different DFT methods and different potentials [39]: DFT – density functional theory; EMTO – exact muffin-tin orbitals method; VASP – Vienna Ab-initio Simulation Package; 2BM – two-band method; CDM - concentration-dependence method; CE - cluster expansion method; CALPHAD – CALculation of PHAse Diagrams approach.

b) Conventional alloying elements

Conventional quantities of the alloying elements in F-M steels are presented in Table 1.2 [32]. Generally, the microstructure of high-chromium F-M steels (7–14%Cr steels) is designed by a suitable balance of ferritic stabilizing (Cr, Si, Al, Mo, W, Nb, V, P, Ti) and austenite stabilizing (Cu, Ni, Mn, N, C) alloying elements in order to produce 100% of austenite upon austenitization (see Figure 1.10*a* [1].), and 100% of martensite upon following quenching or normalizing.

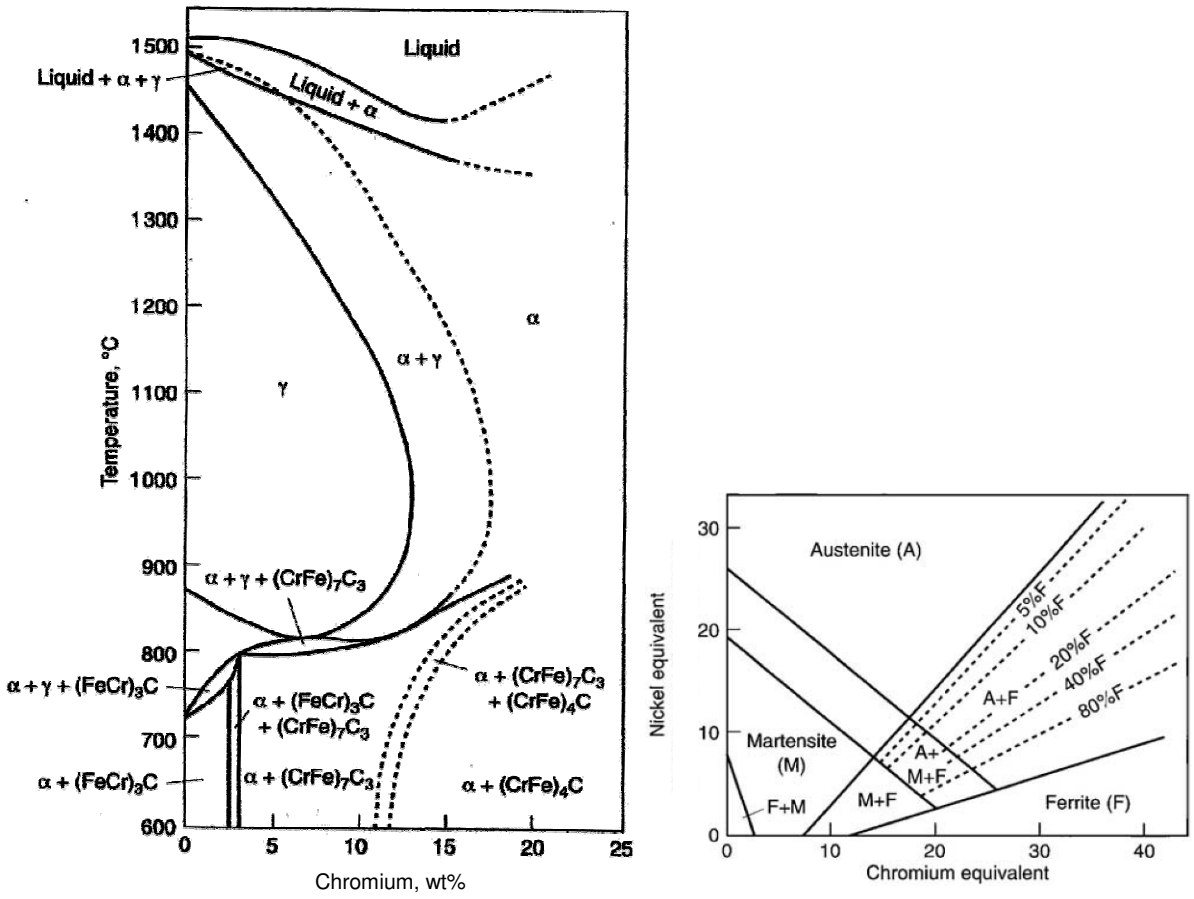

Figure 1.10. (a) Effect of Cr on the constitution of Fe-Cr-C alloys containing 0.1wt%C. $(CrFe)_4C$ is $M_{23}C_6$ carbide [1]. (b) Schaeffler–Schneider diagram [46]

The effectiveness of austenite formers is usually evaluated by the equivalent content of Ni, while ferrite formers are evaluated by the equivalent content of Cr [1]:

$$Ni_{equivalent}\ (wt\%) = (\%Ni)+(\%Co)+0.5(\%Mn)+0.3(\%Cu)+30(\%C)+25(\%N)$$

$$Cr_{equivalent}\ (wt\%) = (\%Cr)+2(\%Si)+1.5(\%Mo)+5(\%V)+1.75(\%Nb)+0.75(\%W)+$$
$$+1.5(\%Ti)+5.5(\%Al)+1.2(\%Ta)+1.2(\%Hf)+1.0(\%Ce)+0.8(\%Zr)+1.2(\%Ge)$$

Using these equivalents [1], a structure of the steel can be estimated owing to the Schaeffler–Schneider diagram [46] (see Figure 1.10*b*). Note that the mentioned equations only count as long as the elements are in solid solution.

Some strong carbide- and nitride forming elements are typically introduced to F-M steels for hardness and strength increase. Carbides and nitrides generally precipitate during the tempering process after quenching (normalizing). In F-M steels large (60-200 nm) $M_{23}C_6$ (*M* is primarily Cr, Fe, Mo) particles precipitate on lath and prior-austenite grain boundaries and smaller (20-80 nm) *MX* (*M* is primarily V, Nb, Ti, Ta, and *X* is C and N) generally precipitate in the matrix [1,47]. Several secondary precipitates, including nitrides, carbides, and intermetallics, are also known to form in high-Cr F-M steels. Formulas, crystal structures, and formation temperatures of these secondary phases are listed in Table 1.4 ([1] and the references cited).

Some alloying elements don't form carbides and nitrides, thus only changing the properties of the ferritic phase [48,49]. Ni increases strength of the ferrite, increases hardenability and impact strength of steels. P increases strength and hardness and decreases ductility and notch impact toughness (thus, P is normally controlled to low levels). S decreases ductility and notch impact toughness especially in the transverse direction. Weldability also decreases with increasing S content. Mn is generally beneficial to surface quality especially in resulfurized steels. It contributes to strength and hardness, but less than C. Increasing the Mn content decreases ductility and weldability. Si is one of the principal deoxidizers used in steelmaking. Si contributes to the increase of as-rolled strength and hardness.

Soluble V, W, Mo, Nb, Ta and Ti also produce solid-solution strengthening and retard recovery and growth of sub-grains at highest tempering temperatures.

c) Thermal grain boundary segregation

Grain boundary (GB) segregation and precipitation have an important technological interest since it changes the microchemistry and as a consequence - properties of GB. GB segregation is classified into equilibrium segregation and non-equilibrium segregation [50] (Figure 1.11). Equilibrium segregation (Gibbsean segregation) is a thermodynamic process [51]. It is caused by impurity atoms moving toward the interfaces (such as grain boundaries and surfaces) and, as a result, reducing their free energy. Once the impurity atoms reach the GB, there is no driving force to remove them if the system is kept at a fixed temperature. Thus, the impurities segregate in a monolayer fashion on the boundary [52]. Normally, the magnitude of equilibrium segregation increases with decreasing of temperature [53].

Table 1.4. Precipitation high-Cr F-M steels in normalized-and-tempered and aged (from 400 to 750ºC) state and after creep-rupture tests (from 550 to 700ºC) (from [1])

Precipitate Phase	Crystal Structure and Lattice Parameter	Typical Composition	Distribution of Precipitates
$M_{23}C_6$	fcc a =1.066 nm	$(Cr_{16}Fe_6Mo)C_6$ $(Cr_4Fe_{12}Mo_4Si_2WV)C_6$	Coarse particles at prior austenite grain and martensite lath boundaries and fine intra-lath particles
MX	f.c.c. a = 0.444-0.447 nm	NbC, NbN, VN, (CrV)N, Nb(CN) and (NbV)C	Undissolved particles and fine precipitates at martensite lath boundaries
M_2X	Hexagonal a = 0.478 nm c = 0.444 nm	Cr_2N, Mo_2C and W_2C	Martensite lath boundaries (Cr_2N and Mo_2C); prior austenite grain boundaries (Mo_2C); intra-lath (Mo_2C and W_2C); δ-ferrite in duplex steels [$Cr_2(CN)$ and $(CrMo)_2(CN)$]
Z-phase	Tetragonal a = 0.286 nm c = 0.739 nm	(CrVNb)N	Large plate-like particles in the matrix after creep straining at 600°C
η-carbide	Diamond cubic a = 1.07-1.22 nm	M_6C $(Fe_{39}Cr_6Mo_4Si_{10})C$	Prior austenite grain and martensite lath boundaries and intra-lath
Vanadium carbide	f.c.c. a = 0.420 nm	V_4C_3	Low number density in matrix
Laves	Hexagonal a = 0.4744 nm c = 0.7725 nm	Fe_2Mo Fe_2W and $Fe_2(MoW)$	Prior austenite grain and martensite lath boundaries and intra-lath; δ-ferrite in duplex steels
Chi (χ)	b.c.c. a = 0.892 nm.	$M_{18}C$ or $Fe_{35}Cr_{12}Mo_{10}C$	Intra-martensite lath; δ-ferrite in duplex steels

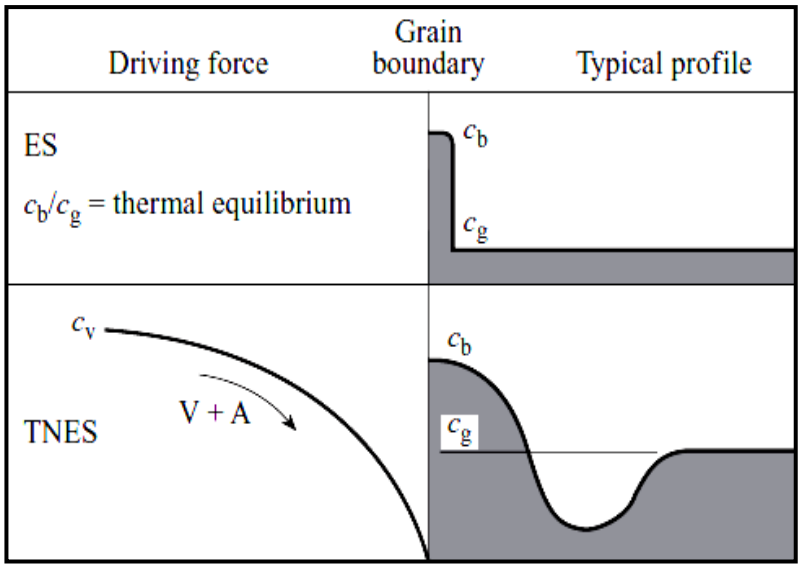

Figure 1.11. Schematic profiles of equilibrium segregation (ES), thermal nonequilibrium segregation (TNES) on grain boundary (after [52]):
C_b - concentration of impurity on the boundary; C_g – matrix concentration.

Non-equilibrium segregation (NES) originates from supersaturation of point defects and their complexes with impurities, that can be created, for example, during quenching [50]. It is a kinetic process. The theory of NES was established by Aust *et al.* [54] and Anthony [55] and the detailed review of some more recent observations and theories of NES are summarized in the work of Faulkner [56]. All these works are based on the existence of vacancy-impurity complexes, hypothesis which can be debatable when a low binding energy between solute atoms and vacancies is assigned. In fact, when the material is quickly cooled through a large temperature range, the concentration of vacancies has to be reduced up to its equilibrium value at the temperature of cooling. This equilibrium concentration is reached at vacancy sinks such as grain boundaries and surfaces. Thus, vacancy concentration gradients are formed in quickly-cooled materials and there is a net flow of vacancies towards the vacancy sinks. The vacancy-impurity complexes are also carried down these gradients and impurity atoms are thus deposited at the sink. Impurity segregation then accumulates near the relevant interface. The impurity removal from the grain involve the appearance of a depleted region in impurities outside the segregated zone (Figure 1.11). In contrast with equilibrium segregation, nonequilibrium segregation is dependent on the binding energy of the impurity atom with vacancy, on the temperature range over which the fast cooling occurs and on the cooling rate.

It should be noted that during non-equilibrium segregation two opposite processes are occurring. There are segregation (impurities are dragged from the grains to the boundaries by motion of point defect–impurity complexes) and de-segregation (back diffusion of impurities down the concentration gradient towards the centre of the grain) that lead to the evolution of

the C_b parameter (segregation atom concentration on the boundary) and the shape of the GB interface (for details see [50]). Finally, after long term holding at a fixed temperature, the non-equilibrium enrichment will die away.

In high-Cr ferritic-martensitic steels interfacial segregation can occur during cooling from the austenitization temperature and also as a result of tempering and aging [1]. The elevated concentration of impurities at the GB observed after tempering of F-M steels results from either non-equilibrium and/or equilibrium segregation, while the interfacial segregation on GB observed after aging occurs just by the latter process.

The database on thermal segregations in F-M steels can be found in [1]. It is possible to conclude that elements such as Cr, Si, B, P, Mo, V and Nb have a tendency to segregate on lath and prior austenite GB after cooling of F-M steels from austenite region and during further tempering at temperatures range of about 500 to 750ºC (see [1,57,58] and references cited), as presented for example in the case of 9Cr-1Mo steel in Figure 1.12 [58]. Generally, the extent of the segregations is found to be lower at martensite lath boundaries than at prior austenite grain boundaries [1].

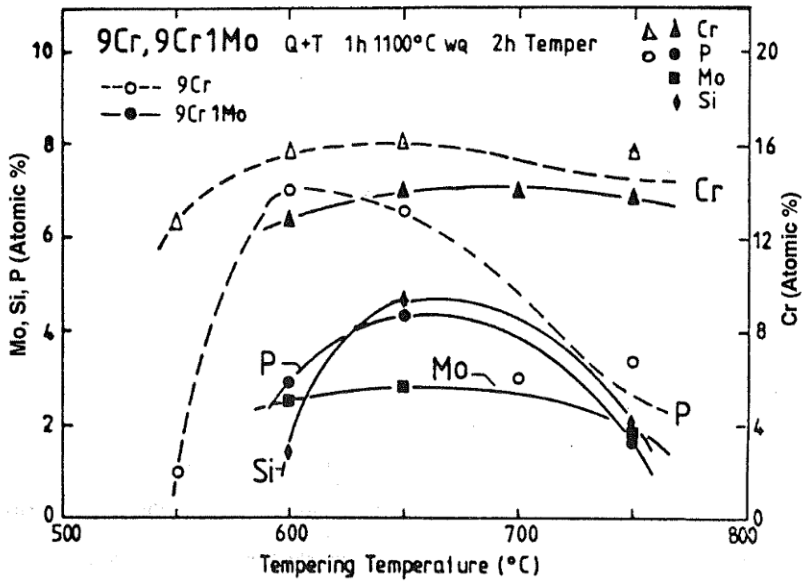

Figure 1.12. Effect of tempering temperature on the grain boundary composition after cooling from 1100°C of 9Cr-1Mo steel (from [58]).

IV. Influence of neutron and ion radiation

IV.1. Introduction: generalities on irradiation

a) Displacement cascades, Frenkel pairs and point defect cluster formation

One of the main mechanisms of radiation damage in metals and alloys is direct displacement of atoms produced by neutrons released during fission reaction [59]. This process occurs as follows [29]: i) the interaction of an energetic incident particle with a lattice atom (Figure 1.13); ii) the transfer of kinetic energy to a lattice atom which becomes the primary knock-on atom (PKA); iii) the displacement of the atom from its lattice site; iv) the passage of the displaced atom through the lattice and the accompanying creation of additional knock-on atoms leading in-fine to the production of a displacement cascade (collection of defects created by the knock-on atoms).

Thus, PKA, by displacing atoms from their equilibrium lattice sites, generates vacancy and self-interstitial point defects in equal numbers. Each pair of these point defects is named Frenkel pair. Many Frenkel pairs are thus created from each single neutron collision event.

Typically, the dimension of the displacement cascades is about 10 nm or less and in the form of a central core of vacancies with the associated self-interstitials ejected to the periphery. For such a defect configuration there is a strong inherent tendency for the cascade core to collapse spontaneously. A large fraction of the displacement cascade defect population is annihilated simply by mutual recombination. After the collapse, a residual amount of defects in the form of mono-vacancies and self-interstitial atoms (SIA) as well as small SIA and vacancy clusters remain, as shown in Figure 1.13 *c.* As shown by modelling of displacement cascades in Fe and Fe-Cr alloys, the fraction of in-cascade clustered SIAs in these material is typically higher than in-cascade clustered vacancies [60,61], however the opposite trend was detected for low PKA energies in [62].

The small proportion of defects escapes the cascade volumes all over the material as freely migrating point defects or mobile small SIA clusters (vacancy cluster are much less mobile). They can meet during their migration within the material. If an interstitial meets a vacancy, there is a recombination and both defects disappear. On the other hand, when two defects of the same nature meet, they can gather together to form a dimer. The arrival of a third defect of the same nature can lead to trimer creation and so on. The same trend is valid for small mobile SIA clusters. Thus defect clusters with a size of few tens of nanometers can be formed by agglomeration of mobile point defects and their clusters. They can eventually form dislocation loops and voids.

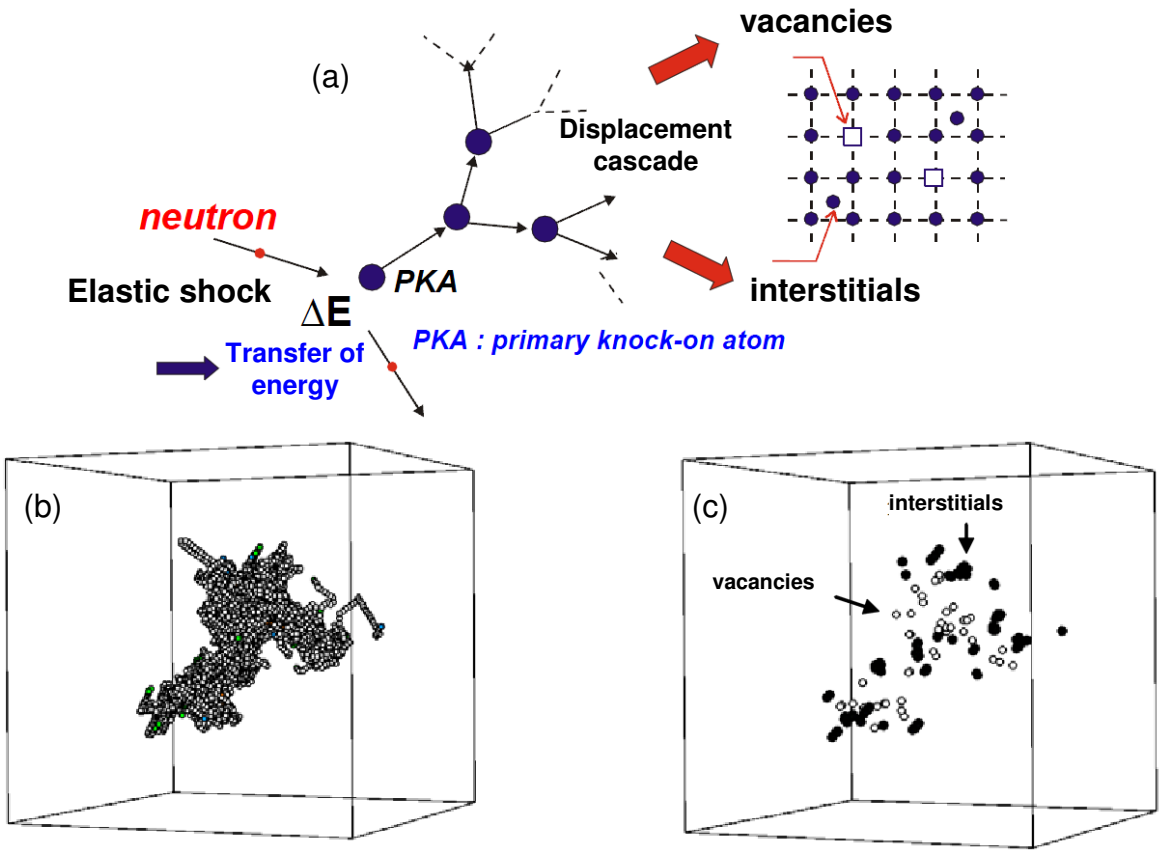

Figure 1.13. Displacements cascade (after[63]):
(a) schematic view of the displacements the cascade formation after the impact of a neutron; (b) atoms which changed positions during the cascade formation; (c) residual defects: vacancies and self interstitial;(b) and (c) – results of molecular dynamic(MD) simulation of a cascade initiated by a PKA of 20keV at 600 K.

The point defect clusters decrease the mobility of dislocations leading to hardening of materials. The presence of cavities can also be responsible for swelling under radiation [28,64,65]. The different point defect clusters formed in ferritic-martensitic steels are more accurately described in section IV.2.

Due to the absorption of point defects by the clusters of point defects, the concentration of defects in the surrounding of these clusters is weak. It creates therefore a concentration gradient and then a flux of point defects towards the clusters. Thus, these clusters play a role of point defects sinks. In the case of interaction of the different atomic species with point defects, the flux of the latter can lead to segregation or depletion of certain elements on the point defect clusters (for details see section IV.1.c).

In order to compare the damage effect of different energetic particles such as neutrons, ions or electrons, and different irradiation conditions, the displacement damage is characterized in terms of the average number of times that an individual atom is displaced from its lattice site. This leads to a damage/exposure unit called ‘displacements per atom’ (dpa) developed within the currently widely accepted NRT (Norgett, Robinson, Torrens)

model [66]. This characteristic is generally used as dose (fluence) parameter for comparison of mechanical property and microstructural changes in irradiated materials.

According to the ASTM (American Society for Testing and Materials) standard [67], an energy transfer of 40 eV is required to displace an Fe atom from its stable lattice position. However, a value of displacement energy equal to 24 eV can be found in literature (for example, see [68,69]). The value of 40 eV is based on simulations carried out by Erginsoy et al. [70] while the value of 24 eV has been obtained by Lucasson [71]. These disagreements originate from the lack of experimental data since experimental values which exist, give only the threshold energy along the low-index lattice directions (see, review [72] and references cited). Currently, the average threshold displacement energy the most frequently used for Fe is 40 eV (the ASTM standard value) and this value has also been used for the calculation in the current research.

b) Enhancement of diffusion and consequences

The diffusion rate in irradiated metal can be much more elevated. This enhancement of atom mobility is due to two factors: (i) the high concentration of vacancy defects, and (ii) the creation of new defect species (such as defect clusters or self-interstitial atoms).

By increasing the diffusion coefficient, irradiation can enhance phase transformations predicted by the thermodynamic. In this case, this process is named irradiation enhanced precipitation.

However, the phases formed under irradiation are not necessarily the equilibrium ones predicted by the phase diagram. Indeed, the process of creation and redistribution of point defects in irradiated metal may involve a coupling of solute fluxes with point defect fluxes leading to the redistribution of the chemical species in the material. This may change the phase stability or induce the appearance of thermodynamically unstable phases on sinks of point defects. In this case, the driving force is kinetic. In an undersaturated solid solution, only the latter mechanism can be observed. This process is called induced segregation/precipitation. Another known effect that influences the stability of phases in the material under irradiation is ballistic dissolution of precipitates by displacement cascades [29]. Because of the competition between kinetic and thermodynamic driving force, it is suggested that the materials under irradiation can only reach steady state not equilibrium [68].

c) Radiation induced segregation and precipitation

As described above, irradiation creates excess of point defects in materials (vacancies and self-interstitial atoms), which can be eliminated by mutual recombination, clustering, or annihilation on pre-existing defects in the microstructure, such as surfaces, grain boundaries (GBs), or dislocations [73]. In alloys bombarded by energetic particles, preferential interactions can exist between the different atomic species, interstitials and vacancies. This

interaction can originate from size differences, electronic structure, etc., and can lead to attraction or repulsion between solute atoms and point defects. Therefore, in case of interactions between solute atoms and point defects, the permanent flux of point defects toward the sinks can result in a coupled transport of solute atoms, thus, giving rise to the non-equilibrium process of radiation induced segregation (RIS).

Nonequilibrium segregation mechanisms could be described by the coupling between solute and vacancy or solute and interstitials fluxes in an A–B alloy:

1. If there is no strong binding energy between vacancy and atoms, the flux of vacancies to free surfaces induces fluxes of atoms in the opposite direction. If A atoms diffuse faster than B atoms ($D_B^V < D_A^V$), the flux of vacancies towards the point defect sink induces a preferential flux of A atoms in the opposite direction (Figure 1.14a). The sink becomes depleted in A atoms and since the concentration of A + B atoms remains constant, the sink becomes enriched in B atoms. In the opposite case ($D_B^V < D_A^V$), one expect an enrichment of B. Such situation is referred as inverse Kirkendall (IK) effect [73,74].

2. If B atoms are bounded to vacancies, solute-vacancy complex exist and the flux of the vacancies and the flux B atoms are in the same direction (Figure 1.14b). B impurity atoms are thus deposited at the sink. Such situation is referred as segregation by drag effects, or by migration of vacancy–solute complexes. The drag effect can also take place for interstitials: the flux of interstitials and the fluxes of atoms which are bounded to the interstitials are in the same direction (Figure 1.14c).

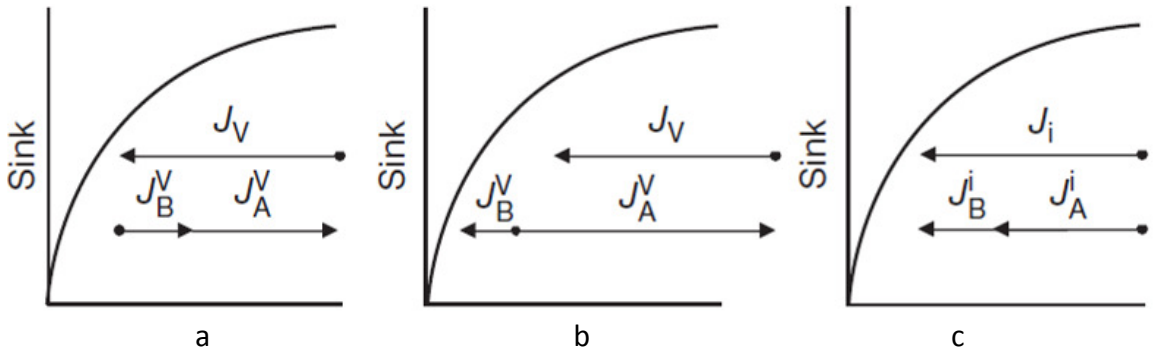

Figure 1.14. Radiation-induced segregation mechanisms due to coupling between point defect and solute fluxes in a binary A–B alloy. (a) An enrichment of B occurs if $D_B^V < D_A^V$ and a depletion if $D_B^V > D_A^V$; (b) when vacancies drag the solute, an enrichment of B occurs; (c) when interstitials drag the solute, an enrichment of B occurs(after [73,74])

RIS typically happens at temperatures between 0.3 and 0.6 times the melting point [74]. If the temperature is too low, vacancies are immobile. It leads to annihilation of point

defects mainly by mutual recombination because of the high density of defects. At higher temperatures, the equilibrium vacancy concentration becomes high, thus decreasing the level of vacancy supersaturation. In this case the back diffusion becomes not negligible and vacancies and self-interstitials annihilate because of their high diffusion coefficient. As a result, RIS is suppressed (see Figure 1.15).

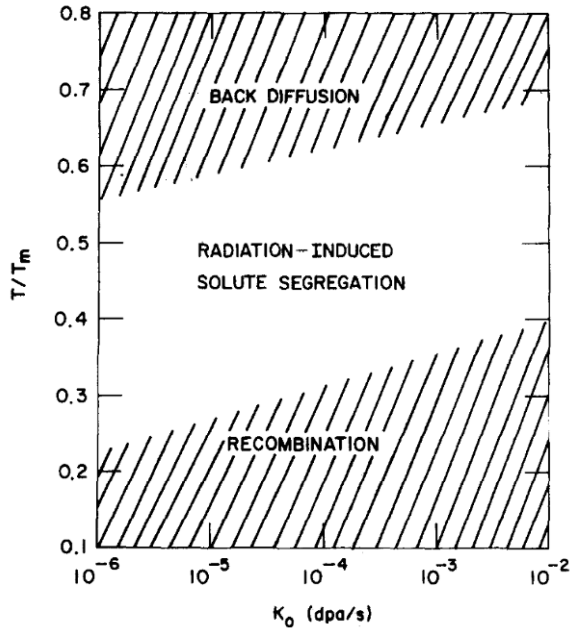

Figure 1.15. Temperature-dose rate diagram for radiation-induced segregation [74]

In some case, the local solute concentration in the vicinity of a point defect sink can reach the solubility limit leading to radiation induced precipitation (RIP). This can occur in an overall undersaturated alloy. Origin of RIP being purely kinetic, some phases which are not expected thermodynamically can appear. These phases dissolute once irradiation is stopped.

Except the heterogeneous precipitation at point defect sinks described above, homogeneous RIP of precipitates can also be expected when a solid solution contains fluctuations of composition [73,75]. If the chemical species have an attractive interaction with vacancies and interstitials, a solute-enriched fluctuation tends to trap both vacancies and interstitials leading to the recombination of point defects. It leads to decrease concentration of point defects, thus a flux of defects (as well as vacancy-solute and interstitial-solute complexes) toward it is produced. In this case, an enrichment of the solute element on the fluctuation appears.

Extensive reviews on RIS and RIP formation can be found in works of Russell [68], Nolfi [76], Ardell [77], Nastar and Soisson [73] and Was [29].

d) Transmutation

Neutron irradiation may also lead to transmutation reactions, whereby a neutron is captured by some atomic nucleus. Such absorption may give rise to various effects including:

(a) Raise of the atomic mass, which gives an atom unchanged chemically, but which may respond differently to subsequent neutrons. For example, Ni^{58} captures a neutron to become Ni^{59}.

(b) Transmutation of the absorbing atom to a new chemical species one mass unit heavier than the original atom (so-called beta minus decay). Thus, Fe^{59}, produced from Fe^{58} by the capture of a neutron, becomes Co^{59} by beta minus decay.

(c) Fission of the nucleus resulting into two atomic nuclei. One nucleus is often a proton or α-particle (hydrogen or helium nucleus, respectively), resulting from so-called (n,p) and (n,a) reactions.

Transmutation reactions are of high importance in phase stability because they change the chemical composition of the irradiated material and lead to formation of gas bubbles in materials. Nevertheless, they are predominant only at high doses.

e) Electron and ion irradiations

In practice, the behaviors of materials under irradiation are often studied using high-energy particles like ions or electrons. An advantage of such irradiations is that they don't lead to activation of samples.

For example, the process of Frenkel pair formations and further evolution of induced point defects such as dislocation loops can be investigated by electron irradiation.

Irradiation by ions is used to mimic PKA induced damage i.e. cascades. Nevertheless, one major difference originates from the fact that ions penetrate only up to a few micrometers (depending on energy and mass of ions) into the surface with damage deposited in a narrow layer whereas neutrons travel large distances through the structural materials (tens of cm) creating an uniform radiation damage. However, using appropriate specimen preparation techniques, ion irradiation permit characterization of microstructural changes using advanced technique such as electron microscopy, atom probe tomography, positron annihilation spectroscopy etc.

Note that results obtained after ion beam irradiation studies need to be evaluated with care to establish representativeness of the data; generally, benchmarking against reactor data and associated correlation procedures are mandatory [1].

IV.2. Effect of radiation on Fe-Cr alloys and Fe-Cr base steels

Changes of mechanical properties during irradiation (hardening, embrittlement etc.) arise from microstructural changes such as formation of dislocation loops and voids, segregation and precipitation under irradiation that change the dislocation mobility [1]. All

these aspects are briefly described in the current section mainly in the context of the effect of Cr (and other alloying elements) on the radiation-assisted changes.

a) Dislocation loops

As explained previously, when migrating point defects of the same nature meet each other they can form vacancy or self-interstitial clusters. Further point defects condensation can result in dislocation loops formation, the structure of which depends on the crystal structure. In b.c.c. metals (for example, in α-iron and Fe-Cr alloys) dislocation loops observed after irradiation are predominantly prismatic dislocation loops (loops whose Burgers vector has a component normal to their habit plane, see Figure 1.16). The Burgers vectors of dislocation loops in b.c.c. iron is either $b=a_0\langle 100\rangle$ or $b=\frac{1}{2}a_0\langle 111\rangle$. The habit planes of the <100>-type loops are {100} (as shown by Figure 1.16 such loops have a pure edge character) while the habit planes of $b=\frac{1}{2}a_0\langle 111\rangle$ loops varied from pure-edge {111} to close to {110}. It should be mentioned that <100>-type loops are not typical for nonmagnetic bcc metal such as V, Nb, Ta, Mo, and W where only ½<111> loops are observed (see [78] for details).

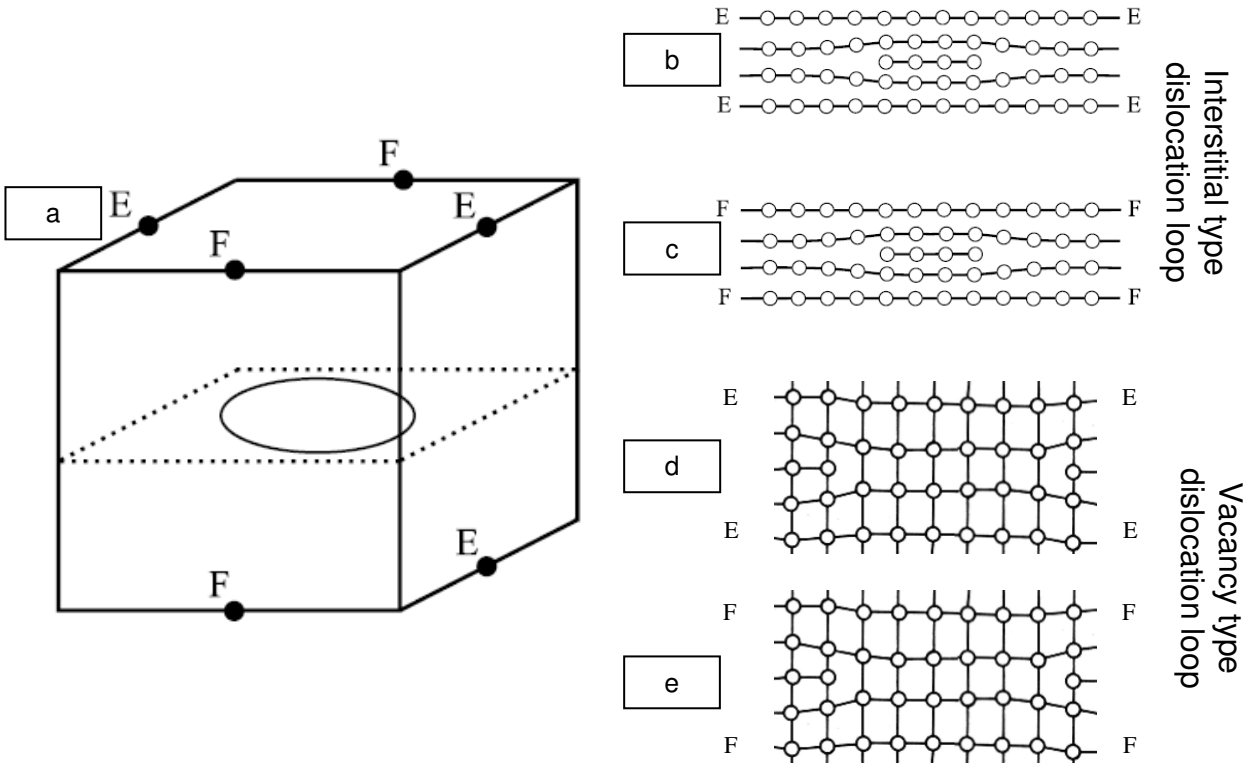

Figure 1.16. (a) Prismatic dislocation loops formed by insertion (b) and (c) or exclusion (e) and (f) of a circular plane of atoms between existing planes in the lattice (after [29])

Dislocations loops can move owing to two modes: glide and climb [29]. Glide of loops occurs in the slip plane. The slip direction for prismatic dislocation loop coincides with Burgers vectors of the loop. Climb mode allows the movement of the prismatic loops in their habit plane. It corresponds to the extension or the recession of the extra half plane of atoms by

absorption or emission of vacancies, absorption of interstitial atoms or emission/absorption of clusters of vacancies or SIAs. <100> and ½<111> type loops in b.c.c. metals are glissile and can exhibit both glide and climb movement [29].

Note, that dislocation loops are biased point defect sinks (for details, see [29]). Because self-interstitials introduce much larger distortion to the lattice, they strongly interact with other distortion centres. This means that loops exhibit preferential attraction for interstitials than for vacancies and thus have a strong impact on the redistribution of point defects and development of the irradiated microstructure (RIS, void formation etc.). The bias induced by of a dislocation depends on the magnitude of its Burgers vector [79]. Thus, the bias of dislocation loops with b= a_0<100> will exceed that of loops with b=½a_0<111>.

Iron

Typical TEM image of dislocation loops which are formed by neutron irradiation of Fe is shown in Figure 1.17 [80].

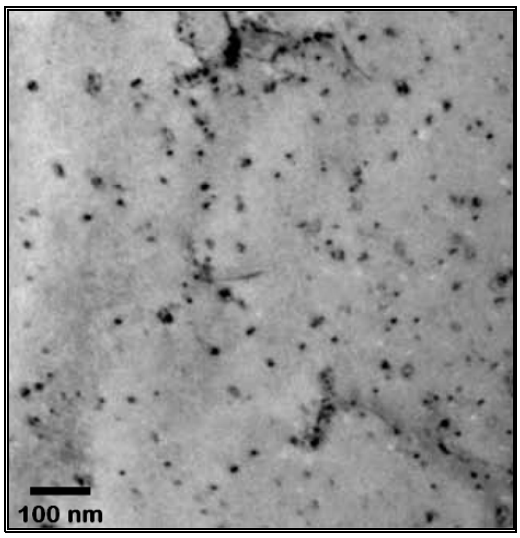

Figure 1.17. Microstructure of pure Fe, after neutron irradiation up to 0.19 dpa at 300ºC [80].

Experimental determination of the nature of the dislocation loops (interstitial versus vacancy) is a difficult task, especially, if loops have small sizes (see Jenkins and Kirk [81] for details). Available studies shows that the majority of the dislocation loops created under irradiation in pure Fe are of interstitial type, that, as shown by TEM in neutron [82–84], ion [69,85], proton [86] and electron [87] irradiated specimens. But some experiments shows that at least some of the loops formed under irradiation in Fe are vacancy in nature [88–90], especially at low doses of irradiation [89].

The ratio of dislocation loops with b=a_0<100> and b=½a_0<111> depends on the temperature of irradiation among others: in general, ½<111> loops are preferentially created

at low temperatures, <100> loops are preferentially created at high temperatures. Thus, most of the loops after neutron irradiation of Fe at 70°C, 0.8 dpa [91] and 60°C [90] had diffraction contrast consistent with ½<111> type while the data on neutron irradiation at the range from 275 to 450°C, from 0.5 to 1 dpa [82], 300°C, 0.2dpa [84] and 400°C, 25.8 dpa [92] showed that created loops were mainly of <100> type. Series of in-situ ion irradiation (150 keV Fe^+, from 1 to 13 dpa) experiments of pure Fe [69,88,93,94] has shown a similar behavior: the microstructures irradiated at T ≤ 300°C was dominated by ½<111> loops; the appearance and increase of the fraction of <100> loops has been observed for higher temperatures and, finally, 100% of <100> type dislocation loop have been found after ion irradiation at 500°C.

Recently this trend was theoretically generalized by Dudarev et al. [78]. The authors developed a formalism based on the anisotropic elasticity theory showing that ½<111> loops are the most stable in Fe at temperature under 350 °C while at higher temperature <100> loops become predominant (Figure 1.18) [78].

Note that the quantification of the ratio of ½<111> and <100> loops appears is difficult during TEM in-situ experiments since the very mobile *a*/2<111> loops can be lost at the free surfaces of the thin foil during ion irradiation (150 keV Fe^+, from 1 to 13 dpa), which are then underestimated [69,88,93]. Their quantity strongly depends on the foil orientation. Indeed, mobile ½[111] dislocation loops can be lost at the surface by glide, in the case of (111) foil orientation. In such a case, just small fraction of loops is retained after irradiation [69]. In a {110} foil, two variants of ½<111> loops have a Burger vectors which lies in the foil plane, and they cannot be lost by glide and larger quantity of ½<111> was observed [69].

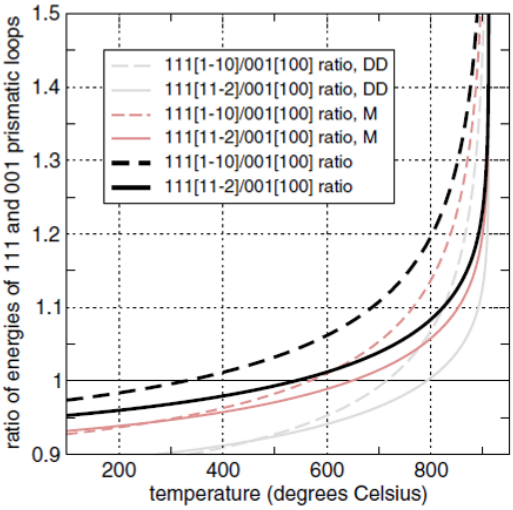

Figure 1.18. Ratio of the total free energies of prismatic dislocation loops with ½<111> and <001> Burgers vectors plotted with different orientation vectors (indicated in square brackets) as a function of the temperature. The two sets of lighter lines correspond to simulation using the different empirical potentials (DD - Dudarev and Derletfor, M - Mendelev et al.) whereas the darker curves represent the best fit to experimental observations. All curves show that <111> dislocation loops are energetically favorable at lower temperatures (from [78])

Fe-Cr based alloys

Experiments on Fe–Cr alloys neutron irradiated at the range from 300 to 425°C [40,95,96] have shown that the presence of chromium increases the fraction of created ½<111> dislocation loops. The same trend have been demonstrated in the in-situ ion irradiation experiments (100–150 keV Fe^+ and Xe^+ ions at room temperature, 300°C and 500°C, from 1 to 13 dpa) of Fe and Fe-Cr alloys [69,88,93]. It has been shown that for similar irradiations, loops with $b=a_0\langle 100\rangle$ predominate in pure Fe while the two types of loops were present in comparable numbers in Fe–Cr alloys.

It is not currently clear if <100> loops are energetically more favored in Fe than in Fe–Cr alloys. After, in-situ ion irradiation experiments, it was suggested that the difference in the $\frac{\frac{1}{2}\langle 111\rangle}{\langle 100\rangle}$ ratio in Fe and Fe-Cr alloys mainly originates from the fact that dislocations in Fe–Cr alloys are less mobile and more ½<111> loops are then lost to free surfaces of the TEM foil in Fe than in Fe–Cr alloys [69,88,93]. Indeed, chromium decreases the mobility and increases the thermal stability of loops as it was experimentally established by Arakawa et al [97]. Theoretical works of Terentyev and co-workers have also shown that Cr atoms decrease the mobility of SIA clusters [98] or small dislocation loops [99] in Fe-Cr alloys.

The mean loop diameter [69,92,95,100,101] (Figure 1.19) and the number density of loops [92,95,101] are generally larger in pure iron as compared with Fe-Cr alloys but without a clear dependence on Cr content. At the same time, in-situ irradiation experiments (100–150 keV Fe^+ and Xe^+ ions at room temperature and 300°C, up to 1 dpa) [88] shows that the number of loops produced in Fe–Cr alloys and pure Fe is similar, but more loops were lost to the thin foil surface during irradiation in the latter case.

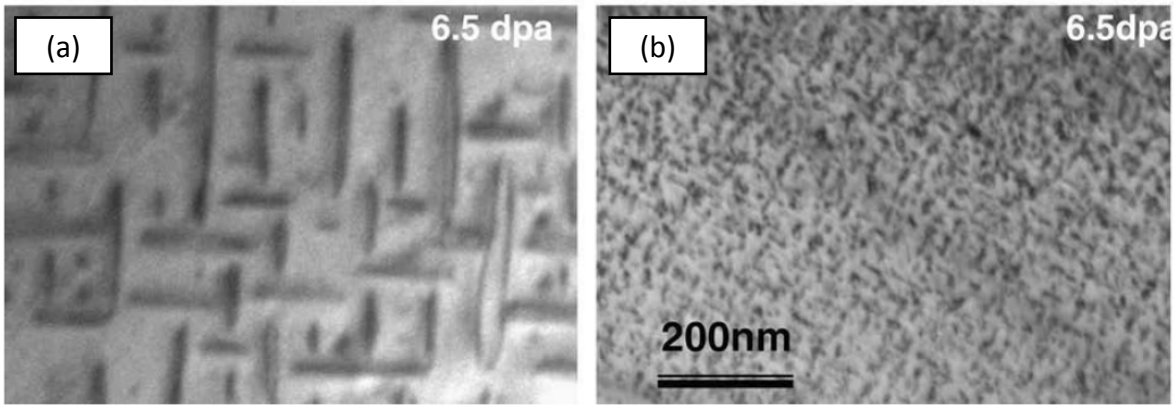

Figure 1.19. Comparison of high dose damage structures in ultra High purity Fe (a) and Fe–8%Cr (b) at irradiated with 100–150 keV Fe^+ and Xe^+ ion irradiation at 500 °C to 6.5dpa (from [69])

Concerning void formation, addition of Cr to Fe decreases the formation of void, as is was shown for neutron irradiated (400ºC, from 5.5 to 26 dpa) Fe – (0 to 18%)Cr alloys [92,95]. And as shown by Terentyev et al. [98], this behavior can originate from the reduction of the SIA clusters mobility by Cr atoms in solution. This results in the decrease of the rate of SIA cluster annihilation at dislocations and grain boundaries and in the reduction of formation rate of dislocation "forests". Finally, this should lead to the increase of the recombination of vacancies with SIAs and hence to decrease the void formation rate.

b) Radiation induced segregation and precipitation. Grain boundary segregation

Experimental observation of Cr behavior at the grain boundaries in ferritic/martensitic alloys does not show any unambiguous trend. Both RIS and RID of Cr at GB has been observed without any clear dependence on Cr concentration, irradiation type, or temperature (see review [57,102,103] and references cited). For example, depletion of Cr have been observed at GB in an irradiated (465ºC, 46 dpa) 12%Cr steel [27] (Figure 1.20) while grain boundary Cr enrichment has been observed in an irradiated (400°C, 10dpa) 9%Cr steel [102].

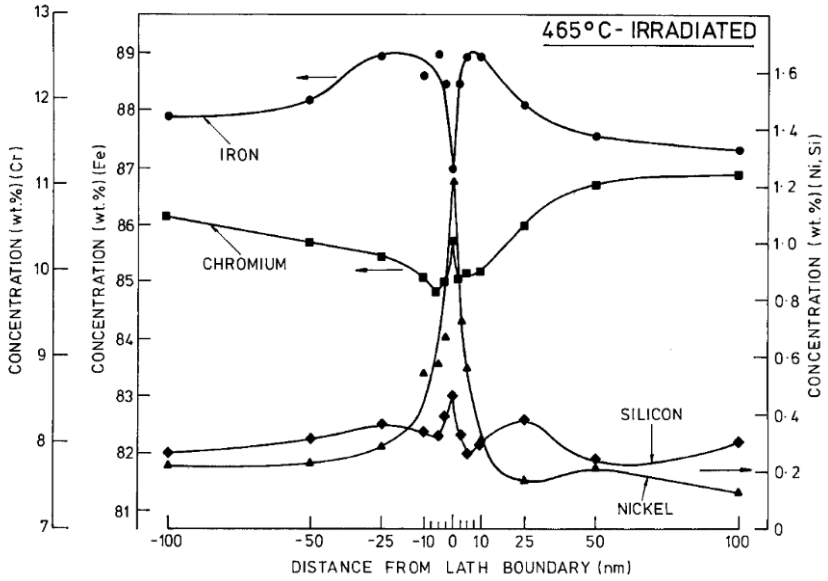

Figure 1.20. Typical concentration profiles for Cr, Ni, Si and Fe on either side of a lath boundary in a 12%Cr martensitic steel after neutron irradiation to 46 dpa at 465ºC (from [27])

Currently, there are two classes of RIS theories: i) theories based on the one of Faulkner et al. [104] which consider the binding between chemical species and point defects and diffusion of vacancy-solute and interstitial-solute complexes (drag effects by vacancy and SIAs, see section III.2.c) p. 22); and ii) Kinetic Rate Theories (KRT) [105,106] which consider the fluxes of diffusing species (point defects and chemical species) in dependence on

their concentration gradients, diffusion coefficients, rates of generation and recombination of point defects, solution thermodynamics and boundary conditions [77].

Let us consider the Faulkner's point of view. Recent experiments [107] and numerical calculations [103,107,108] show that the interaction between Cr atoms and vacancies is weak. So, the vacancy drag of Cr is unlikely to occur. This means that within the RIS theory of Faulkner et al. [104] the interstitial mechanism should play a major role in the behaviour of chromium segregation on sinks during irradiation. In general, undersized atoms are dragged by interstitials toward the SIA sinks thus producing RIS, while oversized atoms exhibit repulsion by SIA's, so RID of this element is expected. In the work of Lu et al. [57] it was suggested that the presence of other alloying elements can change the average lattice parameter of the Fe lattice. As a consequence, in dependence on the alloying Cr atoms in steels may be either oversized or undersized and thus, a change of the binding energy with self-interstitials from positive (for undersized Cr atoms) to negative (for oversized Cr atoms) could occur. This could explain the different directions of Cr fluxes (to GB or from GB), as shown in Figure 1.21(b). However, this model is not well adapted for Fe-Cr alloys without a significant quantity of alloying elements where both the depletion [109] and the segregations [110] on GB under irradiation can also be observed.

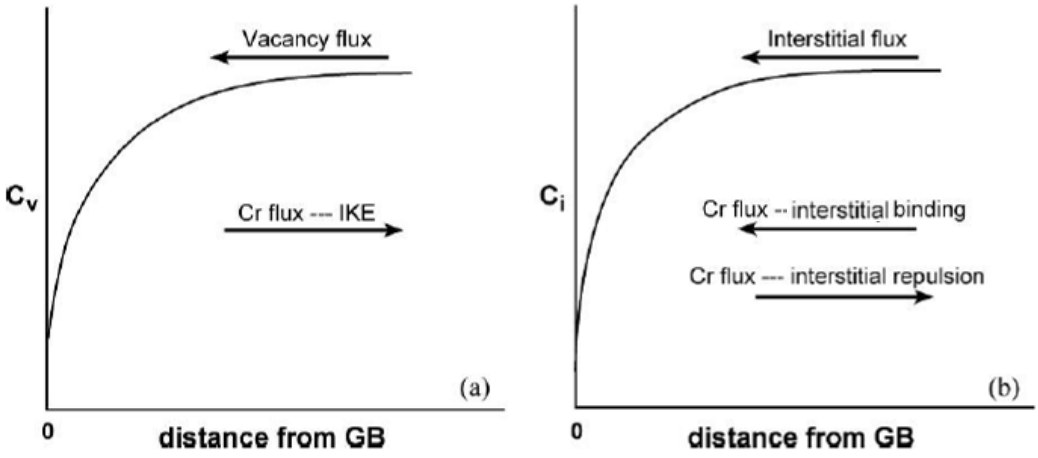

Figure 1.21. Schematic illustration of the segregation tendencies of Cr (after [77]) (a) the flux of Cr owing to the IK effect leads to RID of Cr at boundary [103]; (b) an enrichment by Cr can be owing to the self-interstitial driving mechanism [103] (positive binding of Cr with interstitials [57]) while the flux of Cr can be opposite to that of interstitials due to effect of other alloying elements (in steels) [57].

Let's us now describe some interpretation given by KRT. *Ab-initio* based calculations of Choudhury et al. [103] and KRT have shown that Cr is the faster diffuser by both interstitial mechanism and by vacancy mechanism (inverse Kirkendall effect, see section III.2.c) p.22)). This involves two opposite behavior of Cr: enrichment at defect sinks due to

interstitial mechanism and depletion due to inverse Kirkendall mechanism. Thus, the ambiguous behavior of Cr could be explained in terms of superimposition and competition between these two mechanisms of diffusion. This means also that RIS or RID tendencies of Cr at GB could vary depending on the quantity and distribution of biased sinks (dislocation lines and loops, voids) in the grain as these sinks change the ratio of self-interstitials/vacancies arriving to GB. This could explain the difference between the experimental results. Note that all mentioned mechanisms are summarized in a recent article of Ardell [77].

As described above, the local solute concentration in the vicinity of a point defect sink can reach the solubility limit leading to radiation induced precipitation (heterogeneous – on surfaces, grain boundaries, dislocations or homogeneous – on fluctuations of composition [73,75]). Indeed, as reviewed by Maziasz [111], in F–M alloys, there is an indication of RIS influencing the formation of second phases such as: η (M_6C), Cr_2X, G, χ, σ and α' that is in contrast with data on tempered F-M steels where mainly carbide precipitates are detected (see Table 1.4, p.23).

The phases usually observed in irradiated F-M steels are:

M_6C (η) – phase is a carbide with a diamond-cubic structure enriched by Si, Cr and Ni. It has been found in number of 9-12%Cr steels that contain more than 0.3wt%Ni [111–113]. Also it could be found in some unirradiated material [1].

Cr_2X (M_2X) – hexagonal Cr and V enriched phase has a shape of a fine needles and could be observed after tempering and irradiation [111]. Studies of Little and Stoter showed that once formed, this phase could be dissolved by irradiation at T>380ºC [114].

G phase – usually observed under irradiation, has the stoichiometric composition of $Mn_7Ni_{16}Si_7$, but many variations of this composition have been found [1,111,115,116].

χ (Chi) phase, is a bcc intermetallic phase formed during irradiation, enriched in Fe, Si, Ni and contains a significant amount of Mo and P [1,117]

σ (sigma) phase is a Ni and Si enriched minor irradiation induced phase [1,111]. As proposed by Morgan, Little and Faulkner [118] such phase is observed when the Ni and Si concentration is relatively low and driving forces for irradiation induced segregation are low.

α' (alpha prime) phase, Cr-rich body-centred-cubic phase, coherent with the bcc Fe matrix. Nanometer-size Cr-rich precipitates in the bulk and at dislocations is well known to be the cause of hardening and embrittlement of F-M steels with Cr content more than ~14% after thermal ageing (475 °C embrittlement [35,119]), as well as, at even lower temperature and Cr content, under irradiation, which is found to accelerate the phase separation process [112,113,120,121], or possibly induce it [28,114]. In the work [28] irradiation-induced α' formation has been observed in a high purity binary Fe-10wt.%Cr ferritic alloy following fast reactor irradiation to 30 dpa at 420ºC, and explained in terms of matrix chromium enrichment

caused by chromium desegregation away from voids. Experimental data [122–124] showed that Cr-enrichment and even α' formation on interstitial dislocation loops after irradiation could be expected. Nevertheless, one can note that with the new version of the Fe-Cr phase diagram of Bonny et al. [37], at this temperature α' precipitation is expected in a Fe-10wt.%Cr alloy. In such case, α' formation could be only enhanced.

Note that two alloying elements, Ni and Si, are usually present into the irradiation induced G, η, χ and σ phases in varying proportion. In accordance with Little and Stoter data [114], the ratio of atomic concentration of nickel to silicon determined experimentally decreases in the order: G-phase (2.4 : 1), M_6X (1.1 : 1), χ-phase (0.44 : 1) and σ-phase (0.3 : 1). Likewise the total combined atomic percent of nickel plus silicon decreases in the same order: G-phase (77%), M_6X (33%), χ-phase (23%) and σ-phase (20%). These phases with the exception of the G-phase are also chromium rich [1,111]. It must be also noted that these two elements are also observed to participate to the formation of nanoclusters in the bainitic matrix of pressure vessel steels (in association to copper and manganese) and austenitic stainless steels [111,125–129]. The mechanism of formation of these clusters are also often described as radiation induced segregation on point defects clusters.

c) Property response behaviours

A detailed review of property response of F-M steels (such as irradiation induced hardening, shift of the ductile-to-brittle transition temperature, swelling, changes in corrosion resistance etc.) on irradiation exposure can be found in reviews of Klueh [1,2]. Just two examples will be briefly illustrated in this section to highlight the complex relationship between the Cr content and the response of Fe-Cr alloys to irradiation.

For example, a remarkable non-monotonic effect of the Cr concentration is observed in the shift of the ductile-to-brittle transition temperature (DBTT shift) in irradiated ferritic-martensitic steels (Figure 1.22). This shift is found to reach a minimum around 9%Cr [130] in a range of irradiation temperatures from 300 to 410 °C and for doses from 7 to 36 dpa (Figure 1.22). The fundamentals of relation between irradiation-induced embrittlement versus Cr content remains currently unclear. Nevertheless, one can clearly understand why steels with 9% of Cr are very interesting for nuclear application.

The swelling of Fe-Cr base alloys under irradiation have also a complex modulation versus Cr content. Some experiments showed that the measured swelling under irradiation decreases with the addition of small quantities of Cr, remains low for concentrations between 1% and 10% and then may increase again for higher Cr contents (see [28,65,92,95]). Recently Terentyev et al. [98] have shown by numerical calculations that this behavior could originate from the reduction of the SIA clusters mobility by Cr atoms. This could lead to increase annihilation events between the SIA clusters and the freely migrating vacancies and, hence to decrease the void formation. At the same time, such model is not well adapted to the more

complex swelling evolution with a maximum at ~ 9%Cr that have been reported in works [64,131] (Figure 1.23 and Ref. [131]).

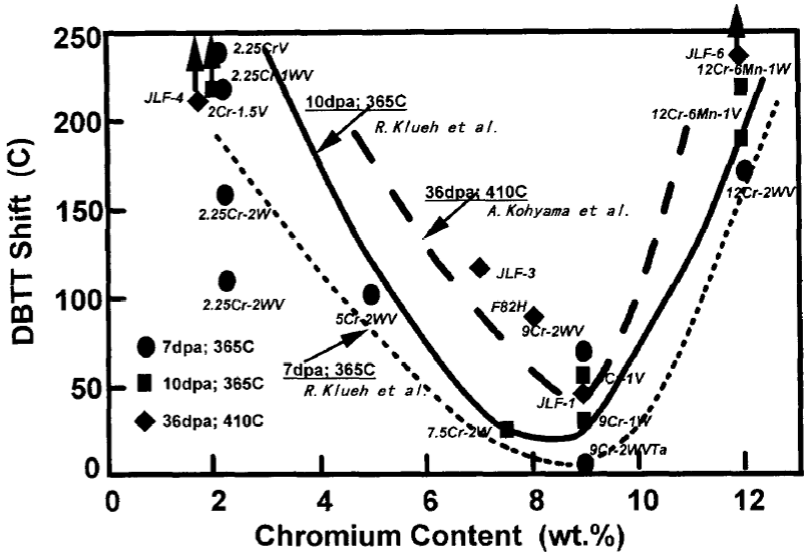

Figure 1.22. Effect of chromium content on DBTT shift of low-activation ferritic and martensitic steels by fast neutron irradiation [130]

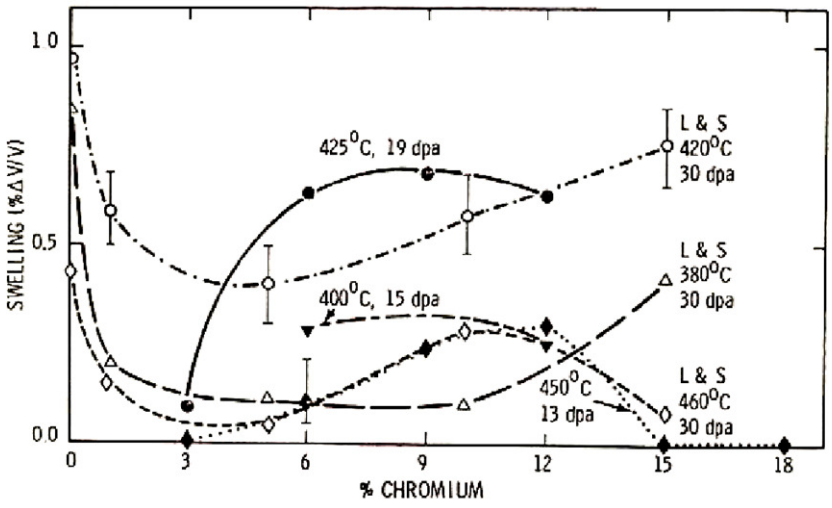

Figure 1.23. Comparison of swelling measurements as a function of alloy chromium content for the indicated irradiation conditions (data from [28,64,65,100]).

Thus, summarizing the aforesaid information, it is possible to say that the non-monotonic influence of Cr content on important technological properties such as ductile-to-brittle transition temperature and swelling under irradiation appears to be a fact. The main mechanisms responsible for such behavior are related to microstructural changes such as formation of radiation-induced dislocation loops and voids, irradiation assisted segregation and precipitation etc. The contribution of theoretical simulations and experiments using advanced techniques, to the understanding of the process of appearance and evolution of these nanoscale features is essential.

V. Conclusions

Fe-Cr base F-M steels are ones of the most promising candidates to withstand the temperature, stress and irradiation fields expected in the reactor core elements and primary system of most of the Gen-IV reactors. In this context, the development and characterization of high-Cr F-M steels, their welding/joining and their qualification, in terms of mechanical and corrosion resistance under working conditions of innovative nuclear system (that is one of the task of European GETMAT project) is of a large scientific and industrial interest.

The Cr concentration in F-M steels is one of the key parameters to be optimized in order to guarantee the best corrosion resistance, together with favorable mechanical properties. The influence of the Cr content on property changes under irradiation is non-monotonic and the understandings of the main mechanisms responsible for such behavior are of large interest.

In this context, the main objective of the current Ph.D. work, which is a part of the GETMAT project, is to provide a wide range of data on the microstructural behavior of irradiated Fe-Cr alloys, model alloys of F-M steels, as a function of variables such as temperature and Cr concentration, in order to understand the role of these variables on the microstructure evolution of the Fe-Cr alloys under irradiation.

As shown, there are still microstructural and mechanical property behaviors of irradiated Fe-Cr based alloys that are not definitely clear. It is believed that the limited understanding of the mentioned above behaviors (RIS, swelling etc.) partially arise from characterization difficulties (for example for nanometric α' precipitation or GB segregation examination). In this context, the combination of conventional analytical (S)TEM methods for the characterization of the evolution of the dislocation structure, with subnanometric scale, 3DAP, which provides 3D atomic reconstruction at near atomic scale and positron annihilation spectroscopy which is sensitive to open volume defect evolution, should be used for providing high level of information.

These three experimental techniques, which have been chosen in the current PhD work, as well as the microstructural data that could be obtained with their help, are described in the next chapter.

VI. References

[1] R.L. Klueh, D.R. Harries, High-Chromium Ferritic and Martensitic Steels for Nuclear Applications, ASTM, Bridgeport, 2001.
[2] Klueh R. L., International Materials Reviews 50 (2005) 287-310(24).
[3] J. Chadwick, Nature 129 (1932) 312.
[4] E. Fermi, Nature 133 (1934) 898-899.
[5] O. Hahn and F. Strassmann, Naturwissenschaften 27 (1939) 11-15.
[6] L. Meitner and O.R. Frisch, Nature 143 (1939) 239-240.
[7] Nuclear Energy Agency (NEA) "Nuclear Energy Today", Url: Www.oecd-nea.org/html/pub/nuclearenergytoday/welcome.html. (p.13).
[8] M.M. Abu-Khader, Progress in Nuclear Energy 51 (2009) 225-235.
[9] IEA Energy Technology Essentials: Nuclear Power, http://www.iea.org/publications/free_new_Desc.asp?PUBS_ID=1916, 2007.
[10] A Technology Roadmap for Generation IV Nuclear Energy Systems. Issued by the U.S. DOE Nuclear Energy Research Advisory Committee and the Generation IV International Forum.(http://www.gen-4.org/Technology/roadmap.htm), 2002.
[11] G. Van Goethem, M. Hugon, V. Bhatnagar, P. Manolatos, M. Deffrennes, Nuclear Engineering and Design 237 (2007) 1486-1502.
[12] Nuclear Energy Agency (NEA) "Nuclear Energy Today": URL Www.oecd-nea.org/html/pub/nuclearenergytoday/welcome.html., p. 16, .
[13] Raymond L. Murray, Nuclear Energy (Sixth Edition), Hardbound, 2008.
[14] U. Fischer, Nuclear Engineering and Design 187 (1999) 15-23.
[15] T. Abram, S. Ion, Energy Policy 36 (2008) 4323-4330.
[16] S.J. Zinkle, J.T. Busby, Materials Today 12 (2009) 12-19.
[17] P. Yvon, F. Carré, Journal of Nuclear Materials 385 (2009) 217-222.
[18] K.L. Murty, I. Charit, Journal of Nuclear Materials 383 (2008) 189-195.
[19] Generation IV and Transmutation Materials (GETMAT) – Collaborative Project, Seventh European Commission Framework Programme, Fission – 2007 – 6.0.02 – Cross Cutting Topic: Materials for Transmutation Technologies and Advanced Reactors, FP7-212175, 2007.
[20] The Generation IV International Forum.GEN-4:Technology:Evolution of Nuclear Energy Systems, from http://www.gen-4.org/Technology/evolution.htm, .
[21] L.K. Mansur, A.F. Rowcliffe, R.K. Nanstad, S.J. Zinkle, W.R. Corwin, R.E. Stoller, Journal of Nuclear Materials 329-333 (2004) 166-172.
[22] C. Fazio, A. Alamo, A. Almazouzi, S. De Grandis, D. Gomez-Briceno, J. Henry, L. Malerba, M. Rieth, Journal of Nuclear Materials 392 (2009) 316-323.
[23] C. Fazio, D.G. Briceno, M. Rieth, A. Gessi, J. Henry, L. Malerba, Nuclear Engineering and Design In Press (2011).
[24] A. Alamo, V. Lambard, X. Averty, M.H. Mathon, Journal of Nuclear Materials 329-333 (2004) 333-337.
[25] P. Pareige, M.K. Miller, R.E. Stoller, D.T. Hoelzer, E. Cadel, B. Radiguet, Journal of Nuclear Materials 360 (2007) 136-142.
[26] M.K. Miller, E.A. Kenik, K.F. Russell, L. Heatherly, D.T. Hoelzer, P.J. Maziasz, Materials Science and Engineering A 353 (2003) 140-145.
[27] E.A. Little, Mats. Sci. Tech. 22 (2006) 491-518.
[28] E.A. Little, D.A. Stow, Journal of Nuclear Materials 87 (1979) 25-39.

[29] G.S. Was, Fundamentals of Radiation Materials Science: Metals and Alloys, 1st ed., Springer, 2007.
[30] F. Tancret, T. Sourmail, M.A. Yescas, R.W. Evans, C. McAleese, L. Singh, T. Smeeton, H.K.D.H. Bhadeshia, Materials Science and Technology 19 (n.d.) 296-302.
[31] F. Masuyama, In: R. Viswanathan and J. Nutting, Editors, Advanced Heat Resistant Steels for Power Generation, The Institute of Materials, London, 1999.
[32] R.L. Klueh, A.T. Nelson, Journal of Nuclear Materials 371 (2007) 37-52.
[33] M. Durand-Charre, Microstructure of Steels and Cast Irons, Springer, 2004.
[34] K.H. Lo, C.H. Shek, J.K.L. Lai, Materials Science and Engineering: R: Reports 65 (2009) 39-104.
[35] P.J. Grobner, Metallurgical and Materials Transactions B 4 (1973) 251–260.
[36] J.-O. Andersson, B. Sundman, Calphad 11 (1987) 83-92.
[37] G. Bonny, D. Terentyev, L. Malerba, Scripta Materialia 59 (2008) 1193-1196.
[38] W. Xiong, M. Selleby, Q. Chen, J. Odqvist, Y. Du, Critical Reviews in Solid State and Materials Sciences Volume 35 (2010) 125 - 152.
[39] L. Malerba, A. Caro, J. Wallenius, Journal of Nuclear Materials 382 (2008) 112 - 125.
[40] M. Matijasevic, A. Almazouzi, Journal of Nuclear Materials 377 (2008) 147-154.
[41] I. Mirebeau, M. Hennion, G. Parette, Phys. Rev. Lett. 53 (1984) 687.
[42] M. Hennion, J. Phys. F: Met. Phys. 13 (1983) 2351.
[43] P. Olsson, I.A. Abrikosov, L. Vitos, J. Wallenius, Journal of Nuclear Materials 321 (2003) 84-90.
[44] P. Olsson, I.A. Abrikosov, J. Wallenius, Phys. Rev. B 73 (2006) 104416.
[45] T.P.C. Klaver, R. Drautz, M.W. Finnis, Phys. Rev. B 74 (2006) 094435.
[46] H. Schneider, 108 (1960) 562.
[47] R.L. Klueh, Journal of Nuclear Materials 378 (2008) 159-166.
[48] H.K.D.H. Bhadeshia, R.W.K. Honeycombe, Steels: Microstructure and Properties, Butterworth-Heinemann, New York, 2006.
[49] F.B. Pickering, Physical Metallurgy and the Design of Steels, Applied Science Publishers, London, 1978.
[50] R.G. Faulkner, Journal of Materials Science 16 (1981) 373-383.
[51] D. McLean, Grain Boundaries in Metals, Clarendon Press, Oxford, 1957.
[52] R.G. Faulkner, Journal of Nuclear Materials 251 (1997) 269-275.
[53] Hondros, E. D.; Seah, M. P., International Metals Reviews 22 (1977) 262-301(40).
[54] K.T. Aust, J.S. Armijo, E.F. Koch and J.H. Westbrook, Trans. ASM 60 (1967) 360.
[55] T.. Anthony, Acta Metallurgica 17 (1969) 603-609.
[56] R.G. Faulkner, Int. Met. Rev. 41 (1996) 198–208.
[57] Z. Lu, R.G. Faulkner, G. Was, B.D. Wirth, Scripta Materialia 58 (2008) 878-881.
[58] M. Wall, A Review of Thermal Aging Effects in High Chromium Ferritic Steels, Atomic Energy Research Establishment, 1987.
[59] W. Schilling, H. Ullmaier, in:, R.W. Cahn, P. Haasen, E.J. Kramer (Eds.) (Ed.), Germany and USA, VCH, 1994, p. 179.
[60] L. Malerba, D. Terentyev, P. Olsson, R. Chakarova, J. Wallenius, Journal of Nuclear Materials 329-333 (2004) 1156-1160.
[61] R.E. Stoller, Journal of Nuclear Materials 276 (2000) 22-32.
[62] K. Vörtler, C. Björkas, D. Terentyev, L. Malerba, K. Nordlund, Journal of Nuclear Materials 382 (2008) 24-30.
[63] E. Vincent, Simulations Numeriques a L'echelle Atomique De L'evolution Microstructurale Sous Irradiation D'alliages Ferritiques, PhD Thesis. L'université des sciences et technologies de Lille, 2006.
[64] D.S. Gelles, Journal of Nuclear Materials 225 (1995) 163-174.

[65] E.A. Little, Journal of Nuclear Materials 87 (1979) 11-24.
[66] M.J. Norgett, M.T. Robinson, I.M. Torrens, Nuclear Engineering and Design 33 (1975) 50-54.
[67] ASTM Standard E693-94, Standard Practice for Characterising Neutron Exposure in Iron and Low Alloy Steels in Terms of Displacements Per Atom (dpa), 1994.
[68] K.. Russell, Progress in Materials Science Volume 28 (1984) 229-434.
[69] M.L. Jenkins, Z. Yao, M. Hernandez-Mayoral, M.A. Kirk, Journal of Nuclear Materials 389 (2009) 197 - 202.
[70] C. Erginsoy, G.H. Vineyard, A. Englert, Phys. Rev. 133 (1964) A595.
[71] P.G. Lucasson, R.M. Walker, Phys. Rev. 127 (1962) 485.
[72] K. Nordlund, J. Wallenius, L. Malerba, Nuclear Instruments and Methods in Physics Research Section B: Beam Interactions with Materials and Atoms 246 (2006) 322-332.
[73] M. Nastar and F. Soisson, in:, Radiation-Induced Segregation. To Be Published in Comprehensive Nuclear Materials, Edited by R. Stoller, Elsevier, in press.
[74] P.R. Okamoto, L.E. Rehn, Journal of Nuclear Materials 83 (1979) 2-23.
[75] R. Cauvin, G. Martin, Phys. Rev. B 23 (1981) 3322.
[76] Nolfi F. V., Phase Transformations During Irradiation. Applied Science: London and New York, 1983.
[77] A.J. Ardell, In: V. Ghetta, Et Al. (Eds.), Materials Issues for Generation IV Systems, Springer, 2008.
[78] S.L. Dudarev, R. Bullough, P.M. Derlet, Phys. Rev. Lett. 100 (2008) 135503.
[79] E.A. Little, R. Bullough, M.H. Wood, Proceedings of the Royal Society of London. A. Mathematical and Physical Sciences 372 (1980) 565 -579.
[80] M. Hernández-Mayoral, D. Gómez-Briceño, Journal of Nuclear Materials 399 (2010) 146-153.
[81] M.. Jenkins, M.. Kirk, Characterisation of Radiation Damage by Transmission Electron Microscopy, 1st ed., Taylor & Francis, 2000.
[82] L.L. Horton, J. Bentley, K. Farrell, Journal of Nuclear Materials 108-109 (1982) 222-233.
[83] I.M. Robertson, M.L. Jenkins, C.A. English, Journal of Nuclear Materials 108-109 (1982) 209-221.
[84] M. Matijasevic, W. Van Renterghem, A. Almazouzi, Acta Materialia 57 (2009) 1577-1585.
[85] S. Xu, Z. Yao, M.L. Jenkins, Journal of Nuclear Materials 386-388 (2009) 161-164.
[86] B.C. Masters, Nature 200 (1963) 254.
[87] D.R. Baker, M.H. Loretto, R.E. Smallman, C.A. English, E.A. Little, MRS Online Proceedings Library 138 (1988) 77.
[88] Z. Yao, M. Hernández-Mayoral, M.L. Jenkins, M.A. Kirk, Philosophical Magazine 88 (2008) 2851.
[89] M.R. Gilbert, Z. Yao, M.A. Kirk, M.L. Jenkins, S.L. Dudarev, Journal of Nuclear Materials 386-388 (2009) 36-40.
[90] B. L. Eyre, A. F. Bartlett, Philosophical Magazine 12 (1965) 261 - 272.
[91] S.J. Zinkle, B.N. Singh, Journal of Nuclear Materials 351 (2006) 269-284.
[92] Y.V. Konobeev, A.M. Dvoriashin, S.I. Porollo, F.A. Garner, Journal of Nuclear Materials 355 (2006) 124-130.
[93] M. Hernandez-Mayoral, Z. Yao, M.L. Jenkins, M.A. Kirk, Phil. Mag. 88 (2008) 2881-2897.
[94] Z. Yao, M.L. Jenkins, M. Hernández-Mayoral, M.A. Kirk, Philosophical Magazine 90 (2010) 4623.

[95] S.I. Porollo, A.M. Dvoriashin, A.N. Vorobyev, Y.V. Konobeev, Journal of Nuclear Materials 256 (1998) 247-253.
[96] D.S. Gelles, Journal of Nuclear Materials 108-109 (1982) 515-526.
[97] K. Arakawa, M. Hatanaka, H. Mori, K. Ono, Journal of Nuclear Materials 329-333 (2004) 1194-1198.
[98] D. Terentyev, L. Malerba, A.V. Barashev, Philosophical Magazine Letters 85 (2005) 587.
[99] D. Terentyev, M. Klimenkov, L. Malerba, Journal of Nuclear Materials 393 (2009) 30-35.
[100] Matijasevic M., Microstructure and Mechanical Properties of Fe-Cr Model Alloys and High Cr Steels Under Neutron Irradiation, PhD thesis., Gent University, 2007.
[101] A. Okada, H. Maeda, K. Hamada, I. Ishida, Journal of Nuclear Materials 271-272 (1999) 133-138.
[102] G.S. Was, J.P. Wharry, B. Frisbie, B.D. Wirth, D. Morgan, J.D. Tucker, T.R. Allen, Journal of Nuclear Materials In Press, Corrected Proof (2011).
[103] S. Choudhury, L. Barnard, J.D. Tucker, T.R. Allen, B.D. Wirth, M. Asta, D. Morgan, Journal of Nuclear Materials 411 (2011) 1-14.
[104] R.G. Faulkner, N.C. Waite, E.A. Little, T.S. Morgan, Materials Science and Engineering: A 171 (1993) 241-248.
[105] H. Wiedersich, P.R. Okamoto, N.Q. Lam, Journal of Nuclear Materials 83 (1979) 98-108.
[106] Y. Grandjean, P. Bellon, G. Martin, Phys. Rev. B 50 (1994) 4228.
[107] J. Kwon, T. Toyama, Y.-M. Kim, W. Kim, J.-H. Hong, Journal of Nuclear Materials 386-388 (2009) 165-168.
[108] P. Olsson, C. Domain, J. Wallenius, Phys. Rev. B 75 (2007) 014110-1--014110-12.
[109] H. Takahashi, S. Ohnuki, T. Takeyama, Journal of Nuclear Materials 104 (1981) 1415-1419.
[110] S. Ohnuki, H. Takahashi, T. Takeyama, Journal of Nuclear Materials 104 (1981) 1121-1125.
[111] P.J.Maziasz, Journal of Nuclear Materials 169 (1989) 95-115.
[112] P. Dubuisson, D. Gilbon, J.L. Séran, Journal of Nuclear Materials 205 (1993) 178-189.
[113] M.H. Mathon, Y. de Carlan, G. Geoffroy, X. Averty, A. Alamo, C.H. de Novion, Journal of Nuclear Materials 312 (2003) 236 - 248.
[114] E.A. Little, L.P. Stoter, Astm-stp 782 (1982) 207.
[115] B.H. Sencer, J.R. Kennedy, J.I. Cole, S.A. Maloy, F.A. Garner, Journal of Nuclear Materials 393 (2009) 235-241.
[116] Gelles D.S, Thomas L.E, Proc. Topical Conf. on Ferritic Alloys for Use in Nuclear Energy Technologies, Eds. J.W. Davis and D.J. Michel.AIME (1984) 559.
[117] J.J. Kai, R.L. Klueh, Journal of Nuclear Materials 230 (1996) 116-123.
[118] T.S. Morgan, E.A. Little, R.G. Faulner, Effect of Radiation on Materials, Eds. R. E. Stoller, A. S. Kumar and D. S. Gelles 16th Intarnational Symposium, ASTM STP 1175 (1994) 607.
[119] F. Bley, Acta Metallurgica Et Materialia 40 (1992) 1505-1517.
[120] M. H. Mathon, Y. De Carlan, G. Geoffroy, X. Averty, C. H. de Novion, and A. Alamo, In Effects of Radiation on Materials: 20th International Symposium, ASTM STP 1405, Edited by S. T. Rosinski, M. L. Grossbeck, T. R. Allen, and A. S. Kumar (American Society for Testing and Materials, West Conshohocken, PA,) (2001) 674.
[121] C. Heintze, A. Ulbricht, F. Bergner, H. Eckerlebe, J. Phys.: Conf. Ser. 247 (2010) 012035.

[122] E. Wakai, A. Hishinuma, Y. Kato, H. Yano, S. Takaki, K. Abiko, Le Journal De Physique IV 05 (1995) 10.
[123] I.M. Neklyudov, V.N. Voyevodin, Journal of Nuclear Materials 212-215 (1) (1994) 39-44.
[124] S. Ohnuki, H. Takahashi, T. Takeyama, Journal of Nuclear Materials 122 (1984) 317-321.
[125] B. Radiguet, A. Barbu, P. Pareige, Journal of Nuclear Materials 360 (2007) 104-117.
[126] P. Pareige, B. Radiguet, A. Barbu, Journal of Nuclear Materials 352 (2006) 75-79.
[127] A. Etienne, B. Radiguet, P. Pareige, J.-P. Massoud, C. Pokor, Journal of Nuclear Materials 382 (2008) 64 - 69.
[128] E. Meslin, B. Radiguet, P. Pareige, A. Barbu, Journal of Nuclear Materials 399 (2010) 137-145.
[129] S. Jumel, C. Domain, J. Ruste, J.-C. Van Duysen, C. Becquart, A. Legris, P. Pareige, A. Barbu, E. Van Walle, R. Chaouadi, M. Hou, G. Odette, R. Stoller, B. Wirth, Journal of Testing and Evaluation 30 (2002) 37-46.
[130] A. Kohyama, A. Hishinuma, D.S. Gelles, R.L. Klueh, W. Dietz, K. Ehrlich, Journal of Nuclear Materials 233-237 (1996) 138 - 147.
[131] F.A. Garner, M.B. Toloczko, B.H. Sencer, Journal of Nuclear Materials 276 (2000) 123-142.

CHAPTER 2.
ALLOYS AND EXPERIMENTAL TECHNIQUES

High-chromium ferritic-martensitic (F-M) steels of technological interest in the nuclear field generally contain between 7 and 14% of chromium. It is therefore important to explore the effect of Cr concentration on the behavior of such steels (and Fe-Cr model alloys that are often used to mimic F-M steels) under irradiation. As it was shown in chapter 1, this effect is non-monotonic and does not lend itself to simple explanations, thus representing the main challenge addressed by the modelling programme of GETMAT/Work Package 4 project.

The main objective of the current thesis, which is a part of the GETMAT/WP4 project, is to provide a wide range of microstructural behavior data using the high resolution techniques on irradiated Fe-Cr model alloys and F-M steels, as a function of three main variables: Cr concentration, dose and temperature.

The description of the investigated Fe-Cr model alloys and F-M steel T91 is given in the first section of this chapter: fabrication of the materials, their chemical composition and mechanical properties in the as-received state.

Irradiations considered within the present PhD thesis are performed by neutrons and ions. Neutron irradiation allows radiation effects in the bulk, as they would occur in a nuclear reactor (but with a higher flux), to be better mimicked and the microstructural characterization of neutron irradiated specimens can be much more thorough and representative. The neutron-irradiated specimens used within the GETMAT/WP4 project have been irradiated in the framework of the MIRE-Cr irradiation program (for details, see [1]). Besides, ion irradiations are considered in this research in order to cover a larger range of irradiation conditions. The neutron and ion irradiation conditions are described in the second part of this chapter.

Changes of material properties under irradiation are based on the creation and redistribution of the defects and their complexes in relation to the formation of dislocation loops and voids, irradiation assisted segregation and precipitation etc. Only few experimental techniques are sensitive to such microstructural changes. This thesis is focused on the use of three fine-scale techniques: **3D atom probe (3DAP)** – for characterizations of the distribution of chemical elements at atomic scale and correlation with crystallographic structure of the specimens; **positron annihilation spectroscopy (PAS)** – for investigation of the distribution of open-volume defects such as vacancies and theirs clusters and **transmission electron microscopy (TEM)** – for characterization of point defects complexes such as dislocation loops. The combination of these advanced techniques is essential to obtain a complete picture of the irradiation-assisted evolution of defects and corresponding changes of the chemical element distributions at nano- and microscopic scales. These techniques are described in details in the third section of this chapter.

Table of content

I. Materials

I.1. Fabrication

The materials used in this work are Fe-Cr based model alloys of industrial purity, namely, Fe-5Cr (4.93 at%Cr), Fe-9Cr (8.93 at%Cr) and Fe-12Cr (12.33 at%Cr). The Fe-Cr model alloys were fabricated at Ghent University Belgium within the PhD thesis of Milena Matijasevic [1] by furnace melting of industrial purity Fe and Cr. After casting, the obtained ingots were cold worked under protective atmosphere to fabricate plates of 9mm thickness. These plates were then annealed for 3 hours at 1050°C in high vacuum for austenisation and stabilization. The duration of the heat treatment was chosen in order to get rid of any possible precipitation or phase transformation that might have been happened during hot rolling and also to allow a maximum degassing of the alloys. This treatment was then followed by air cooling to room temperature. Finally, the tempering procedure has been performed. It is consisted of heating the alloys up to 730°C for 4h followed by air cooling to room temperature.

After the elaboration, the materials have been cut mechanically and delivered from SCK·CEN (Mol, Belgium) to GPM laboratory (Rouen, France).

I.2. Chemical composition

As the Cr content is important for the behavior of the materials, Fe-Cr model alloys were prepared with different concentrations. The nominal chemical composition of each of the model alloys and steel, which was measured within the PhD Thesis of M. Matijasevic [1] using induced coupled plasma mass spectrometry (ICP-MS) and the combustion technique at OCAS (Zelzate, Belgium) is given in Table 2.1 to Table 2.3.

Table 2.1. Nominal chemical composition (at%) of the Fe-5%Cr model alloy measured by ICP-MS [1]

Fe	balance	C	0.09
Cr	4.93	N	0.05
Si	0.08	O	0.21
P	0.02	S	0.01
Mn	0.02	Al	0.01
Ni	0.06	Ti	0.003
V	0.001		

Table 2.2. Nominal chemical composition (at%) of the Fe-9%Cr model alloy measured by ICP-MS [1]

Fe	balance	C	0.09
Cr	8.93	N	0.06
Si	0.18	O	0.23
P	0.02	S	0.001
Mn	0.03	Al	0.014
Ni	0.07	Ti	0.004
V	0.002		

Table 2.3. Nominal chemical composition (at%) of the Fe-12%Cr model alloy measured by ICP-MS [1]

Fe	balance	C	0.129
Cr	12.33	N	0.09
Si	0.22	O	0.22
P	0.09	S	0.012
Mn	0.03	Al	0.006
Ni	0.085	Ti	0.004
V	0.002		

The compositions were also measured by 3D atom probe (3DAP) analysis before any treatment. These data as well as the study of the homogeneity of the chemical composition of the alloys are presented in details in the Chapter 3.

It should be mentioned that within the GETMAT/WP4 program four Fe-Cr model alloys and two F-M steels are investigated, namely Fe-2.5%Cr, Fe-5%Cr, Fe-9%Cr, Fe-12%Cr, T91 and EUROFER 97 (for description, see [1]). The alloy Fe-2.5%Cr as well as the steels T91 and EUROFER 97 have not been explicitly investigated within the current PhD work, but the results obtained from other investigation on these materials are used whenever it is needed for comparison.

I.3. Mechanical properties in the as-received state

Tensile tests and hardness measurement data on the as-received alloys are available in the work [1]. Measurements were done in all directions and average values have been taken. Engineering stress-strain curves are presented in Figure 2.1.

The hardness measurements have been done according to the requirements of ASTM E384. In Figure 2.2, the yield stress (YS), ultimate tensile stress (UTS) and hardness results are plotted as a function of Cr concentration. In the model alloys, a linear increase is found for all three properties with increasing chromium content, while the steels exhibit higher values.

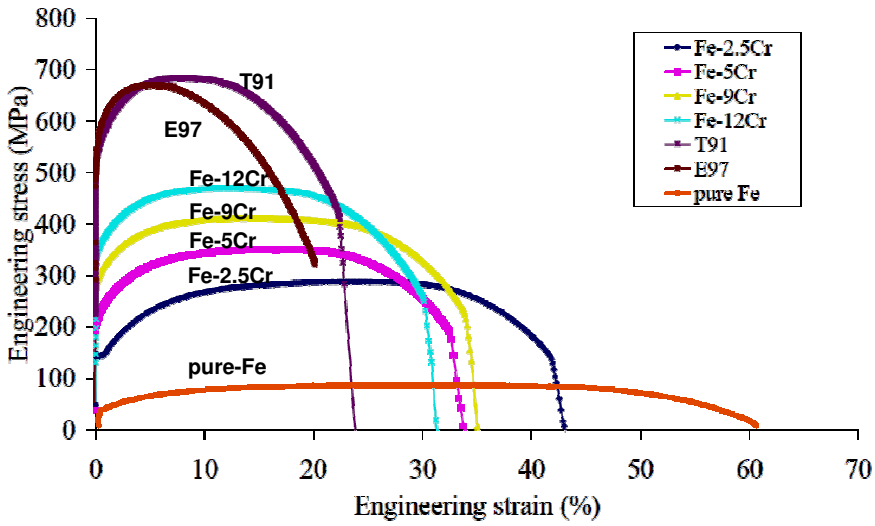

Figure 2.1. Engineering stress and strain curves of as-received Fe-Cr model alloys and F-M steels at room temperature(from [1])

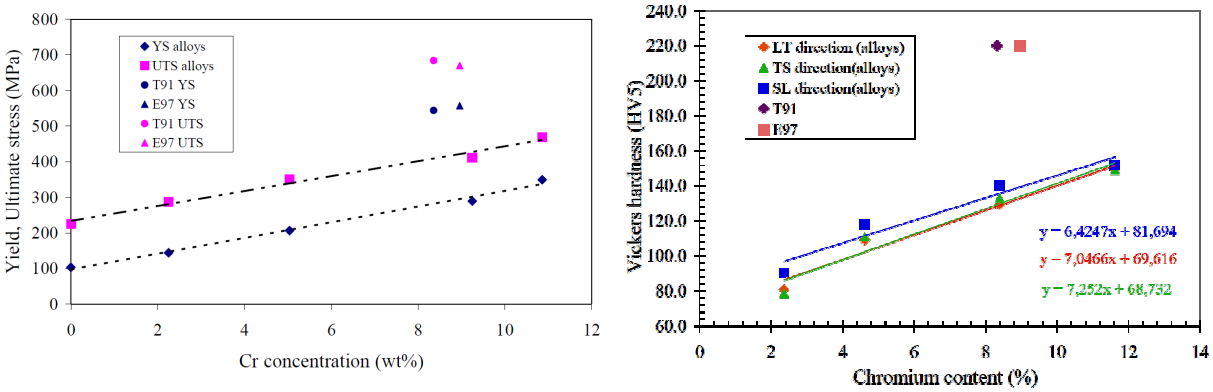

Figure 2.2. The tensile properties and hardness evolution as a function of Cr concentration (in wt%) (from [1])

II. Irradiation experiments

II.1. Neutron irradiation experiments

Samples from each material were neutron irradiated in the CALLISTO loop of the BR2 test reactor at SCK·CEN (Mol, Belgium). During irradiation, the temperature and the pressure were maintained constant at about (300±5)ºC and 15MPa, respectively. These irradiation conditions mimic the situation encountered in a pressurized water reactor.

a) Belgian reactor 2

The Belgian reactor 2 (BR2) is a high flux material test reactor. The reactor has been designed in 1957, became critical in 1963 and has been refurbished in 1980 and 1996. Its nuclear power is nominally 125 MW. The core geometry of the BR2 reactor is illustrated in Figure 2.3, where schematic overview is given. Thanks to its neutron flux and a large amount of irradiation space, BR2 reactor plays a prominent role in the research of the behaviour of materials and fuel under irradiation.

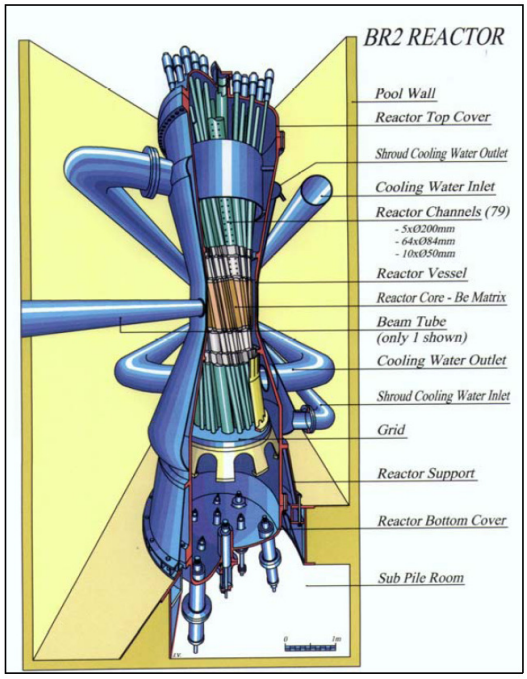

Figure 2.3. General view of the BR2 reactor (from [1])

b) MIRE-Cr irradiation

The neutron-irradiated specimens examined in the current work, have been irradiated in the framework of the MIRE-Cr irradiation program (for details, see [1]). The MIRE-Cr irradiation campaign is the experimental part of the scientific program *"Modelisation of irradiation effects, modelling oriented experiments on pure Fe-Cr-C alloys"*. The MIRE-Cr

irradiation campaign started in 2004 (05/2004) for one cycle and it was followed by four reactor cycles in 2005.

The objective of this irradiation campaign was to provide the necessary experimental support for the validation and further development of the existing computational models for material irradiation damage effects. The amount, size and shape of the specimens loaded in the MIRE-Cr experiment were done in such a way that all fundamental properties of the material can be obtained. Table 2.4 illustrates the test matrix that has been elaborated to fulfil this task. The samples were encapsulated to prohibit reaction with the coolant and to control the temperature by making good use of gamma heating and thermal barriers. The irradiation of MIRE-Cr were conducted at a temperature about (300±5)ºC.

Table 2.4. Test matrix for MIRE-Cr irradiation (from [1])

Groups	Type of test	Material L0251	Material L0259	Material L0252	Material L0253			Total
material		2.25%Cr	5.04%Cr	9.26%Cr	10.86%Cr	T91	Eurofer 97	
I	tensile	6	6	6	6	6	6	36
unloading (18.08.04)	mini CV	0	0	0	0	0	0	0
required dose=(0.075dpa: max=0.1dpa)	small punch/TEM	20	20	20	20	20	20	120
	PAS	3	3	3	3	3	3	18
II	tensile	6	6	6	6	6	6	36
unloading (15.12.04)	mini CV	12	0	12	0	0	0	24
required dose=(0.5dpa: max=0.8dpa)	small punch/TEM	20	20	20	20	20	20	120
	compression	3	3	3	3	3	3	36
	PAS	3	3	3	3	3	3	18
III	tensile	6	6	6	6	6	6	36
unloading (05.06.05)	mini CV	0	0	0	0	0	0	0
required dose=(1.2dpa: max=1.5dpa)	small punch/TEM	20	20	20	20	20	20	120
	PAS	3	3	3	3	3	3	18
0	tensile	12	12	12	12	0	0	48
unirradiated	mini CV	12	12	12	12	12	12	72
	small punch/TEM	20	20	20	20	20	20	120
	compression	3	3	3	3	3	3	36
	PAS	3	3	3	3	0	3	15
total number of specimens								
	tensile	30	30	30	30	18	18	156
	mini CV	24	0	24	0	12	12	72
	small punch/TEM	80	80	80	80	80	80	480
	PAS	12	12	12	12	9	12	69
	compression	6	6	6	6	6	6	36

In total, within Mire-Cr project, 480 specimens were irradiated in BR2, but not all of them have been investigated in the current PhD work. In table 2.6 are shown the 6 groups of different materials for 3 groups of irradiation doses after 1, 3 and 5 cycles (to average neutron exposures of 0.06, 0.6 and 1.5 displacements per atom (dpa) that corresponds to 22.18, 73.87 and 118.68 days of exposure respectively) and also the different types of specimens that have been prepared from each material. The Fe-Cr alloys, investigated within the current work, were irradiated to an average neutron exposures of 0.6 dpa with a neutron flux of 9×10^{13} n/(cm^{2}s) with energy higher than 1 MeV.

After mechanical tests and microscopic investigations [1–3], samples with the size $10\times10\times1$ mm^3 neutron irradiated up to doses 0.06, 0.6 and 1.5 dpa have been shipped to FZD (Dresden, Germany) for small-angle neutron scattering (SANS) measurements (for details, see [4,5]). Subsequently, using hot cell facilities of FZD, the bars for tomographic atom probe (TAP) specimens with the size $7\times0.3\times0.3$mm^3 have been prepared from the four model alloys, Fe-2.5Cr, Fe-5Cr, Fe-9Cr and Fe-12Cr irradiated at 0.6 dpa and delivered to GPM laboratory (Rouen, France). The data on the neutron irradiated samples available in GPM are summarized in Table 2.5.

Table 2.5. Neutron irradiated samples available in GPM

Alloys, quantity	Irradiation dose, dpa	Activity (Co-60), MBq*	Dose rate in a distance of 20 cm, μSv/h*
Fe-2.5Cr 3 bars $7\times0.3\times0.3$mm^3	0.6	0.7	6
Fe-5Cr 3 bars $7\times0.3\times0.3$mm^3	0.6	0.9	8
Fe-9Cr 3 bars $7\times0.3\times0.3$mm^3	0.6	0.9	8
Fe-12Cr 3 bars $7\times0.3\times0.3$mm^3	0.6	1.8	16
		Total activity: 4.3 MBq	

**Measurements have been performed in FZD (Dresden, Germany) in 2009*

To have more details about the material treatment, irradiation conditions and mechanical properties, see Ref. [1].

c) Mechanical properties after neutron irradiation

Tensile tests for studied neutron irradiated Fe-Cr alloys have been performed by M. Matijasevic and co-workers in the temperature range from – 160°C to 300°C[1–3]. Engineering stress-strain curves for all Fe-Cr alloys irradiated up to 0.6 dpa (the state,

investigated within the current work) and tested at room temperature are shown in Figure 2.4*a*.

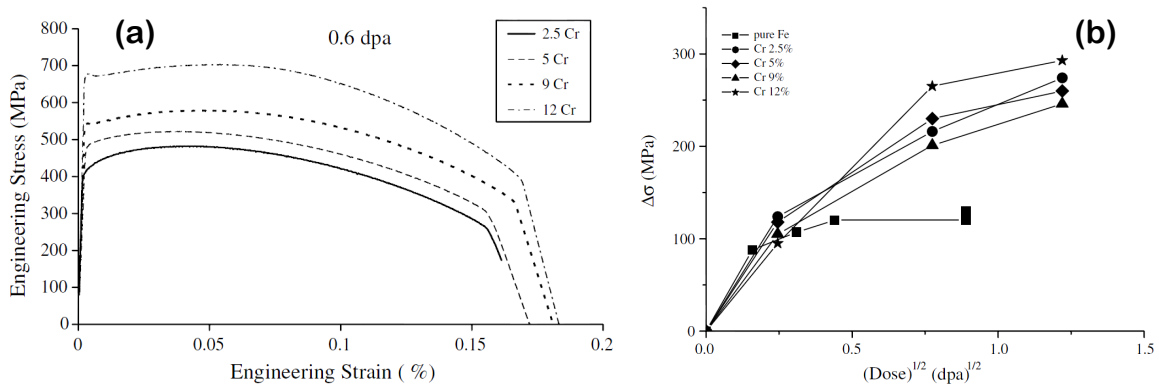

Figure 2.4. a) Tensile tests at room temperature of model alloys after neutron irradiation at 300ºC up to 0.6 dpa; b)increase in room temperature yield strength upon irradiation at 300ºC, $\Delta\sigma_Y$ vs (dose)$^{1/2}$ (from [2])

The stress-strain curves clearly show irradiation hardening of Fe-Cr alloys as presented by Figure 2.4*b*, where the increase of the yield strength is plotted against the square root of the irradiation dose [2]. These data show that Fe-Cr model alloys harden more than pure Fe and saturate at a higher dose when compared to the behaviour of pure Fe irradiated under similar conditions. The yield strength dependence with doses shows that the addition of Cr enhances radiation-induced hardening. A small amount of Cr would increase the hardening drastically but the addition of about 9%Cr seems to moderate this increase, as it can be seen in Figure 2.4b, where a minimum hardening is found for the Fe-9%Cr alloy. Based on this finding and on the comparison with available TEM data [2], the hypothesis have been proposed that there are additional mechanisms of irradiation hardening for alloys with Cr content higher and lower than 9%: i) due to the tendency to short-range ordering of FeCr alloys when Cr concentration is below 9% and ii) due to the appearance of α' phase above this value.

II.2. Ion irradiation experiments

Ion irradiation experiments have been performed in order to focus on the aspects which are not addressed by the neutron irradiation experiments, such as temperature effect and effect of dose at doses higher than 1.5 dpa. The possibility of comparison of neutron and ion irradiation at the same temperature and dose conditions is also of interest.

a) Low energy ion irradiation experiments

Low energy ion irradiations have be undertaken in CSNSM (Centre de Spectrométrie Nucléaire et de Spectrométrie de Masse) at University of Paris-Sud, Orsay 11 (France) with the ion implanter IRMA (Figure 2.5). Hot cathode of Nier-Bernas type of IRMA implanter produces ion beams from hydrogen to lead in the energy range from 5 to 570 keV. Created ions are accelerated by an electrical field and separated according to their masse-over-charge ratio by a magnetic field. The beam of ions then arrives in the analytical chamber. To get uniform doses and to have a better of control radiation, the beam scans the sample. The implantation surface is limited by a diaphragm positioned in front of the target.

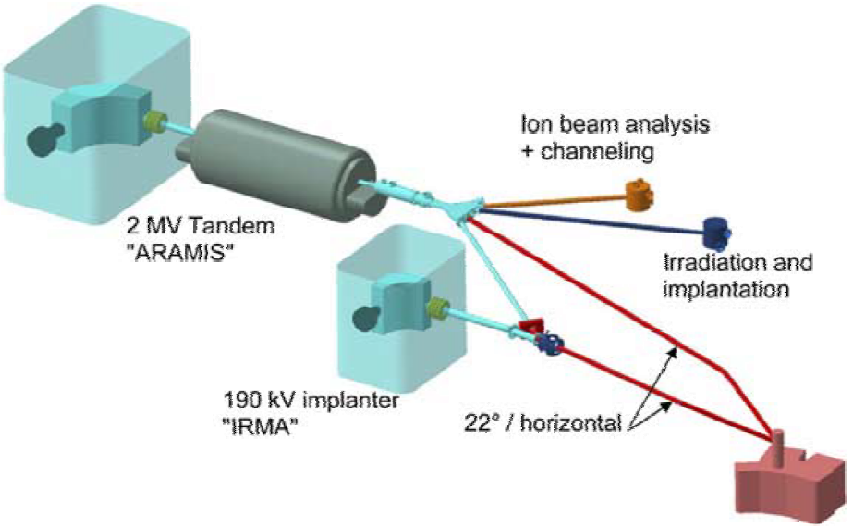

Figure 2.5. Scheme of the facilities of JANNUS installations(Orsay) : ARAMIS accelerator and IRMA implanter and their beam line (from [6]).

Since the objective of the research is to mimic neutron irradiation, self-ions (Fe) have been used for irradiation in order to avoid introduction of foreign atoms. An ion energy of 150 keV has been chosen as it ensures that the damaged layer depth is appropriate for the analysis by TEM and 3DAP facilities. Indeed, according to SRIM (Stopping and Range of Ions in Matter) calculation [7], such irradiation produces a damaged layer which is about 50 to 60 nm deep (Figure 2.6). The parameters of SRIM calculations are listed in Appendix 4.

TEM samples have been in-situ irradiated as 3 mm thin foils (for details of thin foil preparation see Appendix 3). The implanter IRMA is coupled together with a 200 kV transmission electron microscope to allow simultaneous irradiation and observation. The ion beam line enters the microscope column with a tilt of 22° with respect to the sample surface (Figure 2.5). In order to perform ion irradiation and TEM observation simultaneously, an angle of 38° between the ion beam and the normal to the foil has been chosen. Schematically the positions of ion beam, electron beam during irradiation experiment and thin foil are shown

in Figure 2.7. The temperature was controlled by a TEM double tilt sample holder (±60º) which allows the work in the temperature range between liquid nitrogen and 800ºC. The vacuum can be kept as low as 5×10^{-3} Pa under heating.

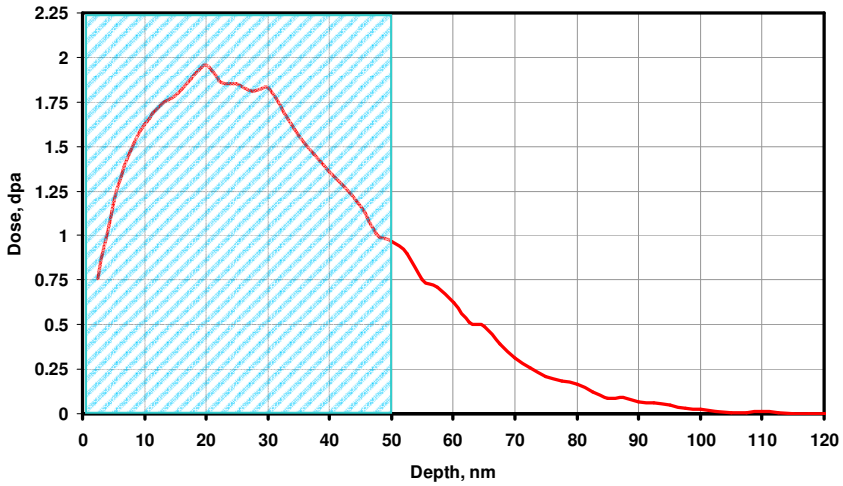

Figure 2.6. Distribution of damage after irradiation with 150 keV Fe+ ions in an Fe-12Cr model alloy, calculated with SRIM 2008. Flux: 1.6×10^{15} $m^{-2}s^{-1}$; fluence: 4.32×10^{18} $ions\cdot m^{-2}$. The estimated fluence on the layer up to 50 nm (adapted to TEM and TAP samples) is 1.5dpa

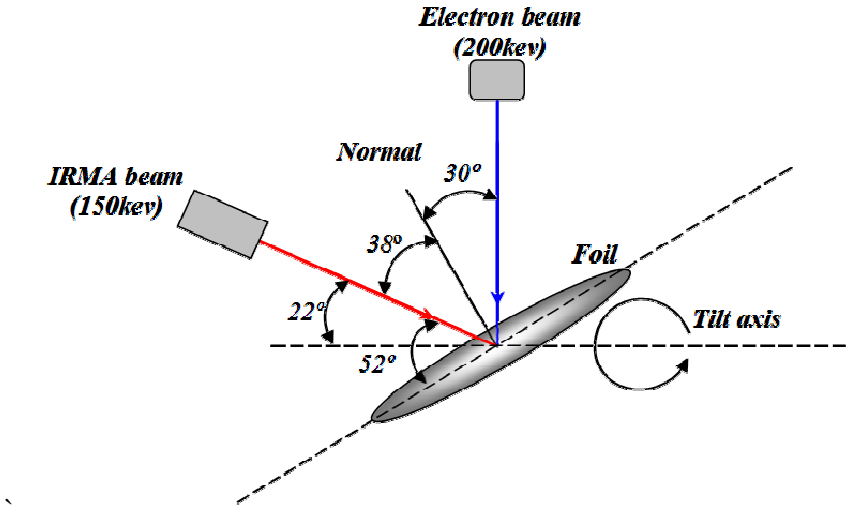

Figure 2.7. Scheme of in-situ TEM ion irradiation experiment.

Samples for 3DAP investigations have been irradiated with an ion implanter IRMA. They were standard 3DAP samples– tips (for details of 3DAP samples preparation see Appendix 1). Schematically, ion irradiation of 3DAP tips is shown in Figure 2.8a. During irradiation, 3DAP samples are arranged on special sample holders made from stainless steel or from copper, covered by stainless steel shield (Figure 2.8b) [8].

The different conditions of low energy ion irradiation experiments are summarized in Table 2.6. As TEM and TAP samples have been irradiated under different angles, slight changes in irradiation conditions have been made to reach the same dose on the layer up to 50nm.

As shown in Table 2.6, both TEM foil and 3DAP tips should be ion irradiated at 500°C and 300°C. The results of TEM and 3DAP study of samples ion irradiated at 500°C are presented in the Chapter 5. However, the ion irradiation experiments at 300°C are still in progress and are not fully presented in the current manuscript. The results of series of ion irradiations at 300°C will be available in a future paper.

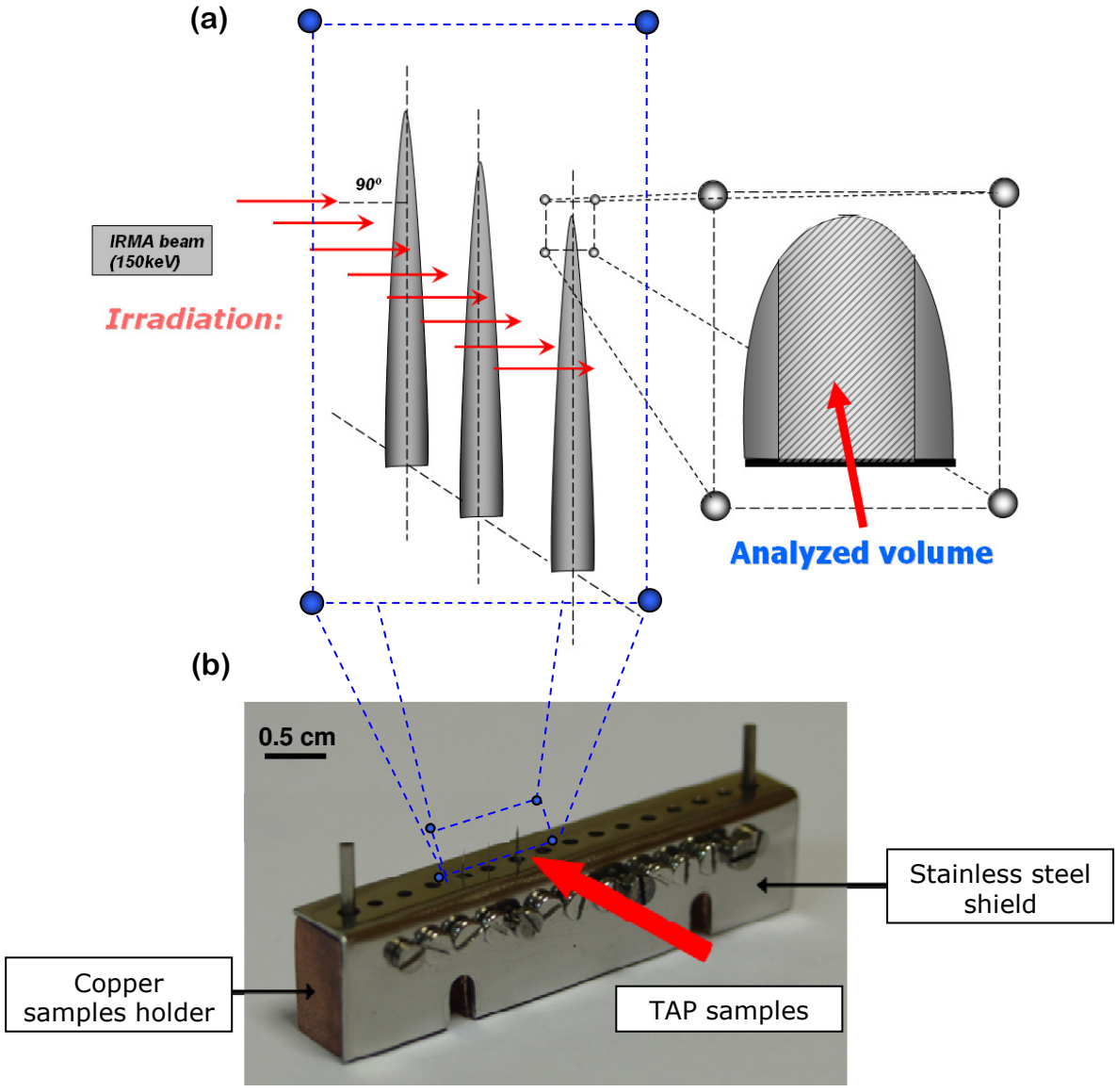

Figure 2.8. (a) Scheme of ion irradiation of TAP samples. (b) Copper sample holder, used for TAP samples irradiation. The using of stainless steel shield allows to avoid the contamination of tips by Cu atoms (from [8]).

Table 2.6. Conditions of low energy ion irradiations of Fe-Cr model alloys by 150 keV Fe+ ions

Samples	Form	Flux, $m^{-2}s^{-1}$	Fluence, $ions \cdot m^{-2}$	Angle of irradiation to normal of the sample surface, °	Dose in the layer up to 50 nm, *dpa NRT*	T, ºC
Fe-9%Cr Fe-12%Cr	TEM foils	1.6×10^{15}	4.32×10^{18}	38	1.5	500
Fe-9%Cr Fe-12%Cr	TEM foils	1.6×10^{15}	4.32×10^{18}	38	1.5	300*
Fe-9%Cr Fe-12%Cr	TAP tips	2.0×10^{15}	5.4×10^{18}	0	1.5	500
Fe-9%Cr Fe-12%Cr	TAP tips	2.0×10^{15}	5.4×10^{18}	0	1.5	300*

**ion irradiation experiments at 300°C are in progress*

b) High energy ion irradiation experiments

In low energy ion irradiation experiments, the free surfaces of specimen are sinks for radiation induced defects and in some cases its effect can be significant and damage accumulation can be different from what can be expected in bulk. Therefore, ion irradiation experiments at higher energy (so, larger penetration depth) have been performed, where surface effect would be avoided and where characterisation techniques such as positron annihilation spectroscopy (PAS), TEM and 3DAP (with FIB method preparation of sample) can be applied.

Since the characterization of samples after high energy ion irradiation is still in progress, the results of this series of experiments are not presented in this manuscript. Subsequently, the results which involve the combination of PAS, 3DAP and TEM study will be available in a paper.

The process of the elaboration of samples for these experiments is presented here in details. The features of the samples surface preparation which includes cutting, mechanical polishing and electrochemical polishing are presented in Appendix 3. The process of irradiation with high energy ions is described below.

High energy ion irradiation has been undertaken in Ion Beam Centre in FZD, Dresden (Germany). As in the case of low energy ion irradiation, self-ions (Fe+) have been used. The irradiation have been performed by 3 stages with irradiation energies 0.5, 2 and 5 MeV in order to get a flat profile of damage up to about 1.5 μm, as shown by SRIM calculations (Figure 2.9).

Samples have been irradiated as PAS samples – plates with size about $7\times7\times1$ mm^3 (for details of PAS samples preparation see Appendix 3). The different conditions of high energy ion irradiation experiments are summarized in Table 2.7–Table 2.10.

Two facts that could affect results must be mentioned: i) the irradiations have been performed with different sequences (see Table 2.10); ii) the temperature of samples wasn't decreased during the changes of the beam energies. For example, it is known, that during the irradiation at 300ºC for 1 dpa, the samples remained additional 1h 05 min at this temperature without irradiation. The time for the irradiation at 300ºC up to 5 dpa was about 7 h. This fact

should be taken into account during the interpretation of results, since it can affect on the redistribution of created point defects.

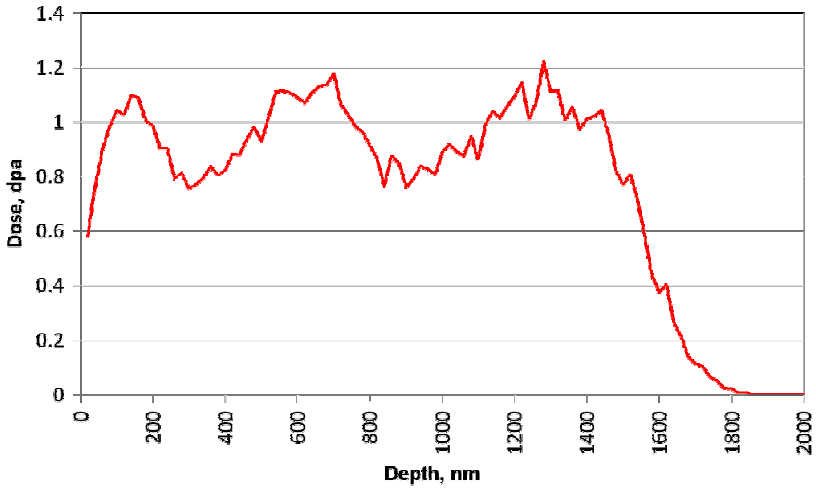

Figure 2.9. Distribution of damage after Fe+ ions irradiation with Fe with 3 different energies: 5 MeV, 2 MeV and 0.5 MeV in Fe-12Cr model alloy, calculated with SRIM 2008. The irradiation produces nearly flat profile of damage (of about 1 dpa) up to about 1.5 μm. Conditions of irradiations are reported in Table 2.8

Table 2.7. Conditions for high energy ion irradiation experiments

MATERIALS	IRRADIATION TEMPERATURES		
	100ºC	300ºC	420ºC
Fe-5%Cr	-	1and 5 dpa	-
Fe-9%Cr	1 and 5 dpa	1and 5 dpa	1and 5 dpa
Fe-12%Cr	-	1and 5 dpa	-

Table 2.8. Irradiation conditions for high energy ion irradiation experiments 1 dpa

E (keV)	Dose (Ions/cm^2)	Flux (Ions/cm^{2}s)	Total dose (dpa NRT)
500	1.82×10^{14}	2×10^{11}	1 dpa
2000	2.86×10^{14}	2×10^{11}	
5000	5.62×10^{14}	2×10^{11}	

Table 2.9. Irradiation conditions for high energy ion irradiation experiments 5 dpa

E (keV)	Dose (Ions/cm^2)	Flux (Ions/cm^{2}s)	Total dose (dpa NRT)
500	$5\times1.82\times10^{14}$	2×10^{11}	5 dpa
2000	$5\times2.86\times10^{14}$	2×10^{11}	
5000	$5\times5.62\times10^{14}$	2×10^{11}	

Table 2.10. Sequences of beam energies during high energy ion irradiation experiments

T ºC	1 dpa	5 dpa
100 ºC	5 MeV → 2 MeV → 0.5 MeV	unknown
300 ºC	0.5 MeV → 2 MeV → 5 MeV	5 MeV → 2 MeV → 0.5 MeV
420 ºC	unknown	0.5 MeV → 2 MeV → 5 MeV

III. Experimental techniques

III.1. Field ion microscopy

The ion microscope, invented more than 50 years ago by Erwin Müller [9] gave the first possibility to make observations of the surface of metals at the atomic scale. This is a qualitative nondestructive technique.

The principle of this technique is based on the field ionization of a noble gas on the surface of the sample. This phenomenon requires a high electric field at the surface of the sample: about 30 to 50 V/nm. For this, the tip effect is used. The radius of curvature R of the sample should be less than 100 nm. Thus, when an electrical potential V of some kilovolts (from about 2 to 12 kV) is applied to the sample, an intense electrical field is created at the surface of the sample. This intensity is given by the following relation:

$$E = \frac{V}{R\beta} \qquad (2.1)$$

where β is a geometric factor which characterizes the shape of the conductor. In the case of a sphere, β would be equal 1. In the case of a tip, β is in between 2 and 8 [10]. The value of the electrical field at the apex of the tip is of the order of few tens V/nm that allows ionization of the atoms of noble gases (He, Ne) introduced in the ultrahigh vacuum chamber (under a pressure of 10^{-3} Pa). For example, the field of ionization of Ne is equal to 34 V/nm.

Produced ions are accelerated by the electrical field towards a phosphor detector (Figure 2.10*a*) and form on the visualization screen an extended image of modulations of the electrical field in the vicinity of the surface of the sample. It allows a projected picture of surface atoms to be obtained.

The picture obtained on the screen is a quasi-stereographic projection of the surface of the tip. The straight trajectories of ions intercept at a point P (Figure 2.10*a*) that differs from the point O (centre of the hemispheric apex of the tip). The distance *OP* is given by $OP = mR$ where *m* is the compression factor. The most intense points recognized on the image in Figure 2.10*b* correspond to the zones of the surface where the electrical field is the most intense, i.e. correspond to the roughness at the atomic scale. Indeed, roughness of the tip induces a local decrease of radius (atomic scale) and, therefore, leads to an increase of the electrical field in accordance with an equation 2.1.

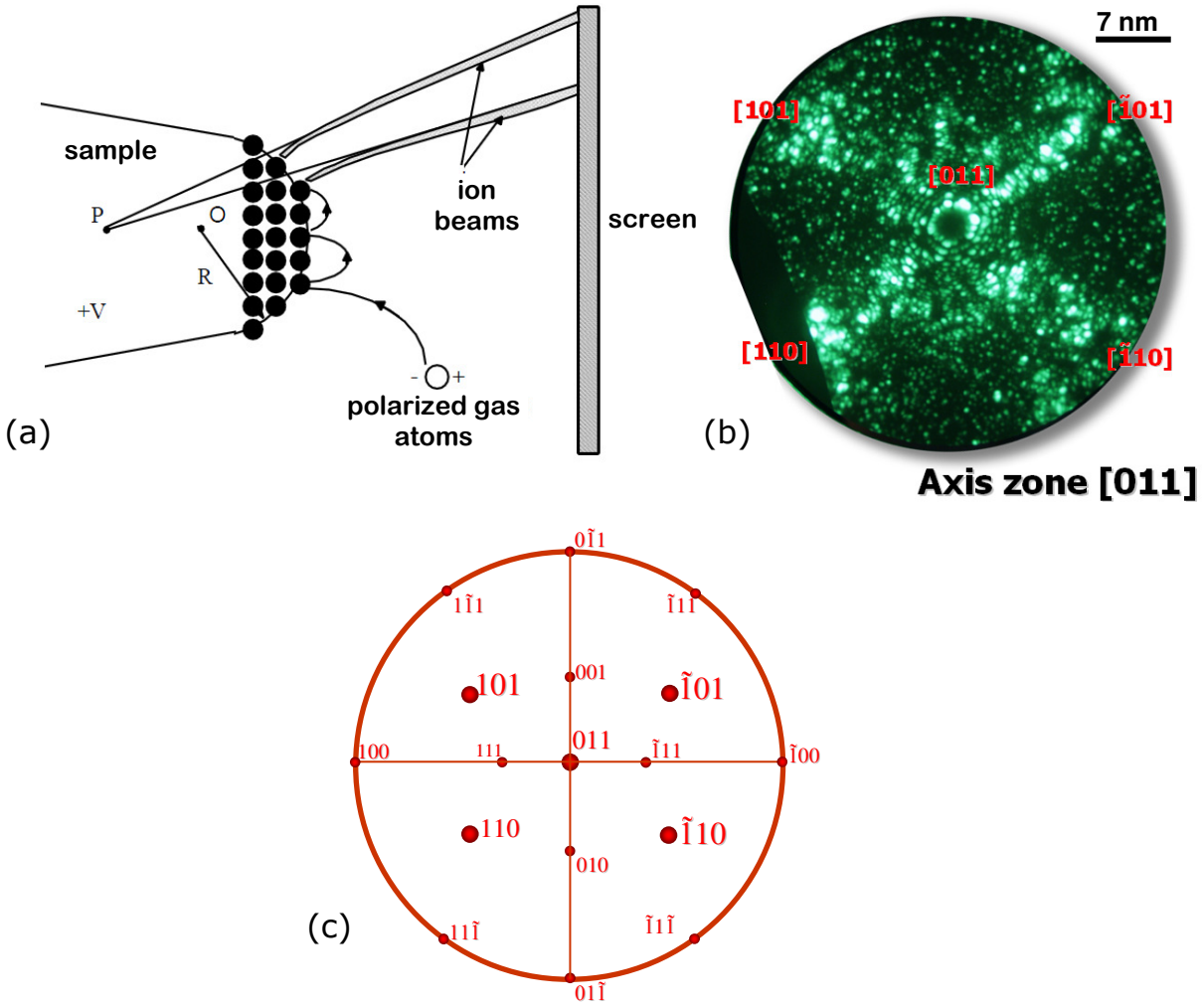

Figure 2.10. a) Principle of the ionic microscope; b) ionic microscope image of Fe-25at%Cr model alloy after ageing for 240h at 500ºC; c) corresponding standard stereographic projection of bcc lattice, axis zone [011].

Crystallographic information can be extracted from field ion micrographs in a straightforward manner. The major low index planes can be identified by the following rule: the planes with the largest atomic step heights (that is largest interplanar spacing) are the most prominent ones on the Field ion image [11]. The Miller indexes can be assigned to the planes once the major symmetry elements of the pattern have been identified. It should be noted that FIM projection is not exactly stereographic [10], but conventionally, stereographic projections could be used for poles indexation. An example of an indexed field ion micrograph with the corresponding stereographic projection is shown in Figure 2.10*b, c*

FIM doesn't allow, in general, identification of chemical nature of the surface atoms. Chemical analysis of the sample is done by the time of flight spectrometry with Atom Probe Tomography.

III.2. Tomographic atom probe

a) Principle

Tomographic atom probe (TAP) is a quantitative and destructive analytical technique. The principle of this technique is based on the field evaporation process. This technique is conceived as a field ion microscope equipped with a time-of-flight mass spectrometer, so that the observed surface atoms can individually be chemically identified [10,12–14].

A general view of the tomographic atom probe is provided in Figure 2.11a. Unlike to ion microscope, in TAP, the sharp needle-shaped specimen (Figure 2.11*b*) is placed in the analytical chamber under high vacuum (with a residual pressure of about 10^{-7}Pa) without noble gas and pointed toward a position sensitive detector. A positive voltage is applied to the specimen and, when the electric field reaches a critical value, the atoms from the sample surface are ionized and field evaporated in the form of n-times charged ions.

For time-of-flight measurements, it is necessary to fix the moment of evaporation of the ion and measure the time of its arriving on the detector. The measurements of the time of departure is achieved by: i) first establishing a standing field, ($V_{DC} \approx 0–20$ kV), below the ionization threshold of the specimen, and ii) by applying short duration electric pulses $Vp \approx (0.2 \text{ to } 0.25)V_{DC}$ to overcome the ionization threshold (Figure 2.11c). The moment at which the pulse is applied corresponds to the time of departure of the ions. The end of the time of flight is fixed by the detection of the impact of the ion on the detector placed at a distance *L* from the tip. Thus, the sample is analyzed atom by atom, atomic layer by atomic layer.

The measurement of the time of flight allows the mass over charge ratio (m/n) to be known and, finally, the determination of the chemical nature of detected ions to be achieved. Indeed, the potential energy of the ion being almost completely converted into kinetic energy when evaporated, it is possible to write:

$$n \times e \times V = \frac{1}{2} m \times v^2 \qquad (2.2)$$

where *m* is the ion mass (a.m.u), v – its velocity, n is the ion charge state (1^+, 2^+...), *e* the electron elementary charge, V – potential applied to the sample.

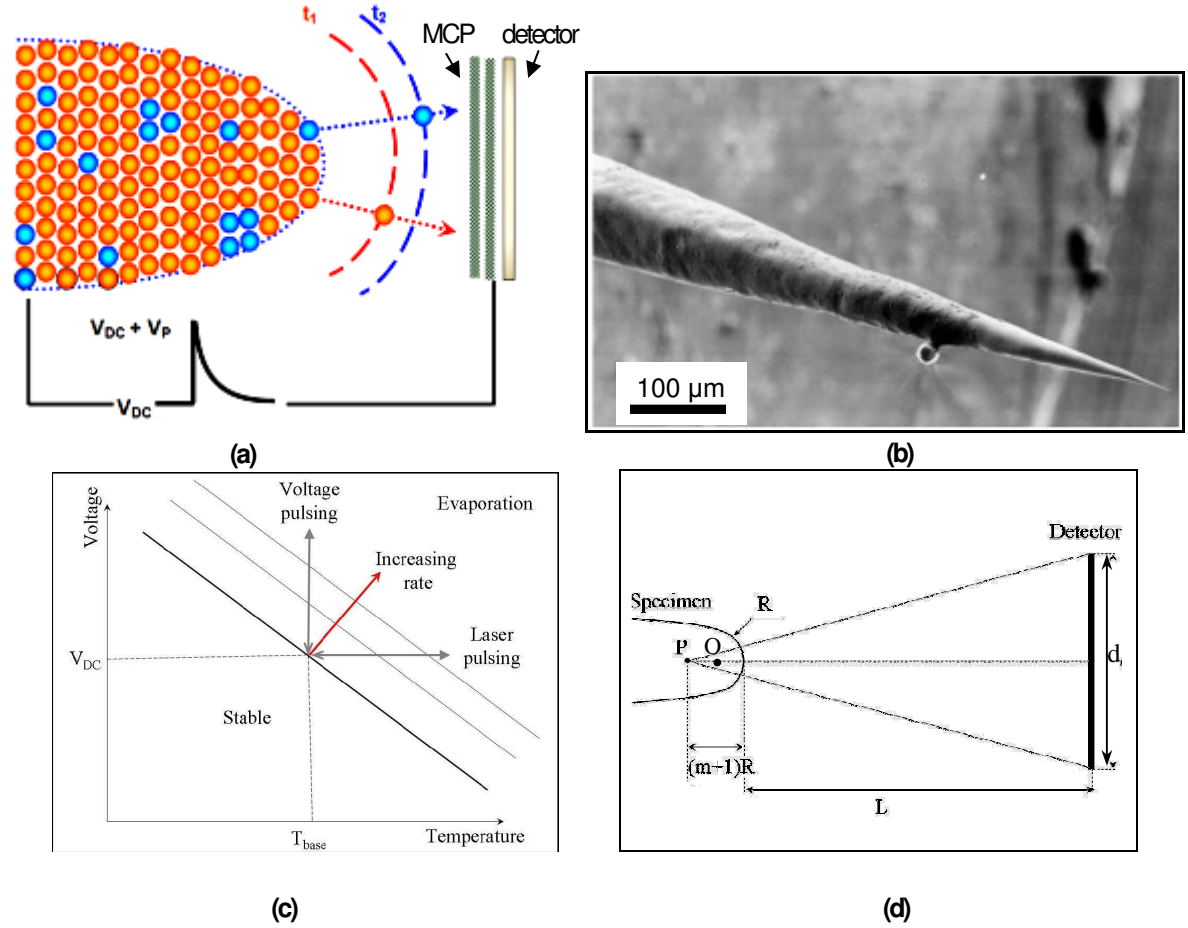

Figure 2.11. a) Schematic view of an atom probe (MCP - microchannel plates); b) SEM image of a conventional needle shaped specimen for use in the TAP; c) evaporation rate as function of tip temperature and applied voltage; d) the tomographic atom probe as a projection microscope. The magnification is $G = \frac{L}{(m+1)R}$

As the evaporated ion reaches its maximum speed almost instantly in comparison with the length of flight between the surface of the sample and the detector, its speed can therefore be considered to be constant and given by the relation v = *L*/*t* with L – the length of flight (distances sample-detector) and *t* – the time of flight. Ion is then identified by its mass-over-charge ratio (M = m/n):

$$M = \frac{m}{n} = 2 \times e \times V \frac{t^2}{L^2} \qquad (2.3)$$

The ratio m/n is expressed in atomic mass unit (a.m.u.).

The detectors of TAP are sensitive to the position of the impacts of ions, simultaneous or not [15–18]. Such detectors consist of an amplifier of signals (two microchannel plates) put in front of an "aDLD" (advanced Delay Line Detector) detector. The latter consists in a double layer of copper wire pairs. When a beam of electrons, created by the impact of an ion

on the amplifier, is intercepted by the wire pair layer, an electrical signal propagates in each wire. The recording of signals at the end of each wire allows to measure the difference of propagation time between the top, the bottom, the left and the right of the detector, and then to deduce accurately the position of the impact. The aDLD also allows the deconvolution of the co-ordinates of a group of ions arrived at the same time. Once the positions of ion impacts on the detector are known, the coordinates of the atoms at the specimen surface can easily be computed by inverse stereographic projection. As shown in Figure 2.11 *d*: determination of atom positions from impact coordinates simply involve the projection point (P). The image magnification is given by the expression:

$$G = \frac{L}{(m+1)R} \tag{2.4}$$

where R is the tip radius calculated as $R = \frac{V}{E\beta}$ (from eq. 2.1), were E is the evaporation field of the material, L is the free flight length of an ion (the estimated specimen to detector distance) and m is the image compression factor related to the position of the projection point (P). The calculation of the magnification requires therefore to know two parameters which depend on geometry and on electrostatic environment of the tip: m and E β. These two parameters differ slightly from one analysis to another. For steels and iron based alloys, the values of $E\beta$ = 21V/nm and (m+1) = 1.45 are usually used for reconstruction in case of electrically pulsed samples. These values are used in the current work.

Knowing the magnification G, the x and y coordinates of the position of the ion in the specimen for an analysis along the specimen axis are given by:

$$x = \frac{X_a}{G} \text{ and } y = \frac{Y_a}{G} \tag{2.5}$$

where Xa and Ya are the coordinates of the ion impact on the detector.

The third dimension, which corresponds to the depth, is obtained from the total number of evaporated atoms. For each detected atom, the analyzed depth is incremented by Δz :

$$\Delta z = \frac{G^2 V_{at}}{Q \cdot S} \tag{2.6}$$

where G is magnification, V_{at} – atomic volume, Q – detection efficiency and S the surface of the detector. The typical detection efficiency Q of an atom probe is from 46 to 60% of the ions evaporated from the specimen. It corresponds approximately to the open surface of the microchannel plates (MCP). As these atoms are lost randomly, it does not affect the quantitative measurements of composition.

As the depth investigation of the material proceeds, an atom-by-atom and a layer-by-layer reconstructions of the analyzed volume can be undertaken and 3D distribution of atoms can be reconstructed.

Laser assisted field evaporation. A new generation of atom probes – Laser assisted atom probes with very short duration of laser pulses (femtoseconds) are developed by the GPM laboratory [18,19] starting from 2006. With this technique surface atoms are emitted from a tip in form of ions by: i) first establishing a standing field, ($V_{DC} \approx 0$ to 20 kV) below the ionization threshold of the specimen, and ii) by applying short duration laser pulse that triggers the ion emission.

Recent studies have shown that the absorption of the laser energy by the tip increases the surface temperature leading to the evaporation of atoms [20,21] as schematically illustrated in Figure 2.11*c* .

Generally, the power set-up of the laser pulse should represents from 20 to 25% of the standing potential that corresponds to general values of electric pulses in conventional atom probes (see above). In order to choose the proper laser power, the equivalent pulse fraction has been adjusted in all experiments according to the geometric procedure illustrated in Figure 2.12.

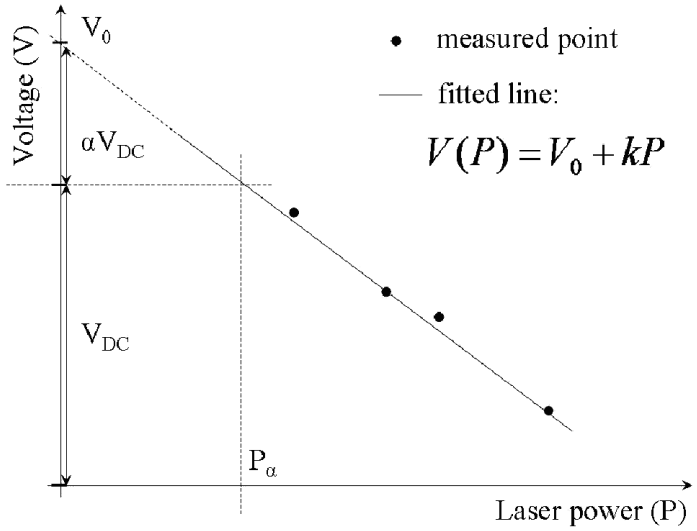

Figure 2.12. An example of equivalent pulse-fraction measurements.

For this purpose, at a fixed value of the evaporation rate, three or four measurements of the standing voltage, V_{DC}, is done for different values of the laser power, P. The dependence V_{DC} versus P is supposed to be linear and can be fitted on the experimental points. From the parameters of the linear fit, V_0 and k, one can find the laser power Pα for a desired pulse fraction α using formula:

$$P_\alpha = -\frac{\alpha V_0}{(\alpha+1)k} \qquad (2.7)$$

b) Spatial resolution

Depth resolution. The depth resolution is determined by the screening distance of the electric field in the specimen. In conductive materials, it is usually about 0.1 nm. This value is comparable with typical lattice interplane distances. Typically, the best spatial resolution is achieved along the direction of analysis and lattice planes with low Muller indexes of a crystalline materials are usually resolved if their normal is close to the direction of analysis, as, for example shown in Figure 2.13.

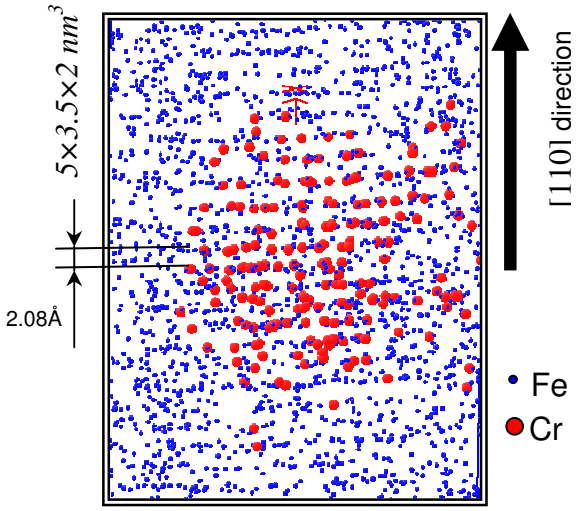

Figure 2.13. 3DAP image obtained in the alloy Fe-12%atCr after neutron irradiation at 300°C up to 0.6 dpa. The analyses have been performed in the [110] direction. Interplane distance in bcc Fe is ~2.03Å that is in good corresponds to the value, obtained by TAP (2.08Å).

Lateral resolution. In the plane perpendicular to the analysis direction, the image of the lattice is "blurred". The lateral resolution is of several Angströms (Å). The physical limit is mainly controlled by the ion-optical aberrations. With the typical magnification G of an atom probe (in order of 10^6), an error in the position of ion impact equal to 1 mm on the detector (caused for example by trajectory aberrations of the evaporating ions in the close vicinity of the specimen surface) leads to uncertainties in the order of Angströms at the surface of the sample. The latter appears to be enough to blur the lattice structure. Deeper discussion concerning spatial resolution of atom probe can be found in the recent work of Gault et al. [22].

Mass resolution. Time-of-flight measurements provide a value for the mass-over-charge ratio of each evaporated ion and therefore their identity. The data collected in an experiment can be represented in the form of a mass spectrum (Figure 2.14). The latter indicates the number of detected ions as a function of their mass-over-charge ratio (given in

atomic mass units, a.m.u). The counting of atoms of each species allows to measure the concentration of the elements in the whole analyzed volume (the so called total composition of the analysed volume).

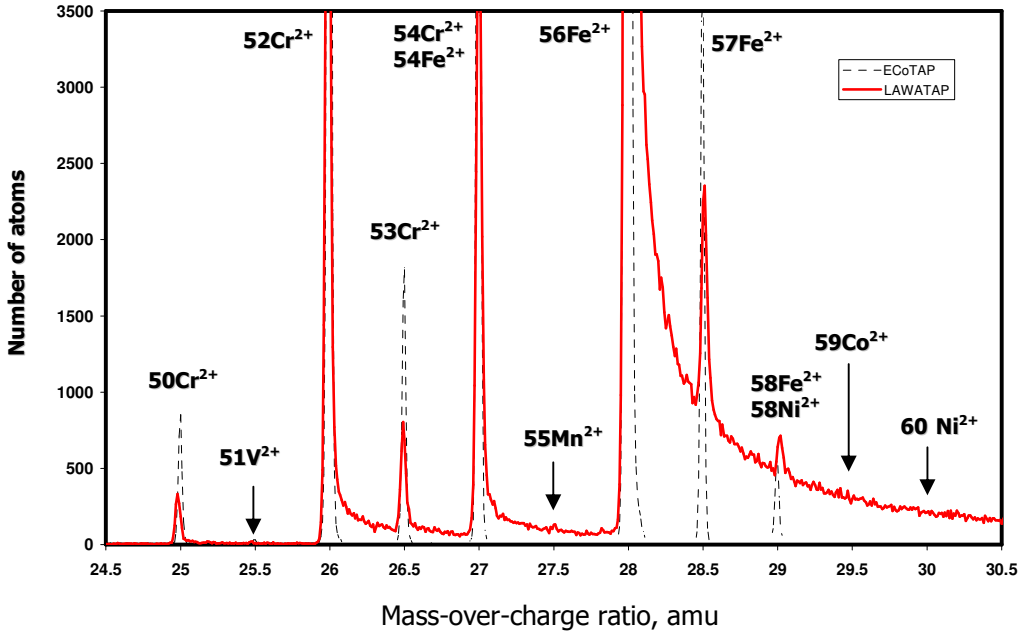

Figure 2.14. Mass spectra obtained by Energy Compensated Tomographic Atomic Probe (ECoTAP) (dashed line) and Laser Assisted Wide-Angle Tomographic Atom Probe (LAWATAP) (solid line) for an Fe-12%Cralloy neutron irradiated at 300°C up to 0.6 dpa (~700.000 atoms), for ECoTAP data $\frac{M}{\Delta M_{10\%}}\left(Fe56^{2+}\right)=560$, *For LAWTAP data* $\frac{M}{\Delta M_{10\%}}\left(Fe56^{2+}\right)=152$

Accurate measurement of composition implies that species can unambiguously be distinguished. One of the important characteristics of TAP is its high mass resolution i.e. its ability to distinguish two neighboring peaks on the mass spectrum. In general, the mass resolution measurements are carried out on the peak of the majoritary isotope of the majoritary specie at 10% of the maximum peak value $\frac{M}{\Delta M_{10\%}}$.

One of the main phenomena which degrades the mass resolution, is the spreading of the energy of ions [23]. Indeed, the ions can be field evaporated on the rising edge, on the top or on the falling edge of the evaporation pulse. Thus, an ion evaporated on the rising or falling edge of the evaporated pulse will not acquire the whole energy provided by the pulse. Its time of flight will be slightly higher and its calculated mass-over-charge therefore will be higher than an ion of the same nature, evaporated at the top of the pulse (eq. 2.3). This energy deficit induces enlargement of peaks.

To resolve this problem, the energy compensated tomographic atomic probe ECoTAP has been developed [23]. The energy compensation is realized with the help of an electrostatic lens: reflectron (Figure 2.15).

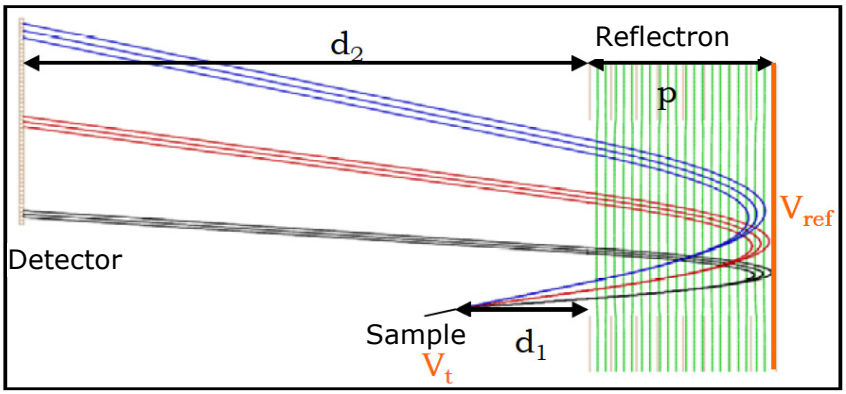

Figure 2.15. Scheme of principle of the reflectron (from [24])

The principle of the reflectron is based on the following: incoming ions with an energy deficit travel with a flight path shorter than that of ions that have the full energy. Time-focusing is thus achieved resulting in an improvement of the mass resolution of spectrum.

During laser assisted TAP experiments, as evaporation is thermal [18,19], there is no energy deficit. In such case, ions are only accelerated by the standing voltage applied to the specimen that involves a higher mass resolution in comparison with electric mode of TAP.

In the present work, Laser Assisted Wide-Angle Tomographic Atom Probe (LAWATAP) has been used. This modification of TAP has enlarged field of view (that allows to analyze larger volumes) owing to the location of the position sensitive detector closer to the specimen [18]. But the decrease of the distance between the tip and the detector leads to degradation of the mass resolution due to the increase of the uncertainties of the "top of departure" of the ion with respect to the time-of-flight. The comparison of the mass resolution of the Energy Compensated Tomographic Atom Probe (ECoTAP) and Laser Assisted Wide-Angle Tomographic Atom Probe (LAWATAP) is presented on the Figure 2.13. In this example, the mass resolution $\frac{M}{\Delta M_{10\%}}$ of the major iron isotope ($56Fe^{2++}$) changes from 152 for LAWATAP experiment to 560 for ECoTAP. It appears that the ECoTAP has a mass resolution few times higher than the one of LAWATAP. This allows more relevant concentration data to be achieved. However, it should be noted that ECoTAP analyses only allow a small volume to be accurately analyzed (typically $10\times10\times100nm^3$), limiting the statistic of the results (number of precipitates detected, for example). The use of the LAWATAP overcomes this problem: analyzed volume is typically $50\times50\times100nm^3$ with however a lower mass resolution. For example, as it shown on the Figure 2.14, accurate

composition mesurements of Ni, Co or Mn are not possible: the isotopes of these elements (60 Ni^{2+}, 59Co^{2+} and 55Mn^{2+}) can not be deduced from the LAWATAP data, because there are not visible due to the superposition with majority peak of iron. Thus, the use of these two techniques allows combination of an accurate chemical composition (ECoTAP) with large statistic (LAWTAP). Some experiments have also been performed with the Energy Compensated Wide Angle Tomographic Atom Probe (ECoWATAP) very recently developed. This AP gives access to the benefits of both techniques described above.

c) Artifacts

During the evaporation of alloys, several events can disturb the assumptions of the reconstruction algorithms and the composition measurements. Some of them, important for Fe-Cr system, are discussed in the following section.

Isotopes overlap. For some materials, some peaks in the mass spectrum can not be unambiguously assigned to elements because of the overlap of two (or more) isotopes of different species which have the same mass-over-charge ratio. It is then impossible to distinguish them on the mass spectrum.

It is the case for the ions 54Cr^{2+} and 54Fe^{2+} which correspond to the same masse-over charge ratio 27 amu on the mass spectrum (Figure 2.14). The natural abundance of the isotopes of chromium is 2.36% (5.8% for the isotope of Fe). This represents a mean concentration of X_{Cr}×0.0236 (X_{Fe}×0.058) on the global composition of the alloy of composition X_{Cr} (respectively X_{Fe}). This means that approximately 96 % of the atoms which are in this peak are Fe atoms for an Fe-9%Cr alloy (98% for an alloy Fe-5%Cr and 95% for an alloy Fe-12%Cr). This isotopes overlap is systematically corrected in this work. The same corrections have been realized for the isotopes 58Fe^{2+} and 58Ni^{+2}.

Preferential evaporation. This effect can arise when one element has a smaller evaporation field than the others.

Let us consider a binary alloy with alloying species A and B, for which the evaporation fields are different $E_B > E_A$. In the Figure 2.16 two different cases are presented.

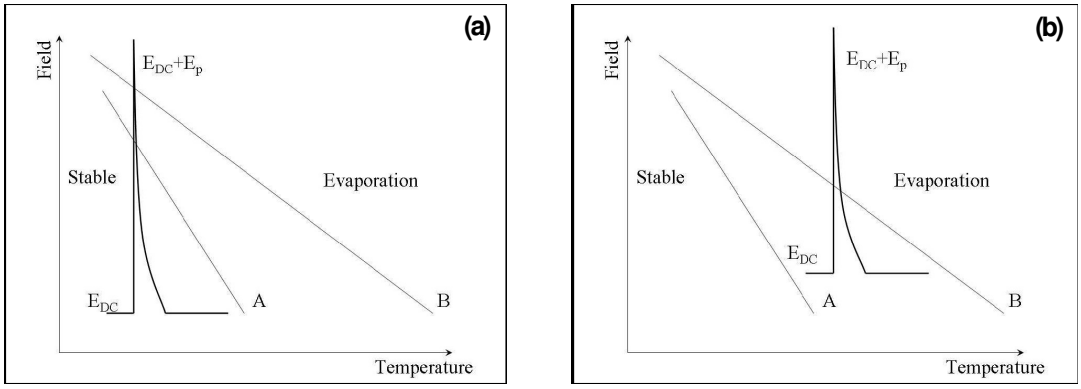

Figure 2.16. Influence of electric field on the specimen's tip on the evaporation conditions of chemical species A and B: a) proper evaporation conditions; b) preferential evaporation conditions for A.

• In the case (a), evaporation field E_A and E_B of the species is reached owing to the addition of the pulse field E_P to the standing field E_{DC}. Both species are field evaporated on pulses and are detected. There is no preferential evaporation. Measured compositions are then correct.

• If the standing field applied to the specimen is higher than the evaporation field E_A of the element A, "A atoms" can evaporate under the standing field i.e. can preferentially evaporate during the time between pulses. In this case (Figure 2.16*b*), some "A atoms" are lost and the measured composition is biased. In order to mitigate this effect, the specimen's temperature is decreased. Indeed, as shown in Figure 2.16 in such a case the gap between the evaporation fields E_A and E_B decreases. Nevertheless, a decrease in temperature implies an increase in the evaporation fields of the chemical species (for a constant flux of evaporation) so it is necessary to increase the value of the field applied to the tip. Thus, the material undergo stronger constrains (cyclic electrostatics pressure) that increase the risk of fracture of the sample during analysis.

The phenomenon of preferential evaporation can also be controlled by the increase in the pulse fraction (V_P/V_{DC}). This can be achieved owning to the decrease of the standing voltage V_{DC}. However, a limit exists as a too weak standing voltage favours pollution of the sample by residual impurities from surrounding environment and increases the amplitude of the cyclic electrostatic pressure which also increases the risk of fracture.

In the case of the analysis of Fe-Cr alloys, the evaporation field of Cr is about 20% less than the Fe one (E_{Cr}=29V/nm, E_{Fe}=35V/nm). A temperature $T_{analyse}$ = 40K and a pulse fraction $V_P = 0.2\ V_{DC}$ have been used to mitigate this artifact [24].

Local magnification. When precipitates with evaporation field different from that of the matrix are present in a material, some aberrations in the ion trajectories appear mostly in the close vicinity of precipitate-matrix interfaces. Indeed, the difference in evaporation fields of the two phases provoke local variations of the curvature radius (see Figure 2.17 [25])

which in turn modify the ions trajectories during the very first moments of their flights from the specimen surface to the detector [26,27]. The local magnification effect is illustrated in the simulations of ion impacts on the detector given in Figure 2.17*c, d* [25].

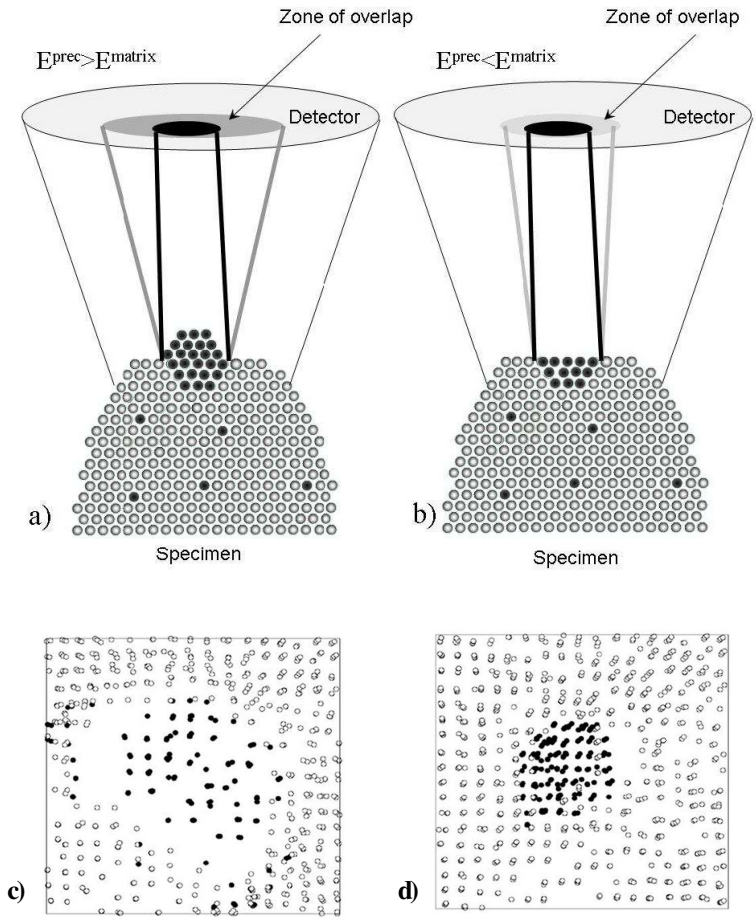

Figure 2.17. Local magnification effect in the case of evaporation of a) a high field precipitate; b) low-field precipitate.
Simulation of impact images for a binary AB alloy containing a spherical β particle (eight interatomic distances in diameter). β phase is pure in B and its environment is pure in A. These two simulated images are cross sections of reconstructed precipitates with c) $E_{prec} > E_{matrix}$ and d) $E_{prec} < E_{matrix}$: B atoms are in black and A are in grey. The images are taken from [25].

For a high evaporation field of the particle, precipitate ions fall outside the particle and a depleted zone forms close to the interface (Figure 2.17c). In contrast, for a low evaporation field of the particle, the image of the precipitate (pure in B atoms) is compressed in the X-Y directions of analysis and ions coming from the surrounding matrix (pure in A) are mixed with atoms of the interface of the particles (Figure 2.17d).

The local magnification can consequently modify the morphology and the characteristic dimensions of precipitated phases and then trajectory overlaps associated to this effect can biased the measured chemical compositions of the phases. Nevertheless, it is worth

noting that the core composition of the precipitates should not be affected by this effect, as shown by Figure 2.17*b*.

This effect is observed in the Fe-Cr alloys [24,28]. α' precipitates (Cr-enriched) are low field regions. This means that spherical α' precipitates can appear as ellipsoids when their Cr content is high enough to significantly decrease the field of evaporation of the precipitates [28]. Even if the shape of the precipitates is modified, it has been shown by Novy [24,28] that the in core Cr content should not be affected. The precipitates which were investigated had a radius ranging from 0.95nm to 2.nm. Moreover, it is worth noting that even if this effect affects composition measurements, a modification of only few percent (≈3%) is expected [25].

d) Experimental conditions

Analysis parameters and conditions used in this study as well as the reconstruction parameters for the Fe-Cr alloys are summarized in the Table 2.11.

Table 2.11. Conditions of TAP experiments and reconstruction parameters used for analysis of Fe-Cr model alloys

Parameter	ECoTAP	LAWTAP	ECoWATAP
m+1	1.45	1.45	1.45
$E\beta$	21	18.5	20
Temperature, K	40-50	40	45
Pressure, Pa	10^{-9} to 10^{-10}	10^{-9} to 10^{-108}	10^{-9} to 10^{-10}
Pulse fraction, %	20	20-25	20
Pulse rate, kHz	2	100	3
Laser wavelength, nm	-	343 (ultraviolet)	-
Detector surface, m^2	0.0064	0.004656	0.004657
Detection efficiency, %	46	60	42 (50 before 2011)

e) Description of atom probe data treatment methods

Cluster identification. In order to calculate composition, number density and size of clusters, it is necessary to distinguish clusters from the matrix, considered to be a cluster. Different algorithms can be used for detection of clusters [12,29,30]. In the current work, the cluster-identification algorithm has been used [29] and its principle is the following:

1. A sphere with a radius R_{max} is centered on each atom of the volume. The concentration C_S of solute atoms in the sphere is measured. If the concentration Cs is higher than the fixed C_S^{min} , this atom is labeled as "clustered". Else this atom is labeled as "non clustered". Atoms are so divided in two categories: atoms located in a cluster and those of the matrix.

2. All "clustered" atoms situated closer than R_{max} one to each other belong to the same cluster.

3. Groups of atoms that contain less than a fixed minimum value N_{min} of atoms are removed.

The scheme illustrating the identification process is given in Figure 2.18. The sphere of radius R^{max} centered on the atom 1 involves enough solute (black) atoms, so that the atom 1 obeys a clustering criteria. Solute atoms within the thick dashed line will be defined as being a single precipitate. The atom 2 within a given distance R^{max} has no solute atoms, and, hence, is not "clustered".

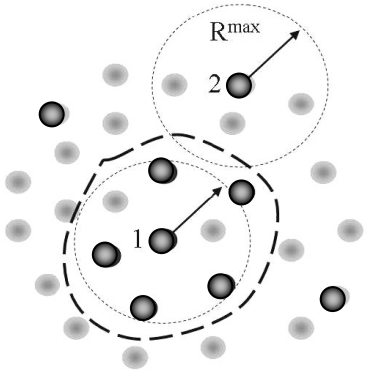

Figure 2.18. Principle of the precipitate selection process.

To choose the value C_S^{min} three criteria must be fulfilled:

i) C_S^{min} must be high enough to avoid appearance of ghost Cr-enriched zones in random solid solution which have the same Cr concentration than the studied alloy. Thus, a minimum value C_S^{min} can be deduced from frequency distribution (FD) of Cr concentration. As shown by Figure 2.19, in the case of random alloy which contains 10% of Cr (whose the FD is a binominal distribution) C_S^{min} must be higher than 23%.

ii) The value of the threshold C_S^{min} must be high enough also to avoid that Fe-atoms of the matrix are associated to α' precipitates i.e. to avoid that Cr-enriched precipitates appear with Fe-shell on the filtered 3D image.

iii) The threshold must be low enough to allows the detection of all the clusters whatever their size or their concentration. A threshold value equal to 28% has been chosen to distinguish Cr-enriched clusters from α matrix in Figure 2.20a.

Depending on the alloy composition, the value of C_S^{min} has to be modified. This will be specified in the corresponding sections of this document.

The local concentrations have been calculated in a sampling sphere of radius R^{max} = 0.82 nm (sampling volume equal to about 100 detected atoms).

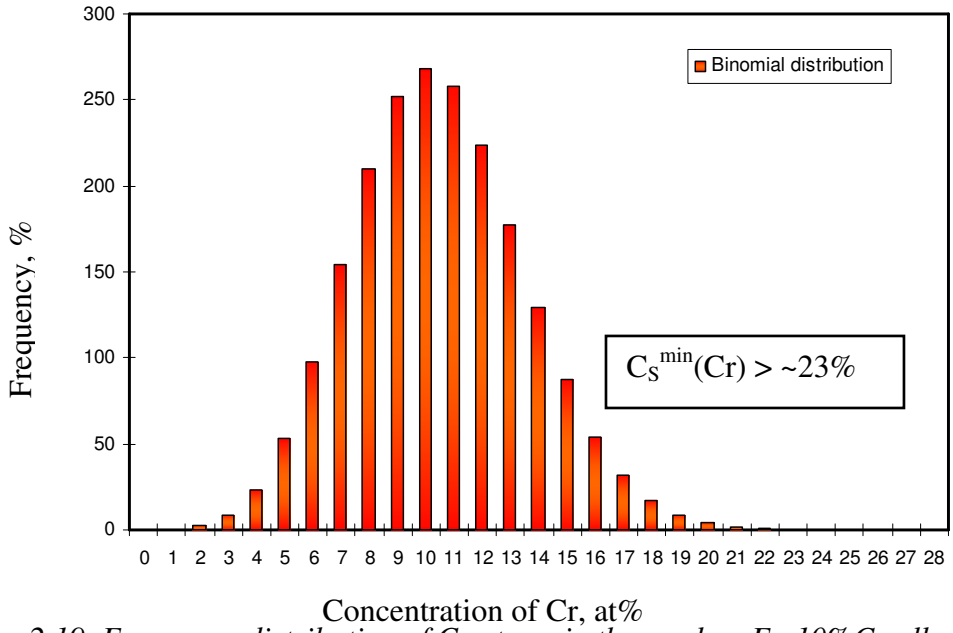

Figure 2.19. Frequency distribution of Cr atoms in the random Fe-10%Cr alloy. Sampling size: 1.3×1.3×1.3nm^3 (corresponds to about 200 atoms).

Concentration profile

One of the most common forms of data analysis is the construction and the statistical analysis of a composition profile. The first step to create a composition profile is to select a volume within the three-dimensional data from which the composition profile is desired. The shape of this selected volume is either a cylinder or a rectangular parallelepiped depending on the type of the feature to analyze.

The size and the position of this selected volume are then carefully adjusted by the user until the desired volume is enclosed. Once the parallelepiped or cylinder is correctly positioned, it is divided into small slices perpendicular to its long axe. The size of the slices may be defined in terms of distance. The concentration of each specie in each slice is then measured as following:

$$c^i = \frac{N_s^i}{N^t} \qquad (2.8)$$

where N^i_s is the number of ions of solute i, and N^t is the total number of ions detected in the sampling volume. The uncertainty (ΔC) on measured concentration (C) is an uncertainty of statistical sampling. It depends on the size of the sample, in other words, on quantity of collected atoms (N) and on the concentration of the specie. It is given by the following expression:

$$\Delta C = 2\sigma \text{ where } \sigma = \sqrt{\frac{C(1-C)}{N}} \qquad (2.9)$$

An example of a composition profile across a Cr-enriched cluster formed under neutron irradiation is shown in Figure 2.20.

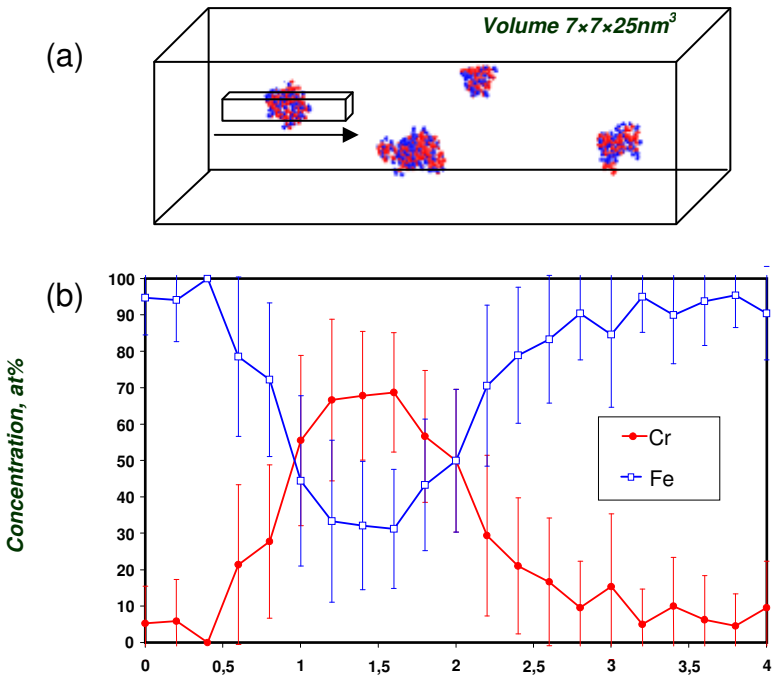

Figure 2.20. Atom probe analysis of the Fe-12Cr model alloy neutron irradiated at 300°C up to 0.6 dpa: a) Filtered 3D image of the alloy. Concentrated zones represent the Cr-enriched clusters. A threshold of 28at% is applied to distinguish α' from α phase; b) composition profile drawn along the parallelepiped indicated in (a). Sampling size: 0.7×0.7×0.7nm^3

Statistical treatment. 3DAP facilities are commonly used to measure fine scale variations of composition in materials. In cases where the variation is large, the results are customarily presented by concentration profiles as described above. However, if the composition varies only slightly, the frequency distribution of the concentration of the solute atoms may reveal microstructural features that are not visible on profile or 3D image (filtered or not).

When atoms are randomly distributed, a binomial distribution (BD) is expected. If the material exhibits unmixing (as precipitation, clustering or segregation), the FD becomes broader than the BD or even consists of well-separated peaks, corresponding to the composition of the different phases. If an ordered material is investigated the FD is narrower than the BD.

Before constructing a FD, the 3D data has to be divided into blocks, usually containing an equal number of atoms (N_{box}), called the sampling block size, which is typically from 50 to 500 atoms. The shape of the FD can change substantially when varying the block size. For

example, Figure 2.21 shows the FD calculated over the same volume but for two different block sizes, 125 and 175, respectively. It is obvious that the shape of these FD curves is different. For such cases, the data has to be analyzed in a more careful way than by constructing only one single FD.

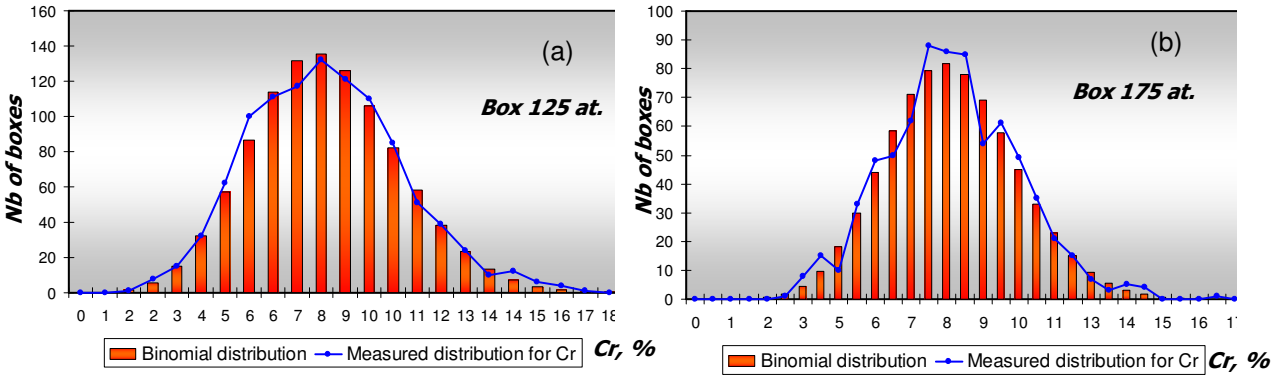

*Figure 2.21. Cr-concentration frequency distribution in the as-received Fe-9at.% Cr model alloy. The experimental distribution (curve) is compared to the binomial one (histogram). Shape of the experimental distributions changes with the chosen size of blocks (125 **(a)** and 175 atoms **(b)**) for same analysed volume. This fact does not allow accurate interpretation of the experimental data*

A convenient method to evaluate and present the data is offered by the work of Thuvander et al. [31]. It applies to situations where small variations in composition or ordering are of interest. According to their method, the estimation of the distribution is carried out by the comparison of the value of the standard error (s) calculated from experimental data (Eq. 2.10) with the standard deviation (σ) of the binomial distribution (Eq. 2.11) for different sampling block sizes.

$$s^2 = \frac{1}{n_b - 1}\sum_{i=1}^{n_b}(c_i - c_0)^2 \qquad (2.10)$$

where n_b is the total number of blocks, c_o is the average concentration of the element B (Cr for our case) in the experimental analyzed volume and c_i is the concentration of the element B in the block number *i*.

$$\sigma^2 = \frac{c_0(1 - c_o)}{N_{box}} \qquad (2.11)$$

where N_{box} is the size of the sampling block.

The use of a series of sampling block sizes should reveal the characteristic information of the width of the FD. Erroneous features appearing only for specific block sizes can be avoided. For randomly distributed element the experimental *s*-curve should coincide with the binomial σ –curve as shown in Figure 2.22. If the composition varies in the material, for example, due to phase unmixing, the *s*-curve will be above the σ -curve, assuming that the

scale is appropriate. On the other hand, if the material is ordered, the *s*-curve will be below the σ -curve, if proper experimental conditions have been used.

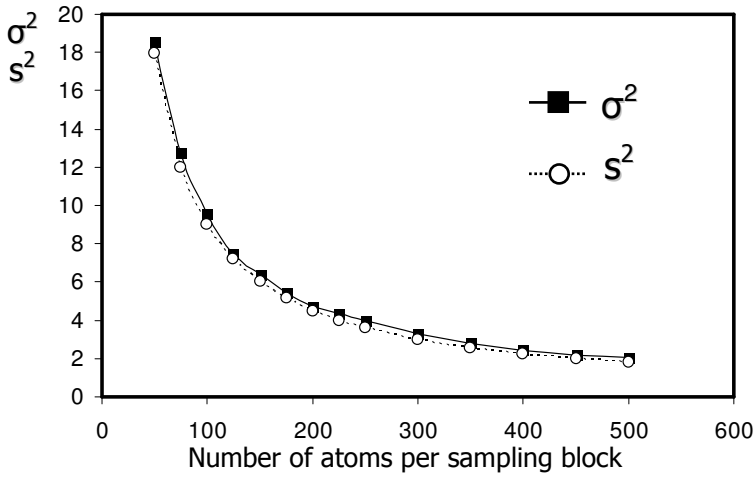

Figure 2.22. Comparison of the standard error (s) of the experimental Cr-concentration frequency distribution with the standard deviation (σ) of the binomial distribution in the un-irradiated Fe-12at%Cr model alloy for sampling volume of different size. Experimental distribution almost coincides with the binomial one. Chromium atoms are homogeneously distributed.

III.3. Positron Annihilation Spectroscopy

Within this PhD thesis, Positron Annihilation Spectroscopy has been undertaken in CEMHTI (Conditions Extrêmes et Matériaux: Haute Température et Irradiation), Orleans. A magnetically guided slow positron beam with variable energy up to 50 keV coupled with a Doppler broadening spectrometer allows to characterise materials in the depth up to 1.5 µm. This facility has been used to characterize the quantity and the nature of the point defects generated with high energy ion irradiation and their evolutions [32].

PAS is a powerful tool for microstructural studies of condensed matter. Atomic-scale details of the microstructure like electronic structure and small-sized open-volume defects can be investigated by PAS. The main advantages of PAS can be summarized as follows:

• Vacancy type defects (mono vacancies up to small voids) at low concentration can be detected by PAS which can otherwise be hardly investigated by traditional basic techniques like, e.g., TEM or X-ray diffraction.

• PAS can probe both the bulk properties of matter as well as near-surface regions structures.

• Reliable theoretical calculations of PAS parameters are nowadays feasible in metals and semiconductors. These may substantially simplify unique interpretation of data measured by PAS.

• PAS is a non-destructive technique.

a) Basic principles of PAS

Positrons can be obtained from the β^+ decay of radioactive isotopes, e.g. from ^{22}Na according to the decay reaction $^{22}Na \rightarrow {}^{22}Ne + \beta^+ + \nu_e + \gamma$. Positrons penetrate the sample, thermalize in few ps, diffuse, form e^+-e^- pairs with electrons of the material and then annihilate (Figure 2.23). Positron annihilation can take place (i) with an electron from the bulk of the material or (ii) after trapping in a defect with an electron from the trap region. The latter occurs due to the large positron affinity to some defects, in particular, open volume or vacancy-like defects where positive nuclei are absent.

The time before annihilation strongly depends on the electron density of the region where positrons diffuse. In the case where the positron is trapped by vacancy, its lifetime is longer in comparison with the case of annihilation in the bulk of the material because the probability to run into for an electron and form a pair is lower.

When a thermalized positron and an electron annihilate, their mass is converted into energy (as per Einstein's equation $E = m_o c^2$). The total amount of energy released when a positron and an electron annihilate is 1.022 MeV. In dense materials, this energy is released generally in the form of two γ-quanta of about 511keV which are emitted in opposite directions.

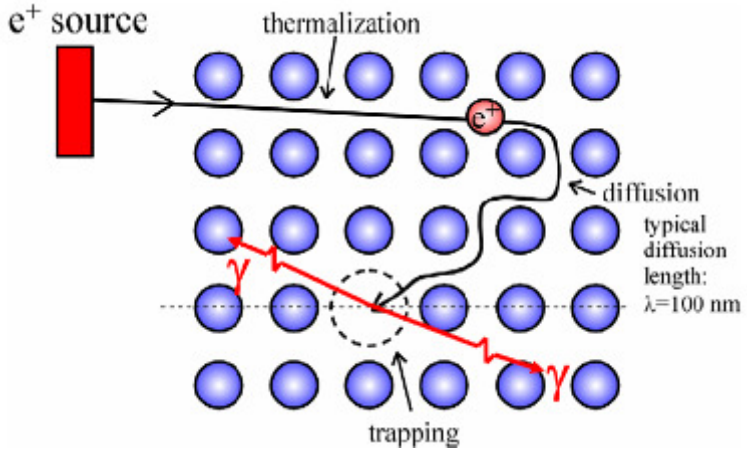

Figure 2.23. Schematic diagram showing various processes that single positron undergo between penetrating through matter and annihilation with an environmental electron.

The principles of different positron techniques are illustrated in Figure 2.24. They can be classified into two principal groups which are distinguished by the sensitivity of positrons to the electron density (positron lifetime measurements) and to the electron momentum distribution in the sample (for example, Doppler broadening spectroscopy).

In a conventional lifetime spectrometer, the positron lifetime is measured as the time difference between the positron emission and the annihilation events. The "start" signal is obtained from 1.28 MeV photon emitted together with the positron from the decay of ^{22}Na. The annihilation signal is given by one of the 511 keV photons emitted from annihilation. In pure defect free metals, lifetime is typically around 100-150 ps.

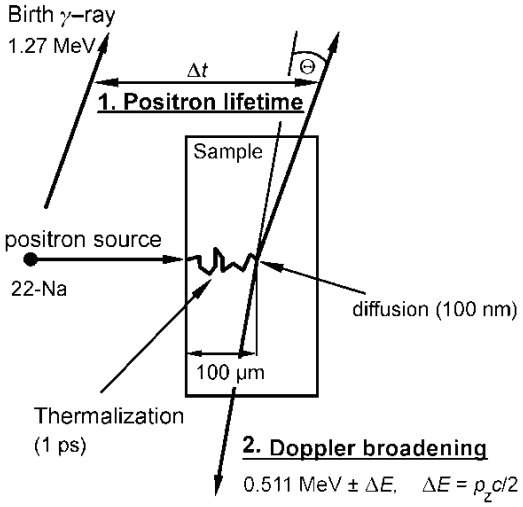

Figure 2.24. Scheme of different positron experiments

In conventional Doppler-broadening measurements, only one of the 511 keV annihilation photons is detected and the other is ignored. The Doppler-broadening of the 511 keV annihilation line was measured with a high purity germanium (HP Ge) gamma detector. The 511 keV photopeak, containing usually 5×10^6 annihilation events is recorded in the memory of a multichannel analyser. The complete principle of these techniques may be found in different books or reviews [33,34].

b) Annihilation-Line Doppler Broadening

The Doppler-broadening spectroscopy which was used for samples characterization is based on the principle of momentum conservation of the electron-positron pair during the annihilation process. It allows to detect vacancy type defects and to give information about their concentration or their chemical environment.

In materials, the positron is thermalized before forming a pair with an electron and the energy of the e^+-e^- pair is mainly due to the momentum of the electron (at least a few eV). Depending on the momentum of the electron-positron pair the annihilation energy of the emitted γ-ray undergo a small Doppler shift ΔE from 511keV (the energy of each photon in the case when the momentum of the annihilation electron-positron pair is not transmitted to the annihilation quanta). Therefore, the Doppler-broadening of the 511 keV annihilation line reflects the electron distribution in the electron structure in the momentum space.

In the case of positrons trapped into open-volume defects, the fraction of valence electrons taking part in the annihilation process increases compared with that of core electrons. Because the momentum of valence electrons is significantly lower, the momentum distribution of annihilating electrons shifts to smaller values. This means a smaller Doppler broadening for the Doppler-broadening spectroscopy. The curve of defect-rich material is thus higher and narrower than that of defect-free reference material, when both curves are normalized to equal area (Figure 2.25.).

Quantitative evaluation can be carried out with specific parameters describing the shape of the Doppler broadening line. The *S* parameter ("Shape" parameter or the valence annihilation parameter) is defined as the area of the central low-momentum part of the spectrum with the centre at 511 keV, divided by the area below the whole curve after background subtraction. The *W* parameter ("Wing" or core annihilation parameter) is taken in a high-momentum region far from the centre, as indicated in Figure 2.25. It is calculated as the area of the curve in a fixed energy interval, divided by the area below the whole curve after background subtraction. S and W parameters are sensitive to open volume defects, they respectively increase and decrease in the presence of vacancy defects. Also, by measuring the momentum distribution of the core electrons (W) specific to each element, it is possible to identify the chemical elements around the positron annihilation sites and to give at least a qualitative idea on the correlation between vacancies and, for example, Cr-atoms. In this work

the S window was accepted at the level [-0.73; 0.73] keV and W windows were accepted at the levels [-6.98; -2.7] [6.98; 2.7] keV both centered around 511 keV.

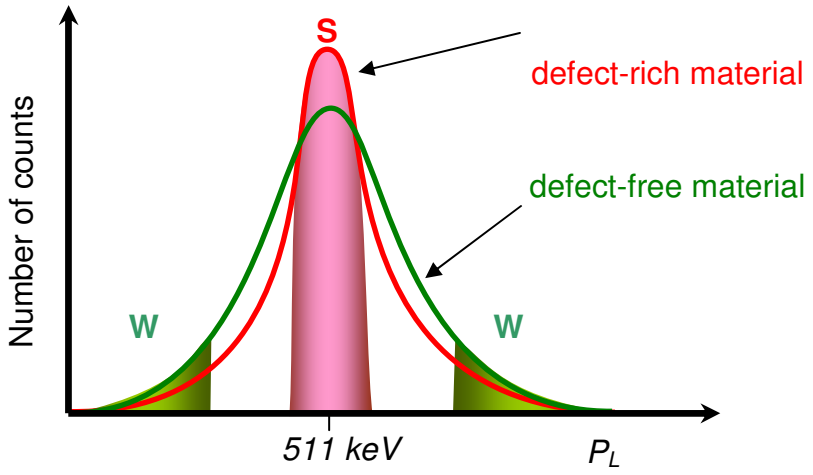

Figure 2.25. Doppler broadening spectra of defect free and defect rich materials. The definition of the S and W parameters in the Doppler-broadening spectra S-parameter corresponds to positron annihilation with the valence electrons and W-parameter corresponds to positron annihilation with the core electrons.

c) Analysis of the Doppler- broadening data in the thin layer and Slow-Positron-Beam Techniques

When the Doppler spectra is recorded as a function of the energy *E* of the positron, the variation of *S(E)* or *W(E)* gives the changing of annihilation characteristics as a function of the depth. Positron implantation profile in iron as the function of the positron energy is shown in Figure 2.26. Implantation profiles enlarge with the positron energy indicating an increase of the depth resolution of this technique. At 5 keV the mean implantation depth of positron Z_{av} is 65 ± 30 nm while at 25 keV, Z_{av} = 1007 ± 800 nm. An example of *S(E)* and *W(E)* curves measured in a defect free pure Fe is presented in Figure 2.27. S-parameter decreases with the energy while the W-parameter increases. At low energies S and W values are mainly due to annihilations at the surface state; but at high energies S and W values are mainly due to the iron bulk state. S and W values between low and high energies represent the mixing of these two annihilation states. Values S_{ref}=0.3570 and W_{ref}=0.1115 measured in this iron sample were the reference values for this work.

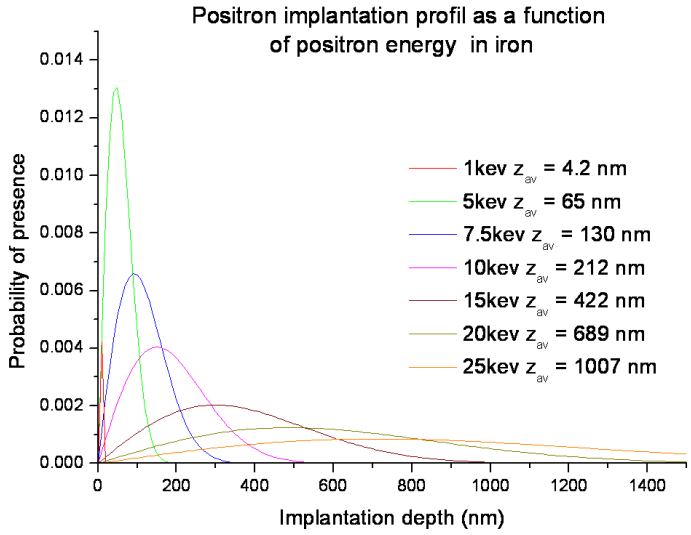

Figure 2.26. Positron implantation profile as a function of positron energy in iron

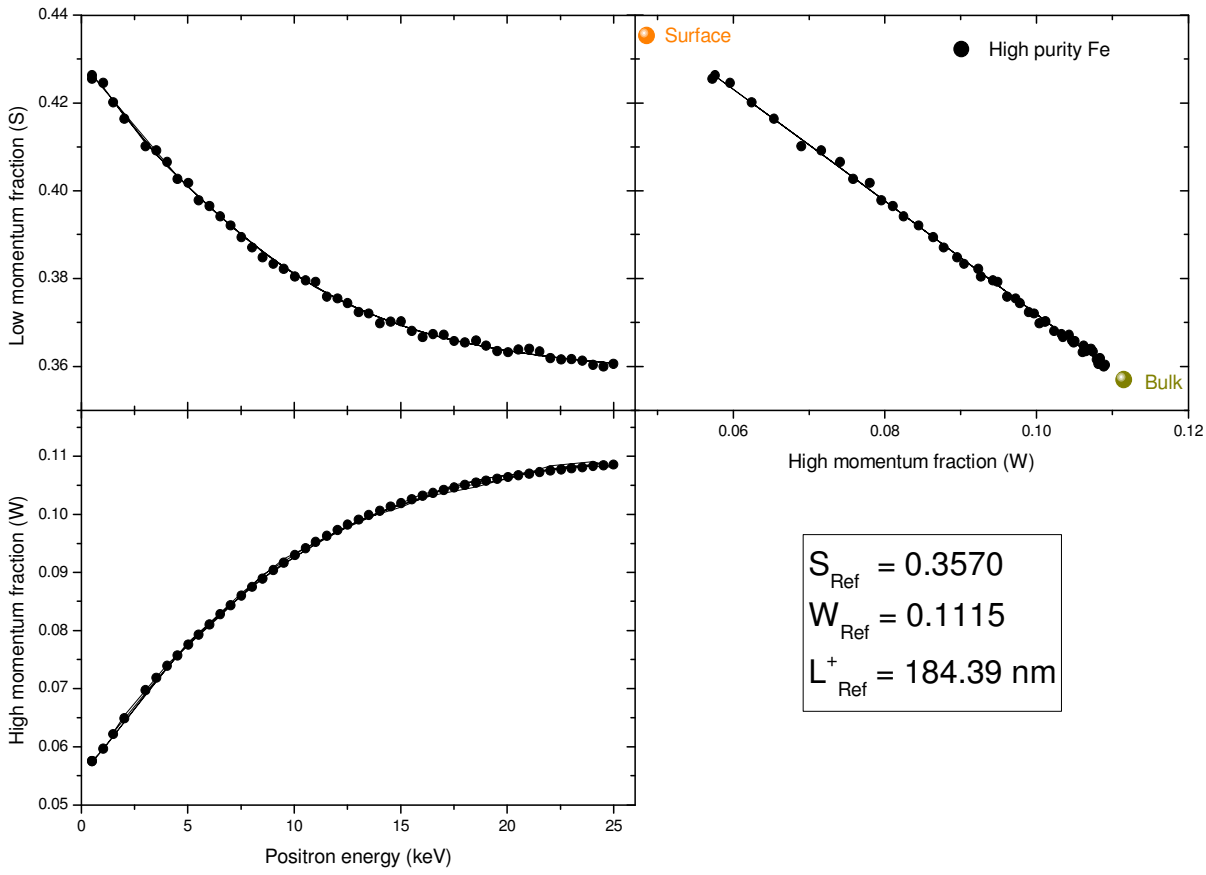

Figure 2.27. Variation of the characteristic S and W as a function of the positron energy for the pure Fe reference sample. The effective diffusion length of positrons L^{+} is equal to about 184 nm

To analyze $S(E)$ and $W(E)$ behavior the material can be considered as a multilayer material composed of n layers i with the thickness Δz_i, localized between z_i and z_{i+1} where the annihilation characteristics S_i and W_i are constant. The value of S or W for the given value of energy is the superposition of annihilations that take place in the layer i with the probability $f_i(E)$ and on the surface with the probability $f_{sf}(E)$

$$S(E) = \sum_{i=1}^{n} f_i(E) S_i + f_{sf}(E) S_{sf}$$

$$W(E) = \sum_{i=1}^{n} f_i(E) W_i + f_{sf}(E) W_{sf}$$

The probability f depends on the profile of the implantation of the positrons and their diffusion. Coefficient $f_{sf}(E)$ becomes important in case of low energy positron (energy in a range of a few eV to several tens of keV), implantation depth is short and positrons can diffuse back to the surface and annihilate there giving a signal characteristic (S and W) of the surface state. Considering a defect rich material (for example after irradiation) the diffusion length L^+ decreases because defects act as traps for positrons. In this case, the surface state disappeared rapidly with the increasing positron energy.

Taking into account the positron implantation profile and a multilayer structure, the VEPFIT program (variable energy positron fit) [35] allows the calculation of the curves S(E) and W(E) by fitting the experimental data. It is possible to determine for each layer the L^+_i, z_i, z_{i+1}, S_i, W_i, S_{sf}. W_{sf} values. In case of one homogeneous material, only one layer and the surface state can be considered to fit the data. In case of inhomogeneous material, several layers and the surface state have to be used.

As an example, the analysis of the PAS measurements of the reference pure iron with VEPFIT program indicates that only one layer can be used to fit the data indicating that the sample is homogeneous. The effective diffusion length L^+ is equal to 184 nm which is in good agreement with the literature [36].

III.4. Transmission Electron Microscopy

As it was mentioned in section II.2, for low energy ion irradiation experiments we used a Transmission Electron Microscope (TEM) 200kV, coupled with the ion implanter IRMA (Figure 2.5) used to perform simultaneous irradiation and observation. TEM was used to obtain information on the structure at the microscopic scale and for localization and characterization of any defect clusters inside the crystals created by irradiation at nanoscale.

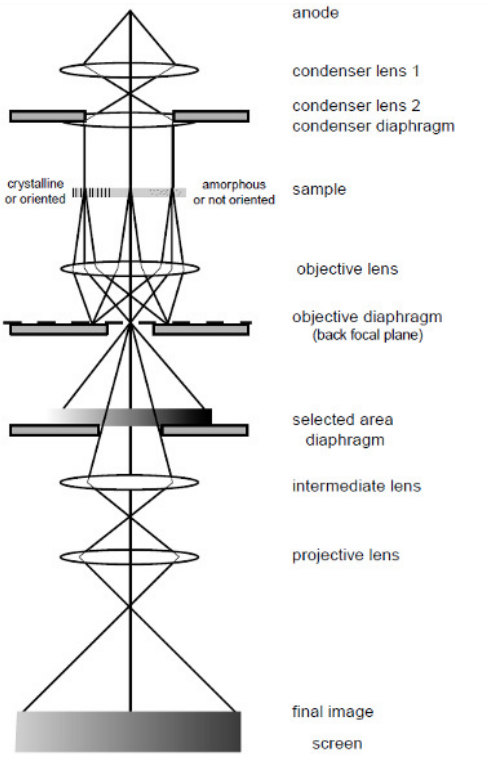

Figure 2.28. A schematic diagram of the transmission electron microscope. A beam of electrons is generated by filament and focused by electromagnetic lenses focuses on the sample. After the interaction with the specimen, the transmitted electrons pass through magnifying lenses and fall on a screen, thus giving an image

The set-up of a TEM schematically presented in Figure 2.28. A beam of electrons is generated by heating a tungsten or LaB6 filament (anode) that has the shape of a sharp tip or, in the newer generation of microscopes, by extracting the electrons from the sharp tip using high voltage (field emission gun). The electrons are accelerated by high voltage varying from 100 kV to more than 1000 kV depending on the microscope used (200kV in the case of current research). Next, a combination of electromagnetic lenses focuses the electron beam on the sample. To avoid undesirable interaction with gas molecules, the electron microscope operates in vacuum. After the interaction with the specimen, the transmitted electrons pass through a combination of magnifying lenses. Finally, the electrons fall on a fluorescent

screen, photographic film or digital CCD-camera where an enlarged image of the sample is obtained.

a) Observation technique

A TEM instrument offers many possibilities and techniques to visualize the defects of interest. The basic principle of TEM technique may be found in different books [37–39]. In the following some of the most useful methods to characterize a ferritic steel are briefly described.

The contrast in TEM-images at a relatively low magnification is determined by the diffraction contrast. If the objective aperture is placed around the transmitted beam, one obtains a bright field image as schematically shown in Figure 2.29(a). If the aperture is placed around a diffracted beam, a dark field image is obtained as illustrated in Figure 2.29(b). This contrast is optimized by working under two beam conditions. This means that in the diffraction pattern only one diffracted beam is present apart from the transmitted beam. In practice, it is sufficient that this diffracted beam is much more intense than all other diffracted beams. Under these conditions, the contrast induced by a defect can be calculated analytically.

Every type of defect introduces a specific type of contrast that allows its characterization. The bright field (BF) and dark field (DF) techniques are in principle enough to get an overview of the microstructure [37].

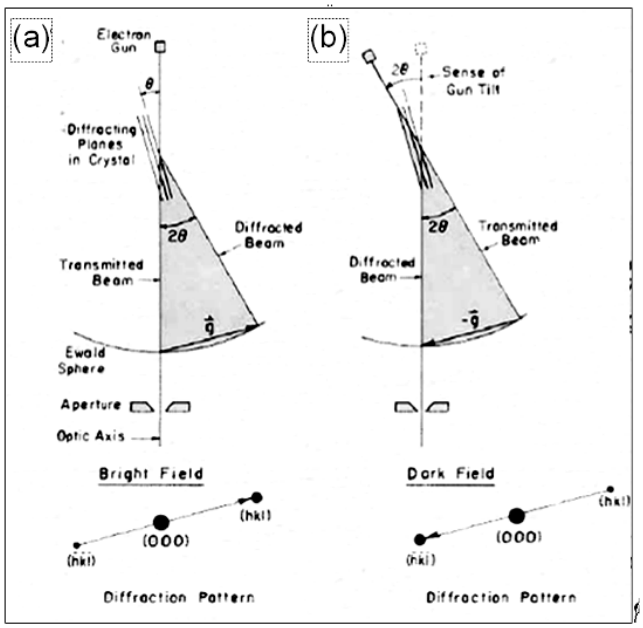

Figure 2.29. Ray diagrams showing how objective aperture is used to produce a bright and dark field images: if the aperture is placed around the transmitted beam, one obtains a bright field image (a); if the aperture is placed around a diffracted beam, a dark field image as is obtained (b).

b) Characterization of dislocations

The determination of dislocation type (slip plane, Burgers vector), size and density is a fundamental issue when investigating the performance of a material.

To determine the density of dislocations it is necessary to know the thickness of the sample that is being observed. For measuring the thickness of the foil there are several methods [38]. In this work the thickness fringes method has been used.

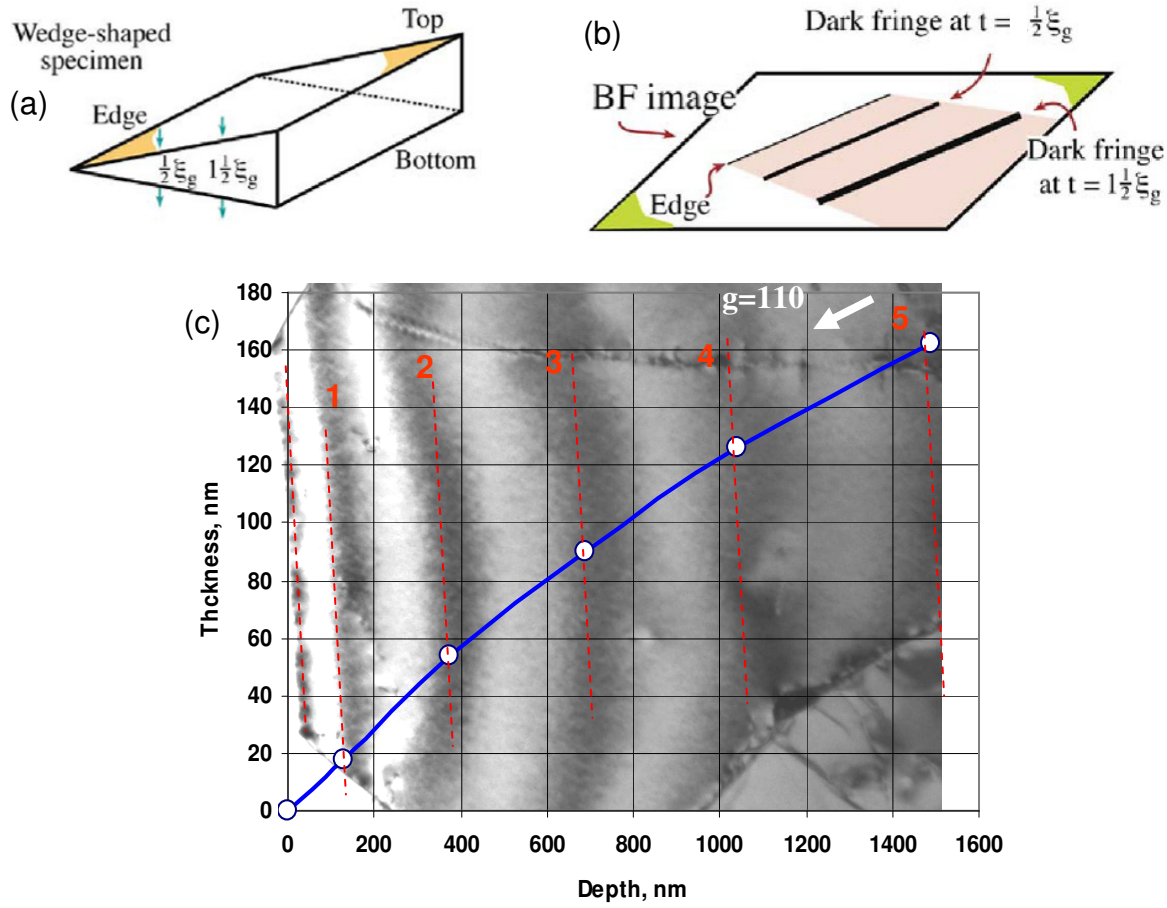

Figure 2.30. A schematic diagram of the determination of foil thickness using a method counting the numbers of thickness fringes (after [38]). (a) – the separation of the fringes in the image for a wedge specimen. (b) – thickness is determined by the angle of the wedge and the extinction distance; (c) – bright field image of the Fe-12%Cr alloy under two-beam condition with the diagram of the thickness. The latter microstructure corresponds to the one in Figure 5.5

This method is based on oscillations of the intensity of the incident beam with the thickness of the foil (details can be found in [38]). The fringes are visible in the background intensity when the thickness of the specimen varies locally. They are often parallel to the edge of the specimen.

As schematically presented in Figure 2.30, the dark fingers under bright field two-beam conditions are observed on the foil areas, the thickness of which is equal to $k \cdot \frac{1}{2}\xi_g$, where k – is the number of fingers and ξ_g is the extinction distance (the characteristic length for the diffraction vector g). For Fe–9 to 12%Cr model alloys, imaged with 200keV TEM (as used in the current study), $\xi_g(101)$ =36 nm; $\xi_g(002)$ =53 nm, $\xi_g(112)$ =70 nm. Thus, with the number of dark fringes and ξ_g it is possible to estimate the thickness of the foil (as demonstrated in Figure 2.30(c)).

Determination of the Burgers vectors. The invisibility criterion is **g·b** = 0 [37], where $\vec{g}$ is the reflection which is used under two beam conditions; $\vec{b}$ is the Burgers vector of dislocation. Physical basis of this criterion is that $\vec{g}$ corresponds to the set of plane that are not deformed by defect, while $\vec{b}$ describes deformation introduced by the dislocation. Although it is not strictly a sufficient condition for vanishing of dislocations in the micrographs, it is generally very useful as a criterion for determining the direction of Burgers vectors. The contrast usually becomes very weak when $\vec{g} \cdot \vec{b} = 0$. Therefore it is necessary to take a series of micrographs of dislocations in various reflections conditions, together with selected area electron diffraction patterns. If enough reflections are examined, it is usually possible to identify the direction of the Burgers vector from one or more vanishing conditions. The example of the Burgers vector determination of the irradiation-induced dislocation loops is given in the Chapter 5 (p. 177).

IV. References

[1] Matijasevic M., Microstructure and Mechanical Properties of Fe-Cr Model Alloys and High Cr Steels Under Neutron Irradiation, PhD thesis., Gent University, 2007.
[2] M. Matijasevic, A. Almazouzi, Journal of Nuclear Materials 377 (2008) 147-154.
[3] M. Matijasevic, E. Lucon, A. Almazouzi, Journal of Nuclear Materials 377 (2008) 101-108.
[4] F. Bergner, A. Ulbricht, C. Heintze, Scripta Materialia 61 (2009) 1060-1063.
[5] C. Heintze, A. Ulbricht, F. Bergner, H. Eckerlebe, J. Phys.: Conf. Ser. 247 (2010) 012035.
[6] Y. Serruys, M.-O. Ruault, P. Trocellier, S. Henry, O. Kaïtasov, P. Trouslard, Nuclear Instruments and Methods in Physics Research Section B: Beam Interactions with Materials and Atoms 240 (2005) 124-127.
[7] J.F. (James F.) Ziegler, U. Littmark, J.P. Biersack, The Stopping and Range of Ions in Solids / J.F. Ziegler, J.P. Biersack, U. Littmark, Pergamon, New York, 1985.
[8] A. Etienne, Etude Des Effets D'irradiations Et De La Nanostructuration Dans Des Aciers Austénitiques Inoxydables, PhD thesis. Université de Rouen, 2009.
[9] E.W. Müller, Z. Physik 131 (1951) 136-142.
[10] M.K. Miller, A. Cerezo, M.G. Hetherington, G.D.W. Smith, Atom Probe Field Ion Microscopy, Clarendon PRESS, Oxford, 1996.
[11] M. Drechsler, P. Wolf, In: Bargmann Et Al., Proc. Intern. Conf. on Electron Microscopy Berlin (1958) p. 835.
[12] M.K. Miller, Atom Probe Tomography: Analysis at the Atomic Level, Kluwer Academic/Plenum Publishers, New York, 2000.
[13] D. Blavette, B. Deconihout, A. Bostel, J.M. Sarrau, M. Bouet, A. Menand, Review of Scientific Instruments 64 (1993) 2911-2919.
[14] D. Blavette, A. Bostel, J.M. Sarrau, B. Deconihout, A. Menand, Nature 363 (1993) 432-435.
[15] A. Cerezo, P.H. Clifton, S. Lozano-Perez, P. Panayi, G. Sha, G.D. Smith, Microscopy and Microanalysis 13(06) (2007) 408-417.
[16] Thomas F. Kelly and Michael K. Miller, Rev. Sci. Instrum. 78 (2007) 031101-031101-20.
[17] A. Cerezo, T.J. Godfrey, S.J. Sijbrandij, G.D.W. Smith, P.J. Warren, Review of Scientific Instruments 69(1) (1998) 49-58.
[18] B. Deconihout, F. Vurpillot, B. Gault, G. Da Costa, M. Bouet, A. Bostel, D. Blavette, A. Hideur, G. Martel, M. Brunel, Surface and Interface Analysis 39 (2007) 278-282.
[19] B. Gault, F. Vurpillot, A. Vella, M. Gilbert, A. Menand, D. Blavette, B. Deconihout, Rev. Sci. Instrum. 77 (2006) 043705.
[20] C. Ropers, D.R. Solli, C.P. Schulz, C. Lienau, T. Elsaesser, Phys. Rev. Lett. 98 (2007) 043907.
[21] F. Vurpillot, J. Houard, A. Vella, B. Deconihout, Journal of Physics D: Applied Physics 42 (12) (2009) 125502.
[22] B. Gault, M.P. Moody, F. De Geuser, A. La Fontaine, L.T. Stephenson, D. Haley, S.P. Ringer, Microscopy and Microanalysis 16 (2010) 99-110.
[23] E. Bemont, A. Bostel, M. Bouet, G. Da Costa, S. Chambreland, B. Deconihout, K. Hono, Ultramicroscopy 95 (2003) 231-238.
[24] S. Novy, Mécanismes De Vieillissement à Très Longue Échéance Des Aciers Inoxydables Austéno-ferritiques, PhD thesis. UNIVERSITE DE ROUEN, 2009.
[25] D. Blavette, F. Vurpillot, P. Pareige, A. Menand, Ultramicroscopy 89 (2001) 145-153.

[26] M.K. Miller, M.G. Hetherington, Surface Science 246 (1991) 442-449.
[27] F. Vurpillot, A. Bostel, D.Blavette, Applied Physics Letters 76-21 (2000) 3127–3129.
[28] S. Novy, P. Pareige, C. Pareige, Journal of Nuclear Materials 384 (2009) 96-102.
[29] G. Da Costa, 3D Data Processing for Atom Probe. Atom Probe Tomography School, GPM - Rouen, 2008.
[30] D. Vaumousse, A. Cerezo, P.J. Warren, Ultramicroscopy 95 (2003) 215-221.
[31] M. Thuvander, H.-O. Andrén, K. Stiller, Q.-H. Hu, Ultramicroscopy 73 (1-4) (1998) 279-285.
[32] P. Desgardin, L. Liszkay, Marie France Barthe et all., Materials Science Forum (Volumes 363 - 365) (2001) 523-525.
[33] Krause-Rehberg R, Leipner H. S., Positron Annihilation in Semiconductors. Defect Studies., Berlin.Heidelberg. New York: Springer-Verlag, 1999.
[34] M.-F. Barthe, C. Corbel, G. Blondiaux, Technique De l'Ingénieur, Traité Analyse Et Caractérisation (2003) 2610-1 2610-23.
[35] V. Veen, H. Schut, J. de Vries, R.. Hakvoort, M.. Ijpma, Positron Beams for Solids and Surfaces AIP Conf. Proc. "Analysis of Positron Profiling Data by Means of VEPFIT," AIP, New York, 1990.
[36] C. El Mazri, P. Desgardin, Rapport De Stage Master II. Comportement Sous Irradiation Des Métaux De Structure Pour Les Réacteurs Du Futur, 2008.
[37] P.B. Hirsch, Electron Microscopy of Thin Crystals, Butterworths, 1965.
[38] David B. Williams, C. Barry Carter, Transmission Electron Microscopy - A Textbook for Materials Science, Springer; 2nd ed. edition, 2009.
[39] P.B. Hirsch, Electron Microscopy of Thin Crystals, Krieger Publishing Company, 1977.

CHAPTER 3.
MICROSTRUCTURE OF THE MODEL ALLOYS IN THE AS-RECEIVED STATE

All Fe-Cr model alloys (namely Fe-5%Cr, Fe-9%Cr and Fe-12%Cr) investigated in the current work, are in normalized and tempered state (see Chapter 2 for details). The response of the microstructure on irradiation depends on the initial microstructure of the model alloys before exposure (homogeneity of alloys, grain structure, dislocations and other defects distribution etc.), in the so-called as-received state. These microstructural characteristics are of large importance and thus have been studied.

The metallographic characterisation of all model alloys has been performed within the current work by visual light microscopy (VLM), scanning electron microscopy (SEM) and transmission electron microscopy (TEM). The homogeneity of the model alloys at the microscopic scale has been checked using TEM-EDS and SEM-EDS techniques while 3DAP experiments have been performed to investigate the randomness of solutes distribution at the nanometric scale. PAS (Slow-Positron-Beam Doppler- broadening Techniques) investigations of all materials were also carried out in order to check the quantity of open-volume defects (vacancies and theirs complexes) in the as-received state.

The data on the as-received state of the model alloys are then compared with the data obtained on the same materials by other laboratories-participants of the GETMAT project [1–6].

TABLE OF CONTENT

I. Fe-5%Cr model alloy

I.1. Metallography

The results of VLM observations are presented in Figure 3.1. The microstructure consists of two well defined microstructural components: polygonal ferritic grains (white after etching) and martensitic or bainitic grains (grey after etching). Polygonal ferritic grains have a size from tens up to few hundreds micrometers that is consistent with the results reported by Matijasevic [2]. Martensitic or bainitic grains consists of parallel thin lathes (of few μm in width) which are typical for lath martensite or upper bainite in low carbon steels [7,8].

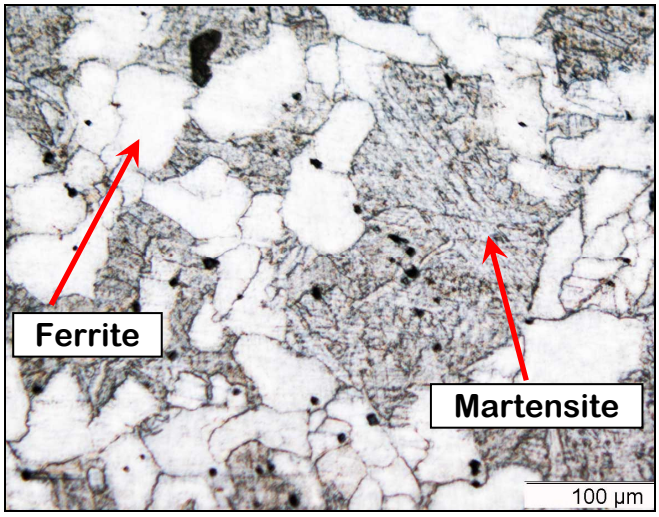

Figure 3.1. Metallography of the investigated Fe-5%Cr model alloy

SEM-EDS (X-ray energy dispersive spectroscopy) investigations revealed that the mean chromium content in the alloy is equal to (5.2 ± 0.5)at% (Table 3.1) that is in good agreement with the data obtained by chemical analysis and given in [2] (Table 2.1, p. 47). Note that EDS analysis is not sensitive to the minor alloying elements, such as Si, P, Mn, Ni, V, C, N, O, S, Al and Ti because of their low levels.

Table 3.1. Chemical composition of the as-received Fe-5at%Cr model alloy (at.%) measured with EDS

Fe	balance
Cr	5.2 ± 0.5
Si, P, Mn, Ni, V, C, N, O, S, Al, Ti	*not measurable*

EDS investigations revealed few microscopic chromium enriched segregations randomly distributed in the alloy (Figure 3.2). They have a size from tens up to few hundreds

micrometers. Some aluminium has also been found to enrich these objects (Figure 3.2). We should also mention that in the area near these segregations, the Cr content was slightly larger than the mean value. Except these segregations, the distribution of Cr in the Fe-5%Cr model alloy was found homogeneous at the microscopic scale.

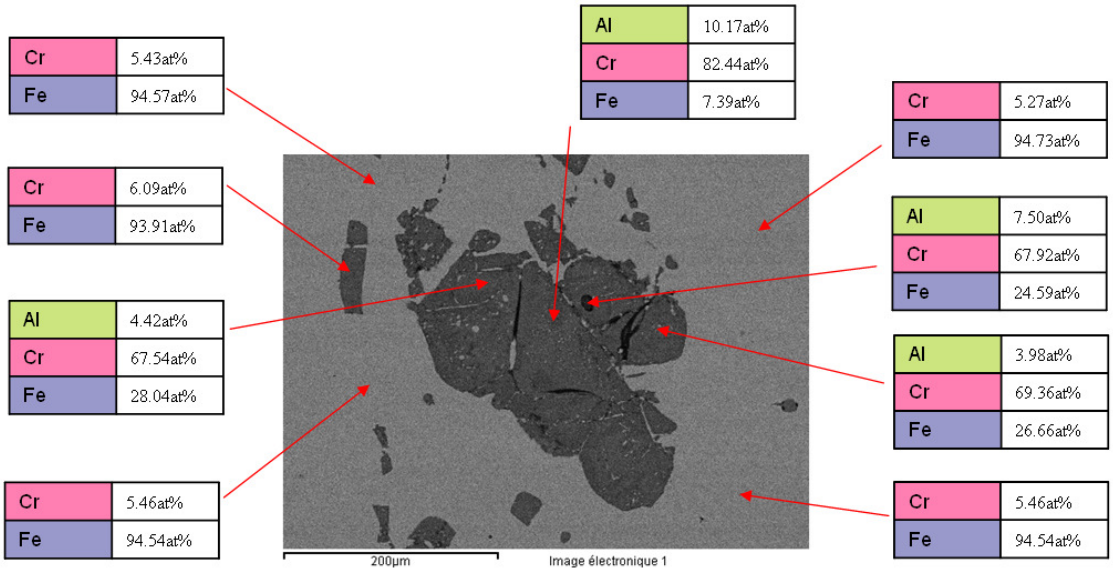

Figure 3.2. Cr-enriched segregation in the Fe-5%Cr model alloy as revealed by SEM. The data on chemical composition were obtained by EDS measurements

I.2. 3DAP

The randomness of the spatial distribution of the alloying elements inside the grains in the Fe-5%Cr model alloy (neglecting the Cr-enriched segregations mentioned above) has been checked at the nanoscale with the 3DAP. The measured chromium concentration in the overall analysed volume is: (4.7±0.1)at.% (Table 3.2). Within uncertainties, this is in good agreement with the chemical analysis given in [2] (Table 2.1, p. 47) and with the one deduced by EDS measurements (Table 3.1).

Data of Table 3.2 have been averaged from few 3DAP experiments. It must be emphasised that, the 3DAP samples being prepared by electrochemical polishing (see Appendix 1), it is impossible to control which microstructural constituent is studied (ferrite or martensite). Any significant differences in composition and chemical specie distributions have been detected in the different analysed volumes.

Chromium appears to be homogeneously distributed inside the grains, as shown by the 3D map of chromium atoms in Figure 3.3. In order to confirm the homogeneous distribution of Cr, the statistical test described in the Chapter 2 (section III.2(e) p. 74) has been used. Figure 3.4 shows that the s-curve of the experimental distribution almost coincides with the binomial one mainly for small sampling boxes, confirming the homogeneous distribution of chromium atoms.

Table 3.2 Chemical composition of the as-received Fe-5at%Cr model alloy (at.%) measured with 3DAP

Fe	balance
Cr	4.7 ±0.1
Si	0.04±0.01
P	0.010±0.001
Ni	0.06±0.01
Mn, V, C, N, O, S, Al, Ti	*not measurable*

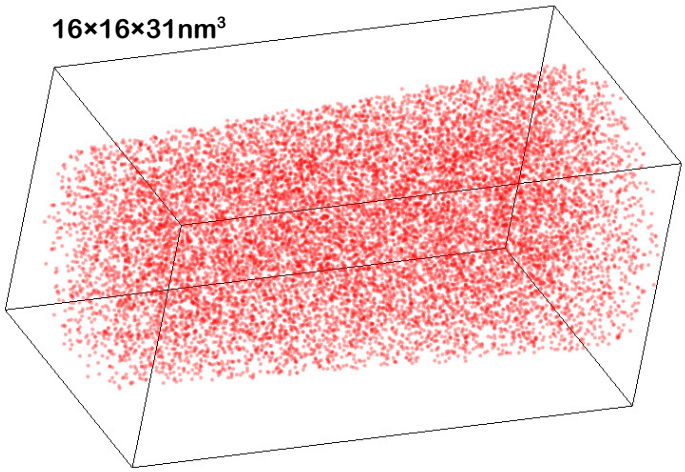

Figure 3.3 3D distribution of chromium atoms in the as-received Fe-5at% Cr model alloy. Each dot represents one atom. For clarity only chromium atoms are represented. Chromium atoms are homogeneously distributed.

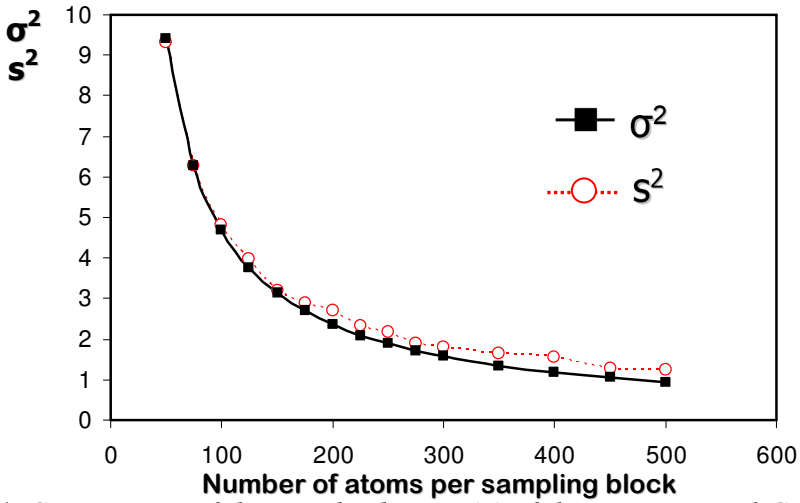

Figure 3.4. Comparison of the standard error (s) of the experimental Cr-concentration frequency distribution with the standard deviation (σ) of the binomial distribution in the un-irradiated Fe-5%Cr model alloy for sampling volume of different size. Experimental distribution almost coincides with the binomial one. Chromium atoms are homogeneously distributed.

I.3. PAS

PAS experiments have been performed in order to estimate the quantity of open volume defects in the Fe-5%Cr model alloy before irradiation experiments. As shown in Figure 3.5, Slow-Positron-Beam Doppler- Broadening technique revealed that annihilation characteristics (S(E), W(E) and S(W) curves) of the alloy are almost identical to the curves measured in the annealed pure Fe reference sample (see for details Chapter 2, section III.3(c), p. 80). It indicates that the quantity of open-volume defects in the as received state is rather low. Fittings of S(E) and W(E) by VEPFIT program using one homogeneous layer (dotted line in Figure 3.5) is not fully accurate. The best fit is found using two layers where the first near-surface layer is 30 nm thick (solid line in Figure 3.5). The nature of this first layer is difficult to determine: it could be due to remaining vacancy defects after mechanical polishing or could correspond to an oxidised layer. The diffusion length in the bulk (second layer) is found to be equal to 129 nm. This value is lower than the one found in pure iron (185 nm) and indicates that vacancy type defects are present in this sample. As the diffusion length decreases rapidly with the defect concentration, the concentration of those defects is relatively low.

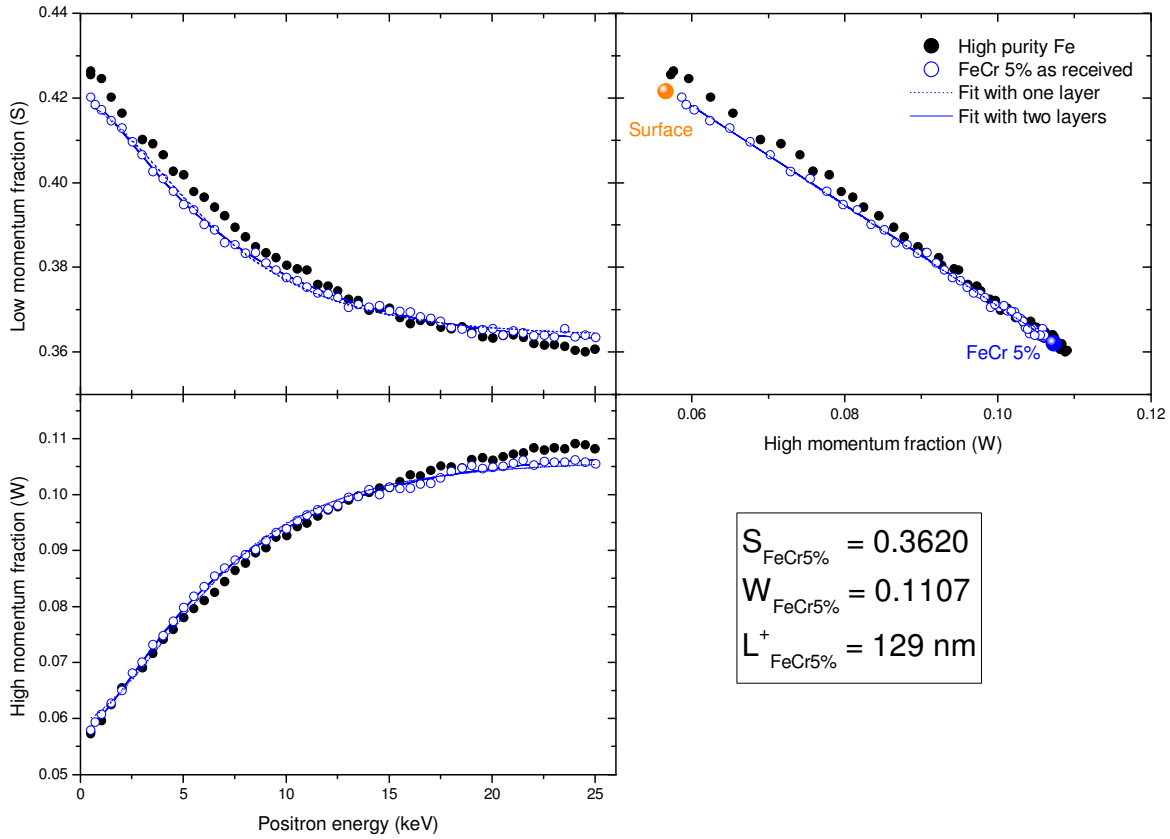

Figure 3.5. Low (S) and high (W) momentum fraction versus positron energy for the un-irradiated Fe-5%Cr model alloy in comparison with the annealed pure Fe

II. Fe-9%Cr model alloy

II.1. Metallography

VLM has shown that the structure of the Fe-9%Cr alloy consists of lathes which form a packet structure (Figure 3.6 *a* and *b*). Such morphology is typical of lath martensite or upper bainite.

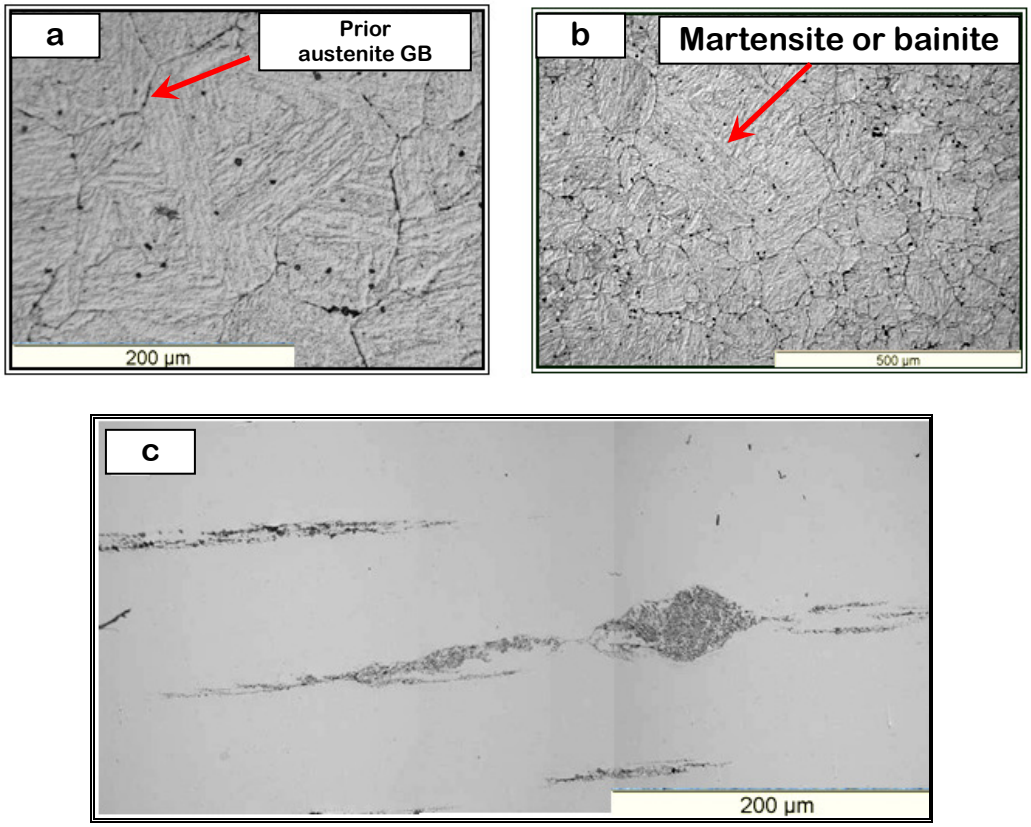

Figure 3.6. Metallography on the Fe-9%Cr alloy.
a, b – light microscopic observation of the alloy structure. Prior austenite has been transformed into lath martensite or bainite, c – segregation which have been observed in sample (sample without etching)

The martensitic or bainitic structure was formed during air cooling from austenitic state (from 1050ºC). Because of the heat treatment that was made at 730ºC after the γ-α transformation, the observed lath structure is a tempered martensite (bainite).

The position of the former austenitic grain boundaries can be recognised owing to the preferential etching at these places. As shown in Figure 3.6(b), distribution of the size of the prior austenitic grains is broad and varies from tens of micrometers up to few hundreds. The broad distribution of the prior austenitic grain size can be a consequence of a secondary

(collective) recrystallization that probably have taken place during annealing of the cold worked alloy at 1050ºC.

The size of the packets and the length of the lathes depend directly on the size of the prior austenite grains. This is due to the fact that the growing laths of martensite (or bainite) which keep their orientation relationship [7,8] cannot go through the boundaries of the austenitic grains. This implies that the distributions of the packet size and the length of the lathes of martensite are also broad.

VL microscopy observations (Figure 3.6(*c*)) also reveal the presence of few large elongated segregations (visible even by eyes) after mechanical polishing as in the Fe-5%Cr alloy.

The same specimens have been studied by SEM. The results have confirmed that the structure of the investigated alloy has packet-lath morphology. Figure 3.7 shows that the prior austenitic grain consists of elongated parallel lathes after transformation.

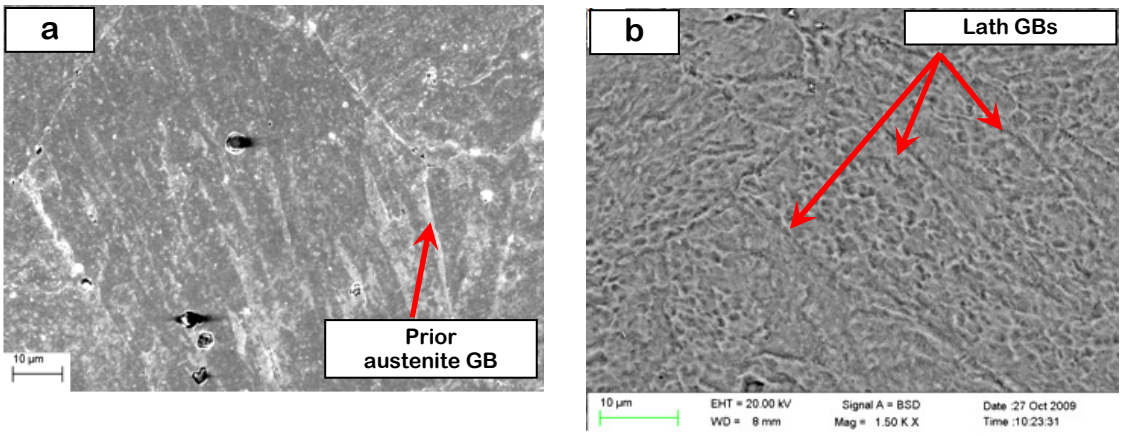

Figure 3.7. Results of SEM observation of the Fe-9%Cr alloy:
a –lathes of martensite (bainite), the grain boundaries of the parent austenitic grain are visible b– lathes of tempered martensite (bainite) which consists of small grains.

SEM results also reveal a complex microstructure of this alloy. Indeed, as shown by Figure 3.7*(b)*, small grains with a size less than a micrometer are observed inside the laths. This structure have been formed rather during the final tempering at 730ºC and the small grains could be the result of recovery processes.

The homogeneity of the chemical composition of the alloy at the microscopic scale was checked by EDS measurements. The mean chromium content was found to be equal to (9.3±0.3)at% (

Table 3.3) that is in good agreement with the reference data (Table 2.2, p. 48).

SEM confirmed the presence of large elongated segregations revealed during VLM experiments, as shown in Figure 3.8. The EDS investigation of these zones showed that they are chromium enriched. Depending on the zone, chromium concentration in these segregations can reach 93%. Except these large elongated chromium enriched segregations, the chemical composition of the alloy has been found homogeneous at the microscopic scale.

Note that the presence of the Cr enriched segregation appears to complicate the process of TEM thin foils preparation. Indeed, these zones were the place of cracking of the thin plates during mechanical polishing.

Table 3.3 Chemical composition of the Fe-9at%Cr model alloy (at.%) measured by EDS

Fe	balance
Cr	9.3 ± 0.9
Si, P, Mn, Ni, V, C, N, O, S, Al, Ti	*not measurable*

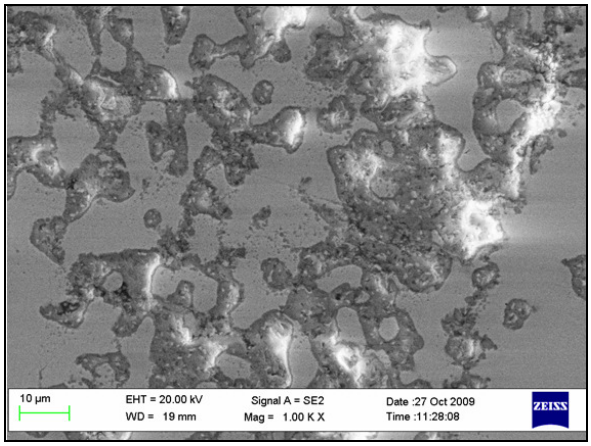

Figure 3.8. SEM observation of the Cr-enriched segregation in the Fe-9%Cr alloy.

The fine scale microstructure of the as-received Fe-9%Cr model alloy is illustrated by the bright field TEM images in Figure 3.9. The distribution of the size of the small sub-grains which form lathes is broad: from few hundreds of nanometres up to few micrometers. TEM revealed that dislocations are non-homogenously distributed in this structure. It can be seen that in some grains dislocations form cellular structures (Figure 3.9 (*a*)).

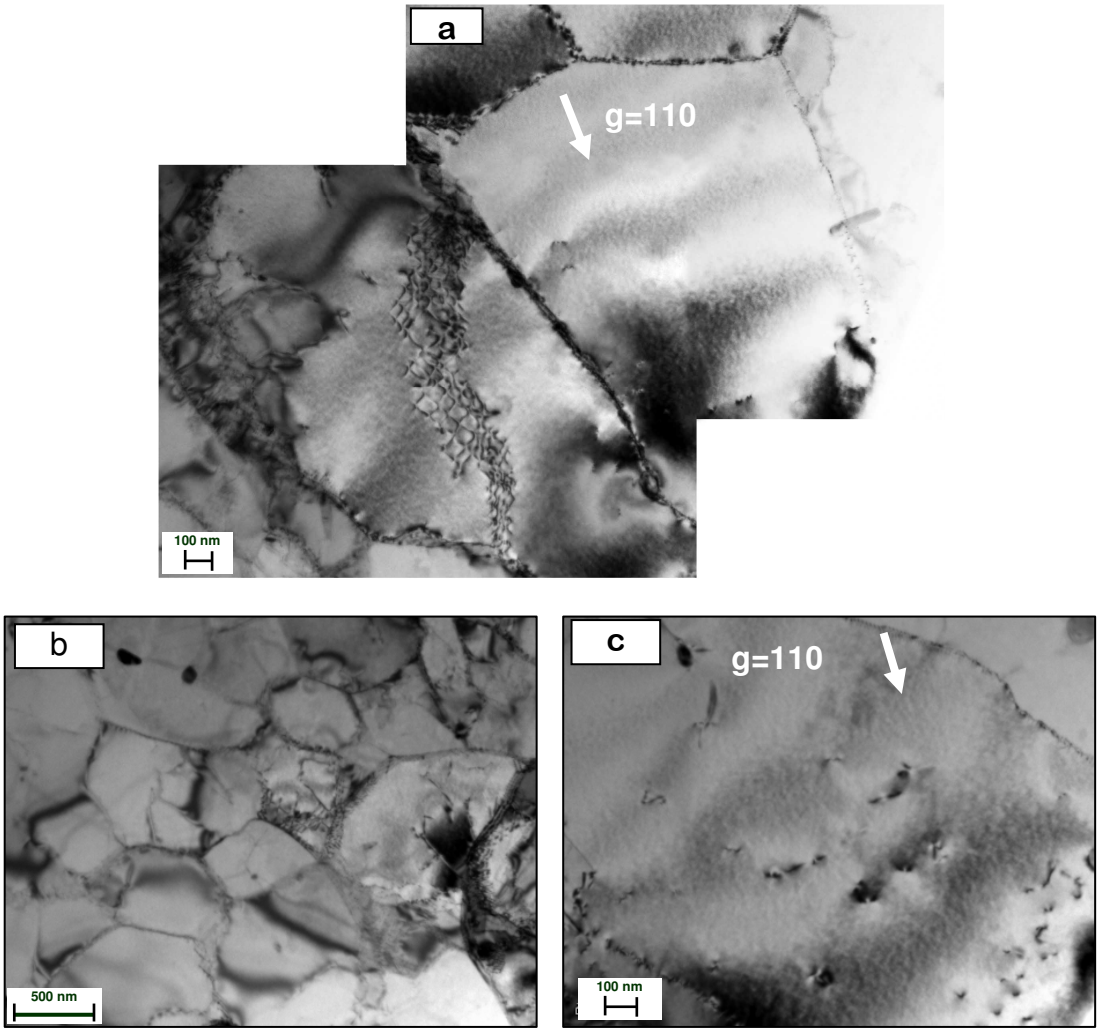

Figure 3.9. Bright field images obtained by TEM on the Fe-9%Cr alloy
a –cellular dislocation structure
b – the small grains which form martensitic lathes
c – dislocations in martensitic lathes

II.2. 3DAP

As in the Fe-5%Cr alloy, the as-received Fe-9%Cr model alloy was investigated by 3DAP in order to check the randomness of the spatial distribution of alloying elements at the nanoscale. Note that, as in the case of thin foils, the presence of Cr enriched segregations mentioned above appears to complicate the process of 3DAP samples preparation, leading to nonhomogeneity of the electrochemical polishing. Thus, the 3DAP samples have been cut in a manner to avoid parts which contain such segregations.

The measured chromium concentration inside grains is: (9.12 ± 0.18)at.% (Table 3.4) that is in good agreement with the reference chemical analysis data [2] (Table 2.2, p. 48) as well as with EDS measurements (

Table 3.3).

Table 3.4 Chemical composition of the Fe-9%Cr model alloy (at%) measured by 3DAP

Fe	balance
Cr	9.12 ± 0.18
Si	0.10 ± 0.03
P	0.06 ± 0.01
Ni	0.076 ± 0.017
Mn, V, C, N, O, S, Al, Ti	*not measurable*

As shown by the 3D distribution of chromium in Figure 3.10, chromium atoms appear to be homogeneously distributed at the nanometric scale inside grains and no particular segregation is observed. In the case of Cr, this fact was confirmed by statistical test (Figure 3.11). Indeed, the s-curve of the experimental distribution coincides with the binomial one. This indicates the homogeneous distribution of this specie in the alloy.

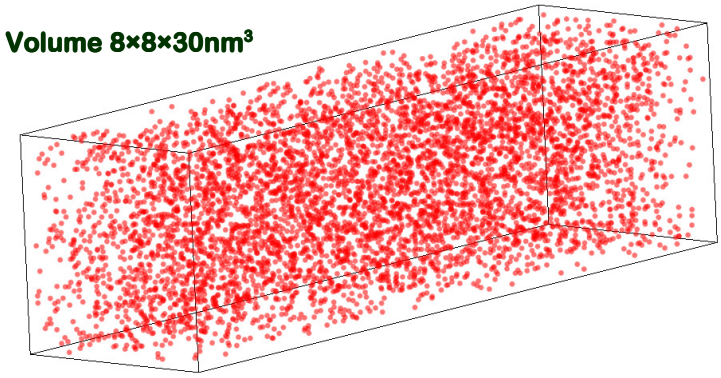

Figure 3.10. 3D distribution of chromium atoms in the as-received Fe-9% Cr model alloy. Each dot represents one atom. For clarity only chromium atoms are represented. Chromium atoms are homogeneously distributed.

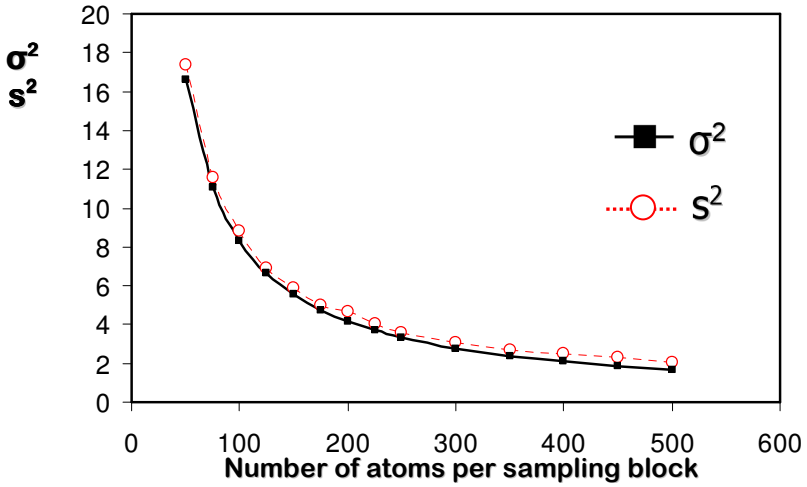

Figure 3.11. Comparison of the standard error (s) with the standard deviation (σ) in the as-received Fe-9%Cr model alloy. Experimental distribution almost coincides with the binomial one. Chromium atoms are homogeneously distributed.

II.3. PAS

The estimation of the quantity of open volume defects in the Fe-9%Cr model alloy before irradiation experiments have been performed by PAS technique. Slow-Positron-Beam Doppler-broadening experiments revealed that S(E), W(E) and S(W) curves have the same shape compared to the annealed pure Fe reference ones (Figure 3.12). As in the case of the Fe-5%Cr alloy, the best fit was obtained using two layers. The first near-surface layer (oxidised or damaged layer) is around 50nm thick. The estimated effective diffusion length L^+ of the second layer (bulk layer) is equal to 132 nm. This value is almost equal to the one, estimated for the bulk layer in the Fe-5%Cr alloy (129 nm) and it is lower than the one found in pure iron (185 nm). It indicates that some vacancy type defects are also present in this sample but their concentration is relatively low.

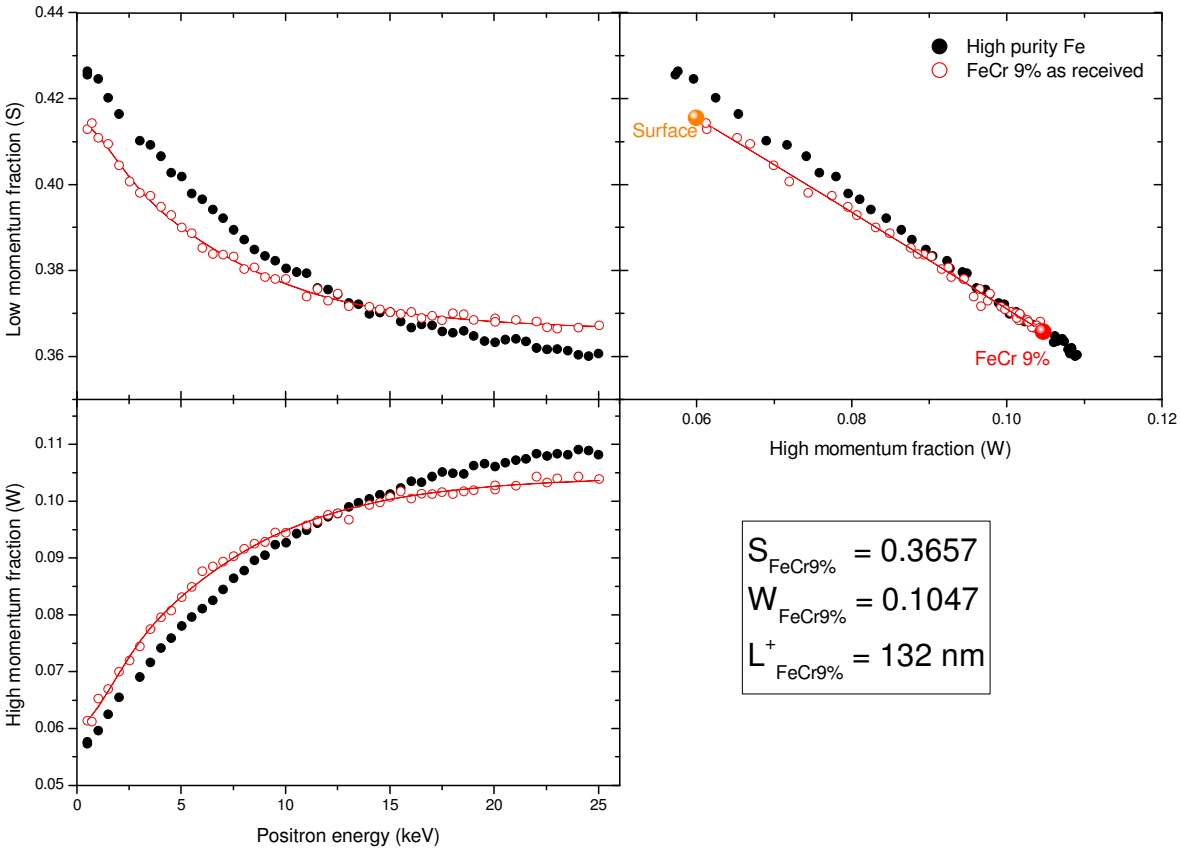

Figure 3.12. Low (S) and high (W) momentum fraction versus positron energy for the un-irradiated Fe-9%Cr model alloy in comparison with the annealed pure Fe after annealing

III. Fe-12%Cr model alloy

III.1. Metallography

As in the case of the Fe-9%Cr, a packet-lath microstructure, typical for the lath martensite or upper bainite, has been observed by light microscopy in the Fe-12%Cr alloy (Figure 3.13). Here also, the prior austenitic grains had a broad distribution of size from few tens micrometres up to hundreds micrometres, as illustrated by Figure 3.13 (b).

VLM also revealed segregations similar to the Cr-enriched one observed in the Fe-9%Cr alloy (Figure 3.9(c)) and in Fe-5%Cr alloy (Figure 3.2). It has been observed that their density was significantly smaller in comparison with the Fe-9%Cr alloy.

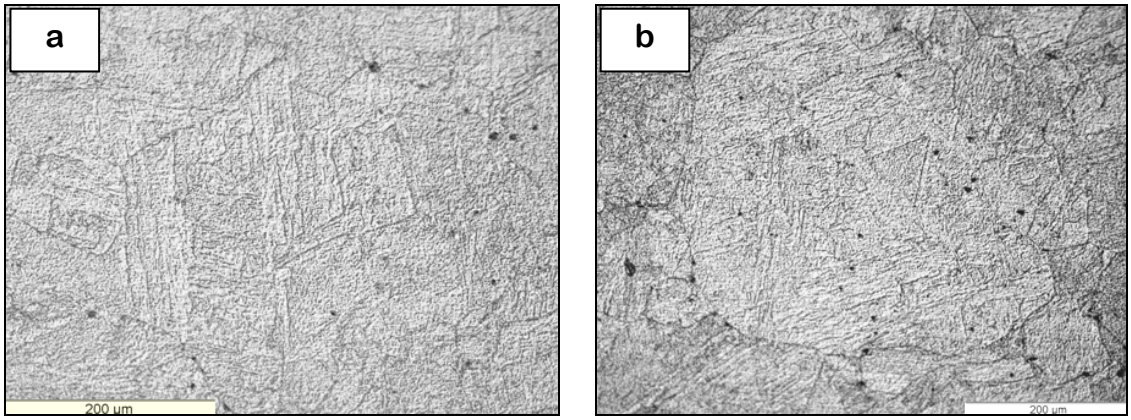

Figure 3.13. Metallography on the Fe-12%Cr model alloy: prior austenitic grains (whit a broad distribution of grain size) have been transformed to lath martensite or upper bainite during γ→α transformation.

The fine structure of the as-received Fe-12%Cr model alloy is shown by the bright field TEM images in Figure 3.14. TEM reveals that the lathes consist of sub-grains unresolved by VLM investigations with extremely broad size distribution from few hundreds of nanometers up to few micrometers, as illustrated by Figure 3.14(c). Dislocations in this alloy are also non-homogenously distributed (Figure 3.14(*a*)) and form cellular structure in some grains.

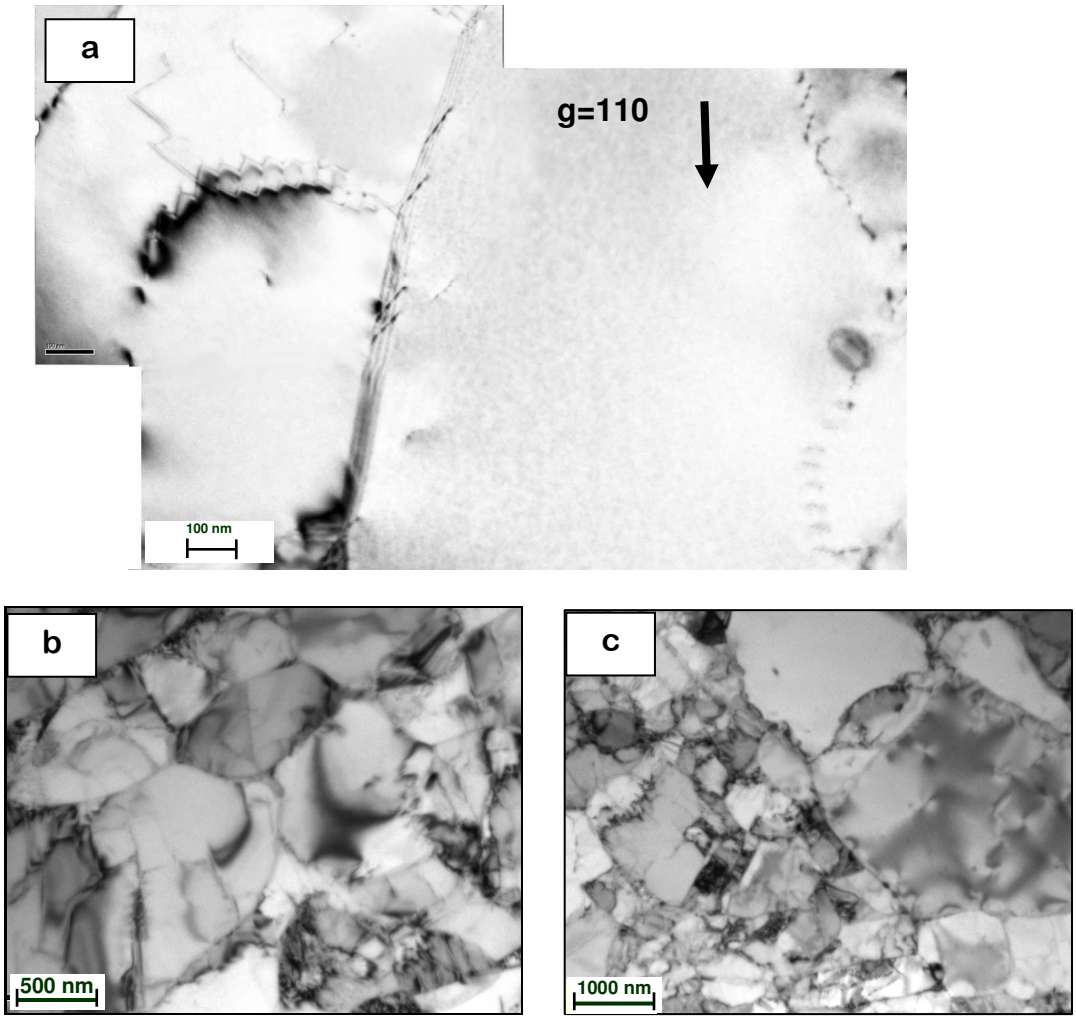

Figure 3.14. Bright field images obtained by TEM on the Fe-12%Cr alloy a – dislocation structure is non-homogenous; b – the subgrains observed inside the martensitic (or bainitic) lathes; c – broad distribution of the sub-grain size

The numerous 3DAP experiments which have been performed on the Fe-12%Cr model alloy (thermal ageing – Chapter 5, part I.2; ion irradiation – Chapter 5, part III.2 and neutron irradiation – Chapter 4, part I.3) revealed that the Cr content inside grains is lower than the expected nominal concentration given by chemical analysis [2]. Cumulating experiments in as-received, ion irradiated and neutron irradiated state the variation for Cr chromium concentration was in the range 9.9at% – 11.5at% from one sample to another. This strongly suggests that Cr heterogeneity exists in the Fe-12%Cr bars. Moreover, some disagreements are also reported in the PhD thesis M. Matijasevic [2]. For example, the chemical analysis data on the as-received model alloy performed within this PhD thesis have shown 12.33at% (11.6wt%) of Cr (see Table 2.2, p.33 of [2]). But this value differs with the value which is given in the same PhD thesis on the composition of the neutron irradiated alloy (see Table 2.6, p.49 of [2]), where just 10.86% of Cr is measured (wasn't specified at.% or wt.%).

In order to clarify this point and then in order to check the chemical homogeneity of the model alloy, measurements of the Cr concentration inside grains in the as-received sample have been performed by means of EDS spectroscopy using a Jeol ARM-200F transmission electron microscope working at 200 kV with a 0.2 nm probe. Two different TEM specimens have been studied: i) a cross-sectional specimen prepared by a standard lift-out TEM thin foil procedure using a Dual-Beam Focus Ion beam (FIB)-SEM (Zeiss NVision 40). The final milling was performed with a Ga beam energy of 2kV - ii) A standard TEM foil made by electrochemical polishing.

The two thin foils have been made from different places of the bar. It was detected that the chromium content varies significantly between measurements, as indicated by the frequency distribution of the Cr concentration presented in Figure 3.15. The mean Cr content in the first thin foil (FIB preparation) is about (11.0±0.5)at.% wile the mean Cr content in the second thin foil (electro-chemical preparation) is about (12.5±0.8)at.%. Summarising the data from these 2 sets of measurements it is possible to conclude that depending on the zone, the Cr level has been found in range between (10.5±1)at.% and (13.2±1.3) at.% with a mean value of (11.7 ± 1.2) at.%. This indicates that a significant inhomogeneity of the Cr distribution exists in the Fe-12%Cr bar at the microscopic scale.

Also, the presence of large Cr enriched clusters mainly along grain boundaries have been revealed by TEM-EDS experiments, as presented in Figure 3.16.

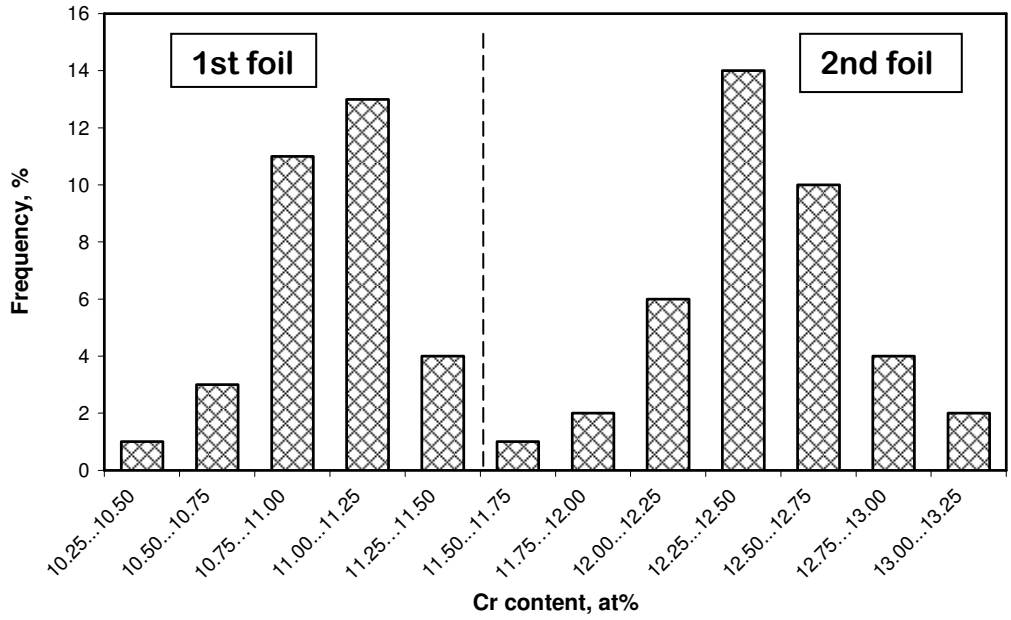

Figure 3.15. Frequency distribution of the Cr concentration in Fe-12%Cr model alloy obtained by TEM-EDS analysis of two thin foils. The large distribution originates from the inhomogeneity of the model alloy. The mean Cr content in the first thin foil (FIB preparation) is about (11.0±0.5)at.%, The mean Cr content in the second thin foil (electro-chemical preparation) is about (12.5±0.8)at.%. The data have been averaged over 71 measurements.

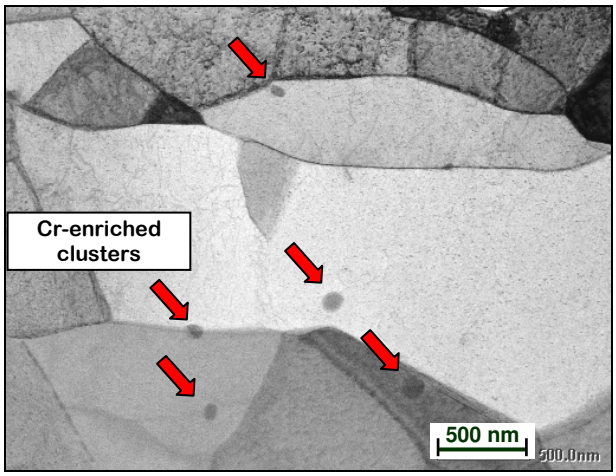

Figure 3.16. Low angle annular dark field micrograph obtained on the Fe-12%Cr alloy revealed the presence of large Cr-enriched clusters (dark rounded particles highlighted by red arrows) mainly along grain boundaries.

III.2. 3DAP

As in the two previous cases, the randomness of the spatial distribution of atoms in the Fe-12%Cr model alloy was checked by atom probe. As reported in the previous part, 3DAP results show that the Cr concentration measured inside grains is lower than the expected nominal concentration given by chemical analysis (12.3at%[1]). Cumulating experiments in the Fe-12%Cr model alloy, the chemical variation for Cr concentration was in the range 9.9at.% to 11.4 at.% from one sample to another with a mean Cr content of about (11.20 ± 0.15)at.% (Table 3.5). This is in very good agreement with the TEM-EDS measurements (Figure 3.15).

Table 3.5. Mean chemical composition of the Fe-12%Cr model alloy (at%) measured with 3DAP

Fe	balance
Cr	11.20 ± 0.15
Si	0.18 ± 0.01
P	0.025 ± 0.002
Ni	0.07 ± 0.01
Mn, V, C. N, O, S, Al, Ti	*not measurable*

Both 3D elemental map of chromium (Figure 3.17) and statistical test (Figure 3.18) show that Cr atoms are homogeneously distributed inside the analysed volume.

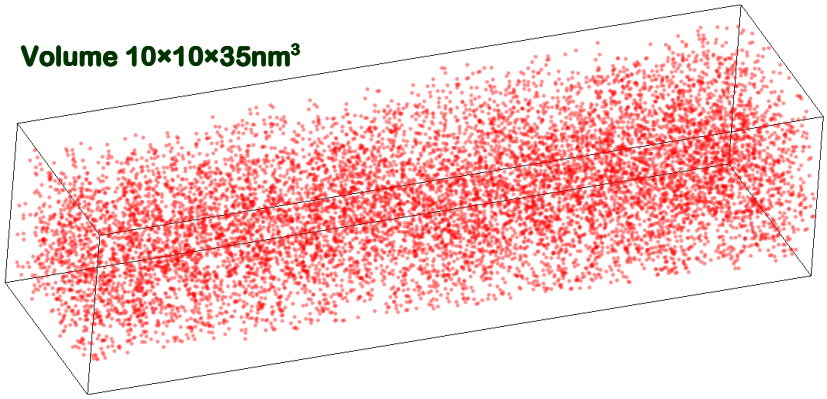

Figure 3.17. 3D distribution of chromium atoms in the as-received Fe-12Cr% model alloy. Each dot represents one atom. For clarity only chromium atoms are represented. Chromium atoms are homogeneously distributed before aging.

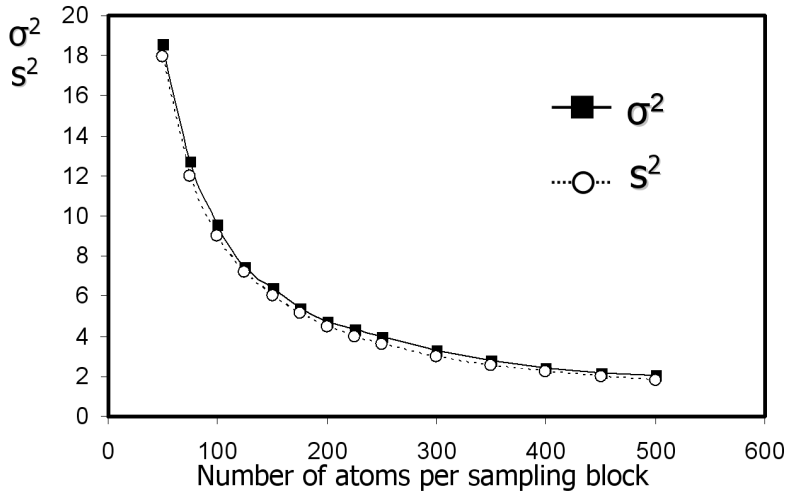

Figure 3.18. Comparison of the standard error (s) with the standard deviation (σ) in the as-received Fe-12%Cr model alloy. Experimental distribution almost coincides with the binomial one. Chromium atoms are homogeneously distributed.

III.3. PAS

Slow-Positron-Beam Doppler-broadening experiments on the Fe-12%Cr model alloy revealed that annihilation characteristics of the alloy (S(E) and W(E) curves) are similar to the one obtained on the Fe-5%Cr and Fe-9%Cr alloys as well as to the annealed pure Fe reference results (Figure 3.19). The best fit was obtained using two layers. The first layer (oxidized or damaged layer) is around 50 nm thick. The estimated effective diffusion length L^+ of the bulk is equal to 113 nm. It indicates that as in the case of Fe-5%Cr and Fe-9%Cr some vacancy type defects are present in this sample. However, the concentration of these defects is low.

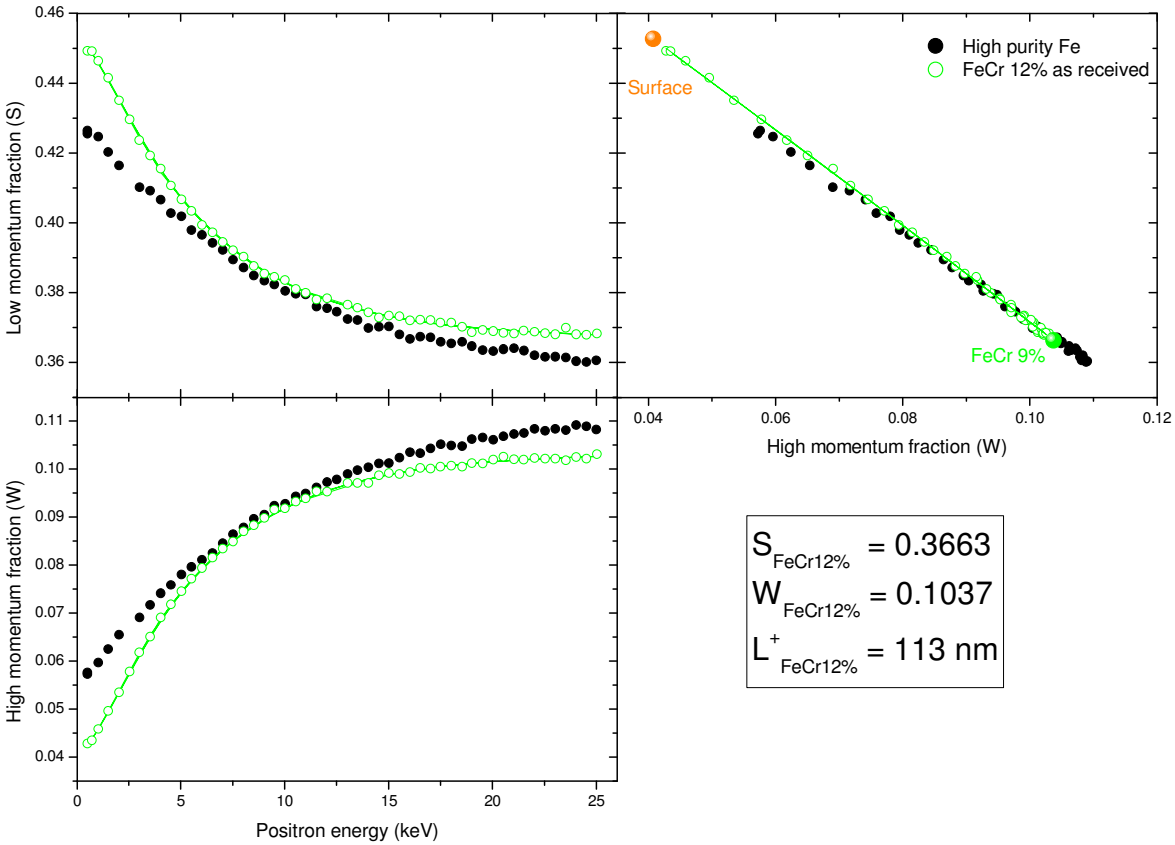

Figure 3.19. Low (S) and high (W) momentum fraction versus positron energy for the un-irradiated Fe-12%Cr model alloy in comparison with the annealed pure Fe.

IV. Discussion

There are some disagreements between the microstructural components identified by VLM in the as-received model alloys in the current work, in the work of Heintze et al. [5] and in the work of Matijasevic et al. [1,2], as presented in Table 3.6

Table 3.6. Microstructure of the Fe-Cr model alloys.

Source :	Microstructure		
	Fe-5%Cr	Fe-9%Cr	Fe-12%Cr
Matijasevic and Almazouzi [1,2]	Ferrite	Bainite	Bainite
Heintze et al. [5]	Ferrite + martensite	Martensite	Martensite
Current work	Ferrite + martensite (or bainite)	Martensite (or bainite)	Martensite (or bainite)

The first obvious difference is that in the Fe-5%Cr model alloy, whereas a dual structure has been found in the current work and in the work of Heintze et al. [5], a single ferrite-phase structure has been reported by Matijasevic and Almazouzi [1,2]. Two possible explanations of such disagreement can be proposed:

i) The microstructure of the Fe-5%Cr model alloy is not uniform. The non-uniform microstructure could originate from a non-uniform heat treatment (temperature, cooling rate etc.) or from non-homogeneity of the chemical element distribution at the scale which is larger that the one investigated by 3DAP and SEM-EDS. For example, different Fe-Cr based steels with chromium content less than 5% can have a final structure which consists of bainite, of ferrite or of the mix of these to constituent [9]. Nevertheless, it is worth noting that in the current work, the metallographic observations have been performed on samples from different parts of the bar (2 samples have been analysed) and they have shown the same ferric+martensitic(bainitic) microstructure. Thus, it is believed that Fe-5%Cr model alloy which is available in the GPM laboratory (University of Rouen), has the ferritic + martensitic(bainitic) structure.

ii) The martensitic(bainitic) lath boundaries were not revealed during the chemical etching in works [1,2]. Indeed, if the metallographic preparation procedure, specifically, the etching procedure, is not well adapted to reveal the lath boundaries, the packet martensite structure can resemble to the ferritic one. In the current work a solution of 925 ml of ethanol with 25 g of picric acid and 50 ml of hydrochloric acid has been used (see Appendix 1). Such etcher is recommended for martensitic stainless steels [10].

Another disagreement applies to the result obtained in the Fe-9%Cr and Fe-12%Cr model alloys. The martensitic structure was detected in the Fe-9%Cr and Fe-12%Cr model

alloys by Heintze et al. [5] while a bainitic microstructure is reported in works of Matijasevic and Almazouzi [1,2]. However, it should be mentioned that the packet-lath microstructure of the Fe-9%Cr and Fe-12%Cr model alloys which is presented in the micrographs in all investigations [1,2] is similar to the one presented in the work [5] and to the one obtained in the present work as well. The morphological distinctions between lath martensite and upper bainite is difficult in the case of almost free of carbon (from 0.02 to 0.03wt%) Fe-Cr alloys (especially by VLM facilities). Since, any specific research for definition of the exact nature of the microstructure in this model alloys has not been reported, it is believed that the difference between microstructure reported in works [1,2,5] could arise in the different terminology used.

As it was mentioned in the introduction, the microstructure of the model alloys is decisive for radiation induced changes, since it determines the creation of features and further redistribution of point defects. Ferrite (and bainite, if it exists) microstructure are characterised by b.c.c. lattices. The martensitic structure in carbon steels has a body-centred tetragonal (b.c.t.) lattice. However, it is believed that no tetragonallity exists in present model alloy, the nominal carbon level in the studied model alloys being very low (less than 0.03wt%). Second, the quenching which produces martensite has been followed by 4 hours of tempering at 730ºC. This should lead to the redistribution of the carbon (carbide formation, atmosphere formation on dislocations etc…). No carbon was detected during 3DAP investigation of model alloys. This gives the basis to assume that the final structure of all model alloys has a typical b.c.c. structure without any tetragonality but with differences in morphology of the grains. Thus, for the irradiation conditions calculations and for the TEM image treatments, the following parameters of crystal has been used:

Lattice constant: bcc (a = b = c = 0.2866 nm)

Space-group: Im3m (#229)

The non-homogeneity of the dislocation distribution as well as the broad distribution of grain size have been revealed by TEM in Fe-9%Cr and Fe-12%Cr. Since, dislocations and grain boundaries are strong point defect sinks, the inhomogeneity in their distribution can lead to a non-uniform response of the material to the irradiation exposure. This is not essential for PAS, since the signal is averaged on a large number of grains during experiments but it can be essential for TEM and 3DAP techniques. So, in order to investigate the Cr and the dose effect on the evolution of the dislocation structure during irradiation, large grains free of dislocations (for example the grain in the micrograph of Figure 3.9(*a*)) have been chosen for characterisation and quantification of dislocation loops formed during the in-situ irradiation TEM experiments (see Chapter V). Concerning the 3DAP samples, during standard electrochemical polishing of 3DAP tips, it is impossible to choose, which grain will be

investigated during atom probe experiment (with low or with high dislocation density). So, a large number of experiments is desirable (the FIB was not used in this case).

PAS results obtained on the three model alloys with different Cr content in the as-received state shows that samples have good quality but they are not homogenous after surface preparation (polishing and electropolishing). At least two layers are necessary to fit the positron data. The nature of the first thin (up to 50 nm) near surface layer is currently unknown.

This layer can originate from the damage introduced during the mechanical cutting procedure or mechanical polishing. Indeed, M. Lambrecht [6,11] has studied the same model alloys with conventional PAS (Lifetime and Doppler broadening) using fast positron sources. In her study, the energies of fast positrons are not controlled and positron signals are integrated from the surface to 100µm depth. Also, the sample preparation was different: samples were cut with Electron Discharging Machine (EDM) and no chemical etching was performed after cutting. It was reported that the lifetime data correspond to defects with an average size of about 5 vacancies. It was suggested that such defects originated from the cutting procedure introduced by EDM cutting [11]. Note that after irradiation, these defects disappear because a chemical solution was used to remove the surface oxide layer (15 ml HF, 250 ml H_2O_2 and 30 ml H_2O. However, it is believed that within the current work, defects which originate from cutting procedure should have been eliminated during the procedure we specially developed for PAS specimen preparation. At the final stage an electrochemical polishing has been applied to decrease the thickness of the specimens over at least 10µm (see Appendix 3).

This layer can originate from the sample surface oxidation. The fact that the samples weren't kept under vacuum during their transportation is in favour of this suggestion. We should mention that the oxidized layers up to several tens nanometers have been also observed by 3DAP on the tips after their irradiation and transportation within the low-energy ion irradiation experiments (see Figure 5.15). So, we believe that layer observed by PAS is more likely an oxidized layer.

The second layers of all the three model alloys with different Cr content correspond to the bulk state. Figure 3.20 shows the evolution of S(W) points which are characteristic of each second layer in comparison with the characteristic points of pure iron, chromium and silicon. It can be observed that the S(W) points are almost aligned on a segment formed by the points of iron and silicon. Since the Doppler broadening spectroscopy is sensitive to the electronic distribution and thus the chemical environment, one would think that the impurities of silicon can play an important role in these measures. While there is no theoretical calculation of S and W values available in the literature for these samples, a simple calculation can be done considering the atomic fractions measured by 3DAP of each major element/impurities (Fe, Cr and Si) and their S and W characteristic values (empty circles in Figure 3.20). It should be noted that the latter calculations are not physically correct but they

could gives us an idea of the influence of the major elements in our measurement. Thus, by this estimation it can be seen from Figure 3.20 that the effect of chemical environment, if it exist, should remain low.

So, the best explanation for this behavior is the presence of vacancy type defects in these layers. All the characteristic points of all Fe-Cr samples have a higher S and a lower W than the calculated ones and the effective diffusion lengths of the positron are respectively 129,132 and 110 nm for the 5, 9 and 12% Cr. These values are low compared to the value found in pure iron (184nm) and are a good indication of the presence of defects. Nevertheless, these concentrations of defects are low and will be negligible compared to the concentration of defect introduced by ion implantation.

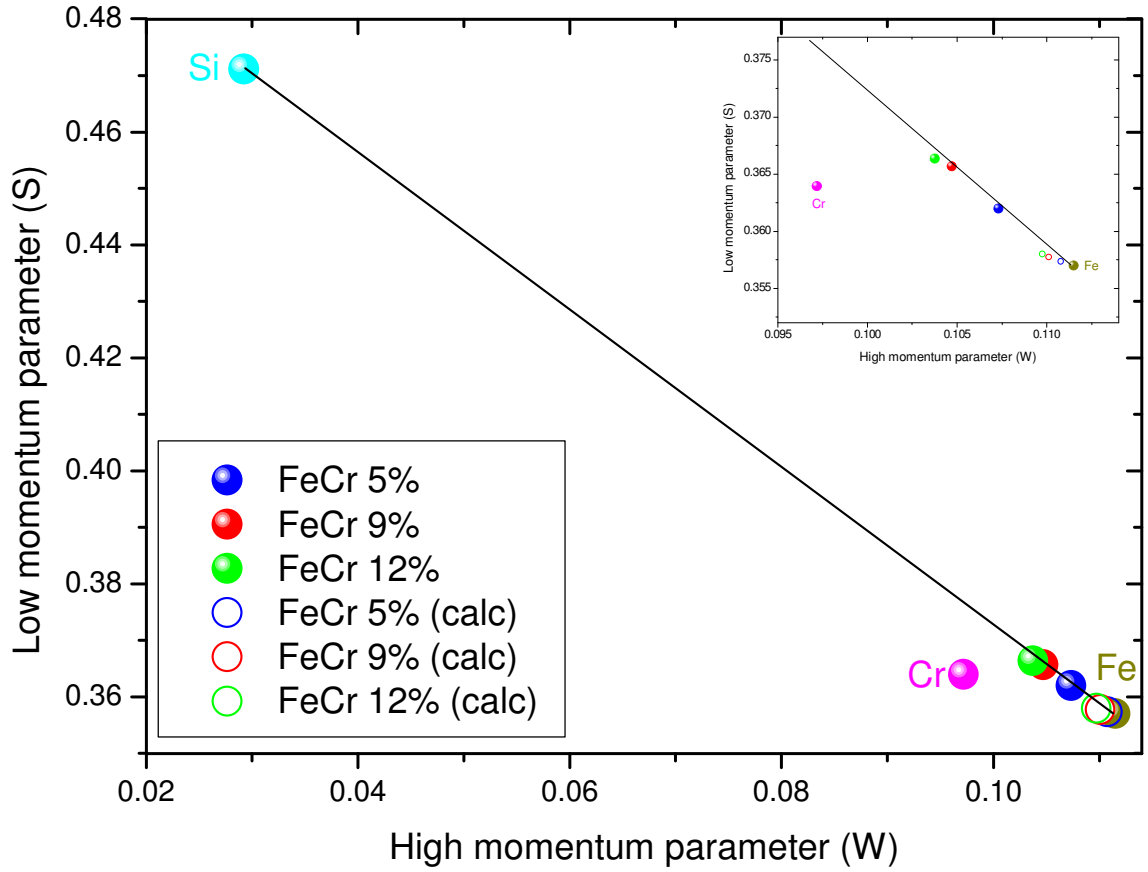

Figure 3.20. Evolution low momentum fraction (S) as a function of the high momentum fraction (W) for the second (bulk) layer in the un-irradiated Fe-5, 9 and 12%Cr model alloy. S(W) characteristic points of pure iron, chromium and silicon are also plotted. Empty circles represent the calculated S and W characteristic values for each model alloy considering their chemical compositions

V. Conclusions

The metallographic observations revealed that the investigated model alloys have the following microstructure:

- Fe-5%Cr model alloy: ferrite + martensite(bainite);
- Fe-9%Cr and Fe-12%Cr model alloys: martensite(bainite).

SEM-EDS and 3DAP measurements revealed the homogenous distribution of the chemical species at the microscopic and nanometric scale in the Fe-5%Cr and the Fe-9%Cr model alloys. TEM-EDS and 3DAP measurements revealed the non-homogeneity of chromium distribution in the Fe-12%Cr alloy with a variation of Cr content in the range 9.9 – 13.2at.% with the mean value equal to (11.7± 1.2)at%

Irradiation experiments are realizable in these model alloys but the broad distribution of grain-size and the non-homogeneity of dislocation distribution revealed in the Fe-9%Cr and Fe-12%Cr model alloys, as well as the non-homogeneity of Cr distribution in the Fe-12%Cr alloy must be kept in mind as they may involve different response of the material in term of dislocation loop distribution, segregation or precipitation.

Doppler Broadening measurements using a slow positron beam have revealed the presence of an oxidized layer at the surface of the samples and the presence of vacancy type defects in the bulk. The oxide thicknesses are small and the defect concentrations of are low. As the high energy ion implantations will introduce defects on a wide depth, the effect of those oxide layers and of those native defects should be negligible.

VI. References

[1] M. Matijasevic, A. Almazouzi, Journal of Nuclear Materials 377 (2008) 147-154.
[2] Matijasevic M., Microstructure and Mechanical Properties of Fe-Cr Model Alloys and High Cr Steels Under Neutron Irradiation, PhD thesis, Gent University, 2007.
[3] F. Bergner, A. Ulbricht, C. Heintze, Scripta Materialia 61 (2009) 1060-1063.
[4] C. Heintze, A. Ulbricht, F. Bergner, H. Eckerlebe, J. Phys.: Conf. Ser. 247 (2010) 012035.
[5] C. Heintze, F. Bergner, A. Ulbricht, H. Eckerlebe, Journal of Nuclear Materials 409 (2011) 106-111.
[6] M.Lambrecht, Experimental Quantification of the Effect of Neutron Irradiation Induced Microstructural Changes on the Hardening of Model Alloys and Steels, PhD thesis, Ghent, Belgium: University of Ghent, 2009.
[7] H.K.D.H. Bhadeshia, R.W.K. Honeycombe, Steels: Microstructure and Properties, Butterworth-Heinemann, New York, 2006.
[8] F.B. Pickering, Physical Metallurgy and the Design of Steels, Applied Science Publishers, London, 1978.
[9] R.L. Klueh, A.T. Nelson, Journal of Nuclear Materials 371 (2007) 37-52.
[10] Metallographic Preparation of Stainless Steel. Struers Application Notes, http://www.struers.com/resources/elements/12/101820/Application%20Notes%20Stainless%20Steel%20English.pdf, 2011.
[11] M. Lambrecht, L. Malerba, Acta Materialia 59 (2011) 6547-6555.

CHAPTER 4.
NEUTRON IRRADIATION EXPERIMENTS

As it was shown in the Chapter 1, during the last years, F-M steels and in particular its representative binary Fe–Cr model alloy, are at the centre of a large amount of basic researches, including specific experimental investigations such as studies of the influence of the Cr content, the irradiation dose and temperature (see for example [1–9] and references cited). Since microstructure evolution under irradiation of these alloys is not yet completely understood, subnanometric-scale studies of microstructural evolution under irradiation of Fe-Cr based alloys are of large interest especially in the case of neutron irradiated materials. It is the reason why 3DAP investigations of the intragranular structure of three Fe-Cr model alloys (namely Fe-5%Cr, Fe-9%Cr and Fe-12%Cr) neutron irradiated at 300°C to 0.6 dpa have been undertaken. Current model alloys after neutron irradiation have been already investigated by different techniques by other laboratories-participants of the GETMAT project: TEM [2,10], SANS [4,5,11]. Thus, the microstructural changes under neutron irradiation observed by 3DAP are presented and discussed in the first part of the current chapter and compared with the data collected by other techniques.

It is known that radiation assisted segregations on grain boundaries and dislocation loops are of large importance in the process of changes of mechanical and corrosion properties of steels under irradiation. At the same time, as it was shown in the first chapter, the segregation mechanism under irradiation in F-M steels as well as in Fe-Cr model alloys is still not fully understood. The second section of this chapter will provide atomic-scale information on the segregations observed on linear and planar defects in the neutron irradiated Fe-Cr model alloys. The obtained data are analyzed and compared with data of other authors.

The chapter ends by a conclusion of the former sections.

TABLE OF CONTENT

I. Intragranular microstructure of the irradiated Fe-Cr model alloys

I.1. Fe-5%Cr model alloy

3DAP experiments reveal that in the initially random Fe-5%Cr model alloy (see Chapter 3) clusters enriched in Ni, Si, P and Cr are formed during neutron irradiation at 300°C (Figure 4.1). As shown in this image, the clusters are not homogeneously distributed. To detect these clusters, for visualization and further analysis, the "Cluster identification" algorithm has been used (see Chapter 2 for details), with the threshold parameter $C_{(Ni+Si+P)} > 3at\%$.

The mean chemical composition of the model alloy analysed after irradiation is given in Table 4.1. About (4.60± 0.02)at% of Cr has been detected. The mean core composition of the NiSiPCr–enriched clusters was quantified by measurements made owing to boxes placed well inside the observed clusters (so-called in-core measurements). The size of these boxes has been adjusted to the geometry of each particle. The results of core composition measurements as well as of enrichment factors of the solutes in the clusters with respect to the matrix concentration (see below in Table 4.3) are given in Table 4.2. These measurements show that in terms of absolute amount of excess solute, Cr is the most segregated element. However, the increase of Si, Ni and especially P inside the clusters relative to the matrix is more significant.

Table 4.1. Average chemical composition (at.%) of the neutron irradiated Fe-5%Cr model alloy (0.6dpa, 300ºC) measured with ECoWATAP

Fe	Balance
Cr	4.60± 0.02
Si	0.059 ± 0.002
P	0.013±0.001
Ni	0.034± 0.002
V, C, N, O, S, Al, Mn, Ti	not measurable

Table 4.2. Average chemical composition (at.%) of NiSiPCr-enriched clusters in the neutron irradiated Fe-5%Cr (0.6dpa, 300ºC) measured with ECoWATAP (average data from 16 clusters)

Element	Concentration, at%	Enrichment factor ($C_{cluster}/C_{matrix}$)
Fe	Balance	
Cr	10.4±0.9	2.27
Si	6.4±0.7	193.9
Ni	1.7±0.4	94.4
P	2.1±0.4	525
C, N, O, S, Al, Ti, Mn, V	not measurable	

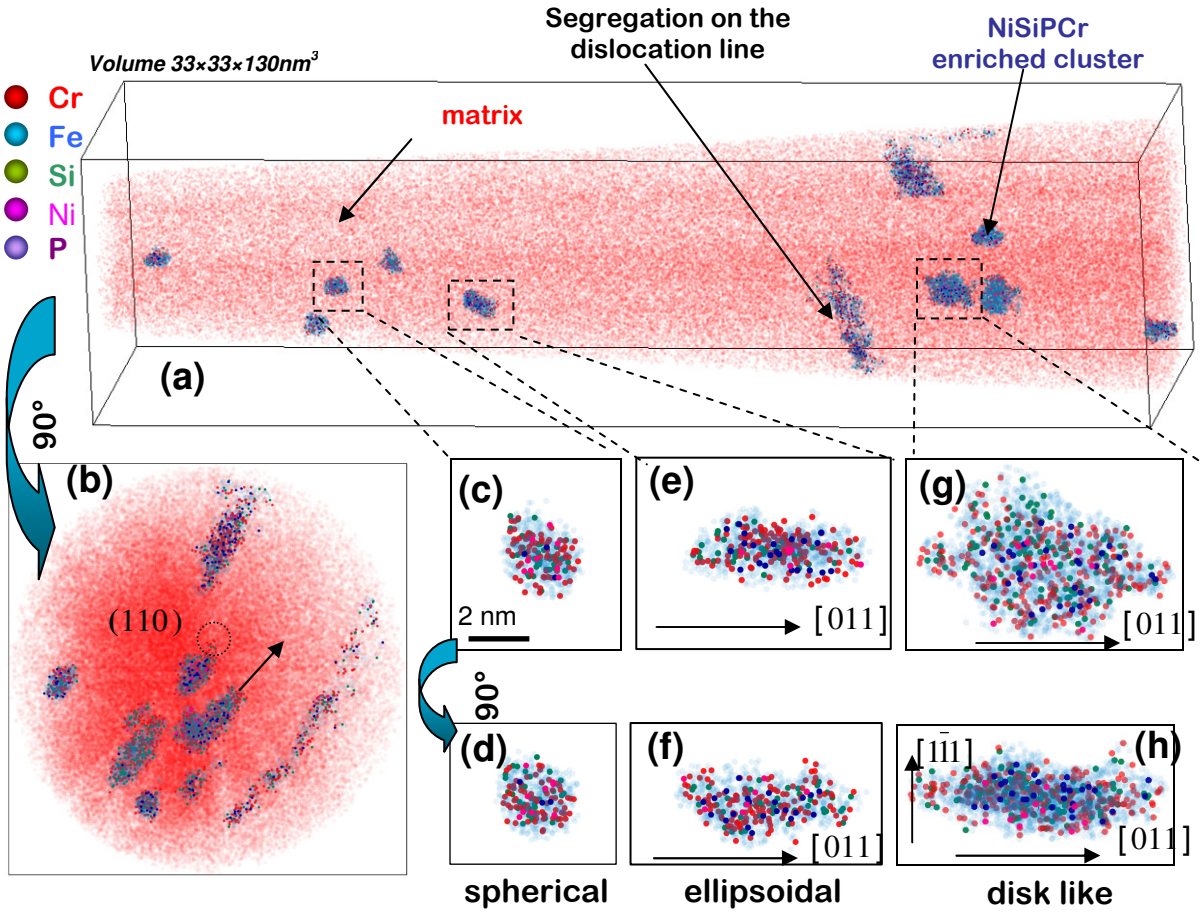

Figure 4.1. (a) 3D reconstruction of an analyzed volume of the Fe-5%Cr alloy after neutron irradiation at 300°C up to 0.6 dpa. For clarity only Cr atoms are presented for the 3D map of the matrix. (b) The "top view" (the tip axis is normal to the figure) of the same analyzed volume. Multicolor areas represent the NiSiPCr-enriched clusters. A threshold of $C_{(Ni+Si+P)} > 3at\%$ *is used to reveal the clusters. The clusters are not homogeneously distributed and have non-regular shape: spherical, ellipsoidal and disk like, as presented on (c)–(h). The crystallographic orientation of these objects has been determined: habit plane of disk like clusters is about* $(1\bar{1}1)$*; two main orientation of elongation of the ellipsoidal clusters have been detected: along ~*$[011]$ *direction (the majority) and along the direction between* $[011]$ *and* $[\bar{1}12]$ (close to $[\bar{1}45]$). *A segregation on a dislocation line elongated in a direction between* $[011]$ *and* $[\bar{1}12]$ *is also revealed. The latter is discussed in part II.1 of the current chapter (p.145)*

The clusters have non-regular shape. Some of them are almost spherical whereas others have ellipsoidal and disk like shapes. The examples of such precipitates are shown in Figure 4.1. The longest axes of the ellipsoidal particles are usually equipollent and lie in a plane parallel to the habit plane of disk like clusters, as it is evident from the so-called "top view" image (tip axis is normal to the figure) presented on the Figure 4.1(b) and Figure 4.2. Indeed, on these figures, almost all particles look like elongated parallel objects.

To estimate the size of the NiSiPCr-enriched clusters whatever their shape, an equivalent radius has been calculated for each particle. It have been deduced from the number

of atoms (n) which constitute the particle ($R = \sqrt[3]{\frac{3nV_{at}}{4\pi Q}}$, where Q is the efficiency of the atom probe detector, and $V_{at}=a^3/2$ is the atomic volume with the lattice parameter $a=0.2866nm$). An average radius equal to (2.0 ± 0.2) nm has been found.

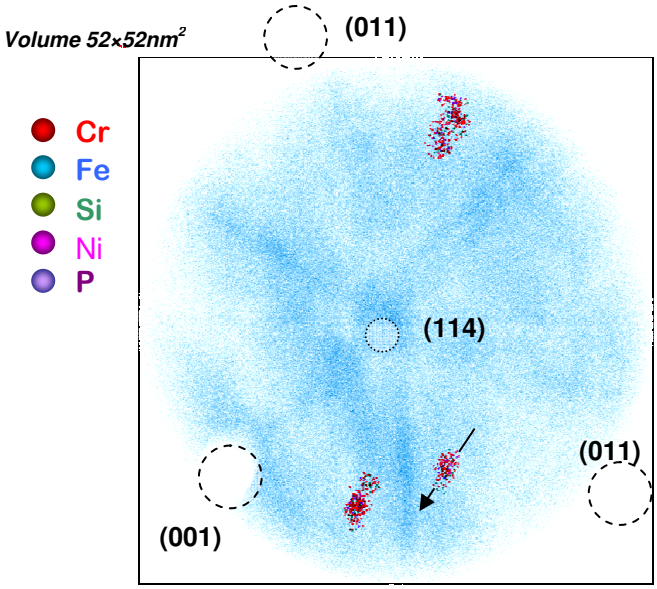

Figure 4.2. "Top view" of an analyzed volume of the Fe-5%Cr alloy after neutron irradiation at 300°C up to 0.6 dpa (the tip axis is normal to the figure) with indexed crystallographic poles. Only 10% of Fe atoms are represented on the 3D map of the matrix. Multicolor areas represent the NiSiPCr-enriched clusters. A threshold of $C_{(Ni+Si+P)} > 3at\%$. is used to reveal the clusters. The clusters have an ellipsoidal shape.

The number density of particles is determined by the ratio of the number of observed particles on the overall analyzed volume. In order to calculate the number of particles, the following conventions were used: a precipitate fully inside the volume contributes for one whereas particles located on the surfaces contribute for 0.5. A value of $(1.3 \pm 0.2)\times10^{23}$ m^{-3} is obtained. Note that the relatively large uncertainty on chemical composition of the clusters (see Table 4.2) comes from the low number density of these clusters.

Composition of the matrix is given in Table 4.3. It is derived from the total number of atoms of the analyzed volume minus the total number of atoms contained in the NiSiPCr-enriched clusters as well as atoms in their vicinity. As it is expected, the composition of the matrix doesn't differ significantly from the nominal one since the phase separation has led to the appearance of a relatively small quantity of NiSiPCr-enriched clusters with a quite low size. A Cr content of the matrix equal to (4.58±0.02)at% of Cr has been found.

Table 4.3. Chemical composition (at.%) of the matrix in the neutron irradiated Fe-5%Cr model alloy (0.6dpa, 300ºC) measured with ECWATAP.

Fe	Balance
Cr	4.58±0.02
Si	0.033±0.002
P	0.004± 0.001
Ni	0.018±0.001
C, N, O, S, Al, Mn, Ti	not measurable

In the following we are going to investigate in more details the geometry of the NiSiPCr-enriched clusters. As it has been mentioned above, the ellipsoidal particles are usually elongated along a common direction and lie in a plane parallel to the habit plane of the disk like clusters. In general, the direction of elongation of the clusters is not normal to the direction of 3DAP analysis, as it is well appreciable on the 3D map in Figure 4.1(a). Elongation of the clusters can be due to several reasons:

i) The shape of the clusters can be modified due to 3DAP artifacts. Indeed, it is known that the field evaporation process, which is the basic process of the 3DAP technique, can induce some artifacts such as the local magnification [12–14] and chromatic aberration [12,15] effects. The origins and consequences of the local magnification effect are described in section III.2(c) of the Chapter 2. It leads to modifications of the ion trajectories and, consequently, to extension or compression of the precipitate in the plane normal to the analysis direction and to changes in the local atom density inside the precipitates as well. A typical example of this effect is shown in Figure 4.3 where Cr, Si and P concentration profiles and the corresponding relative atom density profiles are drawn trough a NiSiPCr-enriched cluster are presented. Profiles have been drawn along the longest axis of the clusters, marked by the black arrow in Figure 4.2. It is shown that the local density of atoms inside the elongated NiSiPCr-enriched cluster is about 2 times larger than the one of the matrix. It indicates that a local magnification effect exists. Nevertheless, such slight difference in the density of atoms can't explain the observed distortion of the shape. For example, the same effect has been observed and studied during 3DAP investigations of the Fe-20%Cr thermally aged at 500°C [6,16]. This alloy exhibits phase separation (Cr-enriched α' phase formation) at this temperature. It has been shown that after 50h of thermal ageing, small α' precipitates (with mean composition of about 61at% of Cr) appear. The atomic density of these objects was from 1.5 to 3 times higher that the one inside the Fe-rich α-matrix, and the shape of these α' precipitates remained quasi-spherical on 3D images [6,16]. Based on these findings, it is possible to suggest that the contribution of the local magnification effect to the distortion of the shape of the observed NiSiPCr-enriched precipitates, if it exists, should be weak.

The chromatic aberration [12,15] is another effect that can also contribute to the distortion of the shape of the observed clusters. This effect, which is a complex artifact arising from the nonhemispheric shape of the tip, the electrostatic field at the emitter surface and the diffusion of atoms on the tip's surface, leads to the redistribution of the atoms towards the major

crystallographic poles of the specimen. For example, this effect has been investigated by Marquis and Vurpillot [15] in the case of Ag rich precipitates in Al-Ag alloy. Authors showed that, as presented in Figure 4.4, the Ag atoms originating from a precipitate are displaced in the plane normal to the tip axis towards certain crystallographic poles, as compared to the Al atoms from the same precipitate. So, this phenomenon alters the relative positioning of atoms originating from the same phase.

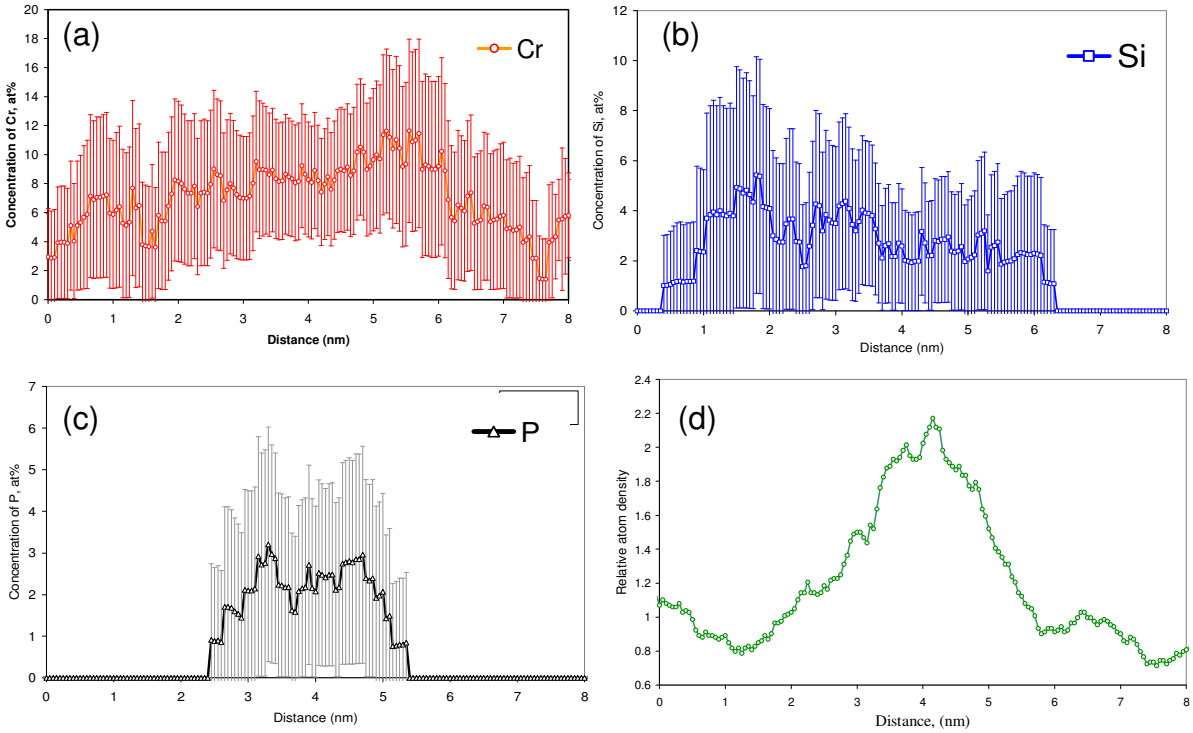

Figure 4.3. Concentration profiles drawn trough a NiSiPCr-enriched cluster in the Fe-5%Cr model alloy. Profiles have been drawn along the long axis direction of the cluster marked by a black arrow in Figure 4.2. Profiles show a rise of the relative atom density inside the cluster (d). Sampling size: 1.5×1.5×1nm^3

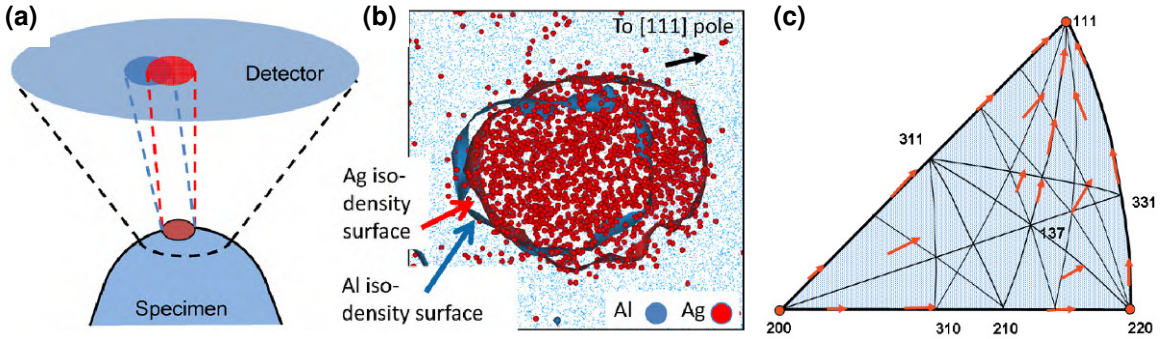

Figure 4.4. Schematic view of 'chromatic' aberrations in the case of small precipitates (b) Case of Ag-rich precipitates in a Al–Ag alloy. The Ag atoms are displaced towards the {111} pole; (c) Pole figure illustrating the direction of the Ag atom movement (from [15,17])

The chromatic aberrations are strictly related to the evaporation field difference between elemental species [15]. This means that in the case of nanometric scale objects composed of different atoms (in term of evaporation field) atoms (as in the case of NiSiPCr-enriched clusters) a different shift of the different chemical species can be expected to affect the observed shape of these precipitates. As it was suggested in [15], in a bcc crystal such as the Fe-Cr based alloys, it is expected that this phenomena leads to the shift of the chemical species in relation to each other toward the low index {110} poles. Thus, owing to chromatic aberrations, NiSiPCr-enriched clusters are expected to be centripetally elongated in the plane normal to the tip axis towards the closest {110} pole. However, as it is evident from the presented results (Figure 4.1, Figure 4.2 and Figure 4.5), the majority of the clusters are elongated in a parallel way at different angles to the normal to the tip axis plane without clear relation with the closest {110} pole. This means that the observed elongation is not due to the chromatic aberrations.

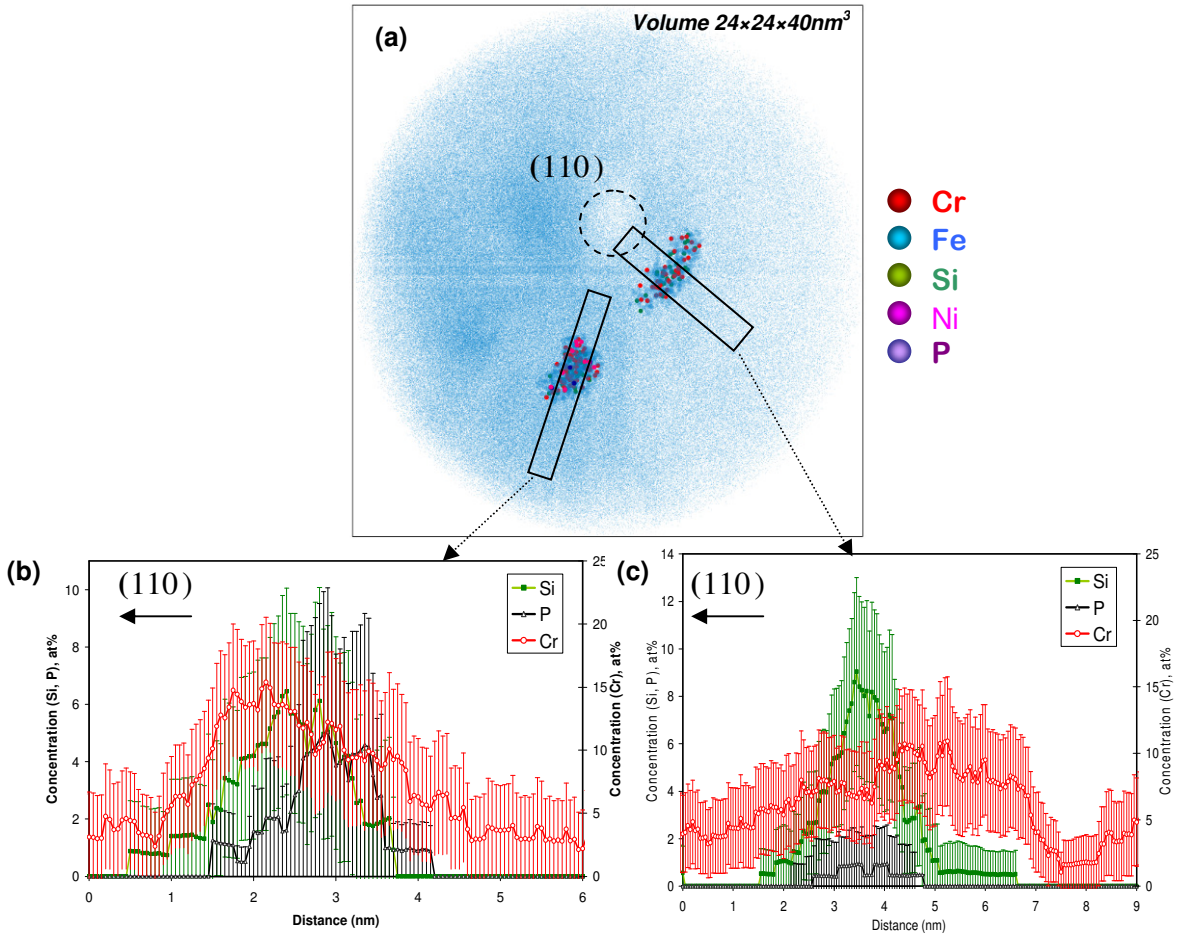

Figure 4.5. (a) The "top view" (the tip axis is normal to the figure) of the 3D reconstruction of an analyzed volume of the Fe-5%Cr alloy after neutron irradiation at 300°C up to 0.6 dpa. Only 10% of Fe atoms are presented on the 3D map of the matrix; (b) and (c) concentration profiles drawn trough NiSiPCr-enriched clusters. The profiles have been drawn towards the (110) pole. The profiles show a non-systematic shift of the chemical species with respect to the (110) pole. Sampling size: (a) 1.5×1.5×1nm^3, (b) 1.6×1.6×1nm^3

It is worth noting that some slight shift of the chemical species inside clusters toward the (110) pole exists as it demonstrated in Figure 4.5. This could be a consequence of the chromatic aberrations. Nevertheless, as it is shown by composition profiles drawn through two different NiSiPCr-enriched clusters, the behavior of the shift is not systematic: in the first cluster (Figure 4.5(b)) the peak of Cr concentration is located closer to the (110) pole with respect to the one of Si and, especially, to the one of P, while in the second cluster (Figure 4.5(c)), Si and P peaks, which almost coincide, are slightly closer to the (110) pole in comparison with the Cr one. It indicates that further systematic work taking into account the crystallographic orientation of the 3DAP samples, the position of each cluster with respect to the crystallographic poles and orientation of the concentration profile with respect to 3DAP sample axis is needed to conclude on this point.

All aforementioned information mean that the hypothesis that the elongated shape of NiSiPCr-clusters is an artifact of the 3DAP is currently not proven.

Moreover, another point needs further work: as revealed by the profiles of Figure 4.5, the different clusters can exhibit different enrichments. For understanding of this behavior, further work with checking of the possible links between the enrichment factors of solutes and the size and shape of cluster is necessary.

ii) to explain the shape of the clusters, a second reason can be proposed. The various shapes and elongations of the NiSiPCr-enriched clusters can arise from the association of these objects to point defects clusters that have non-spherical shape, for example – to small dislocation loops, the evaporation of which should give disk like clusters. In order to check this fact, model bcc crystals, the orientation of which is the same as the one of the analyzed 3DAP volumes, have been constructed and the possible orientations of clusters associated to the typical dislocation loops observed in Fe-Cr alloys have been studied. Examples of clusters (one atomic layer in thickness) with {111} and {100} habit planes, which correspond to clusters associated to ½<111> and <100> type dislocation loops respectively, are shown in Figure 4.6. The orientation of the bcc crystal of Figure 4.6 corresponds to the one of the analyzed volume shown in Figure 4.1(b) and Figure 4.6 (i, j) (zone axis is about [110]). The only habit plane which could correspond to the orientation of the disk like clusters observed by 3DAP is the $(1\bar{1}1)$ (compare Figure 4.6 (i) and Figure 4.6 (b)). This means that disk like NiSiPCr-enriched clusters could be associated with small prismatic dislocation loops with ½<111>Burgers vector, which are typically observed in Fe-Cr model alloys irradiated at temperatures lower than 500°C. This kind of dislocation loops can have the habit plane {111}.

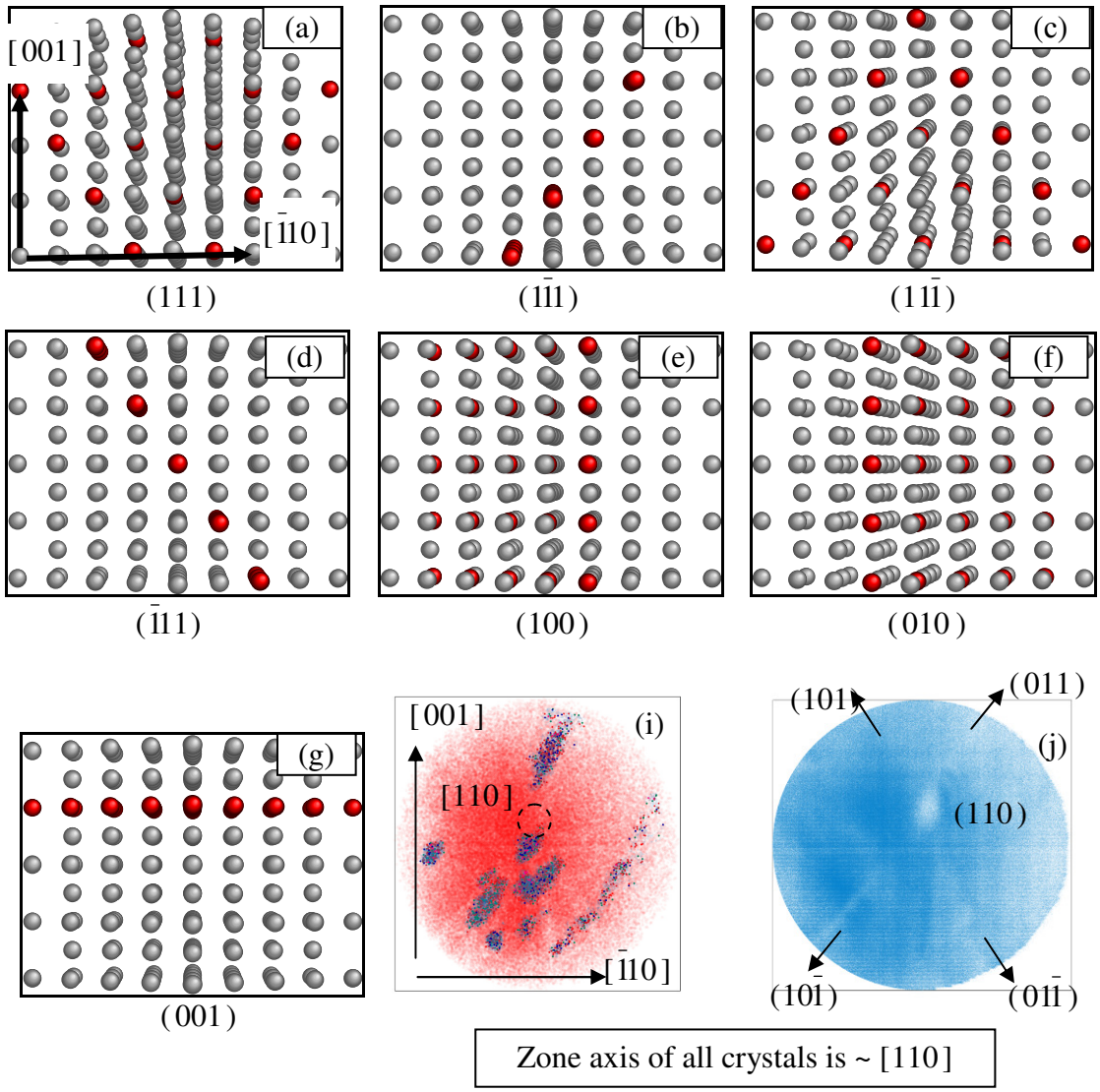

Figure 4.6. (a)-(g) Examples of disk like clusters (one atomic layer in thickness) with {111} and {100} habit planes in the bcc lattice. The habit plane of the cluster is specified under each image. The orientation of all crystals corresponds to the one of the top view image (i and j), also presented in Figure 4.1b. Zone axis is about [110]. Some crystals are slightly inclined for better visualization of the marked plane. The compatibility of the orientations of the precipitate on the image (b) with the observed by 3DAP clusters on (i) is in favor of the fact that these NiSiPCr-enriched clusters can be associated with small prismatic dislocation loops with ½<111>Burgers vector.

We should mention that all disk like NiSiPCr-enriched cluster observed in this volume have the same habit plane (namely, ($1\bar{1}1$)), that is quite surprising, since different variants of habit planes are possible for ½<111> type dislocation loops. However, we must emphasized that a similar tendency has been observed in Fe-Cr model alloys irradiated by low energy Fe^+ ions at 500°C (more details on Burgers vectors of dislocation loops in the ion irradiated Fe-Cr alloys can be found in Chapter 5). Indeed as shown in Figure 4.7, there are some regions of the irradiated thin foil where neighbor dislocation loops often have identical orientation and

Burgers vectors. Even if no specific investigations of habit plane orientations have been performed by TEM, this can indicate that the habit planes of these dislocation loops are identical. So, it appears possible that only one family of segregations associated to such dislocations are observed in a 3DAP volume.

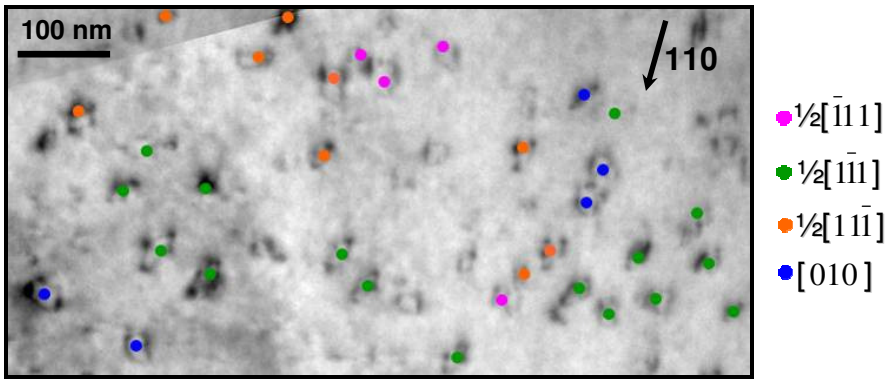

Figure 4.7. Dislocation loops in Fe-12%Cr model alloy irradiated with 150keV Fe^+ ions to a dose of 1.5dpa at 500°C. The micrograph was taken under two beam conditions, zone axis (111), g=1$\bar{1}$0. The dislocations are markets by circle the colour of which depends on the determined Burgers vectors. Some groups of neighbor dislocation loops have identical orientation and Burgers vectors. Details of analysis are given in the Chapter 5.

We should mention that the ($1\bar{1}1$) habit plane is fully consistent with disk like clusters while the ellipsoidal clusters which lies in this plane can also belong to others planes consistent with other dislocation loops. The study of the orientation of the ellipsoidal NiSiPCr-enriched clusters has been performed owing to stereographic projections. It appears that the majority of the ellipsoidal clusters which are presented in Figure 4.1 are elongated along the [011] direction. It means that they could be associated to dislocations loops with habit planes (100), ($1\bar{1}1$), ($11\bar{1}$) and ($01\bar{1}$) and with both Burgers vectors a_0<100> and ½a_0<111>. The second identified system of objects (few NiSiPCr-enriched clusters and dislocation line) are elongated along a direction between [011] and [$\bar{1}$12]. This direction is close to [$\bar{1}$45] that means that it could belong to a dislocation loop with habit plane ($1\bar{1}1$) and b=½a_0<111>. The origin of the elongations in these two directions ([011] and [$\bar{1}$45]) is currently unclear. Possibly this could be linked to the fact that dislocation lines in bcc crystals have slip planes {110}, {112} and {123} [18] that in the case of edge dislocations with b=½a_0<111> correspond to the dislocation line directions <112>, <110> and <145> respectively.

It should be noted, that similar attempts of crystallographic analysis have been undertaken for the volume presented in Figure 4.2. Unfortunately, any clear correspondence between position of NiSiPCr-enriched clusters and habit planes of typical dislocation loops

hasn't been obtained. It indicates that a further systematic work should be made to conclude on the possible link between NiSiPCr-enriched clusters and dislocation loops.

I.2. Fe-9%Cr model alloy

The formation of two distinct families of clusters is observed by 3DAP in the Fe-9%Cr model alloy after neutron irradiation: i) NiSiPCr-enriched clusters, similar to the one observed in the Fe-5%Cr model alloy, and ii) Cr-enriched clusters which correspond to α' clusters. This is clearly revealed in Figure 4.8.

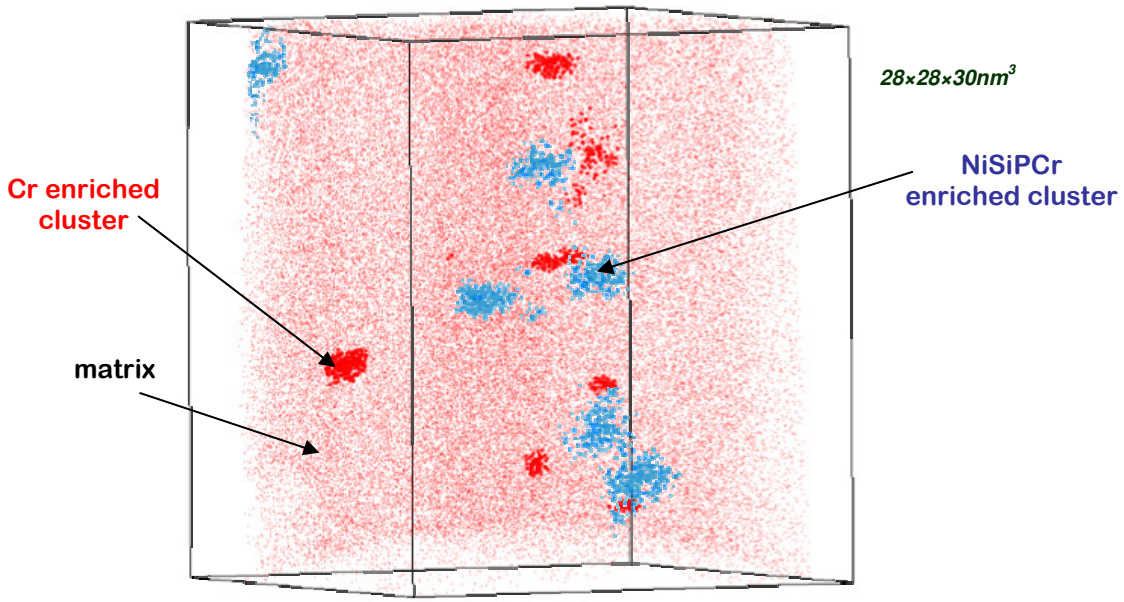

Figure 4.8. 3D reconstruction of an analyzed volume obtained after 3DAP investigation of the Fe-9%Cr alloy after neutron irradiation at 300°C up to 0.6 dpa. Red areas represent the Cr-enriched clusters. The local Cr concentration is higher than 24at.%. Blue areas represent the NiSiPCr-enriched clusters. A threshold of $C_{(Ni+Si+P)} > 3at\%$. is used to reveal the clusters.

The mean chemical composition of the analyzed model alloy after irradiation is given in Table 4.4. It shows good agreement with the data obtained on the as-received model alloy (see Chapter 3).

Table 4.4. Average chemical composition (at.%) of the neutron irradiated Fe-9%Cr model alloy (0.6dpa, 300ºC) measured with ECoWATAP

Fe	Balance
Cr	9.16± 0.03
Si	0.065 ± 0.002
P	0.013±0.001
Ni	0.057± 0.003
C, N, V, O, S, Al, Mn, Ti	not measurable

The concentration threshold $X_{Cr} > 24$at% has been used in order to detect Cr-enriched clusters. This value, which has been chosen after several tests, is well adapted to avoid appearance of artificial Fe-enriched shell around the cluster and to distinguish even small (with a radius of about 0.7nm) Cr-enriched clusters (more details on the procedure of the threshold determination can be found in Chapter 2). The mean core composition of the Cr-enriched clusters is given in Table 4.5. A relatively low chromium content equal to (55.1±3.5)at.% is measured. The Cr-enriched clusters have a spherical shape in main cases, as shown in Figure 4.8.

Table 4.5. Average in-core composition (at.%) of Cr-enriched clusters in the neutron irradiated Fe-9at%C (0.6dpa, 300ºC) model alloy. Measurements are performed with ECoWATAP (data have been averaged from 15 clusters)

Element	Concentration, at%	Enrichment factor ($C_{cluster}/C_{matrix}$)
Fe	Balance	
Cr	55.1± 3.5	6.3
P, Mn, Si, Ni, V, C, N, O, S, Al, Ti	not measurable	

The average radius of the Cr-enriched clusters is equal to (1.1 ± 0.2) nm and their number density value is equal to $(2.1 \pm 0.5)\times10^{23}$ m^{-3}. The volume fraction, which is defined as the ratio of the number of atoms contained inside the particles on the total number of collected atoms, is estimated to 0.14 %.

As in the case of the Fe-5%Cr model alloy, to distinguish NiSiPCr-enriched clusters (the second type of objects created during neutron irradiation in the Fe-9%Cr alloy), a threshold parameter of $C_{(Ni+Si+P)} > 3$at% has been taken. The core composition of the NiSiPCr-enriched clusters and enrichment factors of the chemical species are given in Table 4.6. Similarly to the NiSiPCr-enriched clusters in the Fe-5%Cr model alloy, Cr is the most segregated element in terms of absolute amount of excess solute (about 15.5at% have been measured) but the relative increase of Si, Ni and P is more significant. The enrichment factors of the segregated elements are of the same order of magnitude as the ones calculated for the NiSiPCr-enriched clusters observed in the Fe-5%Cr model alloy.

Table 4.6. Average chemical composition (at.%) of the NiSiPCr-enriched clusters in the neutron irradiated Fe-9%Cr (0.6dpa, 300ºC) measured with ECWATAP (data have been averaged from 20 clusters)

Element	Concentration, at%	Enrichment factor ($C_{cluster}/C_{matrix}$)
Fe	Balance	
Cr	15.5±1.3	1.8
Si	6.6±0.8	165
Ni	1.3±0.4	35.1
P	2.2±0.5	366
C, N, O, S, Al, Ti, Mn, V	not measurable	

A number density of about $(2.4 \pm 0.2)\times10^{23}$ m^{-3} is measured that is almost equal to the value obtained in the Fe-5%Cr model alloy.

As in the Fe-5%Cr alloy, the NiSiPCr-enriched clusters exhibit predominantly an ellipsoidal shape (Figure 4.9). The habit planes of almost all the clusters have the same orientation (this family of clusters is highlighted by the number (2) on the image), while one cluster is elongated in another direction (highlighted by the number (1) on the image).

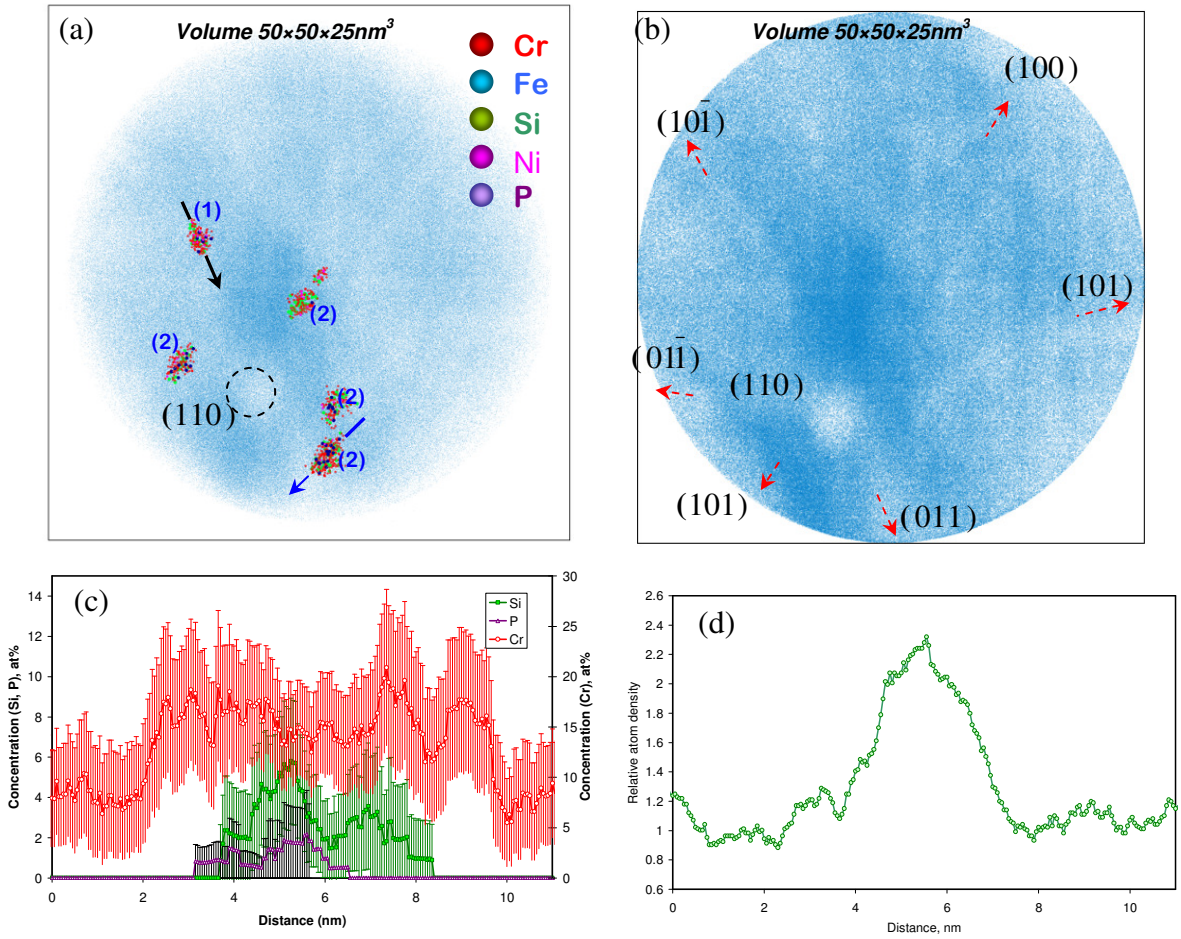

Figure 4.9. (a) The "top view" (the tip axis is normal to the figure) of the 3D reconstruction of an analyzed volume of the Fe-9%Cr alloy after neutron irradiation at 300°C up to 0.6 dpa. (b) the "top view" of the same analyzed volume which shows desorption lines and allows the determination of the directions closest to the low-index poles and further crystallographic analysis. In both images only 10% of Fe atoms are presented in the matrix. Multicolor areas represent the NiSiPCr-enriched clusters. A threshold of $C_{(Ni+Si+P)} > 3at\%$. is used to reveal the clusters. The clusters have an ellipsoidal shape. Cr-enriched clusters are not shown. (c) Concentration profile drawn trough the NiSiPCr-enriched cluster (1) as indicated by the black arrow in Figure 4.9(a). Profile has been drawn towards the (110) pole. (d) Profile which shows the increase of the relative atom density inside the cluster. Sampling size: $1.5\times1.5\times1nm^3$

The cluster (1) is elongated toward the pole (110). The concentration and the corresponding relative atom density profiles drawn through this cluster are presented in Figure

4.9 (c-d). The profiles are drawn along the longest axis of the ellipsoidal cluster and towards the pole (110). As demonstrated by the concentration profiles, even if this particular cluster is elongated toward the (110) pole, the shift of the chemical species, which is expected in the case of chromatic aberration is not obvious. This fact as well as the results shown in the Fe-5%Cr model alloy (see profiles in Figure 4.5), indicate that the behavior of the shift of the chemical species in the NiSiPCr-enriched clusters are not systematic and additional work is necessary to clarify this point.

It is also shown by the profile in Figure 4.9 (d) that the local density of atoms inside the elongated NiSiPCr-enriched cluster is about 2 times higher than the one of the matrix. This is the same value as the one obtained in the Fe-5%Cr model alloy. It indicates that these clusters are prone to local magnification effect [12–14] but its influence on the shape is expected to be minor as discussed above (see p. 118).

As in the case of the Fe-5%Cr model alloy, the hypothesis that the shapes of the NiSiPCr-enriched clusters can arise from the association of these objects to the point defects clusters that have non-spherical shape (such as dislocation loops) has been checked. This study has been performed owing to stereographic projections (Figure 4.10 (a)). It have been obtained that the ellipsoidal clusters highlighted by the number (2) in Figure 4.9 are elongated along the $[1\bar{1}0]$ direction while the cluster highlighted by the number (1) contains the $[1\bar{1}\bar{2}]$ direction.

If we consider that these clusters are associated to dislocation loops, they should belong to the habit plane of these loops. As already noted, it is known that the dislocations loop in Fe-Cr alloys have a limited number of habit plains, namely: {110} and {111} for ½<111>-type loops and {100} for <100>-type loops. Under this hypothesis, the clusters which contain the $[1\bar{1}\bar{2}]$ direction could belong to dislocation loops with $(1\bar{1}1)$ habit plane (the scalar product of $[1\bar{1}\bar{2}]$ on $[1\bar{1}1]$ is equal to zero). The orientation of such clusters is schematically presented in Figure 4.10(b). This orientation is in good agreement with the one observed in the real analyzed volume in Figure 4.9(a) (highlighted by number (1)). However, the clusters which are oriented towards the $[1\bar{1}0]$ direction could belong to the dislocation loops with different habit planes: (111), (001) and (110). It indicates that these clusters could be associated with both ½<111> type dislocation loops ((111) and (110) habit planes) and [011]-type dislocation loops (habit plane (001)).

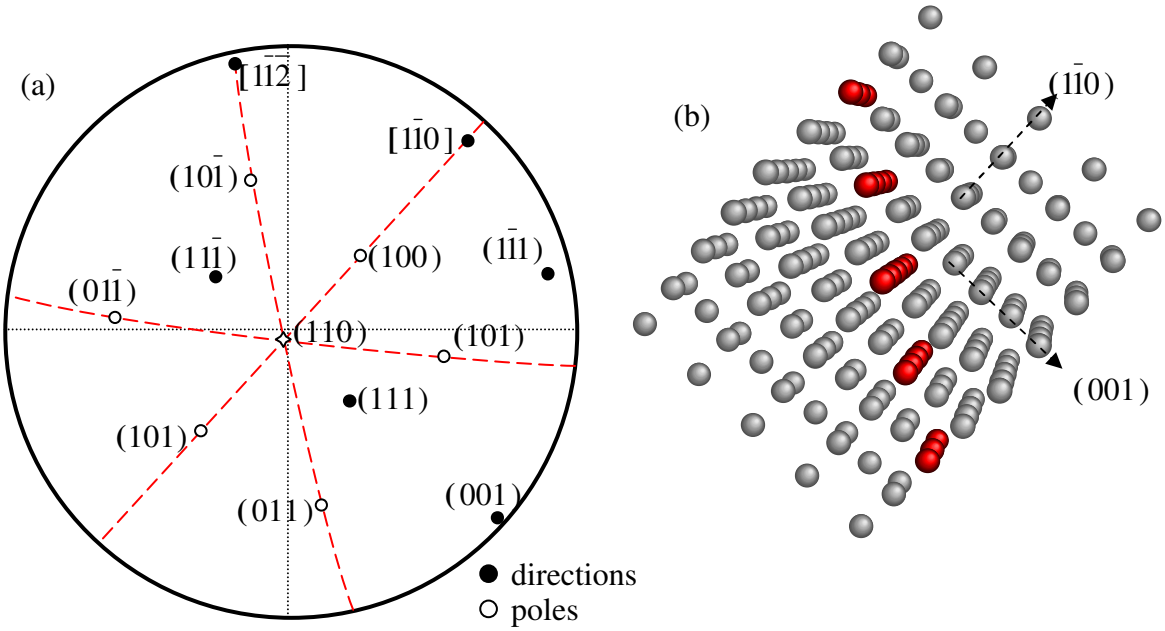

Figure 4.10. (a)– the stereographic projection which corresponds to the orientation of the bcc crystal in Figure 4.9(a); (b)– example of a cluster (one atomic layer in thickness) with $(1\bar{1}1)$ *habit planes in the bcc lattice. The orientation of the bcc crystal corresponds to the one of the "top view" of Figure 4.9(a). The compatibility of the orientation of the cluster on image (b) to the one highlighted by number (1) in Figure 4.9a is in favor of the fact that these NiSiPCr-enriched clusters can be associated with small prismatic dislocation loops with ½<111>Burgers vector.*

As in the case of the Fe-5%Cr model alloy, in order to estimate the size of the NiSiPCr-enriched clusters with different shapes, an equivalent radius has been calculated for each particle. A mean value equal to ~ (1.65±0.2) nm is measured, that is slightly lower than the value obtained for the Fe-5%Cr model alloy.

Composition of the matrix is derived from the total number of atoms of the analyzed volume minus the total number of atoms contained in Cr-enriched and NiSiPCr-enriched clusters as well as in their vicinity. As shown in Table 4.7, the Cr content in the matrix is (8.76 ± 0.02) at%.

Table 4.7. Chemical composition (at.%) of the matrix in the neutron irradiated Fe-9at%C model alloy (0.6dpa, 300°C) measured with ECoWATAP

Fe	Balance
Cr	8.76±0.02
Si	0.040±0.002
P	0.006± 0.001
Ni	0.037±0.001
C, N, V, O, S, Al, Mn, Ti	not measurable

I.3. Fe-12%Cr model alloy

Here also, after neutron irradiation, the formation of two distinct families of clusters is observed: Cr-enriched clusters and NiSiPCr-enriched clusters, as presented in Figure 4.11.

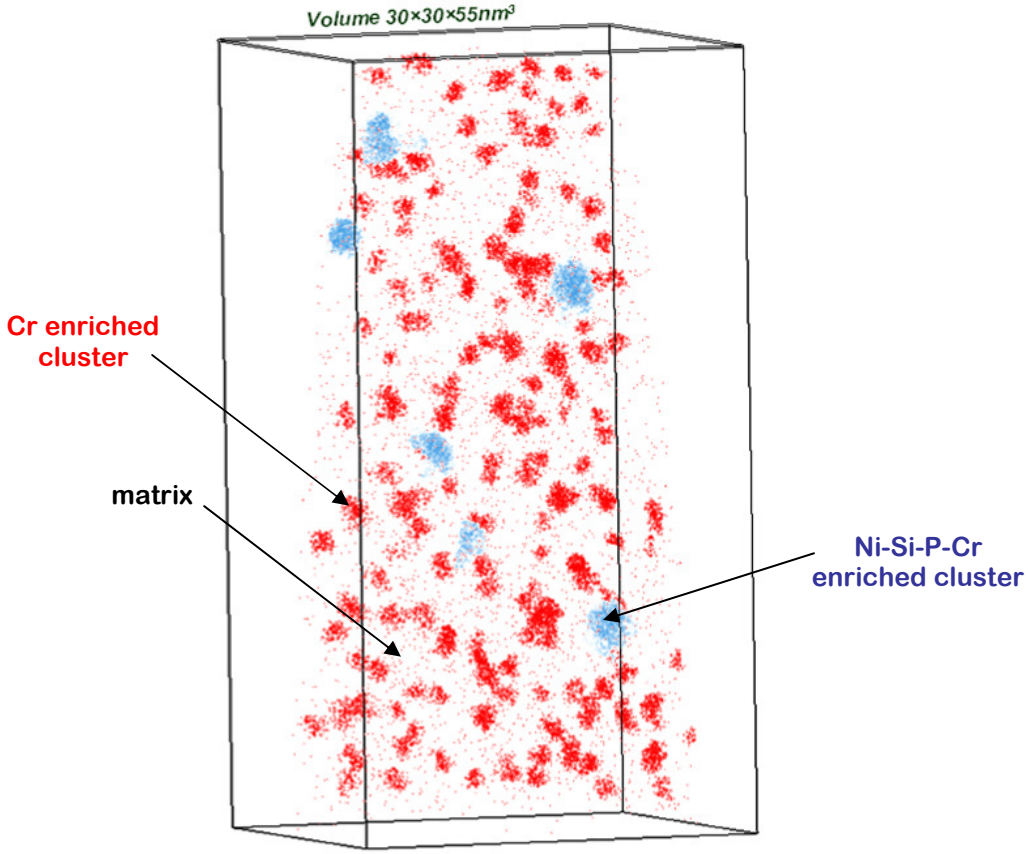

Figure 4.11. 3D distribution of Cr, Ni and Si atoms in the alloy Fe-12%atCr after neutron irradiation at 300°C up to 0.6 dpa. Red areas represent the Cr-enriched clusters. The local Cr concentration is higher than 28at.%. Blue areas represent the NiSiPCr-enriched clusters. A threshold of $C_{(Ni+Si+P)} > 3$at%. is used to reveal the clusters.

Mean chemical composition of the 3DAP volumes obtained after analysis of irradiated samples is given in Table 4.8. The measured Cr composition (10.9 ± 0.05) at% is in good agreement with the data obtained in the as-received state.

Table 4.8. Average chemical composition (at.%) of the neutron irradiated Fe-12%Cr model alloy (0.6dpa, 300°C).

Fe	Balance
Cr	10.9 ± 0.05
Si	0.16 ± 0.01
P	0.013 ± 0.002
Ni	0.06 ± 0.01
V	0.005 ± 0.001
Co	0.013 ± 0.002
Mn, C, N, O, S, Al, Ti	not measurable

Attention was paid on the detection of two new chemical species: slight quantities of V and Co have been detected. The quantity of V is in good agreement with the chemical composition data measured using induced plasma mass spectrometer [2] (see Table 2.3. p. 48). The fact that V wasn't detected in measurable quantities in previous experiments can arise form: i) its non-homogeneous distribution or ii) from the too low mass resolution of previous 3DAP experiments (see Chapter 2 for details). Indeed, V has been detected owing to ECoTAP experiments with a very good mass resolution ($\frac{M}{\Delta M_{10\%}} = 600$ for the major iron isotope ($56Fe^{2++}$)) and wasn't detected during EC_OWATAP and LAWATAP experiments.

As Co atoms weren't observed neither by previous 3DAP experiments nor by induced plasma mass spectrometer measurements, it is possible to suggest that the appearance of this originates from transmutation reaction (see Chapter 1, part IV.1(c)). As in the case of V, Co has been detected owing to ECoTAP experiments. This means that the fact that Co hasn't been detected in another model alloys can originate from the too low mass resolution of the other 3DAP tools (EC_OWATAP and LAWATAP).

For identification of Cr-enriched clusters, a concentration threshold $X_{Cr} > 28at\%$ has been used. This is slightly higher that the one used for the Fe-9%Cr model alloy. The mean core composition of the Cr-enriched clusters is given in Table 4.9 and the frequency distribution of the in-core Cr concentration of the analyzed clusters is presented Figure 4.12a. A chromium content equal to (58.5 ± 1.1)at% is measured. This value is almost equal to the one measured in the Cr-enriched clusters observed in the Fe-9%Cr model alloy. Cr-enriched clusters are also enriched with silicon ((0.65 ± 0.17)at%). It should be mentioned that Cr-enriched clusters in the Fe-9%Cr model alloy contained only Cr and Fe atoms (see Table 4.5). The origin of this difference is currently not clear. Nevertheless, one can note that the nominal Si content in the Fe-12%Cr model alloy is two times higher than the one of the Fe-9%Cr model alloy. It reaches about 0.2at% that is comparable with some industrial F-M steels (see Table 1.2, Chapter 1, p. 16). It should be mentioned that, in irradiated steels, Si was shown to enrich Cr-enriched clusters, as it was demonstrated by EDS studies of Gelles and Thomas [19].

Table 4.9. Average chemical composition (at.%) of the Cr-enriched clusters in the neutron irradiated Fe-12at%C (0.6dpa, 300ºC) model alloy (data have been averaged from 176 clusters)

Element	Concentration, at%	Enrichment factor ($C_{cluster}/C_{matrix}$)
Fe	Balance	
Cr	58.5 ± 1.1	7.1
Si	0.65 ± 0.17	5
P, Mn, Ni, V, C, N, O, S, Al, Ti, Co	not measurable	

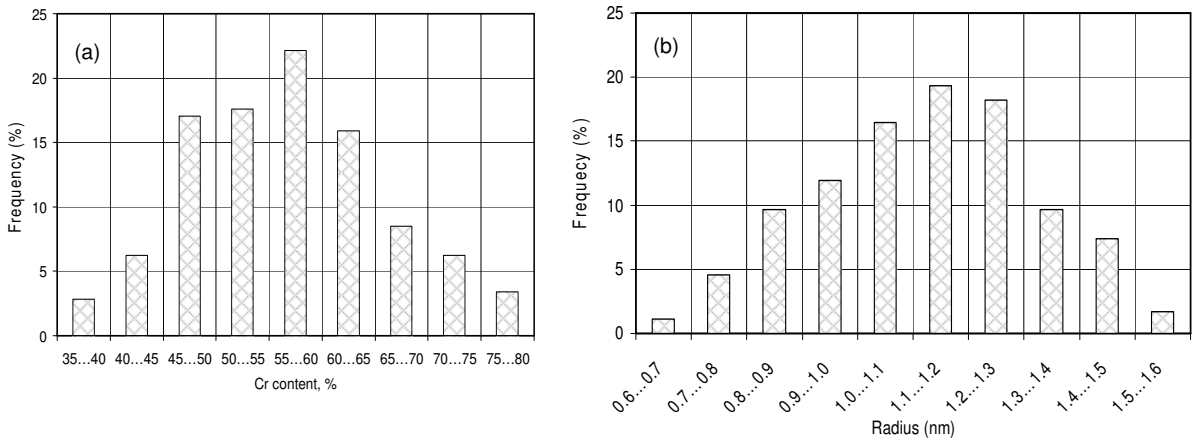

Figure 4.12. a) Frequency distribution of the in-core Cr concentration of the analysed Cr-enriched clusters- b) Frequency distribution of the Cr-enriched clusters' radius.

The shape of the Cr-enriched clusters is mainly spherical, as shown on 3D image in Figure 4.11 and "top view" images on Figure 4.13 (a, b). However, one ECoWATAP experiment revealed the presence of ellipsoidal Cr-enriched clusters which are elongated along a unique direction (Figure 4.13 (c)). The origin of such elongation in this particular experiment is currently unknown as the statistics of experiment is not enough to conclude if it originates from some orientation relationships between these objects and the matrix or if this fact is due to an unknown artifact of the ECoWATAP or to the shape of the sample. It must be emphasized that no significant difference has been obtained in the chemical composition of the clusters in the different experiments.

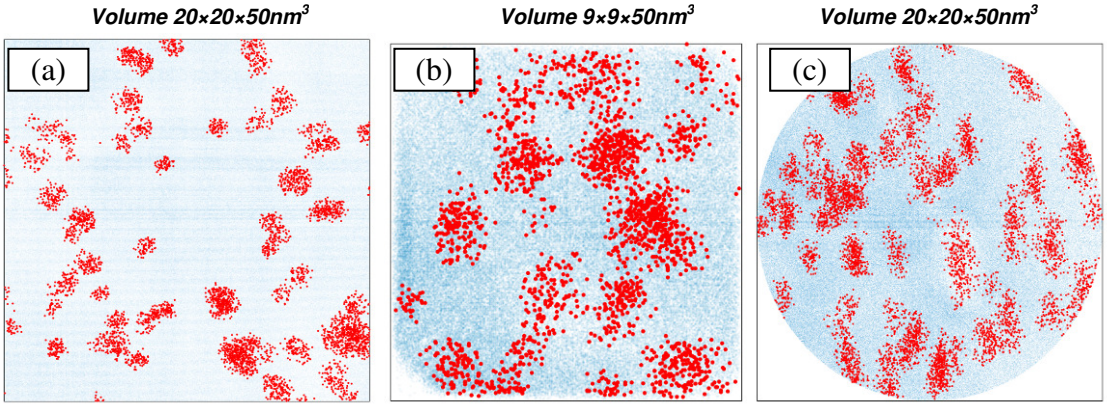

Figure 4.13. "Top views " (the tip axis is normal to the figure) of 3D reconstruction of analyzed volumes of the Fe-12%Cr alloy after neutron irradiation at 300°C up to 0.6 dpa, obtained by three 3DAP techniques: (a) LAWTAP; (b) ECoTAP; (c) ECoWATAP. Only 10% of Fe atoms of the matrix are presented. Red areas represent the Cr-enriched clusters. The local Cr concentration is higher than 28at.%. The clusters are mainly spherical in analyzed volumes obtained by LAWTAP and ECoTAP, whereas they are ellipsoidal and elongated towards a common direction in the case of ECoWATAP analysis. NiSiPCr-enriched clusters are not presented.

The mean equivalent radius of Cr-enriched clusters has been measured. A value equal to (1.1 ± 0.2) nm has been obtained. This value which has been deduced from the total number of atoms inside each cluster is in good agreement with the value deduced from composition profiles drawn up through the clusters along the direction of analysis as well as with Guinier radius calculations. The size distribution of the Cr-enriched cluster's radius is presented Figure 4.12b.

A cluster number density of $(5.0 \pm 0.5) \times 10^{24} m^{-3}$ is measured. Note that this value is more than twenty times higher that the one measured in the Fe-9%Cr model alloy. The volume fraction is equal to 4 %.

As in the case of the Fe-5%Cr and Fe-9%Cr model alloy, to distinguish NiSiPCr-enriched clusters, the threshold parameter of $C_{(Ni+Si+P)} > 3$at% has been used. Mean core composition of these objects and enrichment factors of the chemical species are given in Table 4.9. Almost 25at% of Cr has been detected inside the clusters. Similarly to the Fe-5%Cr and Fe-9%Cr model alloys, the relative increases of Si, Ni and especially P are more significant in comparison with Cr.

Table 4.9. Average chemical composition (at.%) of NiSiPCr-enriched clusters in the neutron irradiated Fe-12%Cr (0.6dpa, 300ºC)

Element	Concentration, at%	Enrichment factor ($C_{cluster}/C_{matrix}$)
Fe	Balance	
Cr	24.2 ± 2.4	2.9
Si	7.9 ± 1.5	60.8
Ni	1.2 ± 0.6	30
P	3.3 ± 1.0	1100
C, N, O, S, Al, Ti, Mn, V	not measurable	

The number density of these clusters is equal to $(1.1 \pm 0.7) \times 10^{23} m^{-3}$ and their mean equivalent radius is (1.6 ± 0.2) nm. The clusters have non-regular shape. Some of them are almost spherical whereas others have ellipsoidal and disk like shape. Examples of such clusters are shown in Figure 4.14.

As in the two previous cases for the NiSiPCr-enriched clusters in the Fe-5%Cr and Fe-9%Cr model alloy, the origin of these variations in shapes is currently not clear. Additional investigations should be performed to conclude if this is an artifact of the technique or it is the consequences of their association with different point defect clusters.

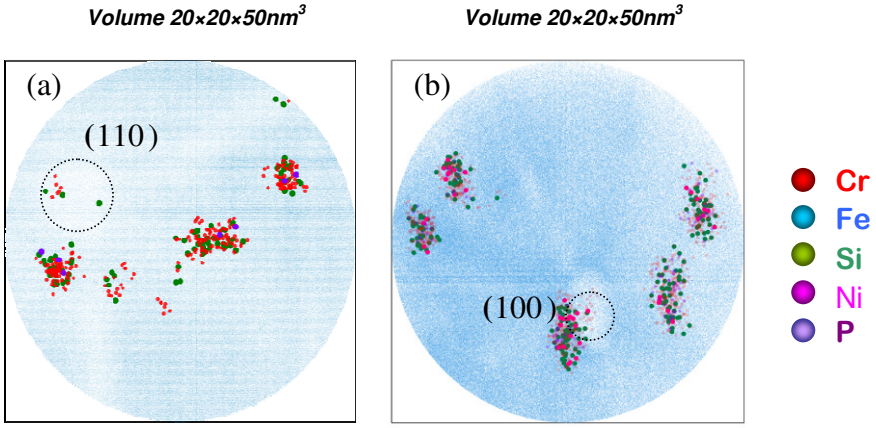

Figure 4.14. The "top view" (the tip axis is normal to the figure) of 3D reconstruction of an analyzed volume of the Fe-12%Cr alloy after neutron irradiation at 300°C up to 0.6 dpa. Only 10% of Fe atoms are presented in the matrix. Multicolour areas represent the NiSiPCr-enriched clusters. A threshold of $C_{(Ni+Si+P)} > 3$at%. is used to reveal the clusters. The clusters have an ellipsoidal shape. Cr-enriched clusters are not presented.

As provided by Table 4.9, the Cr content of the matrix is (8.24 ± 0.05) at.% that is slightly lower than the one measured in the Fe-9%Cr model alloy.

Table 4.9. Chemical composition (at.%) of the matrix in the neutron irradiated Fe-12at%C model alloy (0.6dpa, 300°C).

Fe	Balance
Cr	8.24 ± 0.05
Si	0.13 ± 0.01
P	0.003±0.001
Ni	0.04 ± 0.01
V	0.007 ± 0.002
Co	0.015 ± 0.002
C, N, O, S, Al, Ti, P	not measurable

I.4. Discussion

The current investigation of the Fe-Cr model alloy after neutron irradiation (up to 0.6 dpa) at 300°C revealed the existence of clustering after exposure.

a) Cr-enriched clusters

Homogeneously distributed Cr-enriched clusters have been observed in the Fe-9%Cr and Fe-12%Cr alloys. According to the modified Fe-Cr phase diagram proposed by Bonny et al. [20] and to the CALPHAD phase diagram, Cr is certainly supersaturated in the Fe-9%Cr and Fe-12%Cr alloys at 300°C (Figure 4.15) and α' precipitation during irradiation is expected. Thus, the appearance of the Cr-enriched clusters in the irradiated Fe-9%Cr and Fe-12%Cr alloys should originate from radiation enhanced precipitation due to both the high supersaturation of point defects in the matrix and of Cr.

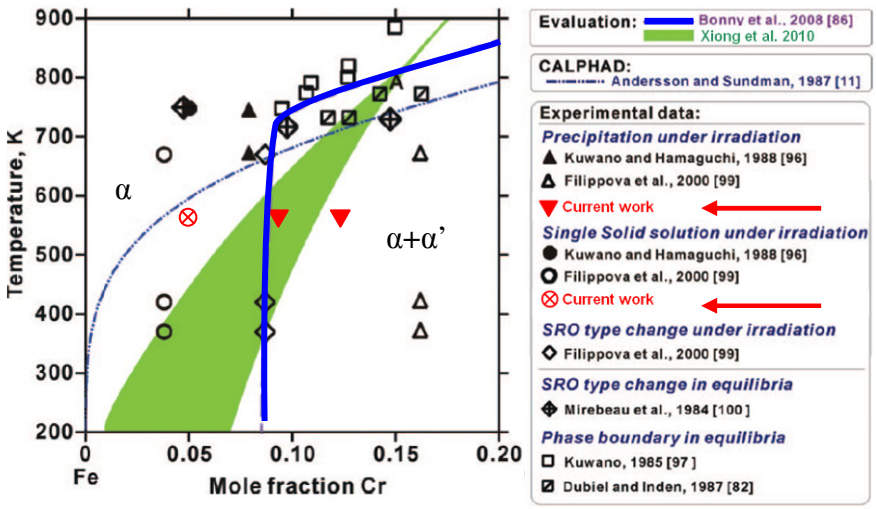

Figure 4.15. Low Cr part of the α-α` miscibility gap (after [21]); the position of the α domain limit, proposed by Bonny et al. is shown in blue [20]; the possible location for Fe-rich solvus determined by Xiong et al. [21] is presented by the green area. The results of the current research are shown by red marks (see explanation in the legend).

According to the CALPHAD Fe-Cr phase diagram, Cr is also supersaturated at 300°C in the Fe-5%Cr model alloy. However, since any evidence of Cr precipitation haven't been detected after irradiation at 300°C, this is in good agreement with the suggestion of Xiong et al. and Bonny et al. (see [20,21] and references cited) that the solubility limit of Cr in α the matrix is higher than 5at% at 300°C and that the current model alloy is undersaturated at this temperature.

According to the modified Fe-Cr phase diagram of Xiong et al. [21], the Fe-12%Cr alloy is also supersaturated at 300°C. Concerning the Fe-9%Cr alloy, at 300°C it belongs to the proposed area of possible location of the solubility limit [21]. This means that in

accordance with this diagram the alloy can be: i) supersaturated and the appearance of the Cr-enriched clusters is enhanced by the irradiation; or ii) undersaturated and the Cr-enriched clusters have been induced by the irradiation. However, since no irradiation induced Cr-enriched precipitates have been observed in the Fe-5%Cr model alloy which is certainly undersaturated in accordance with the phase diagram of Xiong et al. [21] and of Bonny et al. [20], it is possible to argue that Cr-enriched clusters in Fe-9%Cr model alloy originate from irradiation enhanced precipitation. This means that the position of the solubility of Cr in Fe at 300°C is lower than 9at%. Of course, this is under the hypothesis that the solubility limits is not modified by the irradiation.

Another fact that is in favor of an irradiation enhanced origin of the Cr-enriched clusters is that the number density of these objects strongly depends on the content of Cr in the alloy, while during irradiation induced processes it is possible to expect the appearance of objects in all model alloys in comparable quantities after irradiation with similar conditions (flux and dose).

According to CALPHAD calculations [22], the equilibrium composition of the α' phase at 300°C is higher than 90at% of Cr. It is evident that the chemical composition of the observed Cr-enriched clusters (about (55.1±3.5)at% and (58.5±1.1)at% measured in the Fe-9%Cr and Fe-12%Cr alloys, respectively) doesn't correspond to the thermal-equilibrium value of the α' phase. Few scenari can be proposed for the explanation of this fact:

i) On the one hand, as it has been already mentioned, the 3DAP technique has some artifacts such as local magnification effect [12–14]. This effect may influence the shape of the α′ precipitates, leading to trajectory overlaps near the particle/matrix interface (some quantity of matrix atoms will appear in the precipitate interface). This means that such an effect can alter the quantitativity of concentration measurements [14]. α' particles are prone to this effect. As shown in Figure 4.16, the number density of atoms inside Cr-enriched clusters in the Fe-9%Cr and Fe-12%Cr model alloys is about twice the matrix one. Investigation of the influence of this effect on composition has been performed in a Fe-20at%Cr alloy thermally aged at 500°C [6]. Results strongly suggested that the in-core Cr concentration of α' precipitates is not affected. Also, it is shown by modeling of field evaporation of an Fe-Cr tip, [13,16,23] that even for a precipitate with a radius of 1nm, the core composition is not affected. This is illustrated by the concentration profile of Figure 4.17(a) [16]. This profile has been drawn trough a simulated precipitate with a radius of 1 nm and a Cr concentration of 80at.% which was surrounded by an Fe matrix with a Cr concentration of 14at.%. After evaporation, one can note that composition measurement in the core of the precipitate enables to reach the actual composition of the precipitate. It is worth noting that this simulation gives an atom density in the evaporated precipitate about 2.5 times the matrix one (Figure 4.17 (b)). This is in very good agreement with experimental observations (Figure 4.16). Nevertheless, as it is not possible to rule out that the model does not underestimate the local magnification effect, it is not possible to exclude a possible artificial dilution of the Cr-enriched clusters.

The difference of evaporation field induces another well known effect, the preferential evaporation of Cr atoms, that may introduces errors in the evaluation of the Cr-concentration. But, owing to the experimental conditions of analyses, described in Chapter 2, this effect, if it exists, may lower the Cr-concentration of the α′ phase of less than 1 at.% [24].

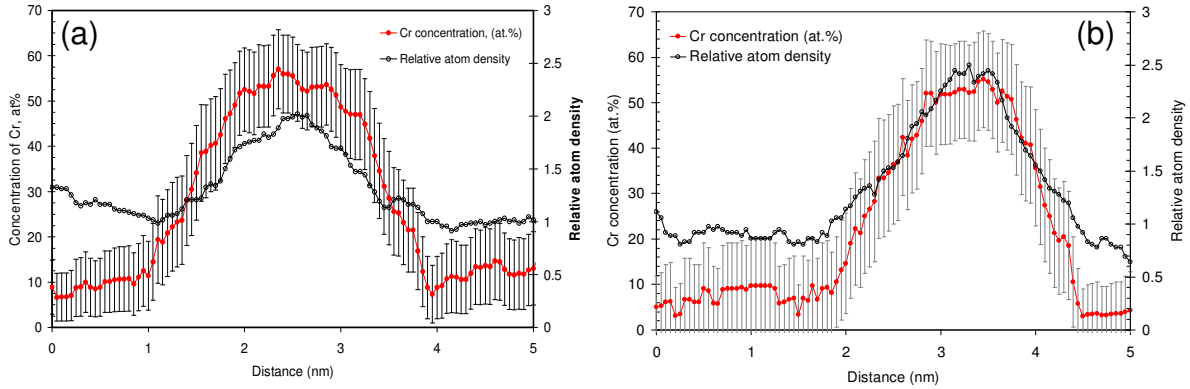

Figure 4.16. Cr-concentration profile drawn trough a Cr-enriched clusters in the (a) Fe-9%Cr and (b) Fe-12%Cr model alloys and corresponding relative atom density.

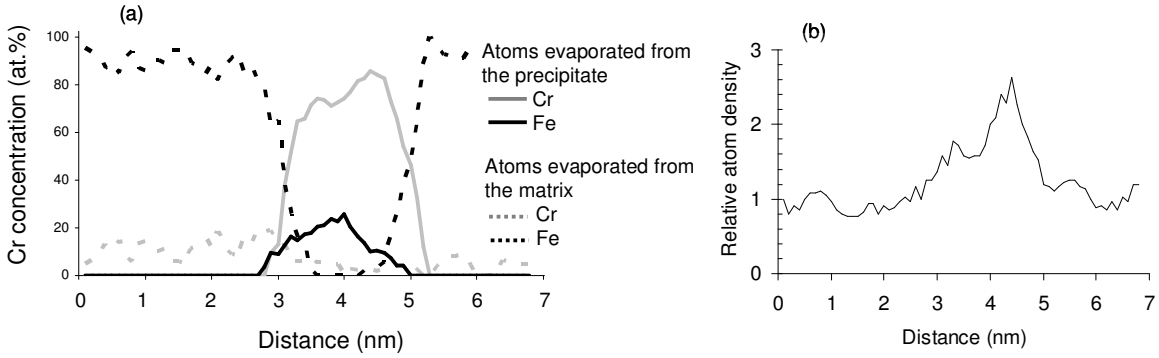

Figure 4.17. Concentration profile drawn trough a precipitate of 1nm in radius which has been evaporated owing to a model that reproduces the field evaporation of an APT sample [23]. The actual Cr concentration of the simulated precipitate was 80%. It was placed in an Fe rich matrix which contains 14% of Cr atoms (after [16]).

ii) On the other hand, the composition of α' precipitates is not necessarily equal to equilibrium value.

First of all, even under thermal ageing the Cr content in the early stages of α' precipitation can be lower than the equilibrium one. Indeed, in the case of non classical nucleation, the Cr concentration of α' precipitates is lower than the equilibrium one in the early stages as it was shown experimentally by Novy et *al.* [6] in a Fe-20at.%Cr aged at 500°C and using analytical model based on a regular solid solution by L'vov et *al.* [25] in the same alloy.

Second, the phases formed under irradiation are not necessarily the phases which are predicted by the phase diagram because of the coupling of solutes to the defect fluxes and

ballistic dissolution of phases. Moreover, as it is suggested in Ref. [26] by Russell, the phases in materials under irradiation can only reach steady state but not equilibrium**.**

SANS data made on the same model alloys after neutron irradiation in the same conditions and after irradiation to 0.6 dpa and to higher dose (up to 1.5 dpa) which have been preformed by Bergner and co-workers [4,5,11] seems to show that, a steady state is established. Indeed, SANS data show that the radius of Cr-enriched precipitates and their volume fraction in the Fe-12%Cr model alloy remained unchanged during the irradiation from 0.6 up to 1.5dpa (in the Fe-9%Cr alloy the radius of Cr-enriched precipitates was constant, while a slight increase of volume fraction has been observed). So, these data can indicate that some kind of steady state between the thermodynamic clustering tendency and a kinetic dissolution, probably owing to the inverse Kirkendall mechanism, is possible. Choudhury et al. [27], owing to *ab-initio* calculation have shown that depletion of Cr is expected on vacancy sinks by inverse Kirkendall mechanism, since Cr is the faster diffuser. Currently there is no data on the possible bias of α′ clusters to the vacancies fluxes. But it is possible to envisage that the α′ clusters could absorb a non-negligible quantity of vacancies which could lead to the depletion of these objects in Cr up to the values observed by 3DAP in the current alloys.

The aforementioned results mean that more experimental data including 3DAP investigation of Fe-Cr alloys irradiated at different doses (and probably different temperatures) are of large interest, since it can contribute to clarify this point.

It is also necessary to point out that if the α′ clusters absorb a non-negligible quantity of vacancies, as it is envisaged above, in turn, it could induce artifacts in 3DAP analysis. This effect was suggested in Ref. [28] for Fe-Cu system and RPV steels in irradiated state and could lead, for example, to the underestimation of volume fraction and Cr concentration of precipitates by 3DAP techniques.

Data on defect changes under irradiation are available from TEM studies which have been performed by Matijasevic et al. [2,10]. No phase separation has been detected (due to the low resolution of the technique) but it has been shown that point defect clusters (interstitial loops) are created during neutron irradiation. As presented in Table 4.10, the radius of the observed dislocation loops decreases from about 8 nm in the Fe-5%Cr model alloy to about 6 nm in the Fe-12%Cr model alloy. The number density of the detected loops is of the order of 10^{21} m^{-3}. It was reported that in the current model alloys, loops are located in the matrix and near the initial dislocation lines or dislocation network as well. It was shown that the trend of association of dislocation loops to the natural defects (dislocation lines or dislocation network) became stronger with increasing of Cr content and almost all loops have been associated to initial dislocation lines in the Fe-12%Cr alloy [2,10].

Experimental data on different irradiations of Fe-Cr based alloys and steels [29–31] showed that Cr-enrichment on interstitial dislocation loops after irradiation is expected. However, the large difference between the number densities of interstitial loops observed by

TEM [2] and of the Cr-enriched particles detected in this work (Table 4.10) show that the clusters observed by 3DAP may certainly not be linked to these loops. Nevertheless, it can not be excluded that some Cr-enriched clusters are not linked to dislocation loops which are not visible by TEM because of their small size (≈1 nm in radius).

Table 4.10. Summary of the available data on the dislocation loops (obtained by TEM [2,10]), clusters and matrix (obtained by SANS [4,5,11] and 3DAP) measured in the investigated model alloys after 0.6dpa neutron irradiation at 300°C

	Fe-5%Cr		Fe-9%Cr		Fe-12%Cr	
Dislocation loops [2,10]						
Number density (m^{-3})	$2.3 \cdot 10^{21}$		$1.9 \cdot 10^{21}$		$1.7 \cdot 10^{21}$	
Radius (nm)	8±2		7±2		6±2	
Clusters						
	3DAP	SANS [5,11]	3DAP	SANS [4,5]	3DAP	SANS [4,5]
Cr-enriched clusters						
Volume fraction, %	0%	0%	0.14%	0.2±0.13%	4%	4.3±0.4%
Number density, m^{-3}	–	–	$(1.3\pm0.2)\cdot10^{23}$		$(5.0\pm0.5)\cdot10^{24}$	
Radius, nm	–	–	1.1±0.2	~ 1	1.1±0.2	~ 1
Cr content, at%	–	–	55.1±3.5	97.5	58.5±1.1	97.5
NiSiPCr-enriched clusters						
Radius, nm	2.0±0.2	–	1.65 ± 0.2	–	1.6±0.2	–
Number density, m^{-3}	$(1.3\pm0.5)\cdot10^{23}$	–	$(2.4\pm0.5)\cdot10^{23}$	–	$(1.1\pm0.7)\cdot10^{23}$	–
Others						
Cr-C, radius, nm	–	bimodal distribution ~ 0.5 to 3	–	3	–	–
Matrix						
	4.58±0.02	–	8.77 ± 0.04	8.8 ± 0.1	8.24 ± 0.05	8.5 ± 0.2

b) NiSiPCr-enriched clusters

Unlike to the Cr-enriched clusters, a radiation induced mechanism should be responsible for NiSiPCr-enriched cluster formation. The extremely low nominal levels of Ni and Si in the alloys exclude any thermodynamic driving force for precipitation process, since the solubility limits of these species in Fe (for binary alloys) at 300°C is significantly higher (about 4.6at% and 10at% for Ni and Si respectively [32–34]). Concerning P, it is not so clear. In accordance with the currently available binary Fe-P phase diagrams, solubility limit of P in α-matrix at 300°C varies from very low (less than 0.1at)% up to 1.7at% [34]. The value obtained by Thermo-calc calculations for Fe-P binary alloy is about 0.2at% [35] that is ten times higher than the P content in the current alloys (the maximum value is equal to 0.025at%). The multicomponent Thermo-calc calculations showed that the presence of Si decreases the solubility of P in the α-matrix, but 0.2at% of Si (the maximum measured content of Si in the model alloys) decreases the solubility of P only down to 0.18at%, that is still much higher that the P content in the alloys.

Multicomponent Thermo-calc calculation, which have been performed considering the composition of the Fe-12%Cr model alloy, shows that under equilibrium at 300°C, three phases are expected: the P-enriched M_3P-phase, Cr-enriched α' precipitates and α-matrix. These phases have the following chemical compositions:

	Cr, at%	*Si, at%*	*Ni, at%*	*P, at%*	*Fe, at%*
α-matrix	*4.1*	*0.18*	*0.05*	*0.001*	*balance*
α' precipitates	*97.8*	*0.002*	*<0.001*	*<0.001*	*balance*
M_3P-phase	*54.7*	*0*	*1*	*25.5*	*balance*

However, the latter theoretical calculation data on phase compositions doesn't corresponds to the one obtained with 3DAP. Indeed, the solubility limit of Cr is estimated by Thermo-calc to be 4.1at%. This means that radiation enhanced precipitation of α' phase at 300°C should appear also in the Fe-5%Cr model alloy, but it hasn't been detected by our 3DAP experiments. This only suggests that these multicomponent Thermo-calc calculations don't predict carefully the real phase transformations in Fe-Cr based model alloy. Of course, one could also argue that 0.6 dpa is not enough to observe α' precipitation because of the very low driving force. It is clear that we can not for sure rule out this argument but all data collected in the literature and the new version of the binary phase diagram are clearly in favor of a wrong estimation of the solubility limit given by Calphad calculations. That is why, considering the binary Fe-P alloy and multicomponent Fe-P-Si alloys data, it is possible to assume that P is undersaturated in all the studied Fe-Cr model alloys.

If Ni, Si and P are undersaturated at 300°C as well as Cr in the case of the Fe-5%Cr alloy, the appearance of the NiSiPCr-enriched clusters, observed in all model alloys, should originate from irradiation induced segregation owing to the coupling of solutes to point defects fluxes. It is known that some radiation induced Ni and Si-enriched phases, such as G-phase, M6X, χ-phase and σ-phase, are usually created in ferritic-martensitic steels under irradiation [1,19,36,37]. These phases (excepted perhaps the G-phase) are also chromium rich [1,37]. However, the total combined atomic percent of nickel plus silicon (minimum 20% in σ-phase) is higher than the one observed in the observed NiSiPCr-enriched clusters. Nevertheless, it is possible that the observed diluted NiSiPCr-enriched clusters are precursors of these phases.

One can note that Ni and Si are also involved in the formation of nanoclusters in the bainitic matrix of pressure vessel steels (in association to copper and manganese) [38–41]. Kinetic of solute clustering in neutron irradiated ferritic model alloys and in a French pressure vessel steel have been investigated by 3DAP [40]. In these materials, the mechanism of formation of these clusters is often described as radiation induced segregation.

Concerning the other characteristics of these clusters, it should be mentioned that the number density of the NiSiPCr-enriched clusters is almost equal in all model alloys (Table 4.10) and their radii are quite similar. There is perhaps a slight decrease of radius with the

increase of Cr. These observations are in good agreement with the hypothesis of radiation induced segregation. Indeed, in such a case, the number density is expected to be flux and dose dependent. Here, the dose and the flux are identical for all the alloys.

Concerning their composition, there is no constant stoichiometric chemical composition of these objects. The chromium content increases with the nominal chromium composition of the alloy while the contents of Ni, Si and P are roughly constant (within uncertainties) for the three model alloys (Figure 4.18). This behavior remains currently unclear. More statistics, including results on irradiation up to different doses but also simulations, are necessary for understanding of the processes of formation and evolution of these clusters.

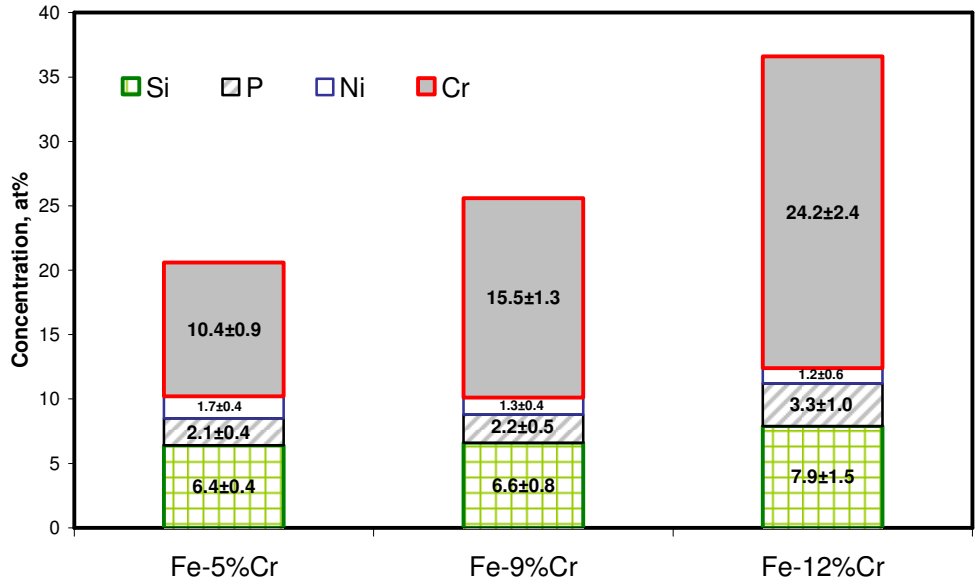

Figure 4.18. Composition of the NiSiPCr clusters (at%) in the different model alloys

As it was shown before, NiSiPCr-enriched clusters usually have three kinds of shapes: spherical, ellipsoidal and disk like. Owing to the fact that orientations of some ellipsoidal and disk like clusters be in the habit planes of ½<111> and <100> dislocation loops, it is possible to assume the association between NiSiPCr-enriched clusters and point-defect clusters such as dislocation loops. Because of the large difference between number densities of interstitial loops, reported in the work of Matijasevic et *al.* [2,10], the NiSiPCr-enriched clusters may not be linked to these loops. But, some nanometric point defect clusters, which have not been detected by TEM are probably present and could be responsible for the shape and orientation of the NiSiPCr-enriched clusters. Further work on the crystallographic orientation of the NiSiPCr-enriched clusters observed by 3DAP and, on observation of dislocation loops by TEM, is of interest in order to clarify this point.

c) Comparison with SANS results

3DAP and SANS results both give information on size, volume fraction and composition of clusters. Thus a cross-checking of the current 3DAP results with the SANS data of Bergner and co-workers obtained for the same model alloys [4,5,11] is a of large interest. Indeed, SANS can detect objects with low number density which are difficult to investigate by 3DAP while 3DAP is sensitive to dilute and small objects invisible by SANS or mixed with other cluster populations. So, the combination of the results of these two techniques is a complement way to obtain more comprehensive information on the phase formation under irradiation.

The SANS data of Bergner and co-workers obtained for the same model alloys [4,5,11] are summarized in Table 4.10.

In the Fe-5%Cr model alloy SANS reveals the presence of irradiation-induced scatters with a binominal size distribution (from 0.5 to 3nm) the mean of which is equal to about 0.9nm [5,11]. The measured A-ratio of these objects is consistent with the presence of Cr-rich carbides which have been associated to some irradiation-induced Cr-C-enriched clusters. It is expected that the number density of these objects is low, so no information have been obtained yet by 3DAP on these objects. At the same time, 3DAP reveals the presence of NiSiPCr-enriched clusters in this alloy after irradiation. It is currently unknown if such dilute clusters can be detected by SANS due to sensibility of the technique or if the signal formed by these objects has been mixed with the one of other scatters (Cr-C-enriched clusters in the case of Fe-5%Cr model alloy).

The SANS data on the Fe-9%Cr model alloy after neutron irradiation (0.6 dpa, 300°C) is consistent with the presence of two families of precipitates: Cr-enriched α' clusters with a radius of about 1 nm and Cr-C-enriched clusters (3 nm in radius) similar to the ones observed in the Fe-5%Cr model alloy [4,5] (see Table 4.10). It is evident that the size ((1.1 ± 0.2) nm as measured by 3DAP and the ~ 1 nm obtained by SANS) and volume fraction (0.14 % for Cr-enriched clusters by 3DAP and (0.2 ± 0.13) % for SANS) of the Cr-enriched clusters obtained by these two techniques are in good agreement.

As in the case of Fe-5%Cr model alloy, Cr-C-enriched clusters have not been detected by 3DAP because of their low number density. Meanwhile, NiSiPCr-enriched clusters revealed by 3DAP remained invisible for SANS. The matrix composition (Cr content in the matrix) deduced from the data of these two techniques also shows a good agreement: about 8.8at% of Cr have been obtained by SANS and by 3DAP.

Comparison of SANS results on the Fe-12%Cr model alloy [4,5] to results obtained with 3DAP shows that, as in the case the Fe-5%Cr and Fe-9%Cr model alloys, no data relative to NiSiPCr-enriched clusters have been described from SANS experiments. Beside this, a good agreement is found concerning the value of Cr-enriched clusters radius: (1.1 ± 0.2) nm as measured by 3DAP and the ~ 1 nm obtained by SANS. A good agreement is

also found for: i) Cr content of the α phase (matrix): (8.1 ± 0.3) at.% for 3DAP and (8.5 ± 0.2) at.% for SANS; ii) volume fraction of clusters: 4 % for Cr-enriched clusters by 3DAP and (4.3 ± 0.4) % for SANS may be including both population of clusters.

So, a relatively good agreement has been obtained between 3DAP and SANS for the Fe-9%Cr and Fe-12%Cr model alloys. The matrix composition, the size and the volume fraction of Cr-enriched clusters are almost equal. At the same time, these agreements conceal some disagreements:

i) first of all, concerning the Fe-12%Cr model alloy, the nominal Cr content which has been considered for SANS data treatment for the Fe-12%Cr model alloy is the value given by the chemical analysis [2] i.e. 12.3 at% whereas the value used in this work is given by the 3DAP measurement (about 10.9 at%). This difference of Cr content originates from the chemical inhomogeneity of the material as reported in Chapter 3. It is evident that if the Cr content equal to 10.9at% will be taken for SANS data treatment, the matrix and volume fraction values will change.

ii) The second and the most important disagreement is that the Cr content of Cr-enriched clusters is drastically different for both techniques. Based on the hypothesis that thermodynamic equilibrium compositions are reached for phases formed under neutron irradiation (see ref. for more details), Bergner et *al.* [4] supposed that Cr-enriched clusters are α' precipitates under equilibrium. Thus, they conclude in fine that the composition is close to the value given by Calphad calculations at 300°C [22] i.e. 97.5at.%. This value is clearly different from the one obtained by 3DAP: (55.1±3.5)at% and (58.5±1.1)at% of Cr has been measured in the Fe-9%Cr and Fe-12%Cr alloys respectively.

Such disagreement between SANS and 3DAP results is not unusual (see for example [42–44]). These disagreements are the consequence of the limits of these two techniques.

The possible reasons why Cr-enriched clusters observed by 3DAP have not the equilibrium Cr content have already been discussed above. Briefly: two scenari can be proposed: i) the dilution of Cr-enriched precipitate due to 3DAP technique artifact, that is currently not proved (see previous discussion) or ii) these clusters have not the Cr content predicted by equilibrium phase diagrams, that is possible either due to early stages of α' precipitation (as shown in the work of Novy et *al.* [6] on thermal ageing of the Fe-20%Cr alloy) or due to fact that the equilibrium composition is not reached under irradiation (see [21,26,45] and Chapter 1, section IV(b) for details).

The aforementioned results mean that a treatment of SANS data using results obtained by 3DAP (as it was made in the work of Carter et al. for example [44]), could be performed in order to check if a convergence could be obtained. The collaboration with F. Bergner and co-workers is in progress. The data on chemical compound has been transferred to FZD. It is believed that this work will clarify the pointed questions.

II. Segregations on natural point defect sinks

The main objective of the current PhD was to provide comprehensive information on the changes of intragranular structure of the Fe-Cr model alloys under irradiation exposure. The detailed description of new phases appeared in the Fe-Cr model alloys during neutron irradiation up to 0.6dpa at 300°C has been given in the previous part of this chapter.

At the same time, other microstructural changes under irradiation such as radiation assisted segregations on grain boundaries and dislocation lines are also of large importance because of their influence on mechanical and corrosion properties of steels. Systematic investigation of GB and dislocation behaviors under irradiations wasn't the primary goal of the given PhD thesis; however some interesting examples of segregations on these microstructural features have been revealed during the research. The detailed descriptions of the observed segregations are presented in this part of the chapter.

II.1. Dislocation lines

The direct observation of the dislocation structure or grain boundaries in general case is not possible by 3DAP, but can be generally inferred from segregation of different chemical species on them. Two examples of such segregations that can be definitely associated to dislocation lines have been observed in the neutron irradiated Fe-5%Cr model alloy. The first example has been already presented in Figure 4.1(a), other dislocation line revealed in the analyzed volume presented in Figure 4.19.

As shown on this 3D maps, dislocation line have been identified owing to segregations of Cr, Si and P. The amount of segregation at the core of two dislocations (both detected in the Fe-5%Cr model alloy) was quantified by comparing the concentration profiles of the relative increase of Cr, Si and P drawn perpendicularly to the dislocation lines through their cores (as schematically shown in Figure 4.19(b)). Concentration profiles of excess solute ($C_{core} - C_{matrix}$) are presented Figure 4.19(c) and Figure 4.20 (3D map of the analyzed volume and dislocation segregation is presented in Figure 4.1(a)). These profiles show that in terms of the absolute amount of excess solute, Cr is the most segregated element.

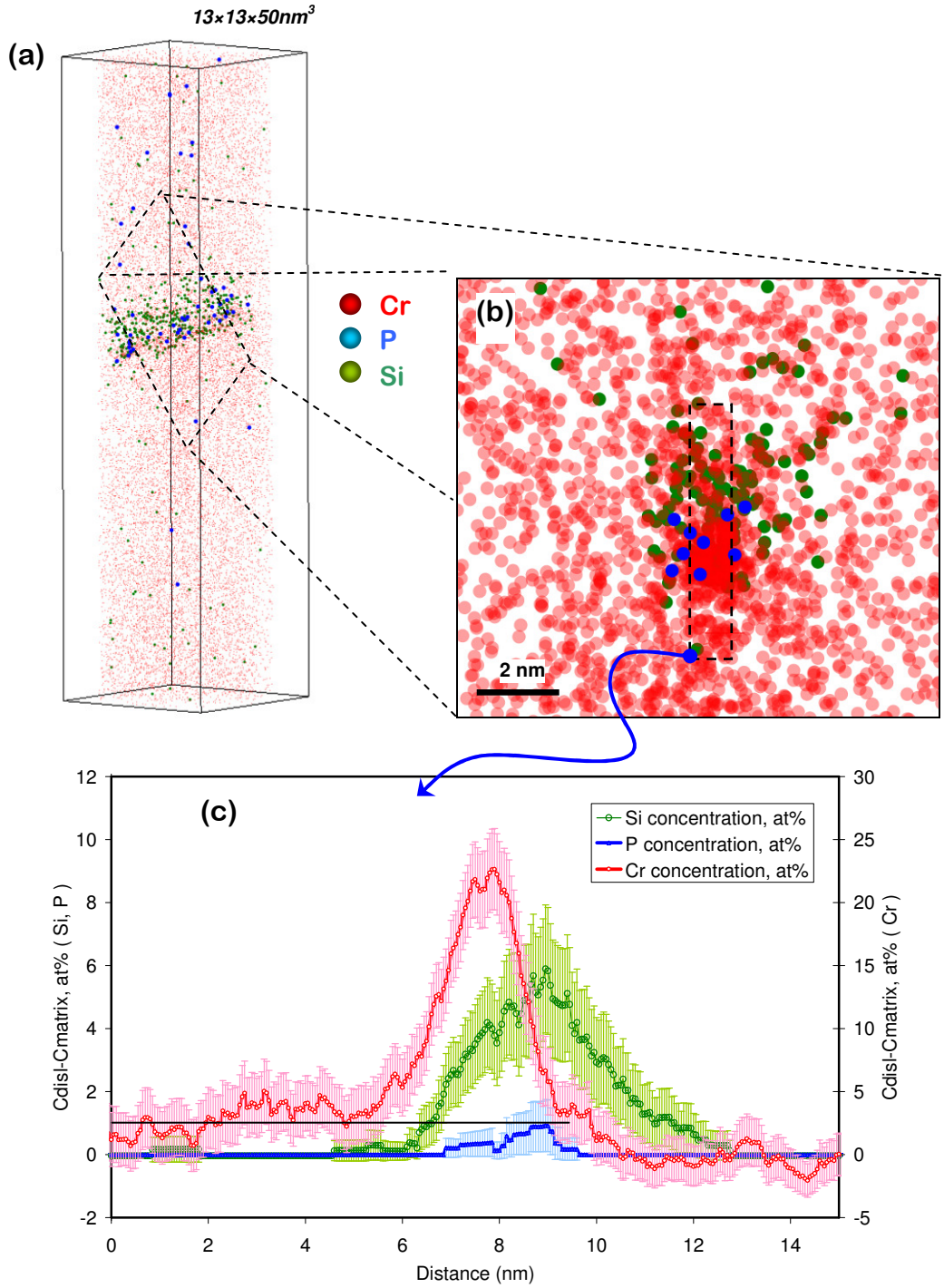

Figure 4.19. (a) 3D map of the analyzed volume of the Fe-5%Cr model alloy after neutron irradiation up to 0.6 dpa at 300°C. Only Cr, P and Si atoms are presented (b) Shift of Cr, Si and P enriched atmospheres with respect to the core of the dislocation; (c) concentration profile of the relative increase of Cr, Si and P drawn perpendicularly to the dislocation line through the core. Sampling box: 15×1×1nm^3.

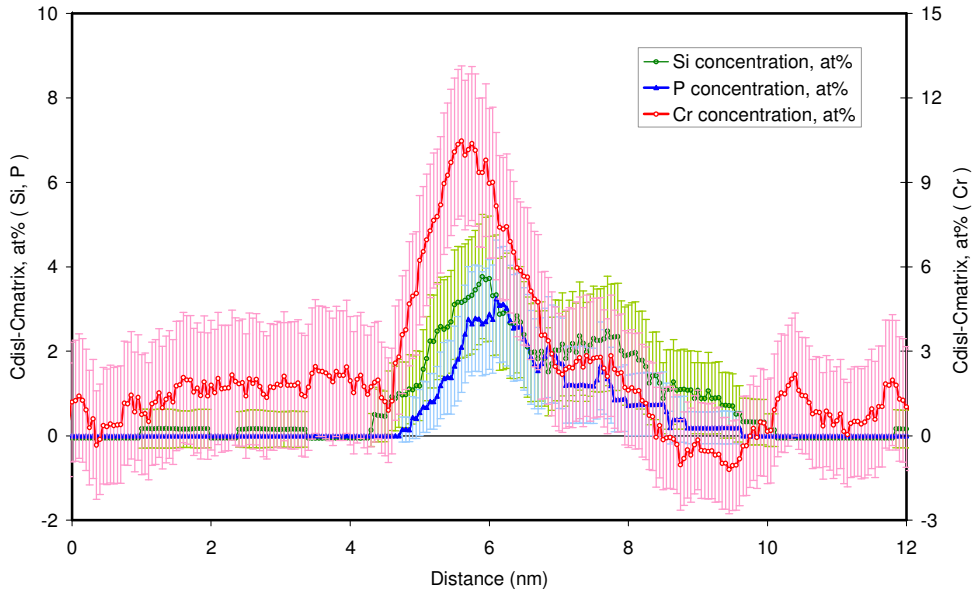

Figure 4.20. Concentration profile of the relative increase of Cr, Si and P drawn perpendicularly to the dislocation line in the Fe-5%Cr model alloy after neutron irradiation up to 0.6 dpa at 300°C imaged in Figure 4.1(a) through the core. Sampling box: 15×1×1nm^{3}.

As it is evident from the comparison of concentration profile drawn through two dislocation lines (Figure 4.19(c) and Figure 4.20), the trend of enrichment by Cr, P and Si is common for these two dislocations while the amount of the maximum enrichment is different. This difference is especially significant in the case of Cr. An absolute excess of Cr of about 23at% have been measured in the first dislocations, while the Cr content in the core of second dislocation is only about 10.5at% higher the one in the matrix. A similar trend has been observed for the maximum of Si excess: an excess of Si about two time's higher has been measured in the first dislocation (~6at% of Si for the first line and ~3.5at% for the second one). At the same time, the maximum enrichment by P is more significant for the second dislocation line in comparison with the first one (only ~1at% of P for the first line and ~3at% for the second one). A probable explanation could arise from the difference of crystallography of these dislocations (Burgers vectors, direction of the line etc.) that leads to differences in strain energies and thereby differences in interactions of these line with point defects and chemical species. Also it could be a consequence of the non-homogeneous distribution of the surrounding defect sinks such as grain boundaries or other dislocations which can affect the redistribution of point defects and associated solutes.

Also attention has been paid on the systematic shift between chemical species with respect to the dislocation lines observed on the 3D atom probe reconstruction (Figure 4.19 (a) and (b)) and on the concentration profiles (Figure 4.19 (c) and Figure 4.20) drawn perpendicularly to the dislocation lines: Si (and probably P in Figure 4.20) maximum peak is shifted with respect to the Cr one. Different hypotheses can be proposed to explain this fact:

- First: If current dislocations are edge dislocations or have an edge component, it gives rise to a stress field around the lines with which solute atoms may interact. Oversize atoms in substitution generally segregate in the dilated part of the edge dislocations, whereas undersize atoms in substitution are likely to segregate in the compressed region. As Si atoms are supposed to be undersized and Cr atoms oversized in Fe-Cr alloys, the repartition of these species in the stress field around the dislocation line could account for the shift observed between Cr and Si concentration profiles, as schematically presented in Figure 4.21.

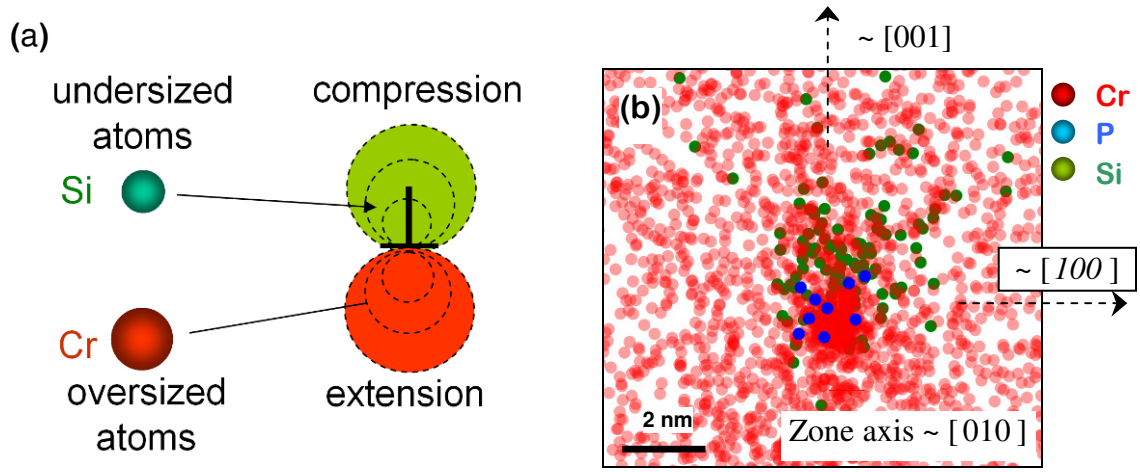

Figure 4.21. (a) Schematic image of the redistribution of undersized Si and oversized Cr atoms around the core of an edge dislocation in Fe. (b) experimental evidence of the shift of Cr, Si and P enriched atmosphere with respect to the core of a dislocation in the Fe-5%Cr alloy after neutron irradiation at 300°C up to 0.6 dpa. The latter image is similar to the one of Figure 4.19(b).

In the general case, it is problematic (or even impossible) to extract an accurate crystallographic information from 3DAP investigations and to conclude on the Burgers vector of observed dislocations. However, owing to the desorption image which reveals low-index crystallographic poles and traces between them (Figure 4.22), the crystallographic information of the analyzed volume have been deduced. Owing to this, it was estimated that the dislocation is elongated along the [010] direction (±5°), and the shift of segregations occurs in the plane ~ (100) toward the direction ~ [001], as presented in Figure 4.21(b). If we consider the general case of mixed dislocation, the line [010] can belong to dislocation with different Burgers vectors ({111} and {100}-type). However, owing to the fact that the dislocation is almost a straight line and under the hypothesis that Si, P and Cr are shifted with respect to the dislocation core (Figure 4.21) because of the stress field around the core, it is possible to suppose that this dislocation is a pure edge dislocation with Burgers vector [100] and glide plane (001).

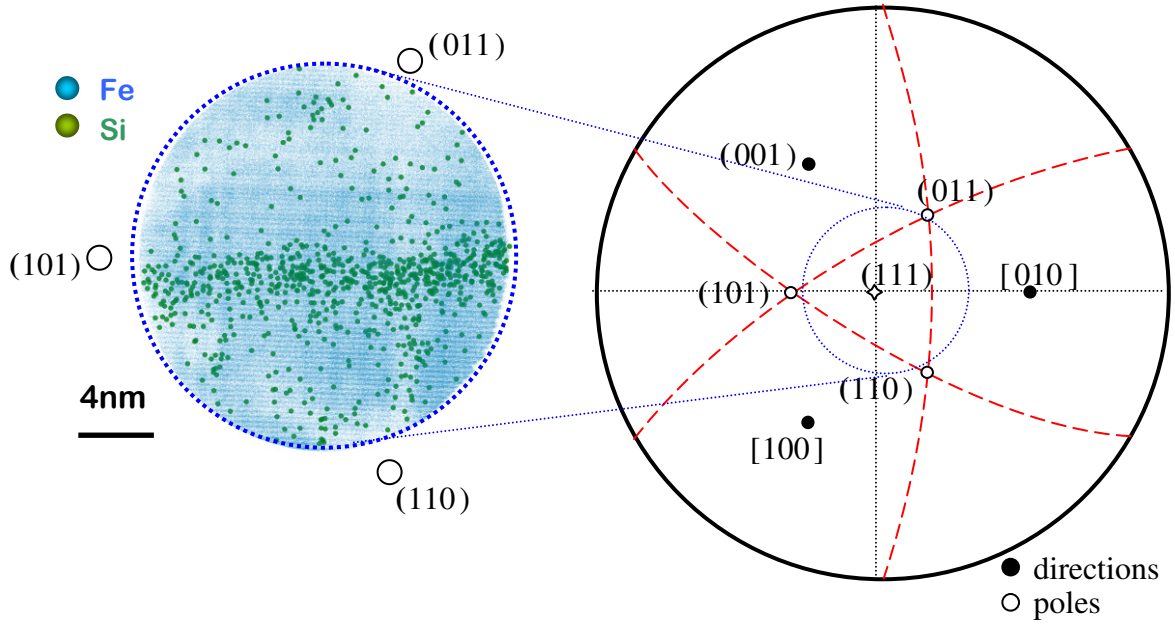

Figure 4.22. The "top view" of 3D reconstruction of an analyzed volume of the Fe-5%Cr alloy after neutron irradiation at 300°C up to 0.6 dpa and the stereographic projection which corresponds to the orientation of the analyzed volume. Only 10% of Fe atoms of the matrix are presented. Green atoms represent Si which mainly segregates on the dislocation line. Desorption lines corresponds to the red traces on the stereographic projection on the right. Zone axis of the tip is ~ [111].

A similar procedure has been performed for the dislocation line presented in Figure 4.1. This dislocation is elongated along a direction close to $[\bar{1}45]$ and the shift of Cr and Si occurs in the plane $(1\bar{1}1)$. By analogy with the previous example, it is possible to make the hypothesis that the given dislocation is an edge dislocation with Burgers vectors $[1\bar{1}1]$. If it is the case, the expected redistribution of oversized Cr and undersized Si around the dislocation core due to stress fields completely corresponds to the one which is observed experimentally.

- Second hypothesis that can explain the shift of Cr and Si segregations with respect to each other is an artificial shift due to the field evaporation behavior of the different chemical species such as chromatic aberrations or surface diffusion of atoms. Such possibilities have been already discussed in the first part of this chapter like a possible explanation of elongated shape of intragranular clusters. Indeed such processes can induce reconstruction artefacts such as a shift in the relative positioning of the atoms toward low index <110> poles [15]. Nevertheless, it must be emphasized that, as it was shown in Figure 4.1, Figure 4.19, Figure 4.21 and Figure 4.22, the shift occurs toward to other poles and definitely not in the plane normal to the tip axis as expected in the case of chromatic aberrations. The first hypothesis then appears as the most probable one.

It is worth noting to mention also, that if the Burgers vectors of the observed two dislocations are right, this validates the proposed above hypothesis we used to explain the different amount of segregation along the two dislocation lines. Indeed, a significantly larger

absolute excess of Cr and Si has been measured for the dislocation which is possibly of {100} type. This dislocation line has a larger Burgers vector than the one of the ½{111}-type dislocation, and the level of the bias on the point defects [46] and thus, on the elements segregation is higher for it. However, it is obvious that more data are needed to give a definitive conclusion, but this gives new approach for 3DAP data treatment.

Attention was also paid on the composition variation along the dislocation lines. As presented by the composition profile in Figure 4.22, which has been drawn along the dislocation shown in Figure 4.1, the concentration distributions are not homogeneous along the dislocation at the nanometric scale.

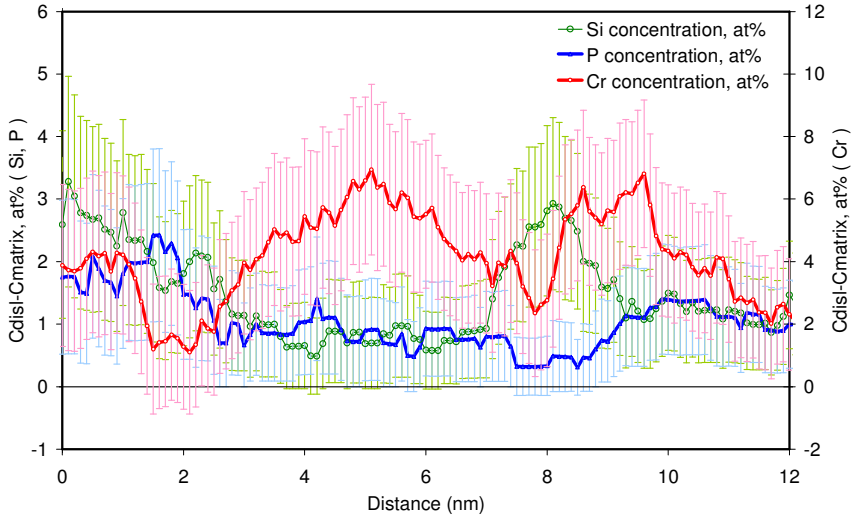

Figure 4.23. Concentration profile of relative increase of Cr, Si and P along the dislocation line, sampling box: 1.5×1.5×1nm^{3}.

Since no 3DAP data are available on dislocation lines in the current Fe-Cr alloys before neutron irradiation, it is impossible to conclude on the nature of these segregations i.e. induced or not by irradiation. Indeed, even without irradiation, it is known that chemical species in alloys interact with dislocations. This interaction leads to equilibrium segregation of solutes along the dislocation line, for example as Cottrell atmospheres [47].

The final heat treatment of the model alloys before irradiation was an annealing of the normalized alloys at 730°C for 4 hours followed by air cooling to room temperature. In such a case, as shown in the work of Williams et al. [48] on the oxide-dispersion-strengthened F-M Eurofer 97 steel (C_{Cr}≈9.0 to 9.5at%) after a similar heat treatment (annealing at 700°C for 2 hours followed by air cooling), segregations of Cr, and traces of P and Si enrichments along the dislocation lines are observed. It indicates that similar enrichment of dislocation lines by Cr, P and Si could be expected in the case of the Fe-Cr model alloys studied here.

It is known that the Cr behavior at the defects sinks in ferritic/martensitic alloys does not show any unambiguous trend and both RIS and RID of Cr can be observed (see review [27,48–50] and references cited). For example, in the work [48], ion irradiation at 400°C up to 2dpa has led to a decrease of the Cr content on the dislocation lines. Of course, the differences

in irradiation conditions in the current experiment and the study of Williams et al. [48] are quite appreciable and can significantly change the segregation behaviors.

It is evident from the comparison of concentration profiles (Figure 4.19(c) and Figure 4.20) of dislocation lines with the chemical composition of NiSiPCr-enriched clusters (Table 4.2) that these two microstructural features exhibit quite similar solute excesses of Cr, Si and P. Taking into account the fact that NiSiPCr-clusters are rather irradiation induce objects (as it is discussed above), it could indicate a similarity of the segregation mechanisms which occur on dislocation lines and on these clusters during neutron irradiation.

II.2. Grain boundaries

a) Non-irradiated GB

The microstructure of the Fe-Cr alloys before irradiation have been characterised in detail by 3DAP, TEM and PAS and is presented in Chapter 3. While the 3DAP data on grain-boundary segregations are currently unavailable, TEM-EDX measurements allowed us to estimate the Cr behavior on GB before neutron irradiation. The profile presented on Figure 4.24 shows a relative Cr enrichment on grain boundary with a segregation width of about 6 nm (EDX analysis was not sensitive to the minor alloying elements, such as Si, P, Ni and others). This finding is consistent with the literature for quenched and tempered high-Cr ferritic-martensitic steels (see review [1,49–51] and references cited). We should mention that the profile in Figure 4.24(b) shows only a trend of Cr enrichment as there is an averaging of the Cr concentration on the overall depth of the sample. 3DAP investigations are desirable to give quantitative description.

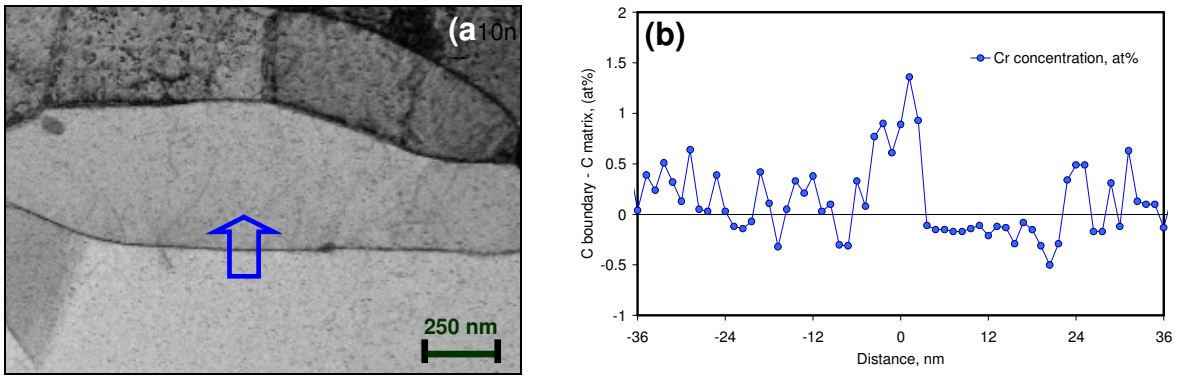

Figure 4.24. (a)Low angle annular dark field micrograph obtained on the as-received Fe-12%Cr (b) variation of $C_{boundary}$ - C_{matrix} measured through the martensitic lath boundary (highlighted by blue arrow) showing Cr segregation across it. $C_{boundary}$ is measured by EDX on the FIB-foil of about 50 nm in thickness, C_{matrix} is equal to the mean Cr content measured inside the two neighboring grains (11.1at%).

b) Irradiated state: low angle grain boundaries

Examples of segregations on low-angle grain boundaries have been observed by 3DAP in the Fe-9%Cr and Fe-12%Cr model alloys. These GB have been revealed on the 3D

images owing to the presence of decorated accommodation dislocation lines which are characteristic of low angle grain boundaries.

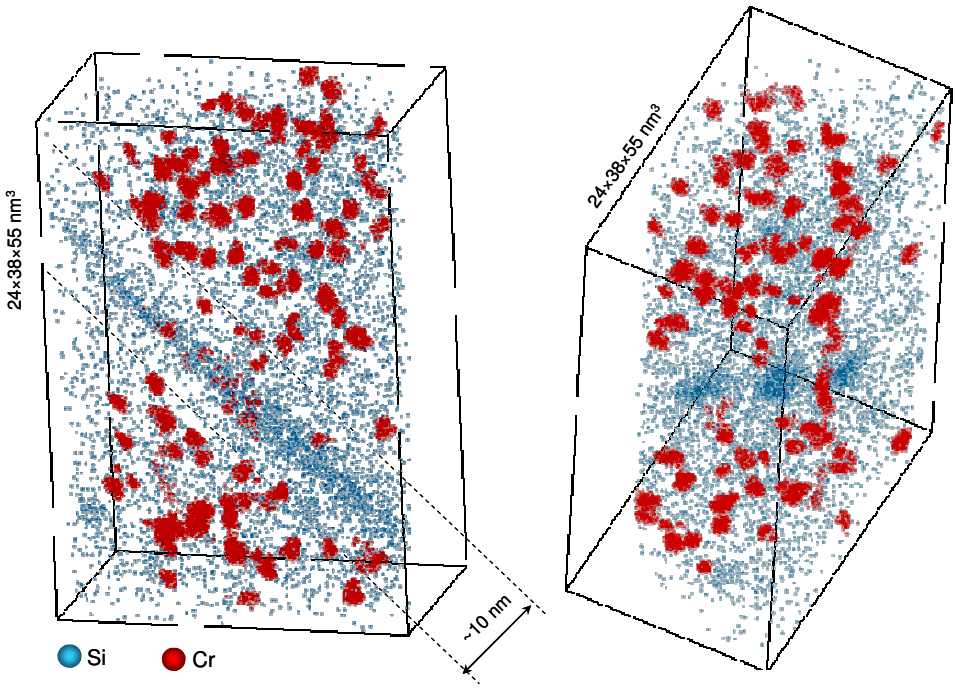

Figure 4.25. 3D distribution of Si and Cr atoms in the alloy Fe-12%atCr after neutron irradiation at 300°C up to 0.6 dpa. Only Cr atoms which are inside Cr-enriched clusters are presented (Cr concentration is higher than 28at%) whereas all the Si atoms are shown (in blue).

Figure 4.25 presents two different 3D views of the same grain boundary intercepted during the analysis of the Fe-12%Cr alloy irradiated at 300°C up to 0.6 dpa. The number density of Cr-enriched clusters after irradiation inside the grains is relatively high (about $(5.0\pm0.5)\cdot10^{24}$ m^{-3}), while only few small Cr-enriched clusters are revealed around the grain boundary in a zone of about 10 nm wide.

As it is evident from Figure 4.25(b), the Si segregation on this GB is not homogeneous inside the plane of the GB. It is mainly located along the lines which must be accommodation dislocation lines. The mean distance between the dislocation lines is about 8 nm.

Owing to the desorption image which reveals low-indexes crystallographic poles and traces between them (Figure 4.26(b)), the crystallographic orientation of the tip has been estimated. Zone axis of the tip is about [156], the major crystallographic directions are presented on the stereographic projection in Figure 4.26(c). Owing to these data, it was obtained that the GB lies in the $(\bar{1}11)$ plane and that the dislocations lie along the [211] direction. Such orientation and distribution of dislocations of a grain boundary is characteristic of a simple tilt boundary which consists of edge dislocations. Schematically the structure of such GB is presented in Figure 4.27. Since only {111} and {100} Burgers vectors are possible for dislocations in bcc iron, current dislocation lines should have $b=\frac{1}{2}a_0[\bar{1}11]$, since this vector is normal to the $(\bar{1}11)$ GB plane and perpendicular to the [211] dislocation lines. The glide plane of these dislocations must then be $(01\bar{1})$.

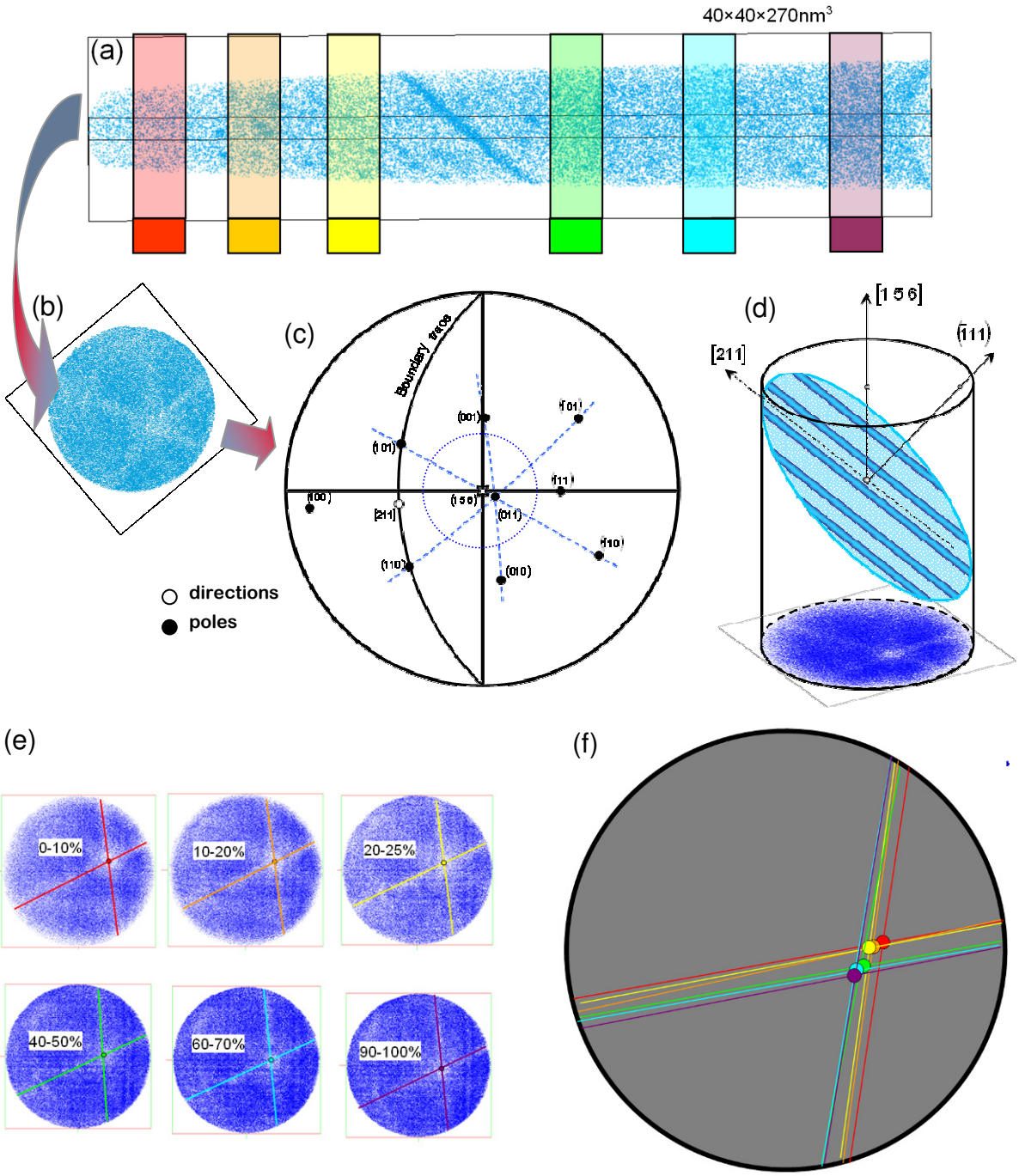

Figure 4.26. (a) – 3D reconstruction of an analyzed volume of the Fe-12%Cr alloy after neutron irradiation at 300°C up to 0.6 dpa and the stereographic projection which correspond to the orientation of the analyzed volume. Only Si atoms are presented; (b) – the "top view" shows the desorption line, which corresponds to the blue lines between low-index poles presented on the stereographic projection presented on image (c). Zone axis of the tip is ~ [156]; (d) – a schematic picture of the orientation of the sub-grain boundary and of the dislocation lines in the analyzed volume. (e) – "top view" images which have been taken at different depth of analysis. They show the shift of the crystallographic directions during the experiment; (f) – summary of successive positions of the (011) pole collected from the images (e) – which highlight the shift of the pole from one grain to the other (between yellow and green positions)

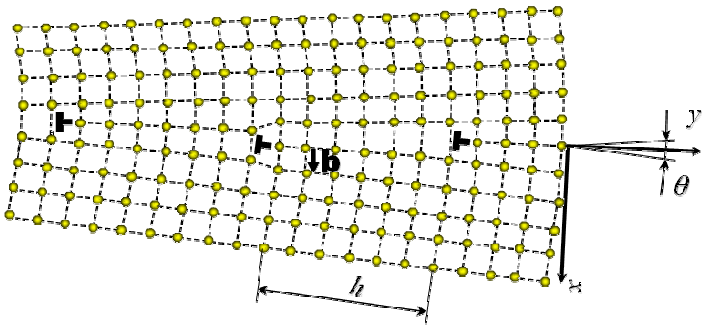

Figure 4.27. Diagram of the structure of tilt sub-grain boundary which consist of edge dislocations

Knowing the distance between dislocation lines (h≈8 nm) and the Burgers vector (b = a/2[111] =0.248nm) it is possible to estimate the angle of misorientation of this sub-grain boundary from the general formula: $tg\left(\frac{\theta}{2}\right)=\frac{b}{2h}$. The angle $\theta = 1.75°$ has been calculated. It is also possible to estimate this angle owing to measurements on the 3DAP analyzed volume. Indeed, as shown in Figure 4.26((e) and (f)), the pole (011), which is well recognizable on the "top view" image, exhibits a slight monotonic shift during experiment. This is most likely due to the fact that the tip axis is not exactly normal to the plane of the detector. However, it is evident that passing the volume which contain the GB, this shift is clearly modified (compare "top view" images 20 to 25% and 40 to 45% in Figure 4.26(e)). It is not obvious to deduce the exact degree value of this shift, but its order of magnitude (up to few degree) is consistent with the one deduced from the geometrical calculation described above. This example illustrates the potential of 3DAP to analyze the crystallographic features of the detected objects at the atomic scale.

Let us now characterize the chemistry of this GB. The composition profiles drawn across and inside the grain boundary are presented in Figure 4.28 (b) and (d). These profiles clearly shows an enrichment of Cr at the GB (in terms of solute excess $C_{boundary} - C_{matrix}$) of about 1.5% across the grain boundary and 4 to 6at% inside the grain boundary plane. Note that the peaks of Cr which are observed outside the GB correspond to Cr-enriched clusters (Figure 4.28(b)). Si and P also exhibit enrichment on the current GB and the absolute solute excess of these species reaches 0.7at% (up to 1.5at% on dislocation cores) and 0.15at% respectively on the profile drawn across the GB. The comparison with the single dislocation lines in the Fe-5%Cr alloy (Figure 4.19(c) and Figure 4.20) shows that dislocation accommodation lines exhibit a lower enrichment by segregated elements. Because of the mass resolution of the LAWATAP, no information concerning Ni atoms have been collected (see Chapter 2 for details).

Both the 3D atom probe reconstruction (Figure 4.28(c)) and the concentration profiles (Figure 4.28(d)) drawn inside the grain boundary plane, perpendicularly to the dislocation lines, reveal a systematic shift between Si and Cr segregations. This behaviour has been already observed for the single dislocation lines observed in the Fe-5%Cr model alloy described previously. As in the mentioned case, two possible phenomena can explain this shift: the redistribution of oversized Cr

and undersized Si with respect to the stress field around the dislocation lines or an artificial shift due to the evaporation behavior of the different chemical species. However, it is possible to emphasize that no correlation was found between this shift and the position of the dislocation lines with respect to the (110) pole: as observed in Figure 4.28(c) and (d), there is no change of the shift along the lines. So, the latter hypothesis appears to be invalidated. At the same time, the fact that Cr and Si exhibit a shift within the grain boundary plane is in a good agreement with the fact that dislocation lines should have $b=\frac{1}{2}a_0[\bar{1}11]$ (see above).

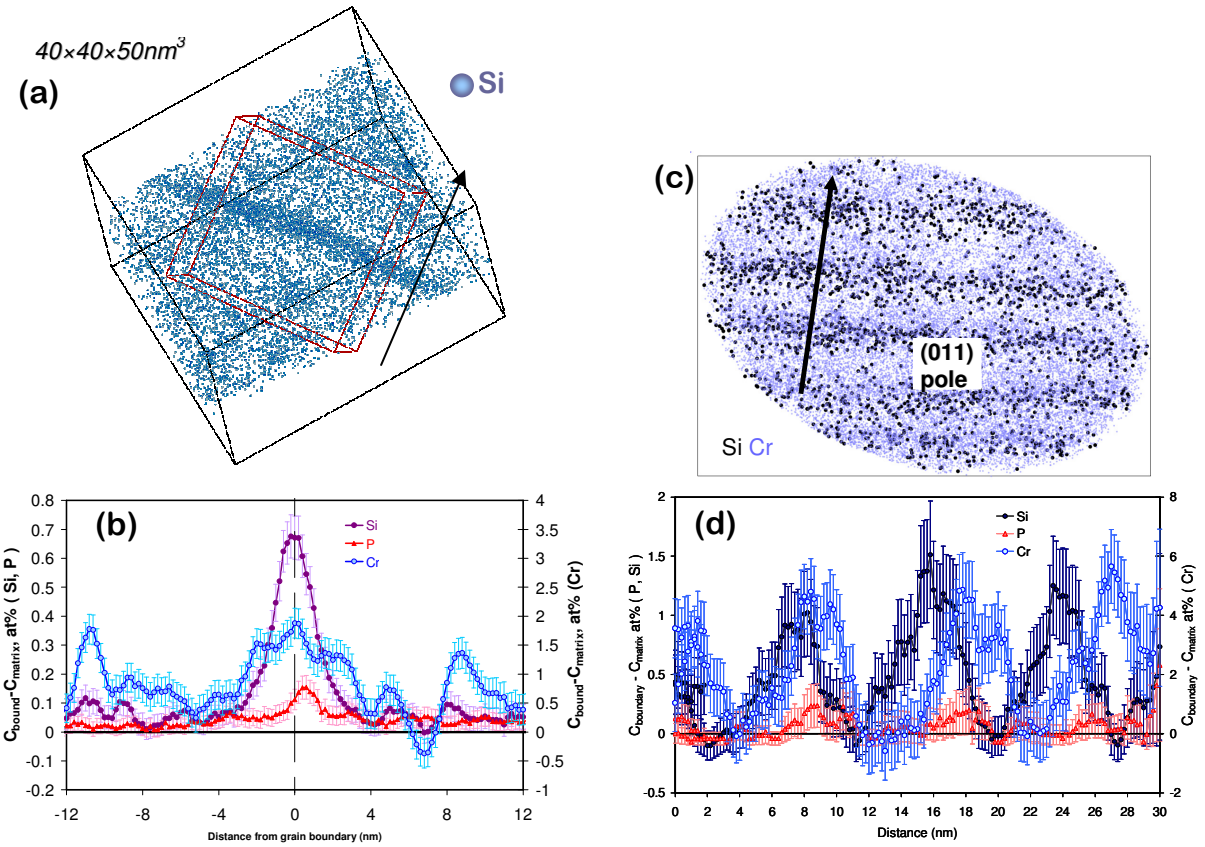

Figure 4.28: (a) 3D distribution of the Si atoms in the alloy Fe-12%atCr after neutron irradiation at 300°C up to 0.6 dpa which reveals the precence of a GB. (b) Variation of Cboundary - Cmatrix measured through the grain boundary plane, (as shown by the arrow in image (a)). $C_{boundary}$ corresponds to the concentration measured in the sampling volume ($30\times30\times1nm^3$) used to construct the concentration profile. (c)3D elemental map of Si and Cr atoms in the grain boundary plane ($V = 41\times59\times4\ nm^3$). (d) Variation of $C_{boundary}$ - C_{matrix} measured inside the grain boundary plane, perpendicularly to the dislocation lines (as shown by the arrow in image (c)). $C_{boundary}$ corresponds to the concentration measured in the sampling volume ($16\times4\times6\ nm^3$) used to construct the concentration profile. C_{matrix} in both cases is equal to the concentration of the elements measured in the α matrix inside the grains.

Another example of a tilt sub-grain boundary (SGB) has been obtained in the Fe-9%Cr alloy irradiated at 300°C up to 0.6 dpa (Figure 4.29). Owing to the segregations on the accommodation dislocation lines one can clearly spot the presence of a GB. The mean

distance between the dislocation lines is about 5nm. It is evident that, as in the case the Fe-12%Cr alloy, the SGB is also surrounded by a zone without clusters. The width of this zone is about 13 nm from each side of the boundary.

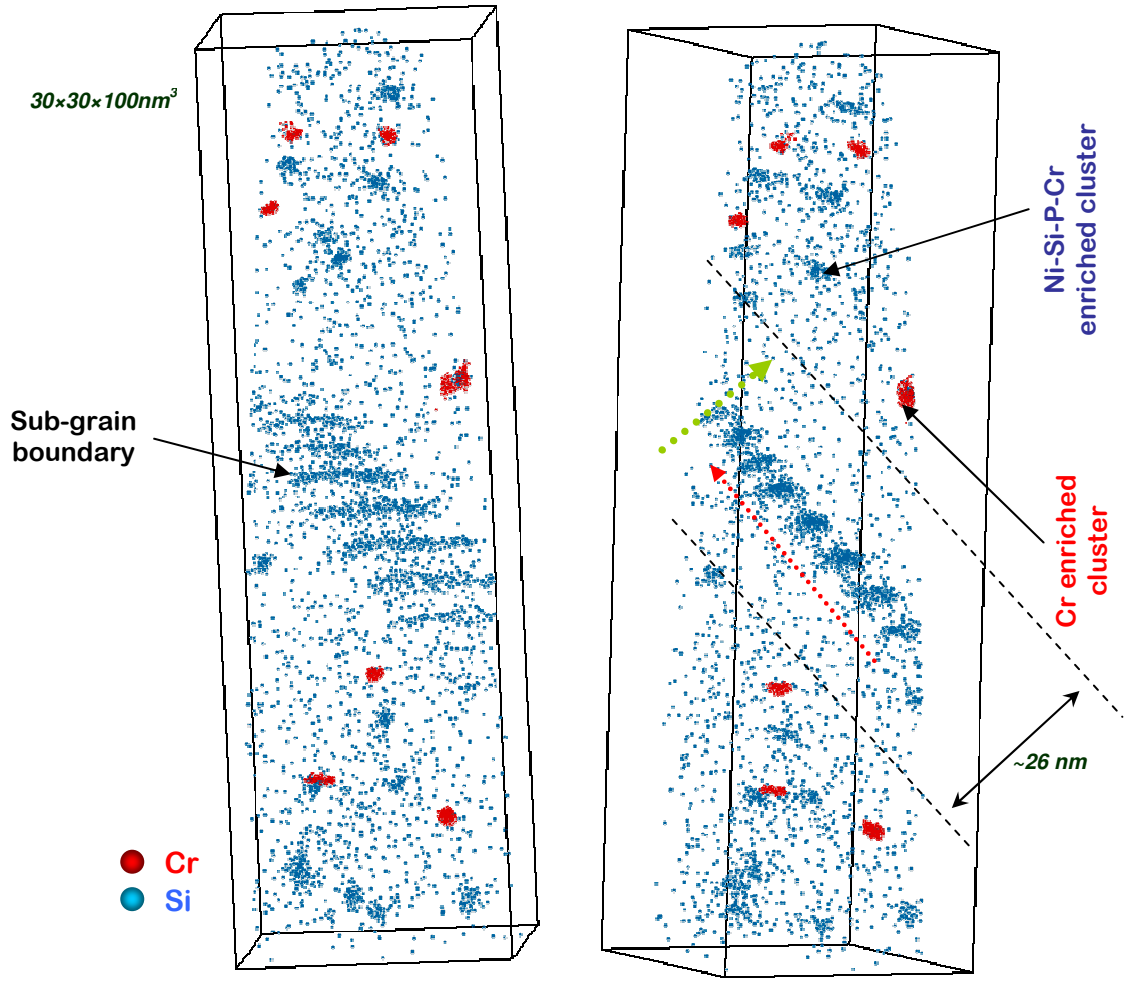

Figure 4.29. (a) and (b) 3D distribution of Si and Cr atoms of an analyzed volume of the Fe-9%Cr alloy after neutron irradiation at 300°C up to 0.6 dpa. Only Cr atoms which are inside Cr-enriched clusters are presented (Cr concentration is higher than 24at.%.) whereas all the Si atoms are shown (in blue). Colored arrows show the direction of the composition profiles drawn across (green arrow, see Figure 4.30(a)) and inside (red arrow, see Figure 4.30(b)) sub-grain boundary.

It is evident from the concentration profile presented in Figure 4.30(a) and which has been made across the GB (along the green arrow), that the dislocation lines are enriched by Cr, P and Si. This is consistent with the previous results. The concentration profile drawn inside the grain boundary plane perpendicularly to the dislocation lines (red arrow in Figure 4.30(b)), also reveals a systematic shift between Si and Cr segregations. One can note that whatever the orientation of the tip, we always observe a similar shift. This clearly is in favor of a redistribution of the species owing to the stress fields.

The concentration profiles in Figure 4.30(a) and (b) show that the maximum solute excess for Cr is about 3.5at% across the grain boundary plane and 6 to 8at% inside the grain

boundary plane. The measured values seem to be slightly higher that the ones observed in the accommodation dislocation lines in the Fe-12%Cr model alloy (Figure 4.28 (b) and (d)).

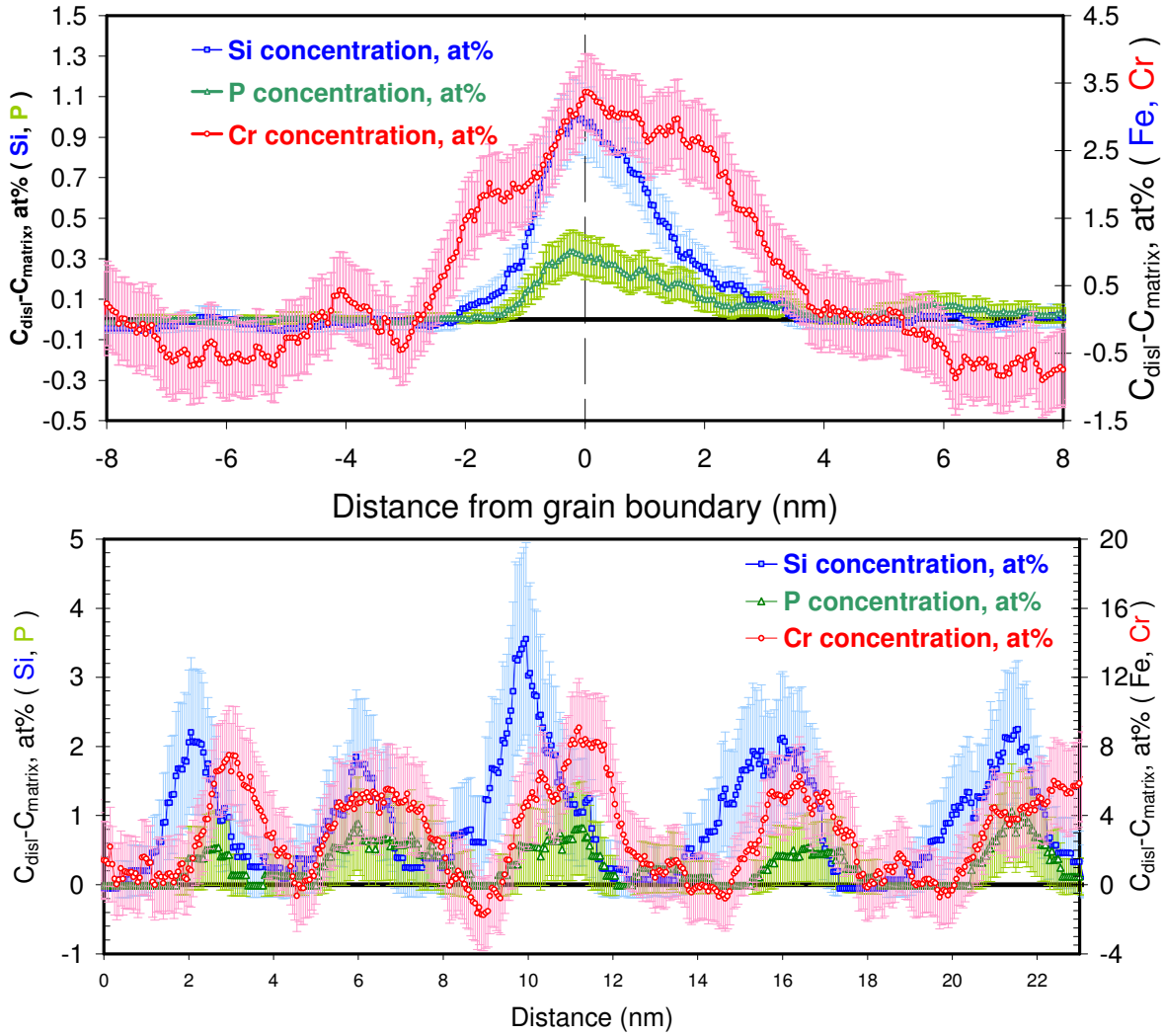

Figure 4.30. (a) Variation of $C_{boundary}$ - C_{matrix} measured across the grain boundary plane, (as shown by the green arrow in Figure 4.29 (b)). $C_{boundary}$ corresponds to the concentration measured in the sampling volume (15×10×1nm^3) used to construct the concentration profile. (b) Variation of $C_{boundary}$ - C_{matrix} measured inside the grain boundary plane, perpendicularly to the dislocation lines as shown by the red arrow in Figure 4.29 (b))). $C_{boundary}$ corresponds to the concentration measured in the sampling volume (10×2 ×1 nm^3). C_{matrix} in both cases is equal to the concentration of the element measured in the α matrix inside the grains.

These two examples of tilt sub-grain boundary shows a quite similar segregation behavior. A more complex grain boundary has been observed in the neutron irradiated Fe-12%Cr model alloy. As shown in Figure 4.31, this grain boundary consists of a network formed by few sets of dislocations. Such shape indicates that this boundary has a twist component. The meshes of the net have somewhat deformed hexagonal shape. Some meshes seem to differ in shape, having different numbers of sides. Such irregularities may arise from the fact that the GB didn't reach full equilibrium during annealing or due to so-called "stranger dislocations" (i.e. dislocations which

have either a different Burgers vector or are not parallel to those of the same Burgers vectors forming the bulk of the net) which join the net and distort the shape of the meshes [52].

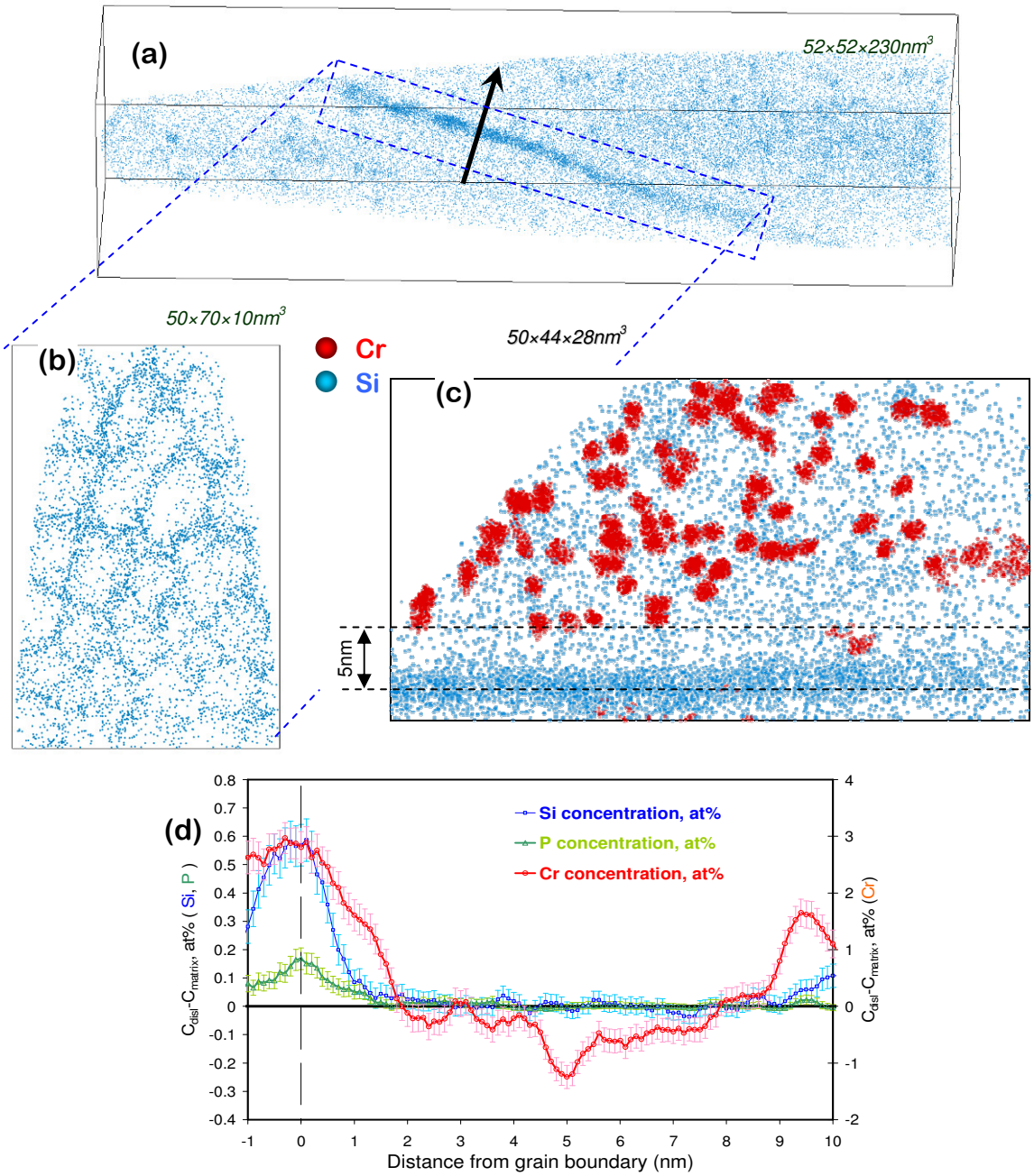

Figure 4.31. (a, b and c) Distribution of Si and Cr atoms inside the sub-grain boundary in the Fe-12%Cr alloy after neutron irradiation at 300°C up to 0.6 dpa. Only Cr atoms which are inside Cr-enriched clusters are presented (Cr concentration is higher than 28at.%.) whereas all the Si atoms are shown (in blue); (d) Variation of $C_{boundary}$ - C_{matrix} measured through the grain boundary plane, (as shown by the arrow in image (a)). $C_{boundary}$ corresponds to the concentration measured in the sampling volume (30×30×1nm^3) used to construct the concentration profile.

A zone of 5 nm in depth from each side of the GB is almost free of clusters, only few small Cr-enriched clusters are exhibited. This value corresponds to the one observed around the tilt subboundary in the same model alloy (see Figure 4.25). The composition profile across the

grain boundary is presented in Figure 4.31(d). As in the case of the previous sub-grain boundaries, this profile reveals an enrichment in Cr, P and Si on the GB. Because of the mass resolution of the LAWATAP, no information concerning Ni atoms have been collected (see Chapter 2 for details). Comparison of concentration profiles in Figure 4.28(b) and Figure 4.31 (d) shows that despite the different structure of these subboundaries in Fe-12%Cr model alloys, the measured maximum enrichment for all segregated elements is quite similar: an absolute excess of Cr of about 2 to 3at%, about 0.15at% for P, and 0.6 to 0.7at% in the case of Si.

c) Irradiated state: high angle grain boundaries

Conventional high-angle grain boundaries have been revealed owing to the flat segregation of Cr, Si and P. Figure 4.32 presents three 3D maps of the distribution of Si, Cr and P which reveal the junction of three grain boundaries in the Fe-9%Cr alloy irradiated at 300°C up to 0.6 dpa.

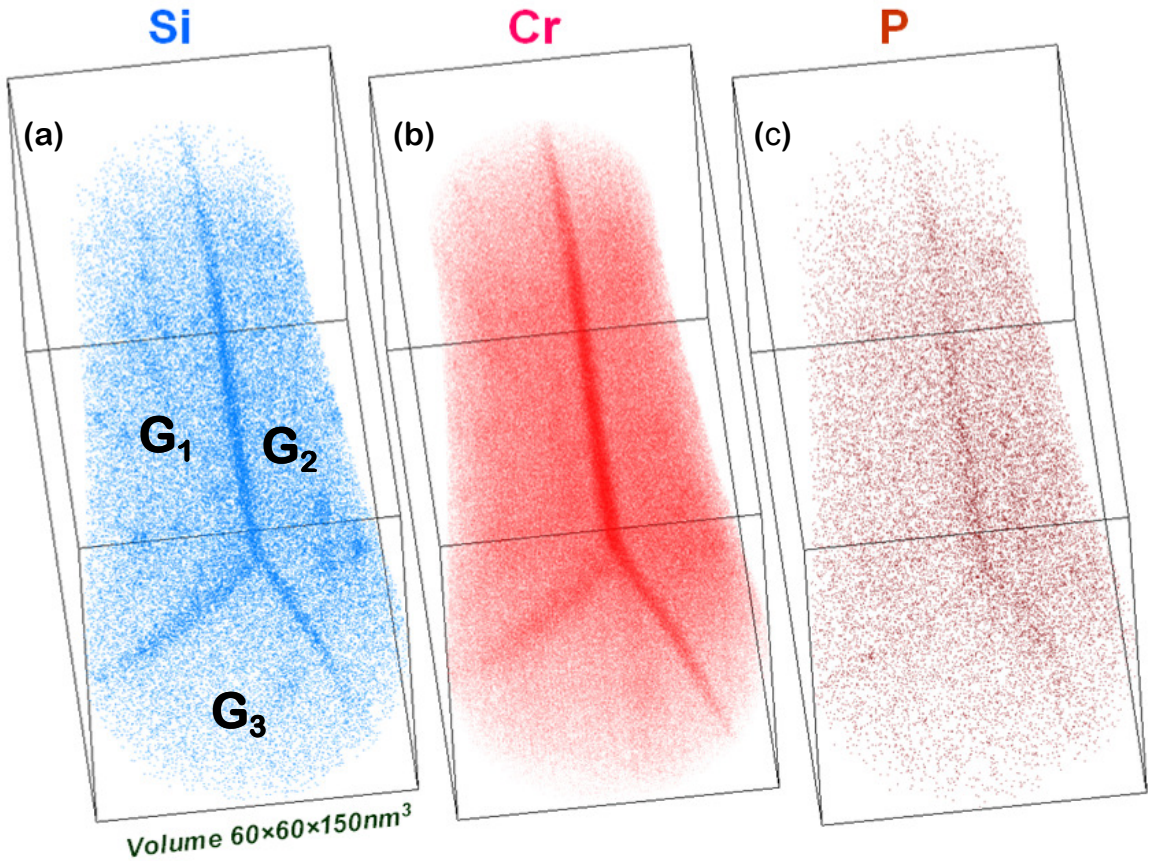

Figure 4.32. 3D distribution of Si (a), Cr(b)and P(c) atoms in the alloy Fe-9%atCr after neutron irradiation at 300°C up to 0.6 dpa. Segregations of highlighted elements reveal the junction of three grain boundaries.

Composition profiles in terms of solute excess ($C_{boundary} - C_{matrix}$) across the three grain boundaries are presented in Figure 4.33. All the three profiles show enrichment in Cr and Si on the GBs. Concerning P, the behavior is not so clear. It seems that small enrichment exists

on boundaries between the first and second grains, as well as between the second and the third ones. It is in good agreement with 3D map of P distribution in Figure 4.32(c). The enrichment by P atoms on the boundaries between first and second as well as second and third grains can be recognized visually, while the P segregation between the first and third grain is quite diffuse and almost invisible.

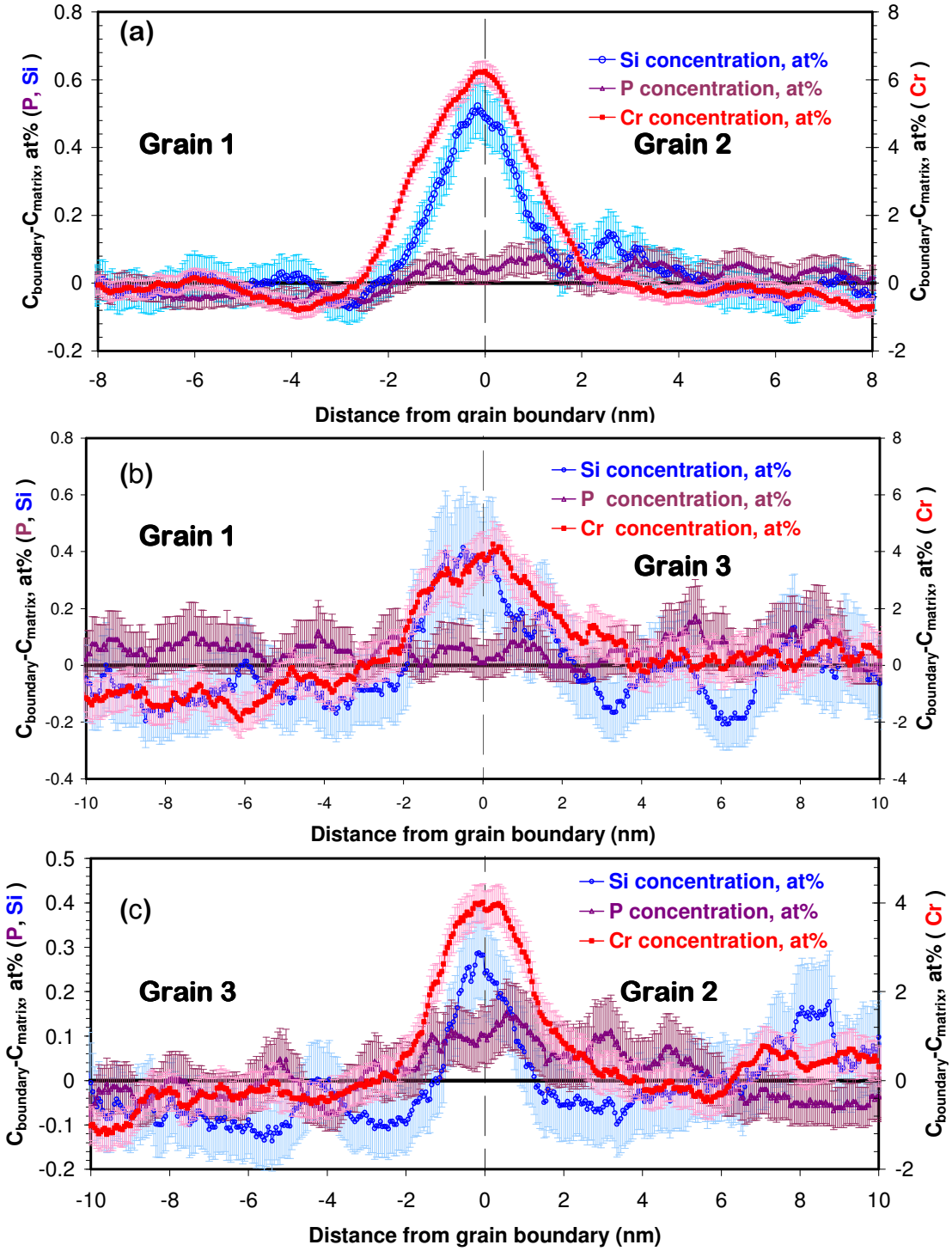

Figure 4.33. Variation of $C_{boundary}$ - C_{matrix} measured across 3 grain boundary planes: (a) – from the grain No 1 to No 2, sampling volume (20×30×1 nm^3), (b) – from the grain No 1 to No 3, sampling volume (10×10×1 nm^3); (c) – from the grain No 3 to No 2, sampling volume (15×15×1 nm^3). The numbers of grains corresponds to the numbers in Figure 4.29

Quantitatively, the enrichment in Cr and Si on the three grain boundaries is quite similar, even if the excess of Cr on the boundary between the first and the second grain is slightly higher, and the excess of Si on the boundary between the second and the third grain is slightly lower. This could arise from differences of grain boundary energies. Indeed, it is known that changes in grain boundary energy affect the values of the chemical potentials of the solute and matrix elements at the grain boundary and results in anisotropy of grain boundary segregation [53].

For example, the study of RIS of Cr in austenitic stainless steel shows dependence of the solute excess on grain boundary orientation and state of the grain boundary before irradiation [54,55]. Similar behaviors are expected to exist in F-M steels and model alloys. But of course, first we have to make sure that these differences are significant. The only way to answer to this question is to undertake systematic investigation of different GB owing to a coupling between EBSD and 3DAP.

Concerning the possible RIS or RID of Cr at grain boundary, the present results (of low- and high-angle GB) exhibit a Cr enrichment. Nevertheless, the lack of 3DAP data on grain boundaries in the as-received states made it impossible to conclude on the behavior of Cr under irradiation in these alloys. Understanding of the RIS behavior of Cr depends on whether the enrichment observed after 0.6 dpa is higher or lower than the enrichment at pre-irradiated grain boundaries. Due to tempering at 730°C for 4 h, thermal segregation of Cr at grain boundaries occur, as it was observed by EDX measurements in Chapter 4.II.2.a) on page 151. However, EDX results can't be quantitatively compared to 3DAP results. The same conclusions are also relevant for Si, P and Ni, since no data on segregation of these elements on GB's before irradiation is currently available. This means that investigations of grain boundaries in the as-received state or in the same alloy irradiated at lower or higher doses, are necessary to go further.

III. Conclusions

Owing to 3DAP, new features of the microstructure of the Fe-5%Cr, Fe-9%Cr and Fe-12%Cr model alloys after neutron irradiation at 300°C up 0.6dpa have been revealed:

NiSiPCr-enriched clusters have been observed in all three model alloys. These are probably irradiation induced clusters and could be precursors of Ni-Si-enriched phases typically observed in high-chromium F-M steels after irradiation. Their contents of Ni, Si and P are roughly constant (within uncertainties) for the three model alloys. About 1.2 to 1.7at% of Ni, 6.4 to 7.9at% of Si and 2.1 to 3.3% of P are detected in these clusters. The chromium content increases with the nominal chromium composition of the alloys and is equal to about 10.4at%, 15.5at% and 24.2at% in the Fe-5%Cr, Fe-9%Cr and Fe-12%Cr model alloys respectively. The number density of these clusters is almost equal in all model alloys ($1.1 \cdot 10^{23}$ to $2.4 \cdot 10^{23}$ m^{-3}) and their mean radii are quite similar (from 1.6 to 2nm). The clusters have non-regular shape: some of them are almost spherical whereas others have ellipsoidal and disk like shapes. Available TEM data don't allow to link these clusters to dislocation loops created under irradiation but the crystallographic study of their orientation in 3DAP volumes allowed to suggest that these clusters are associated to small dislocation loops invisible by TEM.

Almost spherical Cr-enriched clusters have been observed in the Fe-9%Cr (number density equal $(1.3 \pm 0.3) \times 10^{23}$ m^{-3}) and Fe-12%Cr (number density equal $(5.0 \pm 0.5) \times 10^{23}$ m^{-3}) model alloys. These clusters have an irradiation enhanced origin and correspond to α' formation. Their volume fraction is estimated to 0.14% and 4% in the Fe-9%Cr and Fe-12%Cr alloys respectively. Their mean radius is similar in the two model alloys and equal to (1.1 ± 0.2) nm. Cr concentration in clusters reaches (55.1 ± 3.5) at% and (58.5 ± 1.1) at% in the Fe-9%Cr and Fe-12%Cr alloys respectively. The presence of Si is also observed in these clusters in the Fe-12%Cr alloy.

Owing to 3DAP, segregations of Si, P and Cr atoms have been revealed on dislocation lines, low- angle grain boundaries (which consist of accommodation dislocation lines) and high-angle grain boundaries. Some Ni enrichment has been also observed when 3DAP enabled to detect Ni atoms. Zones almost free of clusters are exhibited around all the GBs. 3D reconstructions exhibit a shift between Si and Cr segregations with respect to the cores of the dislocations. This shift is probably a signature of the stress field around the dislocation lines.

IV. References

[1] R.L. Klueh, D.R. Harries, High-Chromium Ferritic and Martensitic Steels for Nuclear Applications, ASTM, Bridgeport, 2001.

[2] M. Matijasevic, A. Almazouzi, Journal of Nuclear Materials 377 (2008) 147-154.

[3] M. Matijasevic, E. Lucon, A. Almazouzi, Journal of Nuclear Materials 377 (2008) 101-108.

[4] F. Bergner, A. Ulbricht, C. Heintze, Scripta Materialia 61 (2009) 1060-1063.

[5] C. Heintze, F. Bergner, A. Ulbricht, H. Eckerlebe, Journal of Nuclear Materials 409 (2011) 106-111.

[6] S. Novy, P. Pareige, C. Pareige, Journal of Nuclear Materials 384 (2009) 96-102.

[7] M. Hernandez-Mayoral, Z. Yao, M.L. Jenkins, M.A. Kirk, Phil. Mag. 88 (2008) 2881-2897.

[8] Z. Yao, M. Hernández-Mayoral, M.L. Jenkins, M.A. Kirk, Philosophical Magazine 88 (2008) 2851.

[9] V. Krsjak, V. Slugen, M. Miklos, M. Petriska, P. Ballo, Applied Surface Science 255 (2008) 153 - 156.

[10] Matijasevic M., Microstructure and Mechanical Properties of Fe-Cr Model Alloys and High Cr Steels Under Neutron Irradiation, PhD thesis, Gent University, 2007.

[11] C. Heintze, A. Ulbricht, F. Bergner, H. Eckerlebe, J. Phys.: Conf. Ser. 247 (2010) 012035.

[12] M.K. Miller, A. Cerezo, M.G. Hetherington, G.D.W. Smith, Atom Probe Field Ion Microscopy, Clarendon PRESS, Oxford, 1996.

[13] D. Blavette, F. Vurpillot, P. Pareige, A. Menand, Ultramicroscopy 89 (2001) 145-153.

[14] F. Vurpillot, A. Bostel, D.Blavette, Applied Physics Letters 76-21 (2000) 3127–3129.

[15] E.A. Marquis, F. Vurpillot, Microscopy and Microanalysis 14 (2008) 561-570, doi:10.1017/S1431927608080793.

[16] M. Roussel, Etude En Sonde Atomique De L'evolution Microstructurale D'alliages Modeles Fe-Cr Vieillis Thermiquement. Master Thesis, GPM, University of Rouen, 2009.

[17] E.A. Marquis, J.M. Hyde, Materials Science and Engineering: R: Reports 69 (2010) 37-62.

[18] Derek Hull, D.J. Bacon, Introduction to Dislocations, Fourth Edition, 4th ed., Butterworth-Heinemann, University of Cambridge, 2001.

[19] Gelles D.S, Thomas L.E, Proc. Topical Conf. on Ferritic Alloys for Use in Nuclear Energy Technologies, Eds. J.W. Davis and D.J. Michel.AIME (1984) 559.

[20] G. Bonny, D. Terentyev, L. Malerba, Scripta Materialia 59 (2008) 1193-1196.

[21] W. Xiong, M. Selleby, Q. Chen, J. Odqvist, Y. Du, Critical Reviews in Solid State and Materials Sciences Volume 35 (2010) 125 - 152.

[22] J.-O. Andersson, B. Sundman, Calphad 11 (1987) 83-92.

[23] F. Vurpillot, M. Gruber, S. Duguay, E. Cadel, B. Deconihout, in:, AIP Conference Proceedings. Eds. Secula, Erik M.; Seiler, David G.; Khosla, Rajinder P.; Herr, Dan; Garner, C.Michael; McDonald, Robert; Diebold, Alain C., Albany (New York), 2009, pp. 175-180.

[24] S. Novy, Mécanismes De Vieillissement à Très Longue Échéance Des Aciers Inoxydables Austéno-ferritiques, PhD thesis. UNIVERSITE DE ROUEN, 2009.

[25] P.E. L'vov, V.V. Svetukhin, A.V. Obukhov, Physics of the Solid State 53 (2011) 421-427.

[26] K.. Russell, Progress in Materials Science Volume 28 (1984) 229-434.

[27] S. Choudhury, L. Barnard, J.D. Tucker, T.R. Allen, B.D. Wirth, M. Asta, D. Morgan, Journal of Nuclear Materials 411 (2011) 1-14.
[28] B. Radiguet, Etude De La Formation D'amas Diffus De Solutés Sous Irradiation Dans Des Alliages Modèles Ferritiques, PhD thesis. UNIVERSITE DE ROUEN, 2004.
[29] E. Wakai, A. Hishinuma, Y. Kato, H. Yano, S. Takaki, K. Abiko, Le Journal De Physique IV 05 (1995) 10.
[30] I.M. Neklyudov, V.N. Voyevodin, Journal of Nuclear Materials 212-215 (1) (1994) 39-44.
[31] S. Ohnuki, H. Takahashi, T. Takeyama, Journal of Nuclear Materials 122 (1984) 317-321.
[32] W.F. Gale, T.C. Totemeier, Smithells Metals Reference Book, Eighth Edition, 8th ed., Butterworth-Heinemann, 2004.
[33] U. Starke, J. Schardt, W. Weiss, W. Meier, C. Polop, P.L. de Andres, K. Heinz, Europhys. Lett. 56 (2001) 822-828.
[34] SpringerMaterials - The Landolt Börnstein Database, http://www.springermaterials.com/navigation/index.html, 2011.
[35] Thermo-calc®, http://www.thermocalc.com/software.htm, database TCFE5., 2011.
[36] T.S. Morgan, E.A. Little, R.G. Faulner, Effect of Radiation on Materials, Eds. R. E. Stoller, A. S. Kumar and D. S. Gelles 16th Intarnational Symposium, ASTM STP 1175 (1994) 607.
[37] P.J.Maziasz, Journal of Nuclear Materials 169 (1989) 95-115.
[38] B. Radiguet, A. Barbu, P. Pareige, Journal of Nuclear Materials 360 (2007) 104-117.
[39] P. Pareige, B. Radiguet, A. Barbu, Journal of Nuclear Materials 352 (2006) 75-79.
[40] E. Meslin, B. Radiguet, P. Pareige, A. Barbu, Journal of Nuclear Materials 399 (2010) 137-145.
[41] S. Jumel, C. Domain, J. Ruste, J.-C. Van Duysen, C. Becquart, A. Legris, P. Pareige, A. Barbu, E. Van Walle, R. Chaouadi, M. Hou, G. Odette, R. Stoller, B. Wirth, Journal of Testing and Evaluation 30 (2002) 37-46.
[42] E. Meslin, M. Lambrecht, M. Hernández-Mayoral, F. Bergner, L. Malerba, P. Pareige, B. Radiguet, A. Barbu, D. Gómez-Briceño, A. Ulbricht, A. Almazouzi, Journal of Nuclear Materials 406 (2010) 73-83.
[43] M.K. Miller, B.D. Wirth, G.R. Odette, Materials Science and Engineering A 353 (2003) 133 - 139.
[44] R.G. Carter, N. Soneda, K. Dohi, J.M. Hyde, C.A. English, W.L. Server, Journal of Nuclear Materials 298 (2001) 211 - 224.
[45] P. Wilkes, Journal of Nuclear Materials 83(1) (1979) 166-175.
[46] E.A. Little, R. Bullough, M.H. Wood, Proceedings of the Royal Society of London. A. Mathematical and Physical Sciences 372 (1980) 565 -579.
[47] A.H. Cottrell, B.A. Bilby, Proc. Phys. Soc. A 62 (1949) 49-62.
[48] C.A. Williams, J.M. Hyde, G.D.W. Smith, E.A. Marquis, Journal of Nuclear Materials 412 (2011) 100-105.
[49] Z. Lu, R.G. Faulkner, G. Was, B.D. Wirth, Scripta Materialia 58 (2008) 878-881.
[50] G.S. Was, J.P. Wharry, B. Frisbie, B.D. Wirth, D. Morgan, J.D. Tucker, T.R. Allen, Journal of Nuclear Materials In Press, Corrected Proof (2011).
[51] E.A. Marquis, S. Lozano-Perez, V. de Castro, Journal of Nuclear Materials In Press, Accepted Manuscript (n.d.).
[52] W. Carrington, K.F. Hale, D. McLean, Proceedings of the Royal Society A: Mathematical, Physical and Engineering Sciences 259 (1960) 203-227.
[53] P. Lejcek, Grain Boundary Segregation in Metals, Springer-Verlag Berlin and Heidelberg GmbH & Co. K, 2010.

[54] T.S Duh, J.J Kai, F.R Chen, Journal of Nuclear Materials 283-287 (2000) 198-204.
[55] S. Watanabe, Y. Takamatsu, N. Sakaguchi, H. Takahashi, Journal of Nuclear Materials 283-287 (2000) 152-156.

CHAPTER 5.

ION IRRADIATION EXPERIMENTS

Non-ODS high-Cr F-M steels are expected to be used from about 300°C up to about 500 to 550°C. The study of the response of the Fe-Cr model alloys under irradiation in this temperature range is of large interest for technological and modeling purposes. In order to investigate the effect of irradiation on the microstructure of the Fe-Cr model alloys the temperature equal to 300°C and 500°C has been chosen for ion irradiation experiments. Two model alloys, namely the Fe-9%Cr and Fe-12%Cr, have been irradiated with 150 keV Fe^{+} ions up to 1.5 dpa and investigated after by means of TEM (irradiation at 500°C) and 3DAP (irradiation at 300°C and 500°C).

As it was mentioned in the first chapter, the position of the solubility limit of the α–α′ miscibility gap position at low temperatures is still debatable. As it has been shown in the Chapter 4, the solubility of Cr in Fe at 300°C is less then 9at% and the irradiation enhanced phase separation is expected in both model alloys. However, in order to adjust the α–α′ miscibility gap position and to define the possible irradiation enhanced processes during irradiation at 500°C, thermal ageing of the chosen model alloys has been performed at the same temperature. The results of 3DAP experiments on the thermally aged Fe-9%Cr and Fe-12%Cr model alloys are presented in the first part of this chapter.

The current chapter describes the effect of the low-energy ion irradiation on both dislocation structure evolution (in-situ TEM investigation) and the evolution of the chemical elements distribution (3DAP experiments). The results of this study are presented and discussed in the second and the third part of the current chapter respectively. The obtained data are analyzed and compared with data of other authors in the forth part of chapter.

The chapter ends by a conclusion of the former sections.

TABLE OF CONTENT

I. Thermal ageing of model alloys at 500°C

I.1. Ageing of the Fe-9%Cr model alloy

The Fe-9%Cr alloy has been aged for 300h at 500°C and investigated by 3DAP in order to check the influence of this treatment on the randomness of the spatial distribution of chromium at the nanoscale. As shown by the 3D distribution map in Figure 5.1, chromium atoms appear homogeneously distributed after this ageing. The measured chromium concentration in the overall analyzed volume is: (9.35±0.10)at.% (Table 5.1). That is in good agreement with the data obtained on this model alloy in the as-received state (Table 3.4, p. 99). Homogeneous distribution of Cr atoms is confirmed by statistical test (Figure 5.2). Indeed, on this figure the s-curve of the experimental distribution coincides with the binomial one that indicates the homogeneous distribution of this specie in the alloy.

Table 5.1 Chemical composition of the thermally aged Fe-9%Cr model alloy (at%) measured by 3DAP

Fe	balance
Cr	9.35 ±0.10
Si	0.17 ±0.01
P	0.05 ±0.01
Ni	0.03 ± 0.01
Mn, V, C, N, O, S, Al, Ti	*not measurable*

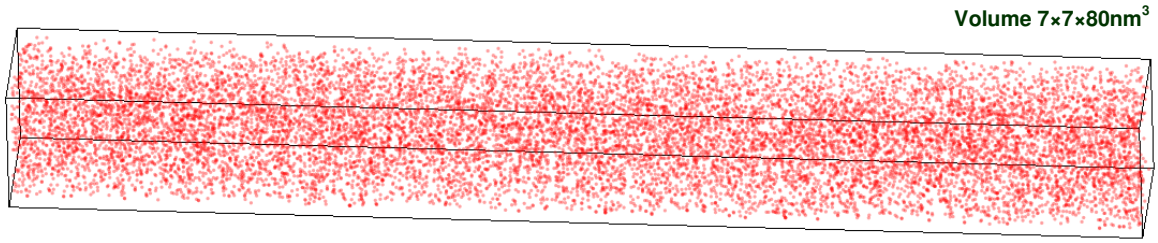

Figure 5.1. 3D distribution of chromium atoms in the Fe-9%Cr model alloy after300h of aging at 500°C. Chromium is homogeneously distributed after aging.

No α′ precipitation has been observed after ageing. The Fe-9%Cr alloy lies in the one-phase region of the phase diagram at 500°C. It is in good agreement with the proposed Fe-Cr phase diagrams [1–3], as it will be shown in the discussion part. This means that just irradiation induced phase separation can be expected during irradiation at this temperature.

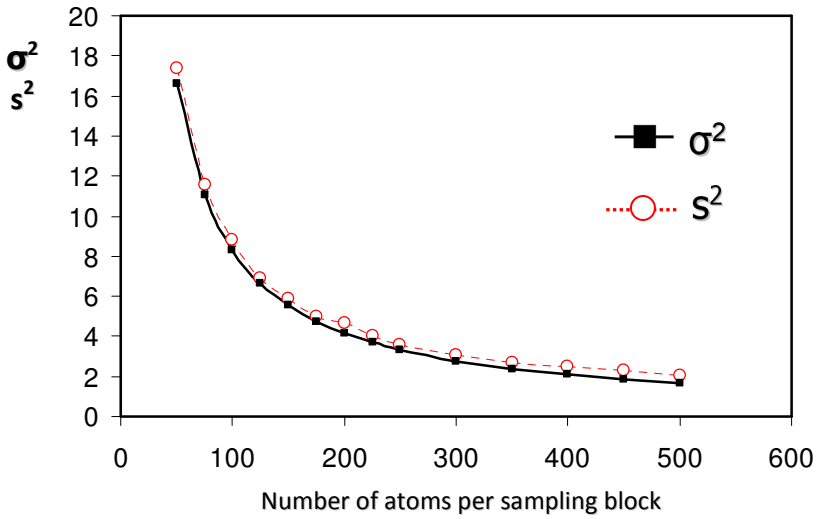

Figure 5.2. Comparison of the standard error (s) with the standard deviation (σ) in the Fe-9%Cr model alloy after 300 h of aging at 500°C. Experimental distribution almost coincides with the binomial one. Chromium atoms are homogeneously distributed.

I.2. Ageing of the Fe-12%Cr model alloy

As in the Fe-9%Cr alloy, thermal ageing of the Fe-12%Cr alloy has been performed at 500°C. The ageing has been performed for 600h and the alloy has been investigated at the nanoscale after by means of the 3DAP.

The measured chromium concentration in the overall analyzed volume is (11.4±0.1)at.% (Table 5.2). This value is in good agreement with the data obtained in the as-received state.

As in the case of Fe-9%Cr model alloy, chromium was homogeneously distributed after this treatment, as presented by 3D map (Figure 5.3). The results of the statistical test are shown in Figure 5.2. It is clear, that the s-curve of the experimental distribution almost coincides with the binomial one. This indicates a homogeneous distribution of Cr in the alloy.

Table 5.2 Chemical composition of the thermally aged Fe-12%Cr model alloy (at%) measured by 3DAP

Fe	balance
Cr	11.4 ±0.1
Si	0.18 ±0.01
P	0.05±0.01
Ni	0.017± 0.002
Mn, V, C, N, O, S, Al, Ti	*not measurable*

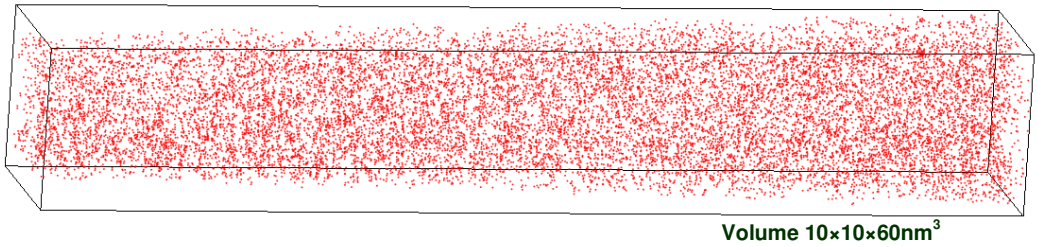

Figure 5.3. 3D distribution of chromium atoms in the Fe-12%Cr model alloy after 600h of aging at 500°C. Chromium is homogeneously distributed after the aging.

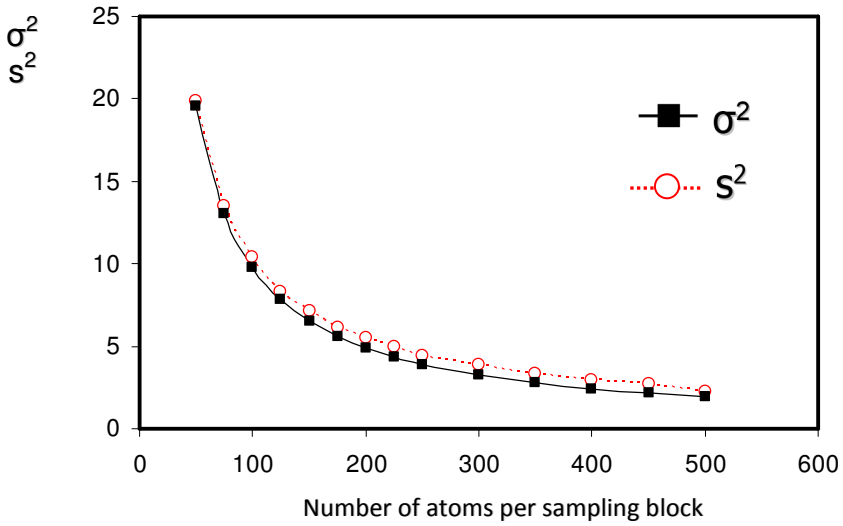

Figure 5.4. Comparison of the standard error (s) with the standard deviation (σ) in the Fe-12%Cr model alloy after 600 h of aging at 500°C. Experimental distribution almost coincides with the binomial one. Chromium atoms are homogeneously distributed.

The obtained experimental data after thermal aging allows us to validate that the Fe-12%Cr alloy is in the α one-phase region of the phase diagram 500°C. This is also in relatively good agreement with the Fe-Cr phase diagrams [1–3] (details are given in the discussion part). Thus, as in the case of the Fe-9%Cr model alloy, just irradiation induced phase separation can be expected during irradiation at this temperature.

II. Evolution of the dislocation structure in the Fe-9%Cr and Fe-12%Cr model alloys

As it was described in the second chapter, self-ion irradiation with an ion energy of 150 keV has been undertaken with the implanter IRMA which is coupled together with a transmission electron microscope. Two materials have been investigated: the Fe-9%Cr and Fe-12%Cr model alloys. The irradiation has been performed at 500°C up to 1.5dpa. (see Chapter 2 for details). This section describes the results of the in-situ TEM observations of the evolution of the dislocation structure. The information on the size distribution and Burgers vectors of the formed dislocation loops deduced within the ex-situ experiments after 1.5dpa irradiation are represented in this section as well.

As it has been described in chapter 3, the distribution of the natural point defects sinks (such as dislocations and grain and sub-grain boundaries) in the Fe-9%Cr and Fe-12%Cr is non-homogeneous. Due to this, in order to make more relevant comparisons of results, in both materials, similar, large and almost free of dislocations grains have been chosen for investigation of irradiation exposure effect. The micrographs of the investigated grains in the Fe-9%Cr and Fe-12%Cr model alloys before irradiation are presented in Figure 5.5 (a) and (b) respectively.

Our previous investigation revealed the non-homogeneity of chromium distribution in the bar of the Fe-12%Cr alloy (see Chapter 3). Due to this, TEM-EDX measurements were made in order to quantify the chromium content in the grain which has been chosen for the investigation of irradiation exposure effect (Figure 5.5 *b*). The Cr content within the current grain varies from 11.76at% up to 12.55at% with a mean value of about (12.1±1.2)at%. These results are in good agreement with measurements performed on the as-received model alloy (see Chapter 3).

II.1. Number density of loops

The evolution of the damage over the whole dose range was followed by recording on a camera under two-beam conditions. Figure 5.6 and Figure 5.7 show an example of the evolution of the dislocation structure in a (110) foil of the Fe-9%Cr and a (111) foil of the Fe–12% Cr alloys respectively, both irradiated with 150 keV Fe^+ ions up to a dose of 1.5dpa (4.32×10^{18} ions·m^{-2}) at 500°C. The images have been taken in the area of the foils with a thickness of from about 80 to 150 nm.

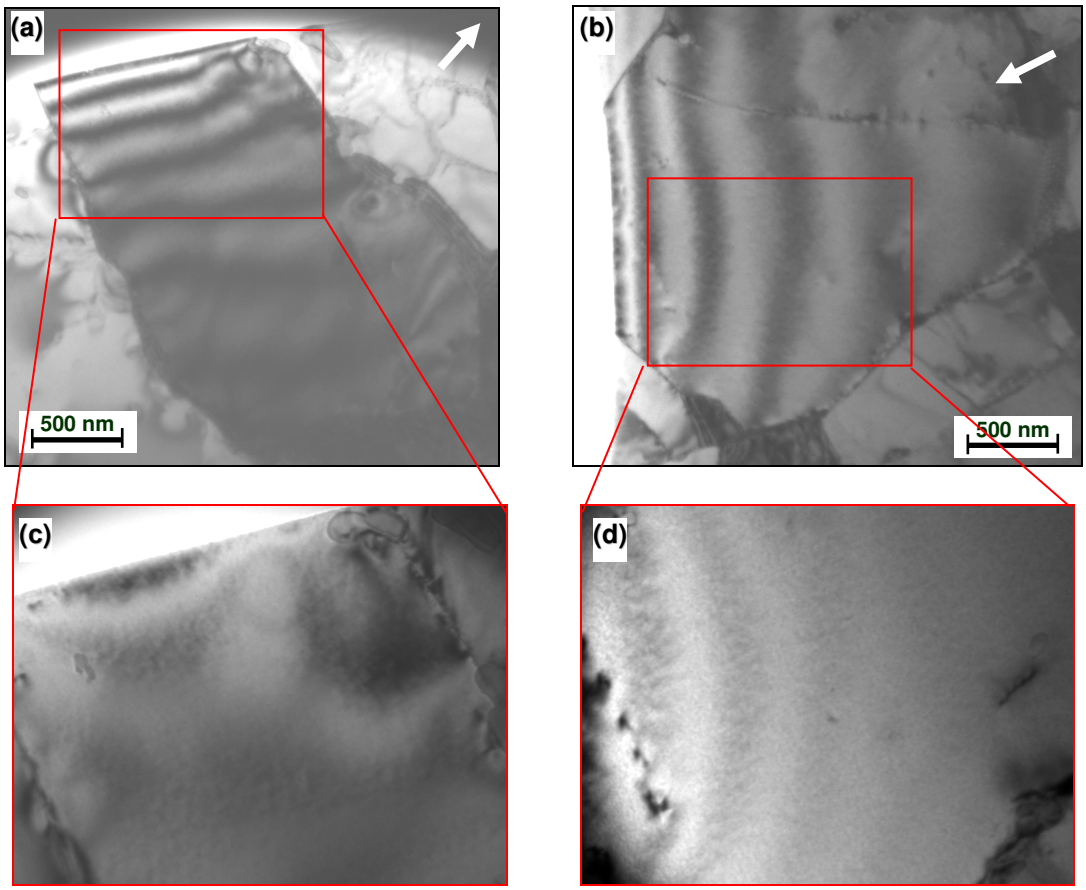

Figure 5.5. TEM bright field images of the investigated grains on the Fe-9%Cr (a and c) and Fe-12%Cr (b and d) alloys before ion irradiation. For investigation of the evolution of the dislocation structure during irradiation, large and almost free of dislocations grains, demonstrated on the current micrographs, have been chosen. The enlarged micrographs demonstrate that the density of dislocations before ion irradiation is low.

During irradiation, for both model alloys, the damage initially took the form of small (less than 10 nm) randomly distributed "black spots" that are expected to be small dislocation loops. They became visible on bright field images under two-beam conditions at dose range of from about 0.25 to 0.3dpa (7×10^{17} to 8.5×10^{17} ions·m^{-2}), as presented in Figure 5.6 (b) and Figure 5.7(c). This threshold dose is of the same magnitude as the one observed in the in-situ ion irradiation experiments (100–150 keV Fe^+ and Xe^+ ions at room temperature, 300°C and 500°C, from 1 to 13 dpa) of Fe and Fe-Cr alloys in [4–6].

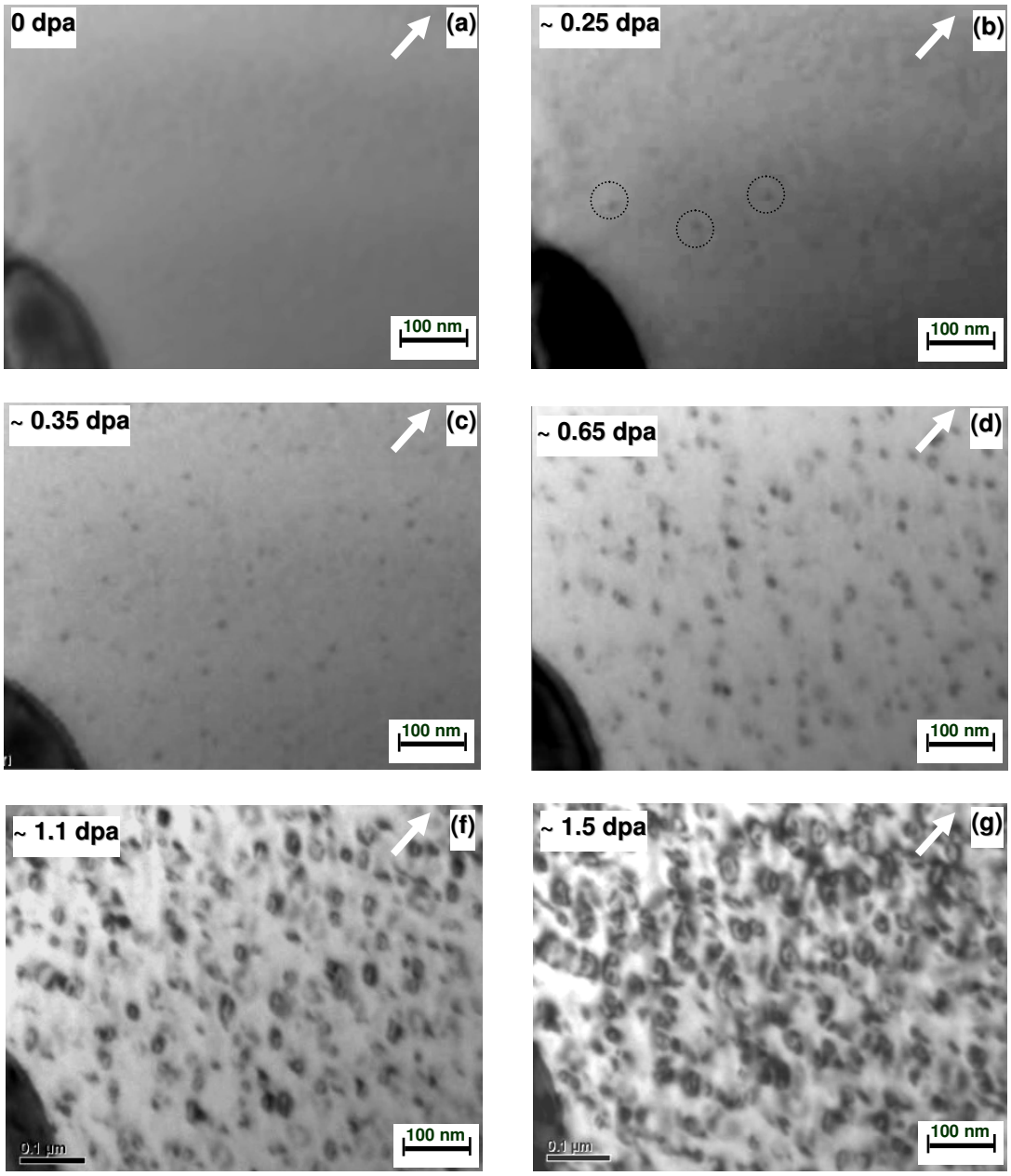

Figure 5.6. Evolution of the dislocation structure in the Fe-9%Cr model alloy during in-situ irradiation by Fe^{+} ions with energy 150keV at 500°C. The mean thickness of the foil in the imaged area is about 140nm. The micrographs have been captured from the film made under bright field conditions. The small dislocation loops became visible at dose range of about 0.25dpa (highlighted by black circles)

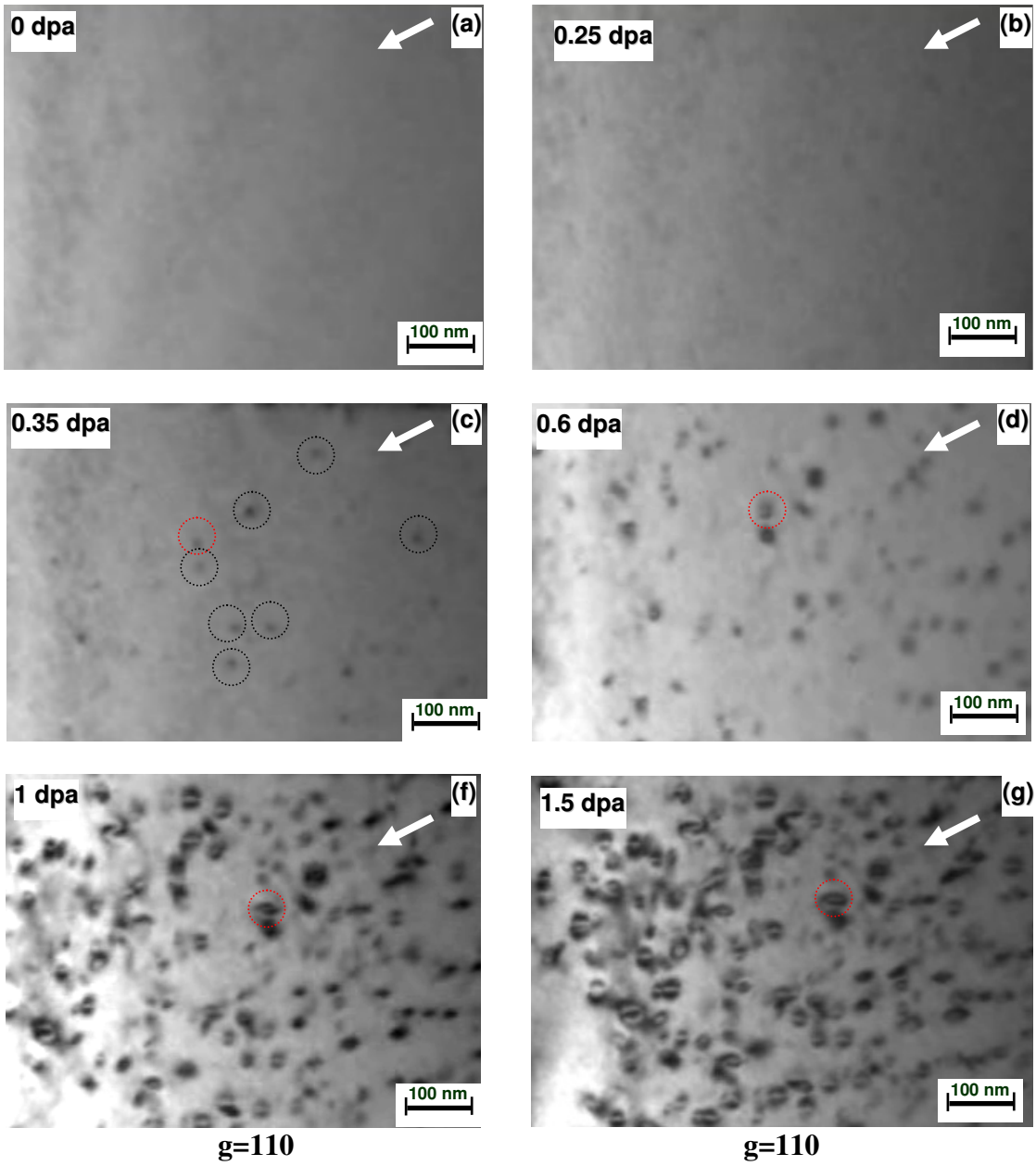

Figure 5.7. Evolution of the dislocation structure in the Fe-12%Cr model alloy during in-situ irradiation by Fe^+ ions with energy 150keV at 500°C. The mean thickness of the foil in the imaged area is about 100 nm. The micrographs have been captured from the film made under bright field conditions. The small dislocation loops became visible at dose range of about 0.35dpa (highlighted by black circles). The evolution of the size of the dislocation loop is highlighted by red circle.

The created dislocation loops are homogeneously distributed in the grain, nevertheless in some cases, dislocation and grain boundary decoration was also observed.

As evident from Figure 5.6 and Figure 5.7, with further irradiation, the evolution of the dislocation structure involves the changes of the number density and the size of the loops. The accumulation of damage is estimated by measurements of the loop number densities as a

function of the dose, as presented in Figure 5.8. The number density measurements presented in Figure 5.8 have been undertaken at thicknesses of from about 100 to 140 nm where a semi-constant areal density (the number of loops per unit area) of dislocation loops is observed (see after).

The evolution of the loop number density with irradiation dose in both model alloys looks very similar; probably the density of loops in the Fe-9%Cr model alloy is slightly higher. However, taking into account the uncertainty of the foil thickness calculation, this difference is believed to be not very significant. For both model alloys, after appearance of the first visible dislocation loops at about 0.25 to 0.3 dpa, their number density increases up to the value of about 1 to 1.2 dpa (that correspond to a density of about 2.7×10^{21} to 3.2×10^{21} m^{-3}). Saturation in visible number density of loops seems to be reached at this dose range. Nevertheless, we can't exclude that the observed saturation could be due to the overlapping of the contrast of new small loops with the large ones created before.

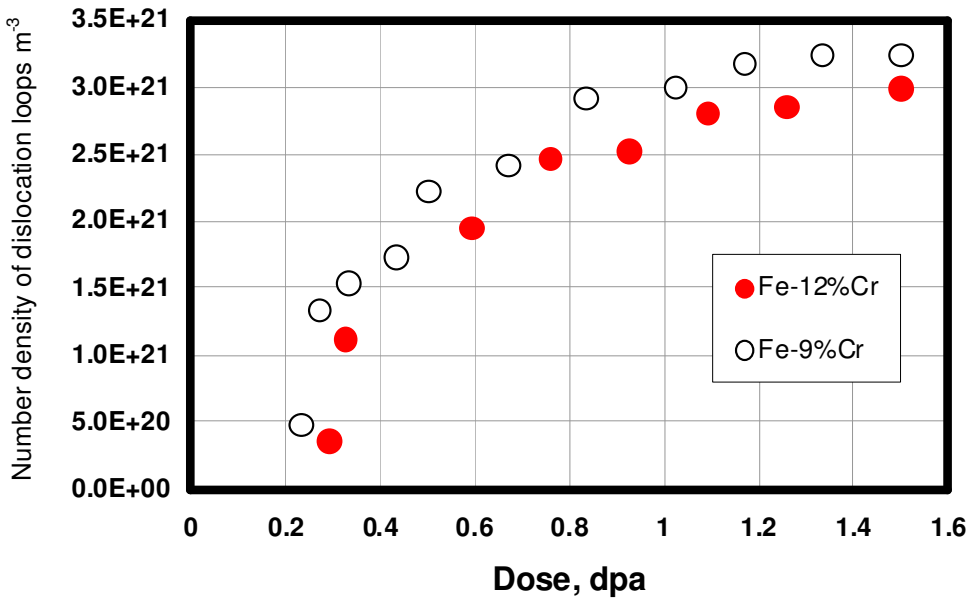

Figure 5.8. Number densities of visible dislocation loops as a function of dose in the Fe-9%Cr and Fe-12%Cr alloys irradiated at 500°C with 150 keV Fe^+ ions.

Besides the number densities per unit volume, areal densities have been measured for the two model alloys irradiated up to 1.5 dpa and plotted as a function of the foil thickness (Figure 5.9). For both model alloys, measurements have been performed in a wedge-shaped foil imaged under two-beam conditions using $\mathbf{g}=1\bar{1}0$ in a foil oriented close to (111). The thicknesses of the foil have been estimated by counting thickness fringes. The graph in Figure 5.9 shows that just few defects have been observed in areas of foil with a thickness less than 30 nm at this dose. The areal density increases in the range of foil thickness up to about 60 to 80nm. It is not unlikely that for the Fe-9%Cr alloy this depth is slightly higher (of about

100 nm). Measurements performed on larger foil thickness don't show a trend for the areal density to change significantly (but we can't exclude the possible lower visibility of small loops in thicker areas of the foils). These findings are not fully consistent with the SRIM simulations for this irradiation condition which shows a peak of irradiation damage in the thickness range from 10 up to 50 nm (see Figure 2.6, p. 55). Probably it could be due to the fact that point defects and small defect clusters can be lost loss during irradiation from the foil surface (which is know to be a strong point defects sink) from both side of the foil when the thickness of the foil is low and then no loops are formed.

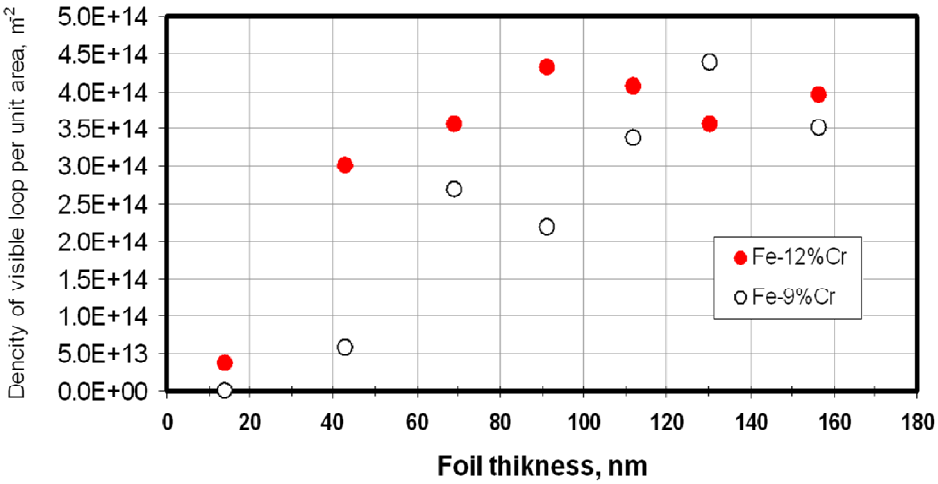

Figure 5.9. The density of visible loops per unit area as a function of foil thickness in the Fe-9%Cr and Fe-12%Cr alloys irradiated at 500°C with 150 keV Fe^+ ions up to 1.5 dpa. Measurements were made in a wedge-shaped foil imaged two-beam conditions using $g=(1\bar{1}0)$ in a foil oriented close to (111).

During the in-situ TEM investigations data on the ion irradiated performed on different Fe-Cr alloys [4–6] (100–150 keV Fe^+ and Xe^+ ions at room temperature, 300°C and 500°C, 1 to 13 dpa) it has been observed that the loops, once formed, are sometimes lost from the foil during or subsequent to ion irradiation. In contrast to this, in our experiments no appreciable mobility and disappearance of dislocation loops has been registered. The probable explanation of this difference can arise from the fact that the Fe-Cr alloys investigated in works [4–6] were of high-purity, while the alloys of the current study contain quite significant quantity of impurities (see Chapter 2). For example, in the work of Satoh et al. [7] it has been demonstrated that 1D migration of small interstitial-type dislocation loops in Fe under electron irradiation becomes significantly slower in the specimens with lower purity.

Note that the number density measurements given above have been made in foils of moderate thickness (up to 150 nm). Also, some loops should be not visible with respect to the invisibility criteria (when $\mathbf{g}\cdot\mathbf{b}=0$). It should also be mentioned that number density measurements have been performed in regions which were exposed to 200 kV electrons

during the ion irradiation. The energy of electrons is well below the threshold for knock-on displacement damage, but as it have been reported in the work of Yao et al. [5], the effect of simultaneous electron and ion irradiation can decrease the measured loop density. This suppressing effect is not fully understood, more information can be found in [5].

II.2. Size of dislocation loops

As evident from Figure 5.6 and Figure 5.7, the dislocation loops formed under irradiation start to grow from some value of the dose. An example can be seen by following the size evolution of the dislocation loop marked by the red circle in Figure 5.7: created at a dose less than 0.35dpa with a loop of size less than 10nm in diameter, it reaches about 30 nm in diameter at a dose of 1.5dpa.

We must note that no systematic investigation of this process has been performed during the in-situ irradiation. The size measurements have been undertaken within ex-situ experiments after irradiation up to 1.5 dpa. The diameter of the loops has been calculated as the mean value of two measurements which have been performed under two-beam conditions in opposite **g**, as illustrated in Figure 5.10. We considered that the diameter of each loop corresponds to its maximum measured dimension.

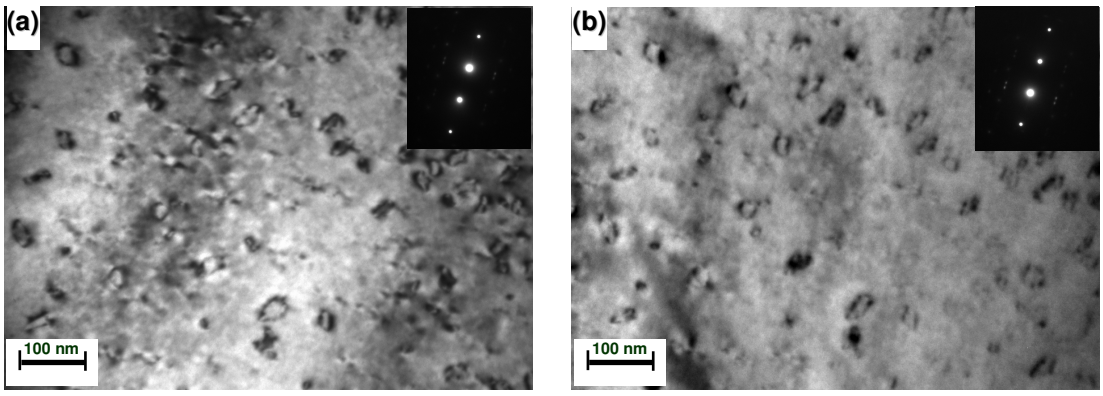

Figure 5.10. Bright field images of the microstructure of the Fe-12%Cr model alloy after irradiation up to 1.5dpa by Fe^+ ions with energy 150keV at 500°C. Micrographs (a) and (b) have been made in a foil oriented close to (111) and imaged under two-beam conditions using opposite g vectors: $g_a = 1\bar{1}0$, $g_b = \bar{1}10$. The size of the same loops differs on the images under deferent conditions. The size of the loops has been deduced as the mean value of two measurements performed on image (a) and (b).

The size distributions of the visible loops in the Fe-9% Cr and Fe-12% Cr model alloys irradiated with 150 keV Fe^+ ions at 500°C up to 1.5 dpa is shown in Figure 5.11. These distributions are rather uni-modal distributions. The distribution in the Fe-9% Cr model alloy is slightly narrower. The mean size of the loops in the Fe-9% Cr alloy is slightly lower (27.5±

1.5 nm) than the one obtained in the Fe-12% Cr model alloy (33.4±1.5 nm). We should note that as in the case of the number density estimation, we can't exclude that some small dislocation loops are invisible either because of the low resolution of the technique or due to an overlapping of their contrast with the one of the large loops. This means that the distribution and the mean loops diameter may be shifted to the lower sizes.

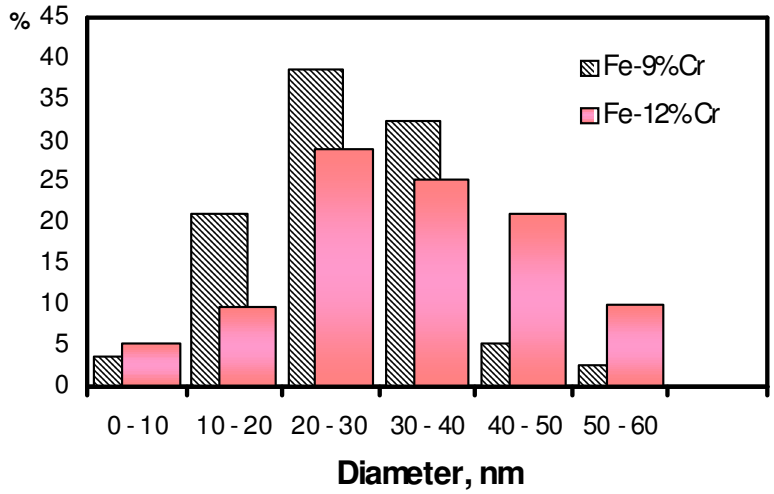

Figure 5.11. The size distributions of visible dislocation loops in the Fe-9%Cr and Fe-12%Cr alloys irradiated at 500°C with 150 keV Fe^+ ions up to 1.5 dpa. Sizes have been deduced as a mean value of two measurements performed under two-beam conditions in the opposite g ($(1\bar{1}0)$ and $(\bar{1}10)$) in foils oriented close to (111). The results are based on measurements of 180 loops for the Fe-9%Cr alloy and 191 loops for the Fe-12%Cr alloy.

As mentioned in the bibliographic chapter, there is no common clear dependence of the mean loop diameter created during irradiation with the Cr content. Our results show that with higher Cr content, the dislocations tend to be larger. But these results have been obtained on few experiments and more statistics taking into account the orientation of the grain with respect to the ion beam and investigations of the Fe5%Cr model alloy are needed to confirm this point.

II.3. Burgers vectors of the loops

Several ex-situ contrast experiments have been performed to determine the Burgers vectors of the loops in the Fe-9% Cr and Fe-12% Cr model alloys. This has been performed owing to series of micrographs taken in various reflection conditions and owing to the invisibility criterion ($\mathbf{g}\cdot\mathbf{b} = 0$, see explanation in the chapter 2).

As presented in Figure 5.12, for Burgers vector determinations in the Fe-12%Cr model alloy, the foil have been oriented in three positions (zone axis (111), (110) and (011)) and 5 micrographs of dislocations have been taken in the various reflection conditions. Table 5.3

gives the expected contrast of the loops according to the different **g·b** conditions. This table shows that the series of images taken in this work enable a complete characterization of the loop Burgers vectors.

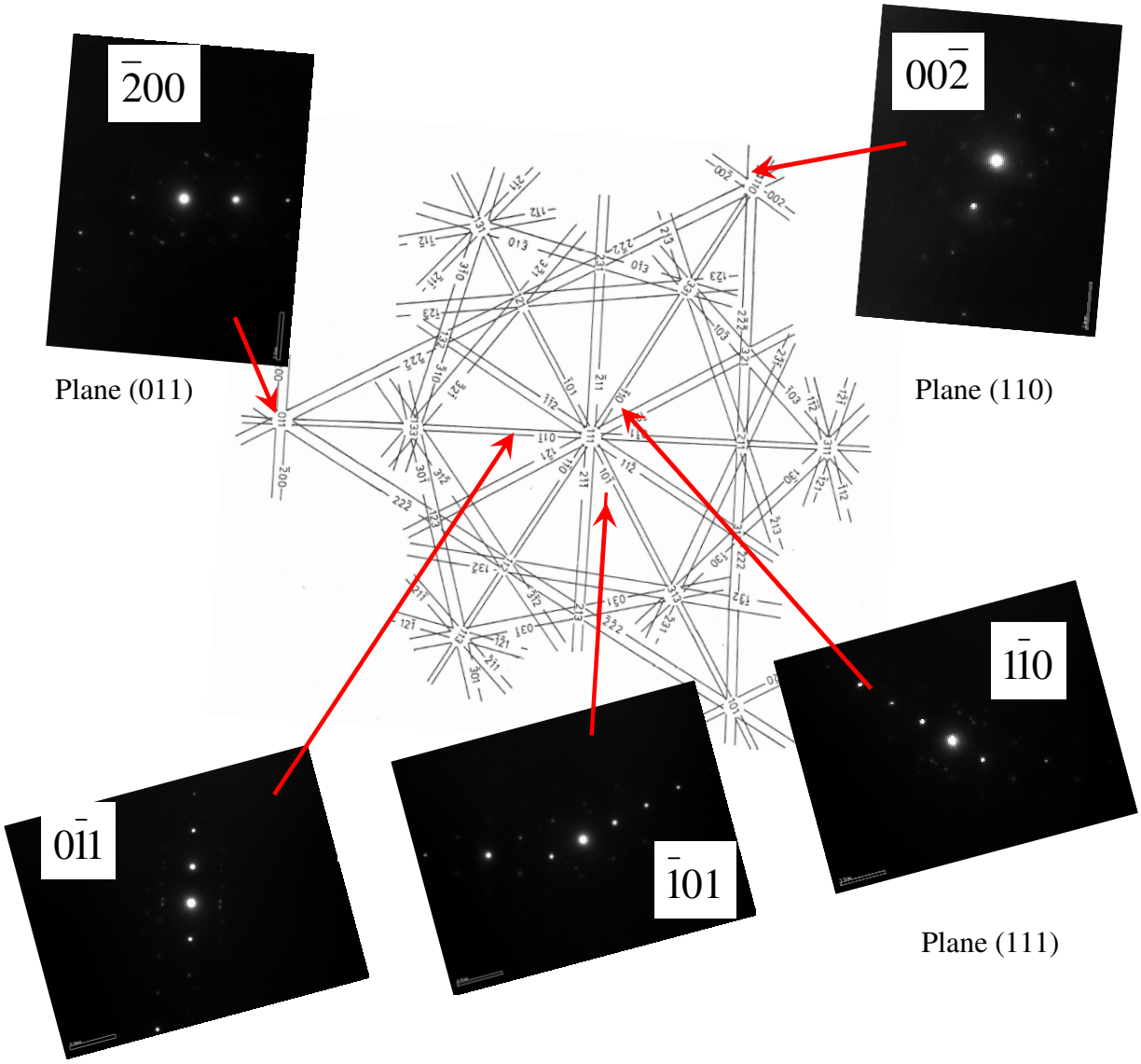

Figure 5.12. Schematic Kikuchi map for a b.c.c. Fe crystal centred on [111] direction. In order to determine the Burgers vectors of the loops in the Fe-12% Cr model alloys irradiated with 150 keV Fe^+ ions at 500°C up to 1.5 dpa, 5 micrographs of dislocations have been taken in various reflection conditions which are presented on the diffraction patterns.

Figure 5.13 shows the series of micrographs obtained for the Fe-12%Cr model alloy imaged in five reflection conditions. In order to determine the Burgers vector, all the dislocations belonging to the selected area have been numbered and identified on each micrograph. Then, to determine the Burgers vector, invisibility conditions are used. For example, the loop number "36" is visible on images under $g_2=\bar{1}01$ (Figure 5.13*c and d*), $g_3=1\bar{1}0$ ((Figure 5.13 *e* and *f*)) and $g_4=\bar{2}00$ ((Figure 5.13 *g* and *h*)) but out of contrast (invisible) in Figure 5.13(*a)* and *(i)* that corresponds to $g_1=0\bar{1}1$ and $g_5=00\bar{2}$. So, in accordance with the invisibility criteria (Table 5.3), this loop should have a Burgers vector $b=a_0[100]$.

Table 5.3. ***g·b*** *table for (111), (110) and (011) foil orientations used for Burgers vector determination for loops of the types expected in Fe and Fe-Cr alloys: 1 – in contrast, 0 – out of contrast*

b	**g**				
	$0\bar{1}1$	$\bar{1}01$	$1\bar{1}0$	$\bar{2}00$	$00\bar{2}$
$½a_0[111]$	0	0	0	1	1
$½a_0[\bar{1}11]$	0	1	1	1	1
$½a_0[1\bar{1}1]$	1	0	1	1	1
$½a_0[11\bar{1}]$	1	1	0	1	1
$a_0[001]$	1	1	0	0	1
$a_0[100]$	0	1	1	1	0
$a_0[010]$	1	0	1	0	0

The overall of the 79 loops observed in this area have been studied by the same procedure (Table 5.4). 20 of them (that corresponds to about ~28% of total quantity) had a Burgers vector of type $½a_0[111]$ and 57 loops (~72%) had a Burgers vector of type $a_0[100]$ (Table 5.5). The Burgers vectors of few dislocations have not been assigned.

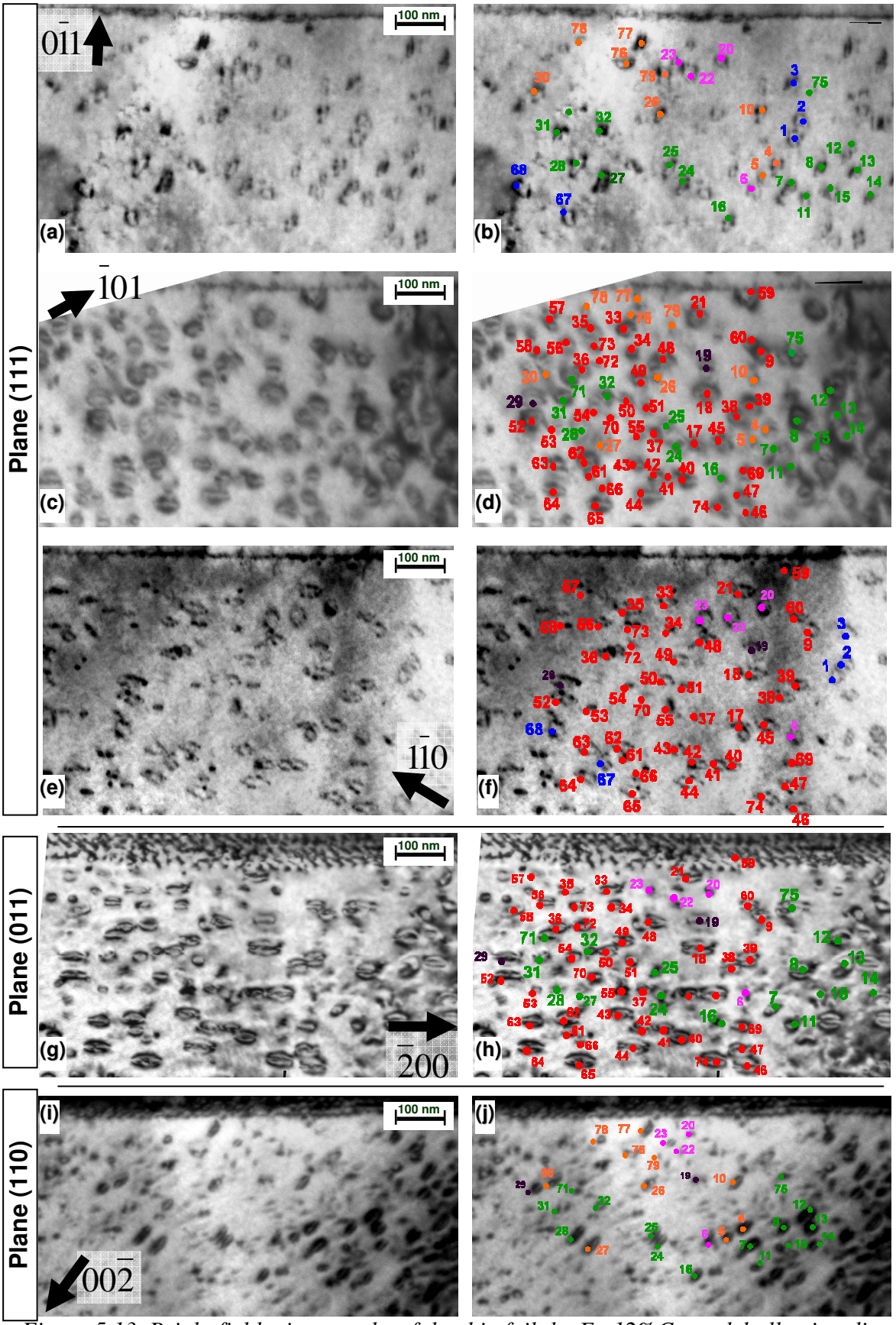

Figure 5.13. Bright field micrographs of the thin foil the Fe-12%Cr model alloy irradiated with 150 keV Fe^+ ions at 500°C up to 1.5 dpa with different orientations imaged in five reflection conditions. Dislocations in the selected area have been numbered and identified on each micrograph (see Table 5.4).

Table 5.4. Burgers vectors of all the 79 dislocation loops observed in Figure 5.13: 1 – in contras; 0 – out of contrast; r.c. – in residual contrast; n.a. – not assigned

N of loop	g_1 $0\bar{1}1$	g_2 $\bar{1}01$	g_3 $1\bar{1}0$	g_4 $\bar{2}00$	g_5 $00\bar{2}$	**b**
1.	1	0	1	0	0	010
2.	1	0	1	0	0	010
3.	1	0	1	0	0	010
4.	1	1	0	0	1	010
5.	1	1	0	0	1	010
6.	1	0	1	1	1	$1\bar{1}1$
7.	1	1	0	1	1	$11\bar{1}$
8.	1	1	0	1	1	$11\bar{1}$
9.	r.c.	1	1	1	0	100
10.	1	1	0	0	1	001
11.	1	1	0	1	1	$11\bar{1}$
12.	1	1	0	1	1	$11\bar{1}$
13.	1	1	0	1	1	$11\bar{1}$
14.	1	1	0	1	1	$11\bar{1}$
15.	1	1	0	1	1	$11\bar{1}$
16.	1	1	0	1	1	$11\bar{1}$
17.	1	1	1	1	0	n.a.
18.	r.c.	1	1	1	0	100
19.	1	1	1	1	1	n.a.
20.	1	r.c.	1	1	1	$1\bar{1}1$
21.	r.c.	1	1	1	0	100
22.	1	0	1	1	1	$\bar{1}11$
23.	1	0	1	1	1	$\bar{1}11$
24.	1	1	0	1	1	$11\bar{1}$
25.	1	1	0	1	1	$11\bar{1}$
26.	1	1	0	0	1	001
27.	1	1	0	0	1	001
28.	1	1	0	1	1	$11\bar{1}$
29.	0	1	1	1	1	$\bar{1}11$
30.	1	1	0	0	1	001
31.	1	1	0	1	1	$11\bar{1}$
32.	1	1	0	1	1	$11\bar{1}$
33.	0	1	1	1	0	100
34.	0	1	1	1	0	100
35.	0	1	1	1	0	100
36.	r.c.	1	1	1	0	100
37.	r.c.	1	1	1	0	100
38.	0	1	1	1	0	100
39.	0	1	1	1	0	100
40.	0	1	1	1	0	100
41.	0	1	1	1	0	100
42.	0	1	1	1	0	100
43.	0	1	1	1	0	100
44.	0	1	1	1	0	100
45.	0	1	1	1	0	100
46.	0	1	1	1	0	100
47.	0	1	1	1	0	100
48.	0	1	1	1	0	100
49.	0	1	1	1	0	100
50.	0	1	1	1	0	100
51.	0	1	1	1	0	100
52.	0	1	1	1	0	100
53.	0	1	1	1	0	100
54.	0	1	1	1	0	100
55.	0	1	1	1	0	100
56.	0	1	1	1	0	100
57.	0	1	1	1	0	100
58.	0	1	1	1	0	100
59.	0	1	1	1	0	100
60.	0	1	1	1	0	100
61.	0	1	1	1	0	100
62.	0	1	1	1	0	100
63.	0	1	1	1	0	100
64.	0	1	1	1	0	100
65.	0	1	1	1	0	100
66.	0	1	1	1	0	100
67.	1	0	1	0	0	010
68.	1	0	1	0	0	010
69.	0	1	1	1	0	100
70.	0	1	1	1	0	100
71.	1	1	0	1	1	$11\bar{1}$
72.	0	1	1	1	0	100
73.	0	1	1	1	r.c.	100
74.	0	1	1	1	0	100
75.	1	1	0	1	1	$11\bar{1}$
76.	1	1	0	0	1	001
77.	1	1	0	0	1	001
78.	1	1	0	0	1	001
79.	1	1	0	0	1	001

The same procedure have been applied for the determination of the loops observed in the Fe-9%Cr model alloy irradiated with 150 keV Fe^+ ions at 500°C up to 1.5 dpa. Figure 5.14 shows the series of micrographs obtained for the Fe-9%Cr model alloy imaged in four reflection conditions. The Burgers vector of the 126 loops have been determined (Table 5.5). 26 dislocation loops (~20%) had Burgers vectors of type $\frac{1}{2}a_0[111]$ and 100 dislocations (~80%) had Burgers vectors of type $a_0[100]$. As in the case of the Fe-12%Cr model alloy, few dislocations have not been assigned.

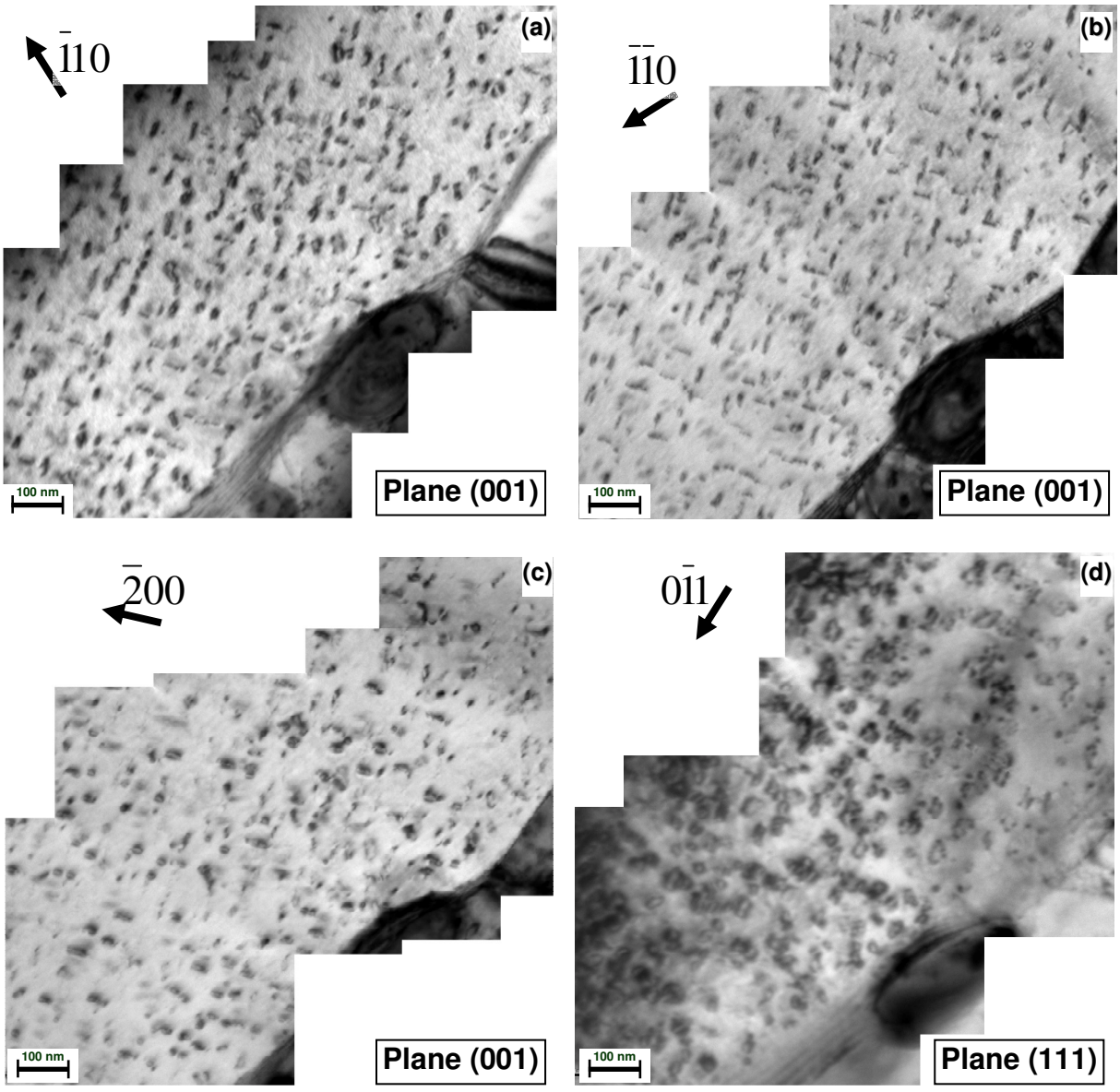

Figure 5.14 Bright field micrographs of the thin foil the Fe-9%Cr model alloy irradiated with 150 keV Fe^+ ions at 500°C up to 1.5 dpa with different orientations imaged in four reflection conditions.

Table 5.5. Relative proportions of ½[111] and [100]-type dislocation loops

	Irradiation conditions	Dislocation analysed	½<111>	<100>
Fe-9%Cr	150 keV Fe^+, 500°C, 1.5 dpa	126	20%	80%
Fe-12%Cr	150 keV Fe^+, 500°C, 1.5 dpa	77	28%	72%

It is obvious that dislocations created in both model alloys during irradiation at 500°C up to 1.5dpa are mainly of [100]-type (Table 5.5). It is known from experimental and theoretical works that the $\frac{1/2\langle 111\rangle}{\langle 100\rangle}$ ratio in b.c.c. iron depends on the temperature of irradiation (see chapter 1 for details). In general, ½<111> loops are preferentially created at low temperatures (< 300 to 350°C [8]), whereas <100> loops are preferentially created at high temperatures (> 450°C [8]). That is in good agreement with our findings.

Similar in-situ ion irradiation (150 keV Fe^+, from 1 to 13 dpa, 500°C) experiments have been performed on pure Fe and Fe-Cr model alloys [4,8]. The results have shown that 100% of <100> type dislocation loop have been found in pure iron, while few dislocations of ½<111> type have been observed in the Fe-8%Cr alloy that corresponds to our results. Table 5.5 shows that for a larger Cr content, more ½<111> type dislocation loops are created (up to 28% in the Fe-12%Cr alloy). Other experiments are needed to confirm this trend. Also the study of the influence of the foil orientation on the results has to be undertaken (to look at, for example, the possible loss of the mobile ½<111> dislocation loops to the surface, see [4,5]).

At the end of this section we want to note that number density measurements done during in-situ experiments have been performed under two-beam conditions, while some other authors (for example in works [4–6,8]) use weak-beam dark field conditions. The latter allows sharp and well-localized strong contrast of dislocation loops to be obtained and is especially well adopted for small dislocation loop investigations. This perhaps decreases the relevance of the direct comparison of our measurements with the results of literature. Nevertheless, the TEM data we collected gives us a good estimation of the evolution of defects during the irradiation, information very important in order to estimate the created damage in the 3DAP tips irradiated in the same conditions. Indeed, one of the main goals of this study is to combine results of these two techniques.

III. Effect of irradiation on chemical elements distribution

As it has been demonstrated in the first part of the current chapter by thermal ageing experiments, no radiation enhanced precipitation can be expected at 500°C. Nevertheless, the redistribution of point defects created during irradiation exposure gives grounds to expect for some irradiation induced phase separation. Indeed, as shown in the previous part, ion irradiation with 150 keV Fe^+ ions at 500°C up 1.5 dpa of the Fe-9%Cr and Fe-12%Cr model alloys lead to the creation of a large number of dislocation loops and, as it have been observed in works [9–11], it can lead to redistribution of chemical species and creation of RIS on loops.

In the current chapter, the results of 3DAP experiments, which have been used to characterize possible changes in solute distributions during ion irradiation with 150 keV Fe^+ ions at 500°C up to 1.5 dpa in the Fe-9%Cr and Fe-12%Cr model alloys, are reported.

The ion irradiation of the same model alloy has been also performed at 300°C. 150 keV Fe^+ ions have been also used and the reached does is 1.5 dpa. Current chapter rapports the results of the 3DAP investigations of the irradiated materials.

III.1. Correlation of in-situ TEM and 3DAP experiments

In order to correlate the population of defects created under irradiation to the appearance of some chemicals heterogeneities, 3DAP specimens have been irradiated in the same conditions that the one used to irradiate the thin foils studied in the previous section. Similar heavy-ion implantation performed directly on the 3DAP needles to simulate the effect of displacement cascades on the segregation and cluster formation has been successfully used in other studies of ferritic steels (bcc structure) and austenitic steels (fcc structure) [12–15]. The tips have been irradiated up to 1.5 dpa in order to have an acceptable probability to observe a loop or a part of a loop in a 3DAP volume. Indeed, as shown by Figure 5.15, a 3DAP volume is small with respect to the investigated TEM volume. At a dose equal to 1.5 dpa, with 150 keV Fe^+ ions, we determined that about 3×10^{21} m^{-3} loops with a size of about 30 nm are formed during the irradiation at 500°C. If we consider that a typical LAWATAP volume is equal to $40\times40\times100nm^3$, we can expect to have half of a full dislocation loop. This means that a large number of experiments is necessary for relevance. For the latter estimation, the thickness of the dislocation loops has been considered to be a lattice parameter in Fe (a=0.286 nm). At the same time, as it was demonstrated in the Chapter 4, the atmospheres created around dislocation lines have a size of ten and more lattice parameters. If it is also the case of the current ion irradiation, this increases the probability of detection of a possible redistribution of chemical species on the dislocations.

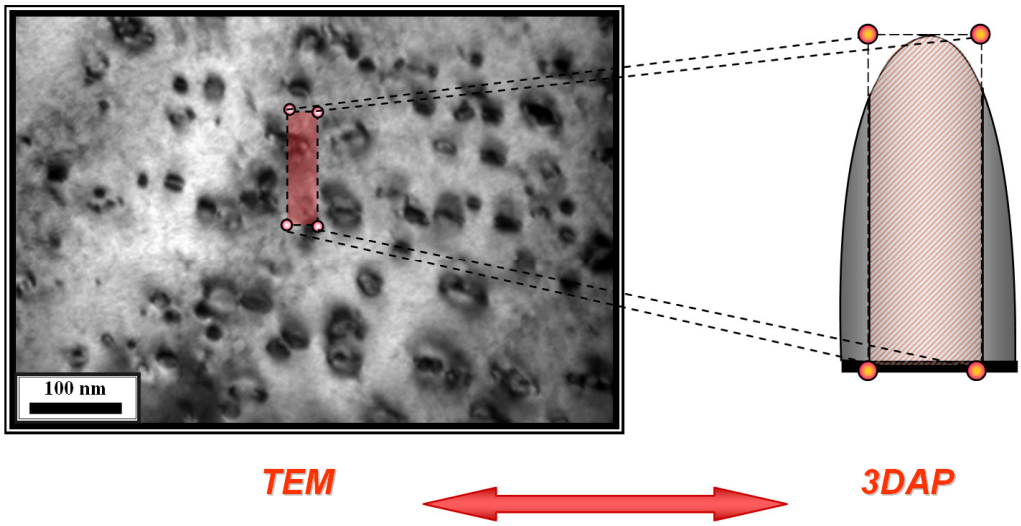

Figure 5.15. Schematic comparison of the scales of investigated by TEM and by 3DAP. Consider the measured number density of the loops during the ion irradiation at 500°C (~3×10^{21} m^{-3}) and their mean size (~30nm), it has been estimated that in the typical LAWATAP experiment (volume of analysis is about 40×40×100nm^3) we can expect to have half of a full dislocation loop

The latter considerations are based on the assumption that the defects distribution during ion irradiation of TEM thin foils and 3DAP tips (see chapter 2 for details of the irradiation procedure) are identical. It is a very strong assumption, taking into account the fact that the effect of the surface (which is strong point defects sink) in 3DAP tips is higher than in the case of thin foil. Unfortunately, no TEM observations of 3DAP tips after ion irradiation at 500°C have been performed. However, TEM observation of 3DAP tips of the Fe-9%Cr and Fe-12%Cr model alloys after irradiation by Fe^+ ions with energy 150keV at 300°C are available (Figure 5.16). The holder which enables observation of 3DAP tips with TEM doesn't allow the reach very good contrast conditions since only rotation of specimens is possible. Nevertheless, it is possible to mention that it exists some features which appears inside the irradiated tips in the TEM micrographs (Figure 5.16 (a) and (b)) and which could correspond to the presence of dislocations. The latter means that we can expect that segregations on dislocations, if they exist, could be observed by 3DAP experiments. It should also be mentioned that a quite significant oxidation of the tips during irradiation and transportation has been observed in both model alloys (Figure 5.16).

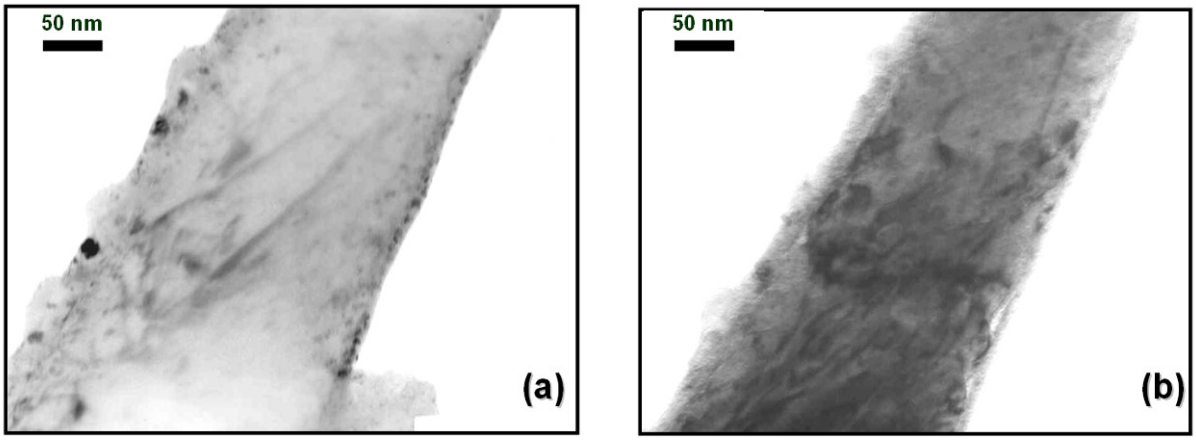

Figure 5.16. TEM investigation of the 3DAP tips of the Fe-9%Cr(a) and Fe-12%Cr (b) model alloys after irradiation by Fe^+ ions with energy 150keV at 300°C. The contrast of some objects appropriates with the presence of dislocations. It can be expected that the possible segregation on dislocations can be registered by 3DAP experiments

III.2. 3DAP study of the Fe-9%Cr model alloy

The Fe-9%Cr alloy has been irradiated by Fe^+ ions with energy 150keV at two different temperatures: 300°C and 500°C. 3DAP investigations have been performed in order to check the influence of the exposure on the randomness of the spatial distribution of chemical species at the nanoscale.

The measured chromium concentrations in the overall analyzed volume are: (8.65 ±0.04)at.% and (9.00 ±0.03)at.% for alloy irradiated at 300°C and 500°C respectively (Table 5.6 and Table 5.7). As shown by the 3D distribution maps in Figure 5.17 and Figure 5.18, chromium, silicon atoms appear homogeneously distributed after the ion irradiation as well as phosphorous atoms observed in the alloy for irradiation at 500°C. Any particular segregation that could be linked to dislocation loop has been observed. We should note that considering all the data collected during the successful 3DAP experiments on this model alloy after ion irradiation at 500°C, it is possible to expect that the total analyzed volume should contained about 3 full dislocation loops. Due to the oxidation, just one successful experiment is made for the irradiation at 300°C. It should be also noted that since Wide-Angle Tomographic Atom Probe have been used for tips investigation (in order to increase the statistics), no information on P distribution after irradiation at 300°C and Ni distribution for both irradiations have been obtained due to relatively low mass resolution of the technique (see Chapter 2 for details).

Table 5.6 Mean chemical composition of the Fe-9%Cr model alloy irradiated up to 1.5 dpa by Fe^+ ions with energy 150keV at 300°C (at%) measured by 3DAP

Fe	balance
Cr	8.65 ±0.04
Si	0.14 ±0.01
P, Mn, Ni, V, C, N, O, S, Al, Ti	*not measurable*

Table 5.7 Mean chemical composition of the Fe-9%Cr model alloy irradiated up to 1.5 dpa by Fe^+ ions with energy 150keV at 500°C (at%) measured by 3DAP

Fe	balance
Cr	9.00 ±0.03
Si	0.10 ±0.01
P	0.02 ±0.01
Mn, Ni, V, C, N, O, S, Al, Ti	*not measurable*

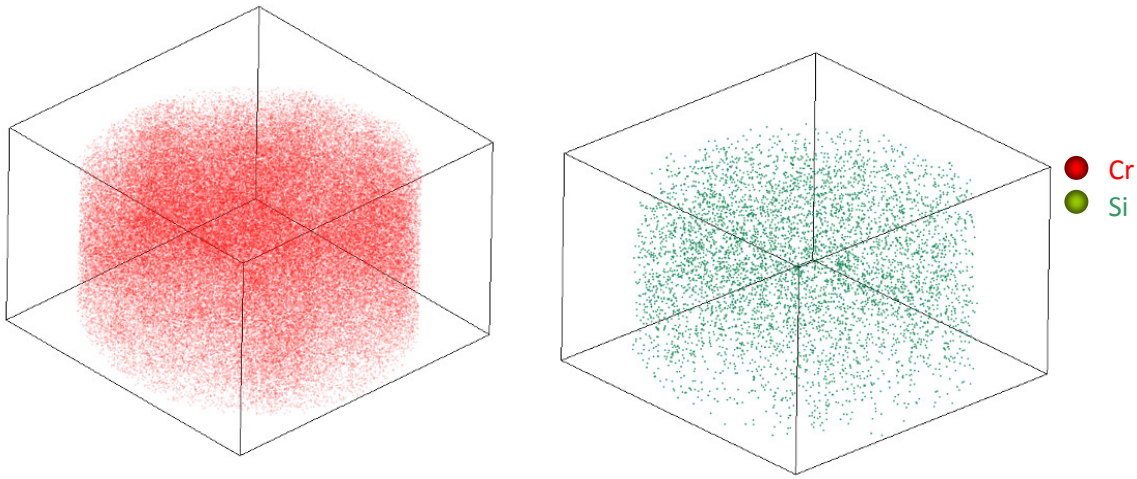

Figure 5.17. 3D distribution of chromium (a) and silicon (b) atoms in the Fe-9%Cr model alloy irradiated up to 1.5 dpa by Fe^+ ions with energy 150keV at 300°C. Chemical species are homogeneously distributed after irradiation exposure

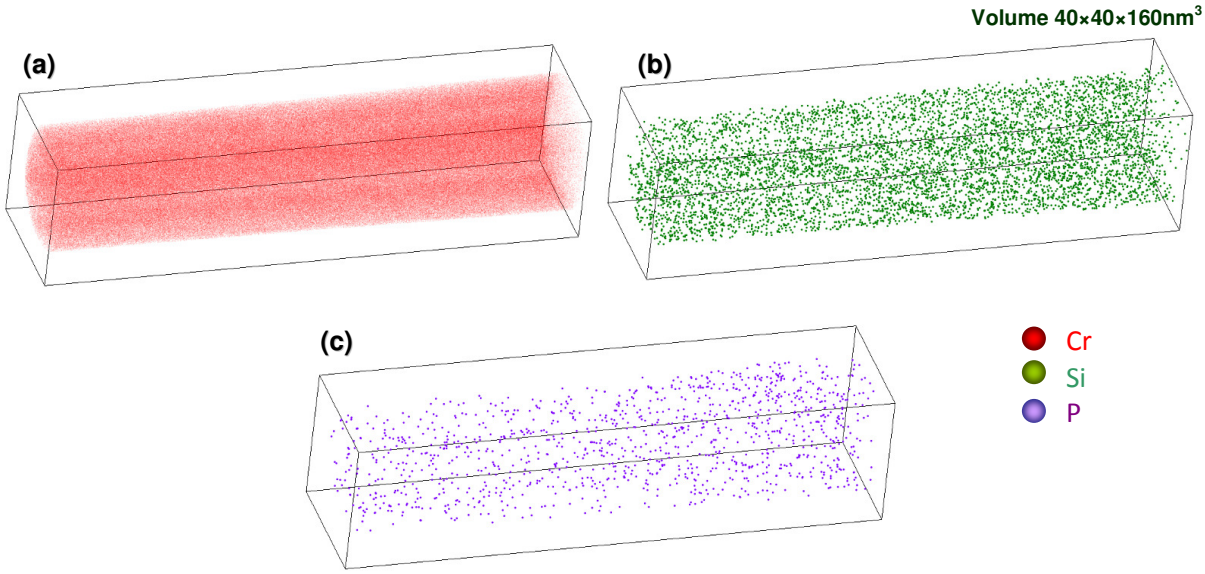

Figure 5.18. 3D distribution of chromium (a), silicon (b) and phosphorous (c) atoms in the Fe-9%Cr model alloy irradiated up to 1.5 dpa by Fe^+ ions with energy 150keV at 500°C. All chemical species are homogeneously distributed after irradiation exposure

III.3. 3DAP study of the Fe-12%Cr model alloy

As in the case of the Fe-9%Cr model alloy, tips of the Fe-12%Cr alloy has been irradiated by Fe^+ ions with energy 150keV at 300°C and 500°C and analyzed by 3DAP in order to check the influence of the ion irradiation on the distribution of alloying elements at nanoscale.

3DAP results (Table 5.8 Table 5.9) show that the Cr concentration measured inside grains equal to ((11.2±0.02)at%) and ((10.5±0.06)at%) for irradiation at 300°C and 500°C respectively. These values are lower than the expected nominal concentration given by chemical analysis (12.3at%[16]) whereas they are in good agreement with previous 3DAP and EDS measurements. It confirms the non-homogeneity of the Cr distribution in the Fe-12%Cr bar (see Chapter 3 for details).

Table 5.8. Mean chemical composition of the Fe-12%Cr model alloy irradiated up to 1.5 dpa by Fe^+ ions with energy 150keV at 300°C (at%) measured by 3DAP

Fe	balance
Cr	11.2±0.02
Si	0.18 ±0.01
P	0.01±0.01
Mn, Ni, V, C. N, O, S, Al, Ti	not measurable

Table 5.9. Mean chemical composition of the Fe-12%Cr model alloy irradiated up to 1.5 dpa by Fe^+ ions with energy 150keV at 500°C (at%) measured by 3DAP

Fe	balance
Cr	10.5±0.06
Si	0.07 ±0.01
Mn, P, Ni, V, C. N, O, S, Al, Ti	not measurable

Figure 5.19 and Figure 5.20 show the 3D maps of chemical species distribution in the Fe-12%Cr model alloy after ion irradiation at 300°C and 500°C respectively. All chemical species appear homogeneously distributed after the exposure and no segregation that could be linked to the dislocation loop or clusters has been observed. Adding up all the data obtained on the ion irradiated 12%Cr model alloy at 500°C, it is possible to expect that the total analyzed volume could contained about 1.5 full dislocation loops. We should note that 3DAP revealed in the 300°C irradiated sample, two linear segregations of chromium. These features are very similar to the ones obtained on dislocation lines in the neutron irradiated samples (Figure 4.19, p. 146). Further investigations will be performed for the details on the characteristics of these segregations.

Note that as in the case of the Fe-9%Cr model alloys, no information on Ni distribution for both irradiations and on P distribution for 500°C irradiation have been obtained due to relatively low mass resolution of the LAWTAP technique (see Chapter 2 for details).

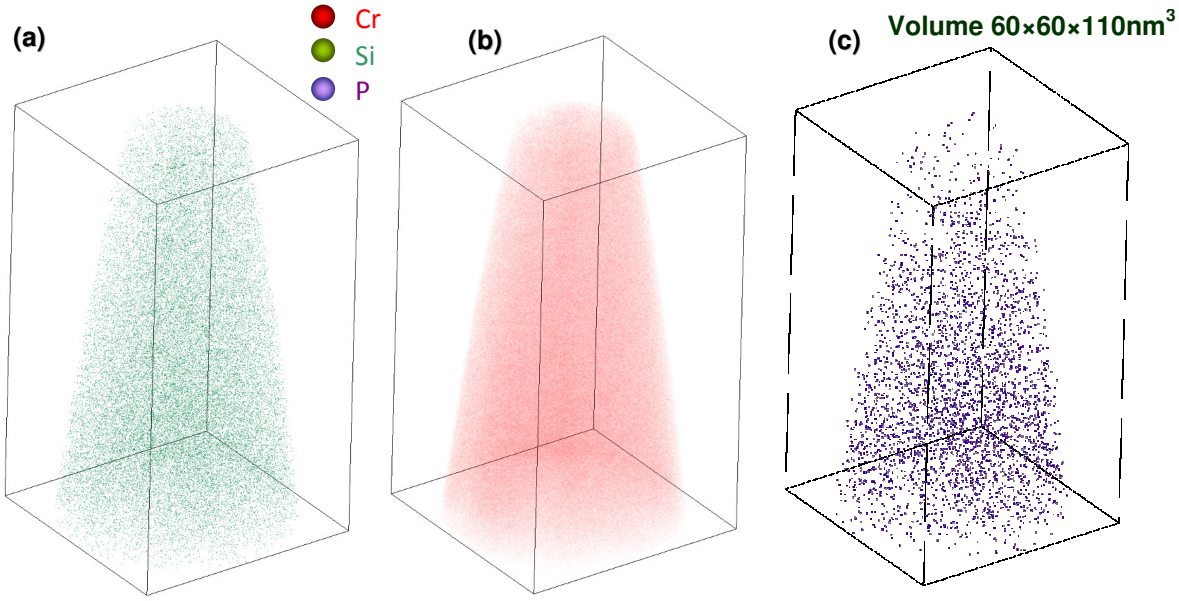

Figure 5.19. 3D distribution of silicon (a), chromium (b) and phosphorous (c) atoms in the Fe-12%Cr model alloy irradiated up to 1.5 dpa by Fe^+ ions with energy 150keV at 300°C. All chemical species are homogeneously distributed after irradiation exposure

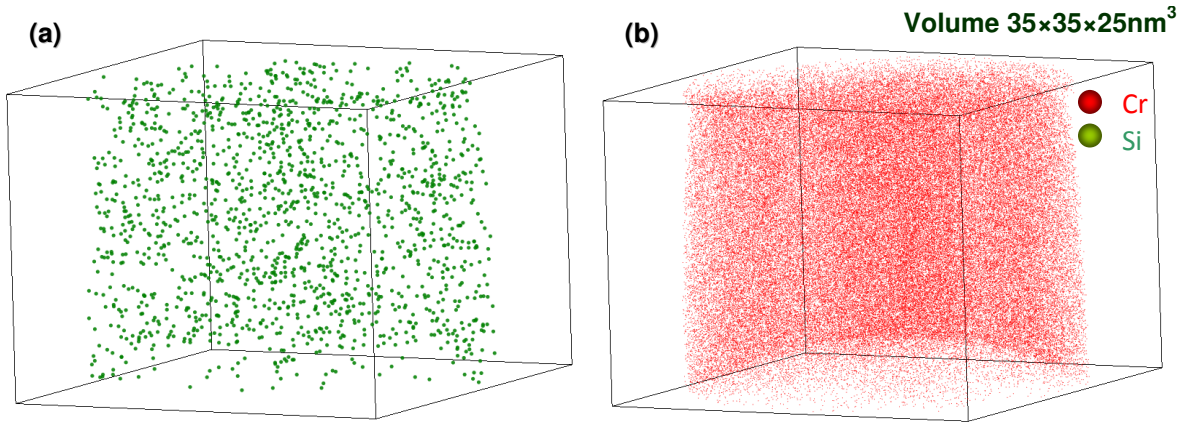

Figure 5.20. 3D distribution of silicon (a) and chromium (b) atoms in the Fe-12%Cr model alloy irradiated up to 1.5 dpa by Fe^+ ions with energy 150keV at 500°C. All chemical species are homogeneously distributed after irradiation exposure

IV. Discussion

Long-term thermal ageing at 500°C hasn't led to chemical element redistribution in the Fe-9%Cr and Fe-12%Cr model alloys. This clearly shows that these two model alloys are in the single-phase area of the Fe-Cr equilibrium phase diagram and that the solubility of Cr in Fe at 500°C is higher than 12at%. As shown in Figure 5.21, this in a good agreement with the miscibility gap position given by CALPHAD phase diagram and with the one proposed by Xiong et al. [2], and in relatively good agreement with the one proposed by Bonny et al. [1]. It must be emphasized that our results are coherent with the results of Novy et al. [17] and Dubiel and Inden [18] which have experimentally shown that the solubility limit of chromium in the alpha phase at 500°C in the binary Fe-Cr model alloy is close to 14 at.%. This indicates that small modification should be made in the Fe-Cr equilibrium phase diagram proposed by Bonny et al. [1].

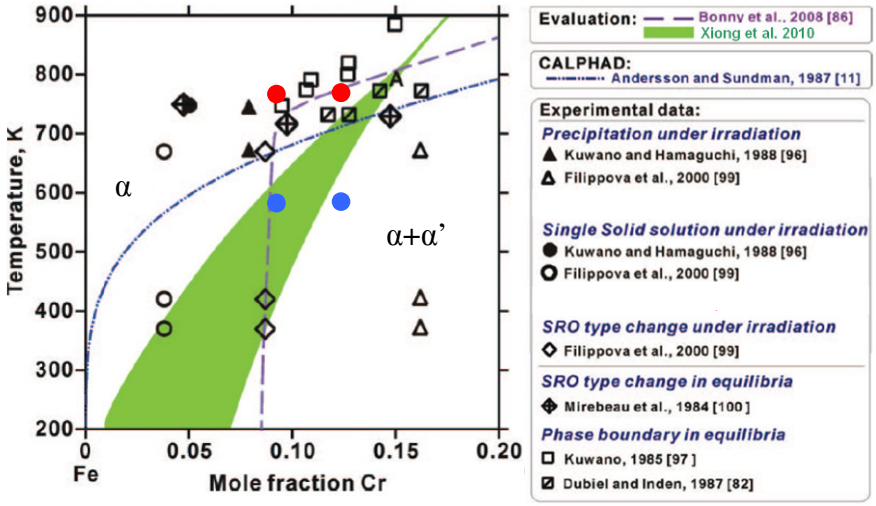

Figure 5.21. Low Cr part of the α-α` miscibility gap (after [2]); the position of the α domain limit, proposed by Bonny et al. is shown by dotted line [1]; the possible location for Fe-rich solvus determined by Xiong et al. [2] is represented by the green area. The results of the current research are shown by red and blue marks: neither thermal ageing at 500°C nor 150keV self-ion irradiation up to 1.5dpa at 500°C has led to chemical element redistribution in the Fe-9%Cr and Fe-12%Cr model alloys. These model alloys are in the single-phase area. In contrary to the neutron irradiation data (see Figure 4.15 p. 136), 150keV self-ion irradiation up to 1.5dpa at 300°C hasn't led to chemical element redistribution. The thermal ageing experiments at this temperature are impossible due to the extremely slow mobility of Cr at this temperature.

As already explained in this chapter, only irradiation induced phase separation is expected after ion irradiation at 500°C. TEM investigation revealed that the ion irradiation damage at 500°C in Fe-9at%Cr and Fe-12at%Cr becomes apparent in the form of relatively large dislocation loops. No particular investigation of the nature of the loops has been

performed. However, regarding the fact that in a majority of TEM studies [4,19–24] the dislocation loops observed are of interstitial type, we believe that in the current study they are also of interstitial type (see Chapter 1 for details). The fact that the loops have relatively large size (about 30nm) is also in favour of their interstitial nature, since, as it have been shown by atomistic simulations of Gilbert et al. [25], a spherical cluster of vacancies (voids) in b.c.c. Fe is systematically more stable than a vacancy loop of equivalent size and the spherical shape becomes more favourable than equivalent vacancy loops with increasing of their size.

This means that during the irradiation a flux of interstitials should exist toward the growing dislocation loops. *Ab-initio* calculations of Choudhury and co-workers [26] have shown that enrichment of Cr is expected on the SIA sinks. Indeed, enrichment of dislocation loops by Cr has been observed experimentally in works [9–11]. So, the enrichment by Cr of dislocation loops in the current study can also be expected. Moreover, Neklyudov and Voyevodin [10] have also observed in F-M steels an enrichment of interstitial dislocation loops by Si.

However, as it has been demonstrated by 3DAP experiments, no particular segregation has been detected in Fe-9at%Cr and Fe-12at%Cr irradiated by Fe^+ ions with energy 150keV at 500°C.

RIS typically happens at temperatures between 0.3 and 0.6 times the melting point (T_m) [27]. This means that for the current model alloys, RIS could be expected up to the temperatures of about 800°C (T_m=1780 to 1800K [2]). 500°C is well inside the temperature range of RIS creation. It is possible that back diffusion due to high temperature could compensate solute flux and then that no segregations are found. However, no segregations that can be associated to dislocation loops are also observed at 300°C whereas the TEM observations of 3DAP tips reveals contrast which could be associated to dislocation loops. Moreover, in contrary to the neutron irradiation data, where Cr-enriched and NiSiPCr-enriched clusters are observed (see Chapter 4), 150keV self-ion irradiation up to 1.5dpa at 300°C hasn't led to chemical element redistribution. This shows that if the back diffusion affects on the redistribution of chemical species during 500°C irradiation, it is not the unique reason of the absence of segregation. Few explanations are also possible:

– this could be due to the elevated flux of ion irradiation (2 dpa/h in contrast to 0.0003 dpa/h during neutron irradiation) and, as a consequence, a high ratio of annihilation of point defects (see Chapter 1 for details). In order to clarify these points it is necessary to perform series of experiments under different temperature-flux conditions.

– the shape of the irradiated sample can also be responsible of these observations: 3DAP samples are in form of very sharp tips. The implantation conditions have been estimated by SRIM calculations which consider the geometry of the specimen as infinite planar surface. Taking into account the complex geometry of the tips, it is possible to suppose that such approximation is more appropriate to estimate the damage in TEM foil with a relatively higher thickness than tips which have a higher surface to volume ratio. So, in the

case of 3DAP samples, the proximity of free surfaces of the tip must reduces the quantity of defect clusters inside the investigated volume in comparison with the predicted one for the bulk irradiation. This means that the reported 1.5dpa irradiation wasn't enough for creation of appreciable RIS in the analysed volume. Moreover, a recent study of A. Volgin and co-workers [28] of the irradiation damage in austenitic Fe-Cr-Ni alloys after 1 and 5dpa Ni^+ ion irradiation at 200°C and 450°C confirms the fact that the behaviour observed in the heavy-ion-implanted 3DAP needles systematically differ from the behaviour of the irradiated bulk materials: the objects observed in the bulk material are not observed in the irradiated tips.

At that stage it is obvious that 3DAP investigation of ion irradiated bulk materials is necessary to go further. To do this, higher energy Fe^+ ion irradiation must be chosen in order to create damage far from the surface. Such irradiation has been undertaken in Ion Beam Centre in FZD, Dresden (Germany) in order to get a flat profile of damage up to about 1.5 μm (see Chapter 2, part ii,2(b) for details). 3DAP study of the irradiated alloys is under progress.

V. Conclusions

Thermal ageing of the Fe-9%Cr and Fe-12%Cr model alloys has been performed at 500°C in order to define the possible irradiation enhanced processes at this temperature. 3DAP study of these alloys has shown that both alloys are in the α single-phase region of the Fe-Cr phase diagram at 500°C and only irradiation induced phase separation can be expected during irradiation at this temperature.

In-situ TEM investigations have shown that during irradiation for the Fe-9%Cr and Fe-12%Cr model alloys irradiated with 150 keV Fe^+ ions at 500°C, small (less then 10 nm) randomly distributed dislocation loops become visible at a dose range of about 0.25 to 0.3dpa (7×10^{17} to 8.5×10^{17} ions·m^{-2}). The created dislocation loops are homogeneously distributed in the grain, only rarely on dislocation and grain boundaries. The evolution of the number density of visible loops with irradiation dose in both model alloys looks like very similar. It increases up to a value of from about 1 to 1.2 dpa (that corresponds to a loop density of about 2.7×10^{21} to 3.2×10^{21} m^{-3}) and saturates after about 1 dpa up to 1.5dpa, the highest dose we studied. The mean size of the loops in the Fe-9% Cr alloy after an irradiation dose of 1.5dpa is slightly lower (27.5±1.5 nm) than the one of the loops observed in the Fe-12% Cr model alloy (33.4±1.5 nm). Dislocation loops created in both model alloys during irradiation at 500°C up to 1.5dpa are mainly of [100]-type: 70% in the Fe-9%Cr alloy and 78% in the Fe-12%Cr model alloy. Other dislocation loops are of ½[111] type, while few loops have not been assigned.

3DAP study of the Fe-9%Cr and Fe-12%Cr irradiated with 150 keV Fe^+ ions up to 1.5 dpa at 300°C and 500°C did not reveal any chemical species redistribution during the exposure that can be linked to the presence of dislocation loops.

VI. References

[1] G. Bonny, D. Terentyev, L. Malerba, Scripta Materialia 59 (2008) 1193-1196.
[2] W. Xiong, M. Selleby, Q. Chen, J. Odqvist, Y. Du, Critical Reviews in Solid State and Materials Sciences Volume 35 (2010) 125 - 152.
[3] J.-O. Andersson, B. Sundman, Calphad 11 (1987) 83-92.
[4] M.L. Jenkins, Z. Yao, M. Hernandez-Mayoral, M.A. Kirk, Journal of Nuclear Materials 389 (2009) 197 - 202.
[5] Z. Yao, M. Hernández-Mayoral, M.L. Jenkins, M.A. Kirk, Philosophical Magazine 88 (2008) 2851.
[6] M. Hernandez-Mayoral, Z. Yao, M.L. Jenkins, M.A. Kirk, Phil. Mag. 88 (2008) 2881-2897.
[7] Y. Satoh, H. Matsui, T. Hamaoka, Phys. Rev. B 77 (2008) 094135.
[8] Z. Yao, M.L. Jenkins, M. Hernández-Mayoral, M.A. Kirk, Philosophical Magazine 90 (2010) 4623.
[9] E. Wakai, A. Hishinuma, Y. Kato, H. Yano, S. Takaki, K. Abiko, Le Journal De Physique IV 05 (1995) 10.
[10] I.M. Neklyudov, V.N. Voyevodin, Journal of Nuclear Materials 212-215 (1) (1994) 39-44.
[11] S. Ohnuki, H. Takahashi, T. Takeyama, Journal of Nuclear Materials 122 (1984) 317-321.
[12] P. Pareige, F. Pérocheau, P. Auger, S. Jumel, H. Bernas, Nuclear Instruments and Methods in Physics Research Section B: Beam Interactions with Materials and Atoms 178 (2001) 233-236.
[13] A. Etienne, B. Radiguet, N.J. Cunningham, G.R. Odette, R. Valiev, P. Pareige, Ultramicroscopy 111 (2011) 659-663.
[14] R. Krummeich, P. Pareige, J.P. Massoud, S. Jumel, Surface and Interface Analysis 36 (2004) 575-580.
[15] C.A. Williams, J.M. Hyde, G.D.W. Smith, E.A. Marquis, Journal of Nuclear Materials 412 (2011) 100-105.
[16] M. Matijasevic, A. Almazouzi, Journal of Nuclear Materials 377 (2008) 147-154.
[17] S. Novy, P. Pareige, C. Pareige, Journal of Nuclear Materials 384 (2009) 96-102.
[18] S.M.Dubiel, G.Inden, Z. Metallkde 78 (1987) 544–549.
[19] L.L. Horton, J. Bentley, K. Farrell, Journal of Nuclear Materials 108-109 (1982) 222-233.
[20] I.M. Robertson, M.L. Jenkins, C.A. English, Journal of Nuclear Materials 108-109 (1982) 209-221.
[21] M. Matijasevic, W. Van Renterghem, A. Almazouzi, Acta Materialia 57 (2009) 1577-1585.
[22] S. Xu, Z. Yao, M.L. Jenkins, Journal of Nuclear Materials 386-388 (2009) 161-164.
[23] B.C. Masters, Nature 200 (1963) 254.
[24] D.R. Baker, M.H. Loretto, R.E. Smallman, C.A. English, E.A. Little, MRS Online Proceedings Library 138 (1988) 77.
[25] M.R. Gilbert, Z. Yao, M.A. Kirk, M.L. Jenkins, S.L. Dudarev, Journal of Nuclear Materials 386-388 (2009) 36-40.
[26] S. Choudhury, L. Barnard, J.D. Tucker, T.R. Allen, B.D. Wirth, M. Asta, D. Morgan, Journal of Nuclear Materials 411 (2011) 1-14.
[27] P.R. Okamoto, L.E. Rehn, Journal of Nuclear Materials 83 (1979) 2-23.
[28] A. Volgin, B. Radiguet, Personal Communication, 2011.

Main conclusions and perspectives

The main objective of the current Ph.D. work was to provide a wide range of data on the microstructural behavior of irradiated Fe-Cr alloys (model alloys of ferritic-martensitic steels which are considered for use in some reactors of new generation), as a function of Cr concentration and temperature.

Indeed, the influence of Cr content on some important technological properties (for example, swelling, DBTT shift) of Fe-Cr alloys is non-monotonic and not completely understood. Therefore, within the current Ph.D. in order to investigate the Cr effect, the investigations of the microstructural response to irradiation have been performed on three low purity Fe-Cr model alloys with different Cr contents, namely: Fe-5%Cr, Fe-9%Cr and Fe-12%Cr.

The irradiation have been performed at two temperatures: 300°C (neutron irradiation up to 0.6 dpa), which represents the minimum operating temperature of F-M steels in Generation IV reactors, and 500°C (irradiation with 150keV Fe+ ions up to 1.5dpa) which represents the range of maximum operating temperatures.

The main technique used in the current study is 3D Atom Probe (3DAP). This instrument allows the investigations of the materials at the atomic scale, in the real space and in three dimensions. The use of 3DAP technique allow an accurate evaluation of the chemical composition, size and shape of nanometric clusters formed under irradiation as well as the study of segregations of the chemical species on dislocations and grain-boundaries. Moreover, some crystallographic information on those features has been also deduced.

Concerning intra-granular precipitation in model alloys after neutron irradiation up to 0.6 dpa at 300°C, the 3D images clearly revealed the presence of two different populations of clusters inside the grains. The first family are NiSiPCr-enriched clusters which have been observed in all the model alloys, and the second one are Cr-enriched clusters which correspond to α' clusters and have been observed in the Fe-9%Cr and Fe-12%Cr model alloys. Owing to the collected results it appears that two different mechanisms must be involved in the formation of these two populations of clusters:

- Cr-enriched α' clusters must have an irradiation enhanced origin. Indeed, they are present in the Fe-9%Cr and Fe-12%Cr, where Cr is supersaturated, but not in the Fe-5%Cr alloy, where Cr is undersaturated. Their number density increases with the Cr content between the 9%Cr and the 12%Cr that is also in favor of an irradiation enhanced origin of these clusters.

- NiSiPCr-enriched clusters must have radiation induced origin and they could be precursors of Ni-Si-enriched phases typically observed in high-chromium F-M steels after irradiation. Few facts are in favor of an irradiation induced origin of these clusters. First, the

extremely low nominal levels of Ni, Si and P in the alloys exclude any thermodynamic driving force for precipitation process. Second, NiSiPCr-enriched clusters are present in all model alloys with an identical number density after irradiation with the same flux up to the same dose. This is an indication of irradiation induced processes.

Considering these results, further work can be envisaged. 3DAP investigation of the same model alloys neutron irradiated at the same temperature up to other doses could give an important contribution to the understanding of the formation and evolution of the α' and NiSiPCr-enriched clusters. For example, samples neutron irradiated up to 0.06 dpa and 1.5dpa have been already investigated owing to TEM [1,2] and SANS [3–5] and the combination of these data with 3DAP could give very important information. 3DAP data on these alloys could also contribute to the interpretation of the irradiation induced hardening behavior [1].

Concerning the segregations on natural point defect sinks studied by 3DAP in the neutron irradiated model alloys, enrichment of Si, P and Cr atoms have been revealed on dislocation lines, low-angle grain boundaries (which consist of accommodation dislocation lines) and high-angle grain boundaries in all model alloys. Some Ni enrichment has been also observed when 3DAP enabled to detect Ni atoms. Zones almost free of clusters are present around all the GBs. 3D reconstructions exhibit a shift between Si and Cr segregations with respect to the core of the dislocations. This shift is probably a signature of the stress field around the dislocation lines.

It is known that experimental observation of Cr behaviour at the grain boundaries in ferritic/martensitic alloys does not show any unambiguous trend: both RIS and RID of Cr at GB has been observed without any clear dependence on Cr concentration, irradiation type, or temperature (see review [6–8] and references cited). Our results show a Cr enrichment. Nevertheless, the lack of 3DAP data on grain boundaries in the as-received states made it impossible to conclude on the behavior of Cr under irradiation in these alloys. Understanding of the RIS behavior of Cr (as well as other alloying elements) depends on whether the enrichment observed after 0.6 dpa is higher or lower than the enrichment at pre-irradiated grain boundaries. It means that 3DAP data on the as-received model alloys is of very large interest. The mentioned above experiments on the samples neutron irradiated to lower (0.06dpa) and higher (1.5dpa) doses are also desirable for clarifying the RIS behavior.

We should add to this, that as it has been mentioned in the Chapter 4, the solute excess of Cr and Si differs quantitatively from one grain boundary to another. This could arise from differences of grain boundary energies. Indeed, it is known that changes in grain boundary energy result in anisotropy of grain boundary segregation. The good way to clarify this question is to undertake systematic investigations of different GB owing to a coupling between EBSD and 3DAP. It is a very important work.

In order to study the effect of irradiation on the microstructure at elevated temperatures (planned in Generation IV reactors), ion irradiation of the Fe-9%Cr and Fe-12%Cr model alloys has been performed at 500°C. For providing more complete information on irradiation effect on microstructure, the combination of TEM and 3DAP has been used for the microstructural investigation.

At this temperature, only radiation induced precipitation is expected. Indeed, in good agreement with the new version of the Fe-Cr phase diagram proposed by Bonny et al. [9], we have shown that no precipitation occurs after thermal ageing for alloys with Cr content equal or lower than 12at%.

In-situ TEM study has shown that during 150 keV Fe^+ ion irradiation at 500°C of the Fe-9%Cr and Fe-12%Cr model alloys up to 1.5 dpa, damage becomes apparent in the form of randomly distributed dislocation loops. The evolution of the number density of visible loops with irradiation dose in both model alloys looks like very similar. It increases up to a value of about 1 to 1.2 dpa and saturates after. The contrast experiments have shown that the dislocation loops created in both model alloys after 1.5dpa irradiation are mainly of [100]-type: 80% in the Fe-9%Cr alloy and 72% in the Fe-12%Cr model alloy. Other dislocation loops are of ½[111] type, while few loops have not been assigned.

While the redistribution of point defects created during irradiation led to the formation of a large number of dislocation loops, 3DAP study of the same alloys irradiated under the same conditions but in the form of sharp tips did not reveal any chemical species redistribution. As it has been discussed in the Chapter 5, the geometry of the irradiated samples could have a high influence on the irradiation effect on the microstructure since the surface effect is not negligible. It means that the damage in the samples with the shape of 3DAP tips could differ from the one of the ion irradiated bulk material. This clearly shows that 3DAP investigation of ion irradiated bulk materials is necessary to go further. To do this, higher energy Fe^+ ion irradiation must be used in order to create damage far from the surface. Such irradiation has been undertaken in Ion Beam Centre in FZD, Dresden (Germany) in order to get a flat profile of damage up to about 1.5 μm (see Chapter 2, part ii,2(b) for details). 3DAP study of the irradiated alloys is under progress.

References

[1] M. Matijasevic, A. Almazouzi, Journal of Nuclear Materials 377 (2008) 147-154.
[2] Matijasevic M., Microstructure and Mechanical Properties of Fe-Cr Model Alloys and High Cr Steels Under Neutron Irradiation, PhD thesis., Gent University, 2007.
[3] F. Bergner, A. Ulbricht, C. Heintze, Scripta Materialia 61 (2009) 1060-1063.
[4] C. Heintze, A. Ulbricht, F. Bergner, H. Eckerlebe, J. Phys.: Conf. Ser. 247 (2010) 012035.
[5] C. Heintze, F. Bergner, A. Ulbricht, H. Eckerlebe, Journal of Nuclear Materials 409 (2011) 106-111.
[6] Z. Lu, R.G. Faulkner, G. Was, B.D. Wirth, Scripta Materialia 58 (2008) 878-881.
[7] G.S. Was, J.P. Wharry, B. Frisbie, B.D. Wirth, D. Morgan, J.D. Tucker, T.R. Allen, Journal of Nuclear Materials In Press, Corrected Proof (2011).
[8] S. Choudhury, L. Barnard, J.D. Tucker, T.R. Allen, B.D. Wirth, M. Asta, D. Morgan, Journal of Nuclear Materials 411 (2011) 1-14.
[9] G. Bonny, D. Terentyev, L. Malerba, Scripta Materialia 59 (2008) 1193-1196.

APPENDIXES

TABLE OF CONTENT

APPENDIX 1.
3DAP SPECIMEN PREPARATION PROCEDURE

High electric field (from about 30 to 50 V/nm) is needed at the surface of the 3DAP sample for the evaporation of the atoms. For this, the tip effect is used (see Chapter 2 for details). The radius of curvature R of the sample should be less than 100 nm. Two electro-chemical polishing techniques are mainly used to reach such sharpness: the "double layer" method and the "micro-loop" method [1].

"Double layer" method

The principle of preparation by this method is presented in Figure 1. The sample should be cut in the shape of a thin rod with square section of few tenth of millimetre. This rod is dip into a thin layer of electrolyte (75 % acetic acid + 25 % perchloric acid) floating on an inert liquid (Galden).

The sample (anode) is plugged to a positive potential (≈ 10 to 18 volts) and placed into the electrolyte. The neck starts to form in the active part of liquid. To avoid a preferential etching in the area of "electrolyte-air" interface, it is necessary to move the anode up and down (stage 1).

When the formed neck is thin and long enough, the sample is then dip into a second electrolyte composed of 2% of perchloric acid and 98 % of ethylene glycol monobutyl ether. A tension of 4 to 7 volt is then applied, until the neck breaks and the lower part of the rod fall down (stage 2). If the lower part of the rod is long enough, it can be used for preparation of a second tip by the "micro-loop" method (see below).

After electro polishing, the tip is cleaned in alcohol and its radius is controlled by TEM. Samples should be kept under vacuum until experiment is carried out.

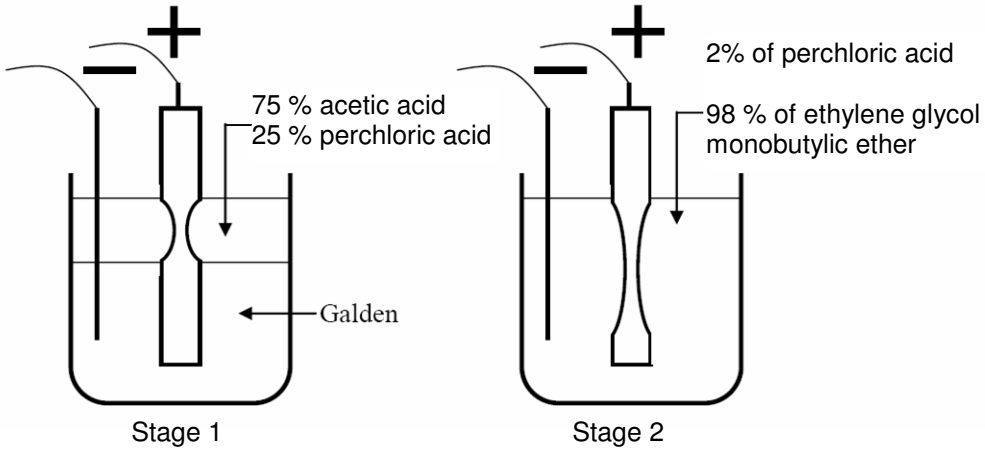

Figure 1. 3DAT tip preparation by the "double layer" method (from [2])

"Micro-loop" method

The micro-loop method allows to re-sharpen tips already analysed in 3DAP or to make tips from the short rods, when the double layer method can't be used. This method also allows to minimise the quantity of material necessary for the realisation of 3DAP experiments. This can be very useful, for example, in case of radioactive samples.

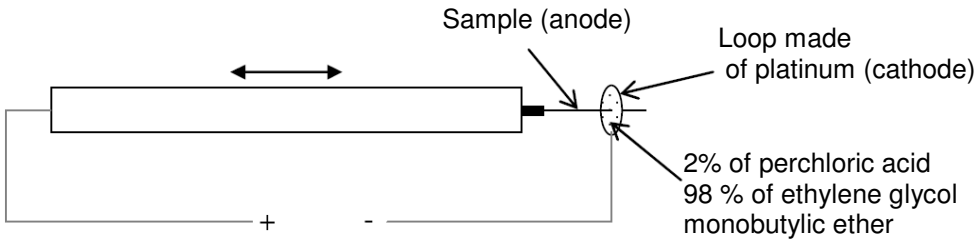

Figure 2. 3DAT tip preparation by the "Micro-loop" method (from [3]*)*

A loop made of platinum is filled with electrolyte (2% of perchloric acid and 98 % of ethylene glycol monobutylic ether) and a constant voltage is applied between the loop and the specimen. The specimen is moved frequently through the loop and polishing takes place (*Figure 2*). To control the polishing process the loop is mounted under an optical microscope.

As in the "double layer" method, a neck forms during the moving of sample. When the neck is ready to break, the tension is applied only when the neck comes out from the electrolyte it the direction of sample free end (during the sample movement to the left in *Figure 2*). This procedure is repeated until the break of the neck.

As in the "double layer" method, after electro polishing, the tip is cleaned in alcohol and the tip radius is controlled in the TEM.

APPENDIX 2.

TEM SPECIMEN PREPARATION PROCEDURE

The thickness of a specimen suitable for conventional TEM investigation is limited to about 200 nm. An ideal specimen for TEM should be thin, representative of the bulk sample, clean, stable, easily handled, conductive, free of surface segregation and selfsupporting.

The preparation of TEM specimens can be divided into an initial preparation step (cutting and mechanical polishing) and a final thinning step (electropolishing).

In the current work, the cutting was made with a rotating diamond wire up to a thickness of about 300μm.

The specimens were then prepared as flat and parallel sided samples using waterproof silicon-carbide papers. Papers with grit sizes of 600, 800, 1200 and 4000 were used. The thickness was reduced to about 100 μm.

After the mechanical polishing stage, specimen preparation continues with electrochemical polishing. It has been done using a Struers Tenupol-5 instrument. In electrochemical polishing, an acid solution (the electrolyte) is sprayed on the specimen until a hole is formed.

In this work, the following chemical solution was used: 87% ethanol, 11% acid perchloric, 2% butoxyethanol at – 10°C and 20 V.

APPENDIX 3.
PAS SPECIMEN PREPARATION PROCEDURE

Surface of PAS specimens should be prepared before PAS measurement to remove the deformed surface layer or oxide layer. It is also important to ensure that defects are not present in the sample before irradiation or it could lead to misinterpretation. PAS specimens were characterised before irradiation to determine the best way to remove surface defects created during cutting. Annealing to remove defects is non-desirable: this treatment could change the microstructure leading to difficulties to compare the results received from others laboratory working in the project.

To obtain the data on as-received state, few kinds of samples preparation were tested. The first measured specimens (Fe-5%Cr, Fe-9%Cr and Fe-12%Cr alloys) were cut at SCK (Mol, Belgium) with a size of $10\times10\times1mm^3$. The Slow-Positron-Beam experiments on the Fe-9%Cr and Fe-12%Cr alloys showed that S parameter of the sample is larger than S parameter of the pure iron reference sample and W parameter smaller than W reference, as shown in Figure 3, where the ratios of S/S_{ref} and W/W_{ref} are represented (S_{ref}=0.3570 and W_{ref}=0.1115, see Chapter 2). The VEPFIT fittings considering one layer gave a value of the diffusion length of 50 nm that is less then for the iron reference (184 nm). These results indicate that samples are not defect free or the presence of an oxide layer at the surface. This kind of preparation has appeared unsatisfactory.

To remove the deformed surface layer all the specimens were mirror polished and then chemically etched using a (15 ml HF – 250 ml H_2O_2 – 30 ml H_20) solution. After etching the surface was inhomogeneous and rough. The PAS experiments on the Fe-9%Cr and Fe-12%Cr showed that defects still exist in the bulk of the investigated samples ($S > S_{Ref}$,$W < W_{Ref}$) but in smaller amount compared with as-cut samples.

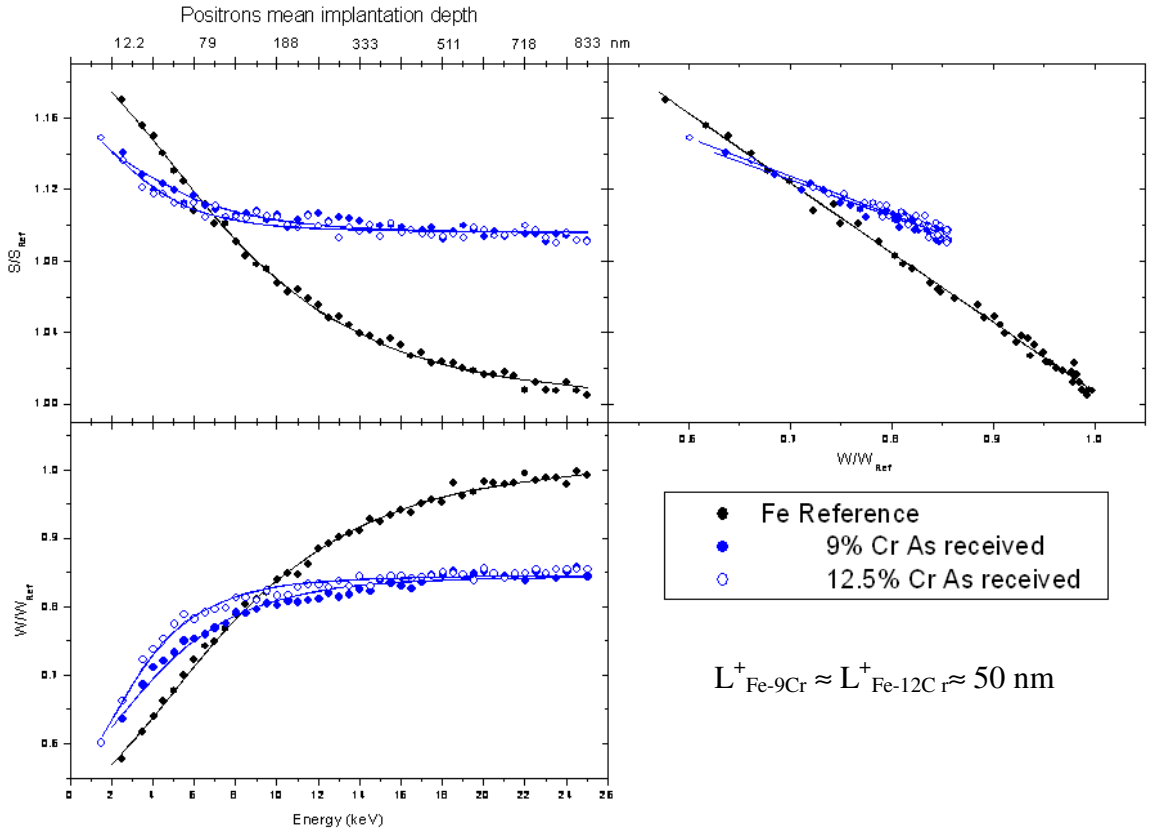

Figure 3. Variation of the characteristic S and W as a function of the positron energy for the pure Fe reference sample and after mechanical cutting.

To increase the quality of the surface, electrochemical polishing in a solution of 2% of perchloric acid and 98 % of ethylene glycol monobutyl ether after mechanical polishing has been undertaken (Figure 4). The sample (anode) is plugged to a positive potential (≈ 80 volts) and placed into the stainless cup (cathode) with the electrolyte (~250ml). The temperature of the electrolyte should be kept in the range of 0 to 20°C. The sample should be shaken in the electrolyte to ensure the homogeneity of the polishing process. After the electrochemical polishing, the samples were cleaned in acetone and ethanol.

The PAS experiments on the Fe-5%Cr, Fe-9%Cr and Fe-12%Cr model alloys after the electrochemical polishing show the best agreement with the reference results (Figure 5). The fitted diffusion lengths of the bulk layers are 129, 132 and 110 nm for the 5, 9 and 12%Cr model alloys respectively. This indicates that some defects are still present in the sample but in small quantity (see Chapter 3 for details). This is reflected in the value of the diffusion lengths that is smaller than the one received in the annealed pure Fe.

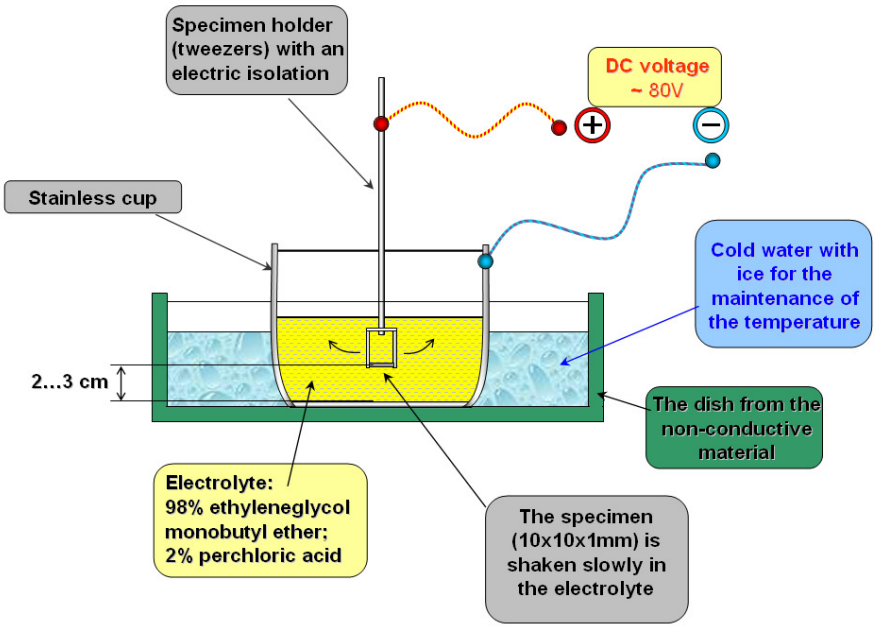

Figure 4. The scheme of the electrochemical polishing of PAS samples in GPM

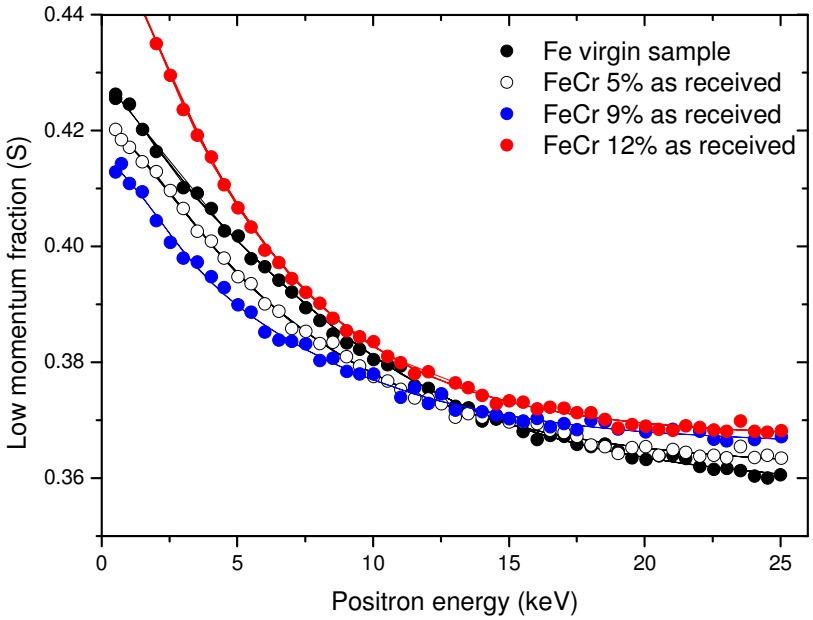

Figure 5. Variation of the S characteristic as a function of the positron energy for the pure Fe reference sample and for the Fe-Cr model alloys after electrochemical polishing

The comparison of different ways of preparation of sample shows the strong dependence of results of PAS experiments from the quality of the surface treatment. It has appeared that it is impossible to get rid of the deformed surface layer by simple mechanical polishing. It is related to the fact that this process also introduces defects. The results of experiments after mechanical polishing and electro-chemical polishing have shown that the decreasing of the size on the depth in average from 10 to 15 μm is sufficient to remove the defect rich layer.

APPENDIX 4.
PARAMETERS OF SRIM CALCULATIONS

The irradiation damage of materials is generally characterized in terms of the average number of times that an individual atom is displaced from its lattice site (so-called 'displacements per atom' (dpa) value) [4]. Since during ion implantation the accelerators deals with the fluence and flux parameters (in [ions·m^{-2}s^{-1}] and [ions·m^{-2}] respectively), the specific calculations, which consider the interaction of implanted ions with the matter, are needed to estimate the dose rate and irradiation dose (in [dpa·s^{-1}] and [dpa] respectively).

Stopping and Range of Ions in Matter (SRIM) – is a group of programs which allows the estimation of interaction of ions with materials using a quantum mechanical treatment of ion-atom collisions. In the current Ph.D. thesis the TRIM (Transport of Ions in Matter) software (which is a part of SRIM group of programs) has been used for dose rate and dose parameter estimation during ion irradiation experiments (see Chapter 2 and Chapter 5). A description of the calculation can be found in the tutorial book [5], several lessons to help learn how to use SRIM/TRIM are also available on-line [6]. Just a brief description of parameters of calculation is presented in the current appendix.

The next parameters have been used (Figure 6):

Type of TRIM calculation: – the option "Detailed Calculation with full Damage Cascades" is used. This option allows to take into account every recoil until its energy drops below the lowest displacement energy of any target atom.

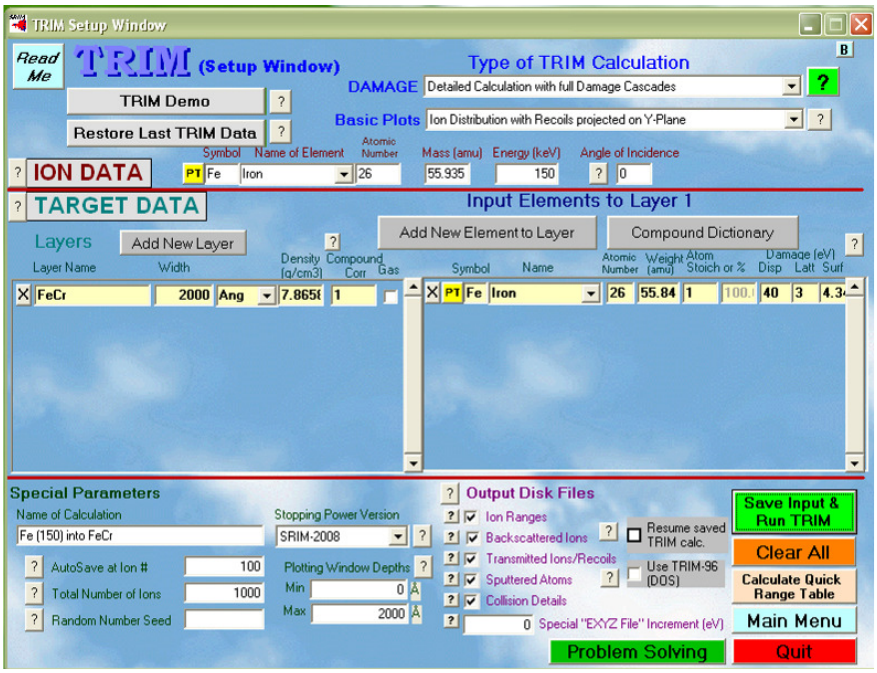

Figure 6. View of window for the TRIM Setup with the parameters used for calculation of the damage in 3DAP tips from the Fe-Cr model alloy during irradiation with 150 keV Fe^+ ions

Ion data: according to the experiment conditions (see Chapter 2), Fe ions have been chosen with energy of 150keV. Angle of incidence equal to 0° is used for damage calculation in 3DAP tips, and equal to 38° – for damage calculation in TEM thin foils. The latter angle is chosen in order to perform ion irradiation and TEM observation simultaneously. Schematically the positions of ion beam, electron beam during irradiation experiment and thin foil is shown in Figure 2.7 (p.___)

Target data: for calculation of irradiation damage the density of all the Fe-Cr model alloys has been considered to be equal to the one of pure Fe (7.86 g/cm^3). It is believed this approximation doesn't strongly affect the calculation results.

The width of the layer has been considered to be 2000 Å (200nm). This is the maximum thickness of thin foils suitable for conventional TEM investigation and the maximum diameter of 3DAP tips. This width is large enough to ensure that any damage cascade created by Fe^+ ions (150keV) will not cross through the all target width.

The displacement energy has been considered equal to 40 eV – the energy which is required to displace an Fe atom from its stable lattice position according to the ASTM (American Society for Testing and Materials) standard [7].

Special Parameters: at least 1000 ions have been used for calculation of the damage cascades during irradiation.

References

[1] M.K. Miller, Atom Probe Tomography: Analysis at the Atomic Level, Kluwer Academic/Plenum Publishers, New York, 2000.

[2] S. Novy, Mécanismes De Vieillissement à Très Longue Échéance Des Aciers Inoxydables Austéno-ferritiques, PhD thesis. UNIVERSITE DE ROUEN, 2009.

[3] A. Etienne, Etude Des Effets D'irradiations Et De La Nanostructuration Dans DesAciers Austénitiques Inoxydables, PhD thesis. UNIVERSITE DE ROUEN, 2009.

[4] M.J. Norgett, M.T. Robinson, I.M. Torrens, Nuclear Engineering and Design 33 (1975) 50-54.

[5] J.F. (James F.) Ziegler, U. Littmark, J.P. Biersack, The Stopping and Range of Ions in Solids / J.F. Ziegler, J.P. Biersack, U. Littmark, Pergamon, New York, 1985.

[6] SRIM - Lessons and Tutorials, http://www.srim.org/SRIM/Tutorials/Tutorials.htm, 2011.

[7] ASTM Standard E693-94, Standard Practice for Characterising Neutron Exposure in Iron and Low Alloy Steels in Terms of Displacements Per Atom (dpa), 1994.